A study of zeolite's catalytic deactivation and its effect on the crystal structure

Kristoffer Grimstvedt

60 ECTS

Master thesis in Chemistry

Department of Chemistry

Faculty of Mathematics and Natural Science

University of Oslo

2022

Acknowledgements

This master thesis is the result of work performed at the Department of Chemistry, University of Oslo (UiO), from 2019 to 2022 under the supervision of prof. Stian Svelle. Most of the work presented in this thesis has been carried out at the Department of Chemistry, University of Oslo.

I want to especially thank prof. Stian Svelle as well as Georgios Kalantzopolous for guiding me during this work. As well as Nico König, Nicolai Junge, Sebastian Prodinger, Odd Bygnes, Chris Affolter, Daniel Firth and the rest of the catalysis group at UiO for assisting me and supporting me during the time I have been working on this project.

I would like to thank David Wragg and Martin Jensen for instructing me and training me on using the XRD instruments and SEM microscope.

I would also like to thank my family and friends for supporting and believing in me during the period of the work.

2022

A study of zeolite’s catalytic deactivation and its effect on the crystal structure

Kristoffer Grimstvedt

http://www.duo.uio.no

Abstract

Zeolites are used in catalysis due to their highly porous structure which yield high surface area and potential high catalytic activity. In catalysis, catalyst deactivation continues to have a major focus and deactivation by coke is one way zeolite catalysts are being deactivated. When carbon is present during a catalytic process it is likely to result in formation of coke over time. One raw material for catalytic process that contain carbon is methanol. Methanol is used as a raw material for the methanol to hydrocarbon (MTH) process, which is a route for production of gasoline, olefins and other hydrocarbons that is used in the industry.

In this work deactivation by coke has been studied by methanol to hydrocarbon conversion (MTH) over the ZSM – 5 zeolites ACS extrudates and two homemade ZSM – 5 zeolites (denoted as HM02 and HM03) as well as four Beta zeolites. The conversion was carried out at reaction temperature of 400°C and WHSV = 2.95 $g_{MeOH}\, g_{catalyst}^{-1}\, h^{-1}$. The deactivated materials have been investigated by x – ray diffraction (XRD) and thermogravimetric analysis (TGA).

Large differences in catalyst lifetime were observed with rapid deactivation of the Beta zeolites, compared to the ZSM – 5 zeolites. HM02 was the ZSM – 5, that deactivated fastest and HM03 was the material with the longest lifetime. Where HM02 had 14% yield at 38 hours (end time of experiment) and HM03 had 51% yield at 69 hours (end time of experiment).

TGA has been applied to determine the amount of coke in the ZSM – 5 zeolites. It was determined that the ACS extrudates contained 10 wt.% of coke, HM02 contained 1.3 wt.% of coke and HM03 contained 8 wt.% of coke.

By use of XRD on the materials in this work, HM01 (first homemade) was identified as the least crystalline material with 50.1% crystallinity and HM02 was identified as the most crystalline material with 95.4% crystallinity.

By performing XRD on deactivated and non – deactivated HM02 and HM03, it was determined that there were distinct differences between the patterns of the deactivated and non – deactivated form of the materials. It was also determined that HM03 had more changes to its XRD pattern due to coke in its structure than HM02.

The differences in properties between HM02 and HM03 is caused by use of different alumina sources during the synthesis, where an alumina source from Fluka was used for HM02 and an alumina source from Aldrich was used for HM03. By use of scanning electron microscope (SEM) it was identified

that these two materials had different particle size, where HM02 had crystals with an average particle size of $35\ \mu m \times 16\ \mu m$ and HM03 had varying crystal size from 15 μm to 60 μm.

From this work it is concluded that HM03 and MFI – 27, can be used for future studies of catalyst deactivation, since HM03 was the material with the highest catalytic activity and there has been done previous studies on MFI – 27 which can be continued.

List of abbreviations

AlPO	Aluminophosphate
AN	Atomic number
BEA	Zeolite Beta polymorph A
BET – theory	Brunauer Emmet Teller theory
BSE	Backscattering of electrons
CBU	Composite building unit
DME	Dimethyl ether
DSC	Differential scanning calorimetry
EA	Element analysis
EDS	Energy dispersive spectroscopy
EDX	Energy dispersion x - ray analysis
EL	Element
FWHM	Full width at half maximum
FID	Flame ionization detector
GC	Gas chromatography
HF	Hydrogen fluoride
HM	Homemade
ICP – AES	Inductively coupled plasma atomic emission spectrometry
ISMA	In situ mass analyzer
MeOH	Methanol
MFI	Mobil five

MP-AES	Microwave plasma atomic emission spectrometer
MS	Mass spectroscopy
MTH	Methanol to hydrocarbons
PFR	Plug flow reactor
PTFE	Polytetrafluoroethylene
SAPO	Silicoaluminophosphate
SBU	Secondary building unit
SDA	Structure directing agent
SE	Secondary electron
SEM	Scanning electron microscopy
TC	Thermal conductivity
TGA	Thermogravimetric analysis
TOS	Time on stream
TPABr	Tetra propyl ammonium bromide
TPO	Temperature programmed oxidation
TPR	Temperature programmed reduction
UiO	University of Oslo
WHSV	Weight hour space velocity
wt.	Weight
XRD	X - ray diffraction
ZSM	Zeolite Socony Mobil

Table of content

1 Introduction

1.1 Porous materials

Porous materials have pores that differ from nanometers to millimeters. Terms that are used for porous materials with different pore size are microporous, mesoporous and macroporous materials. Microporous materials have pore diameters less than 2 nm, mesoporous materials have pore diameters between 2 and 50 nm and macroporous materials have pore diameters greater than 50 nm (1). The pore size of materials gives materials different chemical and physical properties. What's great about porous materials, is that they have large surface area, which gives the opportunity for functionality. They also have low density, making them light weights. Porous materials are made up by various chemical compositions and they have ordered or irregular arrangements of pores. Porous materials have been used for catalysis, insulation, membranes, construction materials and more (2). One group of such porous materials are zeolites. Zeolite pores are illustrated in Figure 1-1.

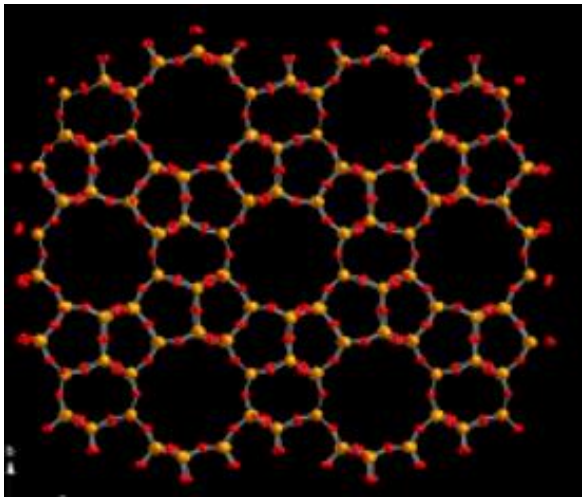

Figure 1-1: An image of ZSM – 5 zeolite pores from difference Fourier mapping. The yellow balls represent silicon and the red balls represent oxygen. Adapted from (3).

1.2 Zeolites

Zeolites were first described by Axel Fredrik Cronstedt in 1756. He discovered zeolites, when a sample upon heating produced large amounts of steam, which was desorbed by the material (4).

The initial synthesis of zeolites was based on observations and analysis of natural zeolites. Later the chemists started trying to replicate the conditions that the zeolites were formed upon in the laboratory. Zeolites are synthesized at hydrothermal conditions and hydrothermal synthesis was first reported to be used in zeolite synthesis by Richard Barrer and Robert Milton in the 1950s (4).

Zeolites are defined as aluminosilicates with open 3 - dimensional framework structures composed of corner - sharing TO_4 tetrahedra, containing voids, where T is Si or Al. Zeolites are microporous inorganic solids and voids in zeolites are unoccupied space in their structure. They are crystalline, which gives them identical pores through the entire crystal structure (4).

A general zeolite formula can be: $M_{x/y}[(Al_xSi_{1-x})O_2] * qQ$, where $M_{x/y}$ are exchangeable cations, Q are sorbate molecules (usually water) and $(Al_xSi_{1-x})O_2$ are the anionic framework (4).

Zeolites has obtained attention for its properties for adsorption and ion exchange for purpose of potential environmental pollution. The main uses of zeolites today are as detergents, for separation and as catalysts. They are used in industrial scale and in ordinary products such as in toothpaste, where it is used to bind Calcium (Ca). Reasons for the use of zeolites in catalysis, is that zeolites have highly porous structures, which leads to high surface area and high surface area gives it potential for catalytic activity. Zeolites have pores with molecular dimensions, which leads to shape selectivity. The material has also high thermal stability, which makes it possible to work at high temperatures.

There exist many different zeolites, both natural and industrially synthesized. The silicon and aluminum ratio in their framework differ between these different zeolites. The Si/Al ratio can differ from approximately 1 to above 100, where a ratio of 1 is considered as the highest possible aluminum content in tetrahedral aluminosilicate framework (5).

Structure directing agents (SDAs) for zeolites are metal hydroxides or organic materials like NaOH and tetra propyl ammonium (TPA) respectively. An SDA is an additive which is required to direct the reaction in the synthesis to the desirable product (6).

pH during synthesis is usually approximately 12, because it is needed for Al to be in the correct state, which is tetrahedral $Al(OH)_4^-$. A high pH is also important during synthesis because the silica is more soluble at higher pH.

Zeolite acidity originate from its hydroxy – groups, as illustrated in Figure 1-2. The acid site shown is a Brønsted acid sites. A zeolite act as a Brønsted acid by being able to donate the hydrogen from the hydroxy – group and its properties are dependent on a zeolite's structure (7).

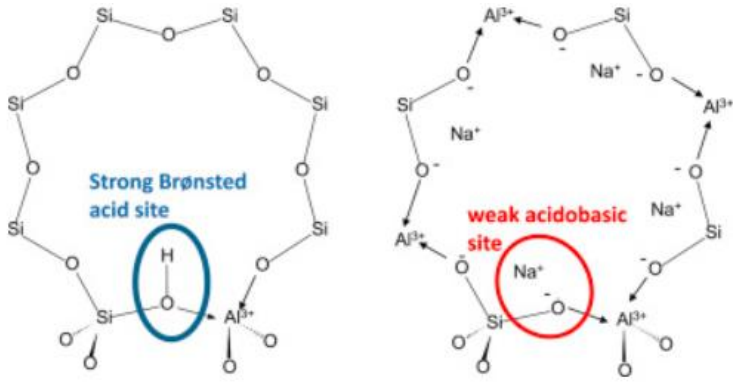

Figure 1-2: Example of acid site of an 8 membered ring zeolite. Adapted from (7).

Crystal size, acidity and pore size is properties of zeolites that is possible to control during synthesis. Crystal size can be controlled by controlling the nucleation and crystallization, which can be done by varying the structure directing agent, use of different Si and Al sources, use of different heating techniques and biphasic synthesis (the growing crystals are encapsulated by external molecules). Since Al^{3+} and Si^{4+} has different charges and different acidities, each Si/Al ratio will have an impact on a zeolite's properties (5). Thus, the acidity can be controlled by changing the Si/Al ratio for the zeolite.

Protonic zeolites are zeolites on their protonic form, where they have protons in their framework to balance the structure for Al substitution in the structure**.** Protonic zeolites are today largely used in the industry for catalytic cracking. Some zeolites with substituted transition metals find applications within catalysis as redox catalysts, such as for reduction of NOx with ammonia (8).

Cationic zeolites are largely used in the industrial adsorbents for gas purification. Including CO_2 capture, to produce membranes for gas separation and as ion exchangers (9).

The pore size can be controlled during synthesis of zeolites by choosing a proper template (7). A zeolite template is an organic or inorganic additive that is used to help the zeolite grow and stabilize the zeolite structure by filling the empty space. The number of atoms in the zeolite ring affects the pore size of the zeolite as illustrated in Figure 1-3.

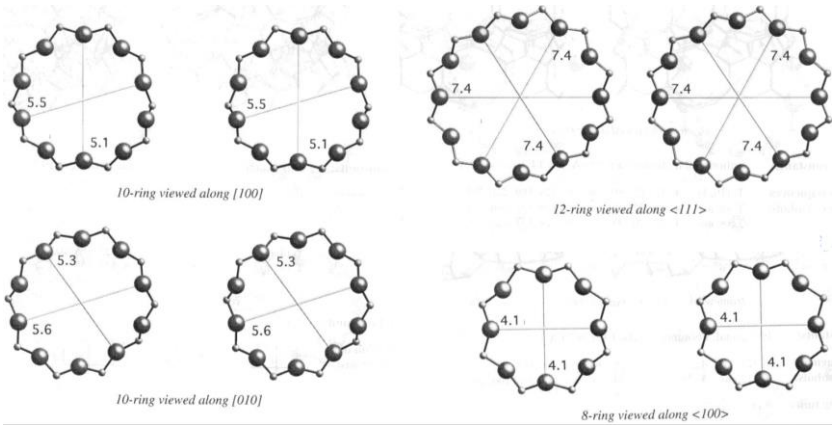

Figure 1-3: Different zeolite ring sizes, with 8 membered rings, 10 membered rings and 12 membered rings. Adapted from (10).

Different orientations and arrangements of zeolite's tetrahedra leads to different composite building units (CBUs) or secondary building units (SBUs). Figure 1-4 illustrates some examples of SBUs.

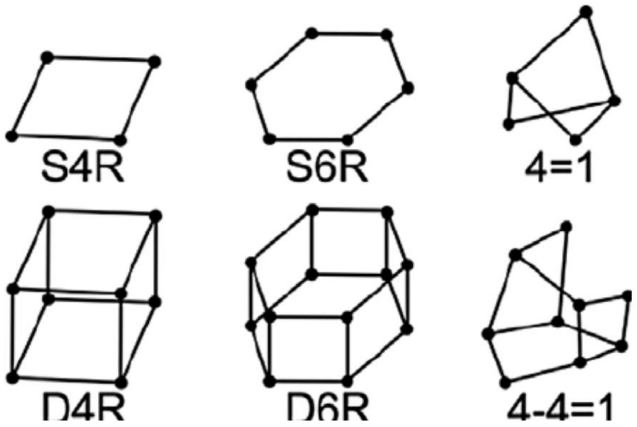

Figure 1-4: Examples of SBU's for zeolites. Adapted from (11).

A ZSM - 5 (zeolite Socony Mobile) zeolite is in the Pentasil family of zeolites, where ZSM – 5 is a trade name. It has an MFI (CBU) type framework, where MFI is an abbreviation for 'Mobil five' which is based on the patented company, Mobil oil and that the Pentasil units is

composed of five - membered rings. The zeolite's framework composes of MFI units that are linked together to form chains. It is a 3 – dimensional structure (as illustrated in Figure 1-5) and the channels in its structure have 10 membered rings with approximately 5.5 Å diameters (as is illustrated in Figure 1-3) (12). Its unit cells are orthorhombic (13, 14). The ZSM – 5 zeolites used in this work is ACS extrudates (which is a ZSM – 5 material from ACS Materials), MFI – 27 (which is a commercial ZSM – 5 material from Süd Chemie), CBV 8014 (which is a commercial ZSM – 5 material from Zeolyst) as well as two homemade ZSM – 5 zeolites, which is denoted HM02 and HM03. Unlike the rest of the ZSM – 5 materials, the ACS extrudates are not 100% zeolite. The composition of the material is 70% zeolite and 30% alumina (15).

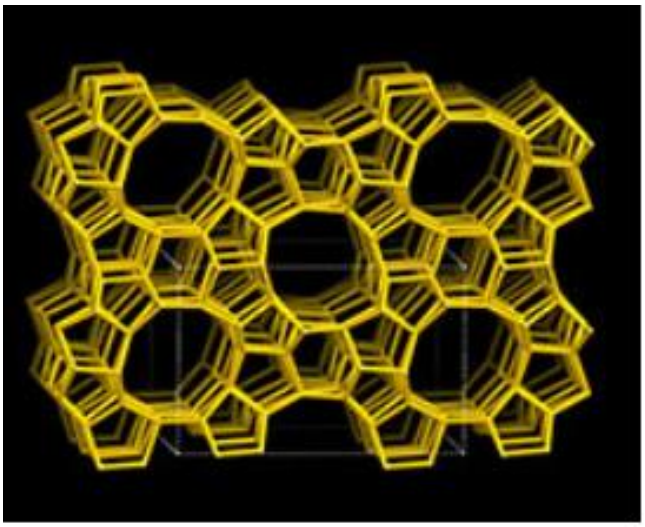

Figure 1-5: An MFI framework viewed along the (010) plane. Adapted from (13, 14).

A Beta zeolite has a 3 – dimensional framework and it has a BEA (zeolite Beta polymorph A) type framework (as illustrated in Figure 1-6). The zeolite framework is disordered and is composed of mor (mordenite) units, that are linked together via 4 – rings to form a layer of saddle – shaped 12 rings. The channels in its structure have 12 membered rings with pore diameters of approximately 7 Å (as is illustrated in Figure 1-3) (16, 17). The Beta zeolites used in this work is denoted 09-00243/1, SK_CP814C, CP806B-25 and CP811BL-25.

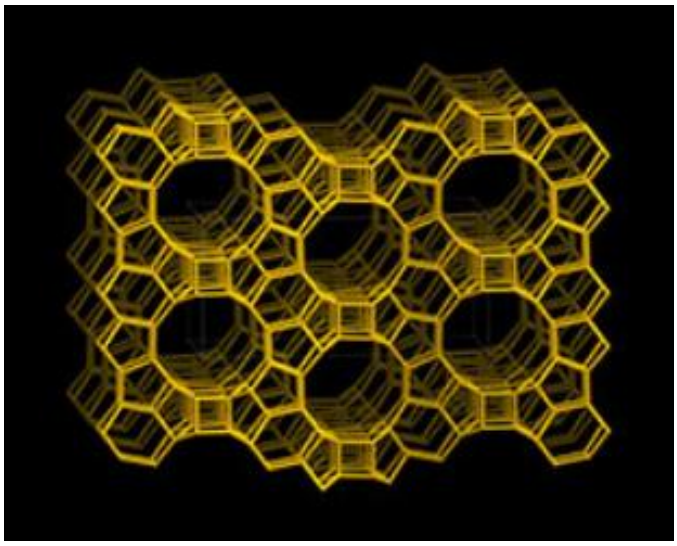

Figure 1-6: A polymorph in the BEA framework viewed along the (100) plane. Adapted from (13, 16).

1.3 Porosity and selectivity

Porosity is one of the key properties of zeolites, which give them properties of interest. There are many different zeolites with different structures, which give rise to different pores and channels. The shape of zeolite pores and channels determine its selectivity. The selectivity is decided on which molecules go through the channels and what comes out. Selectivity is used to describe the relative composition of the products and is often given in percentage of the amount each product makes among all products (18). Selectivity is defined as:

$$Selectivity = \frac{n_A}{n_A + n_B + \ldots} \times 100\% \qquad \text{(eq 1)}$$

Where A and B is reactants,

n_A is the initial amount of A and n_B is the initial amount of B.

There are three types of zeolite shape selectivity, which is reactant shape selectivity, product shape selectivity and restricted transition state selectivity. The reactant selectivity excludes reactants based on shape and size. Product selectivity allows for specific products to diffuse out. Restricted transition state selectivity makes only transition states leading to fit some structures to occur. The three types of shape selectivity are illustrated in Figure 1-7.

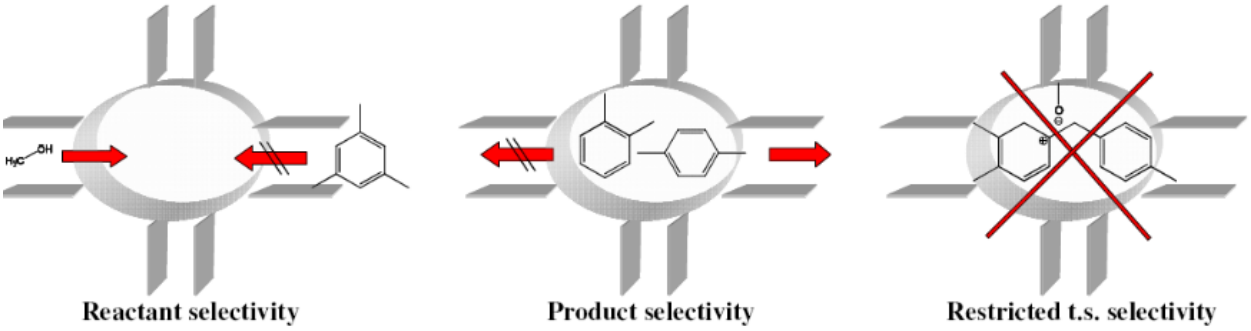

Figure 1-7: Reactant selectivity, product selectivity and restricted transition state selectivity for zeolites. Adapted from (10).

1.4 Zeotypes

There are 'look - a – like' materials of zeolites. Two of them are silicoaluminophosphates (SAPO) and aluminophosphates (AlPO) materials, which has the same structure as zeolites, but different compositions.

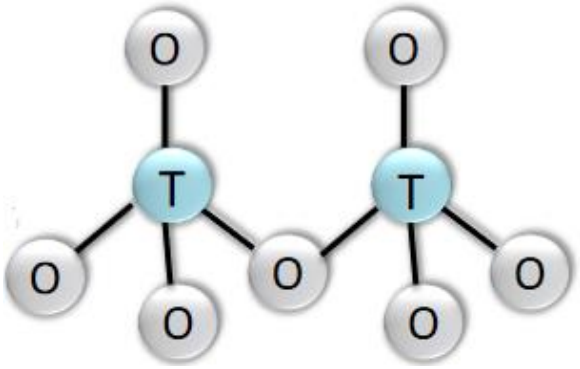

Figure 1-8: TO_4 structure. Adapted from (10).

SAPO and AlPO has a crystal structure as illustrated in Figure 1-8, where O is oxygen and T is either aluminum or phosphate for AlPO or either aluminum or silicon for SAPO. For SAPO the silicon is introduced by substituting a few of the aluminum atoms. In an AlPO material, there are no extra charges, since Al are 3+ and P are 5+ and thereby compensating for the charges from O. For an Al/Si SAPO however, P is substituted by Si which gives rise to extra charges that must be compensated for, since Si is 4+. The structure will in total have one negative charge, which can be balanced with either a proton or a metal cation to make it either a Lewis acid or a Brønsted acid (10).

1.5 Methanol to hydrocarbons conversion

The methanol to hydrocarbons (MTH) technique is a step to produce hydrocarbons, which represents a route for formation of gasoline and olefins by use of methanol (MeOH) (19, 20). The reaction is a flexible alternative step in the upgrading of natural gas, coal or biomass. The methanol to hydrocarbons conversion reaction is an important process, where methanol is dehydrated under formation of dimethyl ether (DME) and water, followed by formation of alkenes. By tuning the catalyst and process conditions, methanol can be converted into a variety of hydrocarbon products (21). Because the reaction occurs within pores of molecular dimensions, the product selectivity is highly dependent on the size and arrangement of the channel system.

1.6 Deactivation

The main challenge for zeolites is catalytic deactivation, which reduces the performance of the zeolite. Yield and conversion are two factors, which describes a catalyst's performance. Conversion is used for stating and comparing zeolite activity (18). It is defined as:

$$Conversion = \frac{n_{A_0} - n_A}{n_{A_0}} \times 100\% \qquad \text{(eq 2)}$$

Where:

A is the reactant,

n_{A_0} is the initial amount of A,

n_A is the amount of A at a given reaction time.

Yield is used to describe each of the formed products (18) and is defined as:

$$Yield = \frac{Selectivity \times Conversion}{100\%} \qquad \text{(eq 3)}$$

Three types of catalyst deactivation are sintering of metal or support, poisoning and coke formation. Sintering occurs when small particles form larger particles, which decreases the surface area of catalysts. Metal sintering proceeds by diffusion of single metal atoms over the support surface, or by diffusion of the metal particle over the surface. Sintering may occur by evaporation followed by deposition on the surface. The metal sintering stability increases with increasing melting point, because of higher bond strength in the metal.

Poisoning happens to catalysts when impurities in the reactor feed form bonds (chemisorb) on the catalyst surface and thereby blocking active sites on the catalyst surface.

Coke formation is when carbon is formed, deposited on a catalyst surface and blocking the catalyst's pores and active sites for reactant molecules, which results in the catalyst losing its catalytic properties (22). Coke is another word for carbon and carbon formation tend to happen over time during catalytic reaction, when compounds containing carbons are present. Coke formation is the main reason for catalyst deactivation in MTH conversion. The reaction for methanol conversion in MTH is:

$$CH_3OH + RH \rightarrow CH_3R + H_2O \qquad \text{(eq 4)}$$

Where R is a carbon chain.

Coke will gradually deposit on the catalyst over time during MTH conversion. The rate of coke formation is dependent on reactant composition, reaction temperature, pore diameter and acid strength of the catalyst (22).

The deposited coke can be removed by combustion for reuse of catalyst (known as regeneration).

1.7 XRD as a method to investigate the deactivation of zeolites

It is demonstrated by Daniel Rojo-Gama in *'A straightforward descriptor for the deactivation of zeolite catalyst H – ZSM - 5'* (23) that a unit cell may change upon deactivation. As - synthesized ZSM - 5 catalysts are orthorhombic, where the a and b vectors differ and it has been reported that upon deactivation, the difference between these two vectors are gradually decreasing. If the difference between the a and b vectors (vector in x and y direction as illustrated in Figure 1-9) get close to zero, a zeolite may change symmetry to tetragonal.

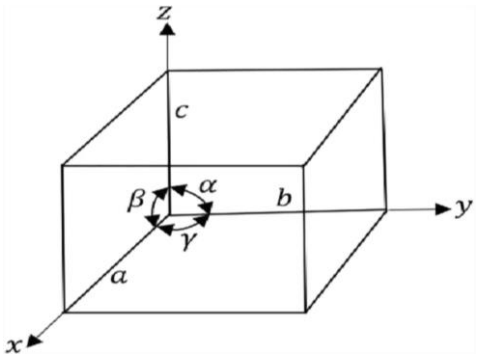

Figure 1-9: 3 – dimensional unit cell for a crystal. The dimensions of a unit cell are designed by 3 unique edges (a, b and c) and 3 unique angles (α, β and γ). The difference in these parameters gives rise to multiple geometries. Adapted from (24).

The change in symmetry happens, because of buildup of coke in the zeolite's pores. This change in a material's symmetry can be detected by use of XRD as a method. Figure 1-10 shows how XRD diffractograms of a ZSM – 5 zeolite changes with change in coke content, where a gradual change in the XRD pattern as the zeolite becomes more deactivated can be observed (illustrated by the double peak at 45.05° that gradually becomes a single peak). For a ZSM – 5 zeolite, there are changes in several diffraction peaks at different angles that can be observed, like at 8.82°, 23.08° and 23.32° to mention some (23).

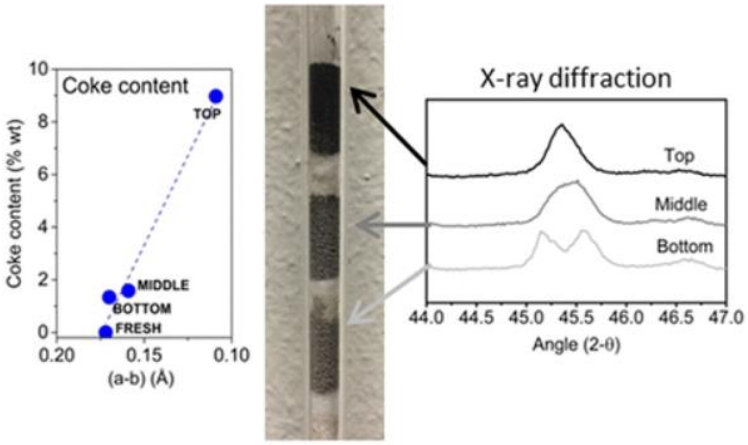

Figure 1-10: In the middle, three layers of a ZSM – 5 zeolite in a reactor with difference in coke content is shown, where the material increases in coke from bottom to top. On the right, XRD diffractograms for the three layers are given and, on the left, a distribution is given for how the difference between the a and b, unit cell parameters change for the zeolite, as the coke content for the material increases. The instruments used to gather the XRD patterns was operated in Bragg – Brentano geometry and with Cu K_{a1} radiation. Adapted from (23).

2 Project motivation

Zeolites are microporous crystalline materials of huge industrial importance for catalysis, gas separation and ion exchange (9). ZSM - 5 (structure is illustrated in Figure 2-1) is one example of an aluminum silicate zeolite catalyst (25). Industrial catalysts tend to suffer from loss in activity and lifetime by coking on the catalyst's surface. There are much to gain by improving the efficiency of industrial catalysts, by reducing coke deposition on their surface. This is possible by monitoring the procedure and getting more insight and knowledge about the coking process. Further will this give the possibility to understand and ultimately control the coking, or at least the opportunity to reduce the effects of coking.

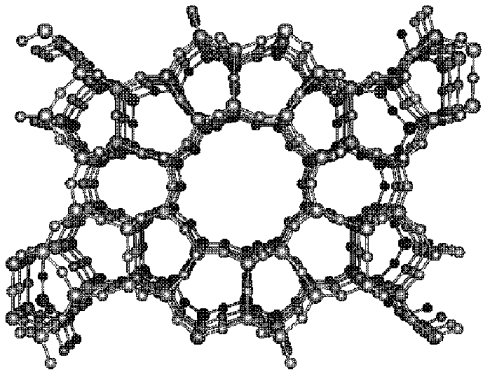

Figure 2-1: Illustrates a unit of a molecular structure of the zeolite ZSM - 5. Adapted from (26).

The original plan (pre-pandemic) was to use the new micro balance reactor developed by SINTEF, which is called in situ mass analyzer (ISMA) in this thesis and compare it with measurements from the thermogravimetric analysis (TGA) available at the University of Oslo (UiO). The instruments were supposed to be investigated to compare the accuracy and precision of measurements for these two instruments.

Due to the global pandemic of Covid-19, which requires restrictions for personnel and work permittance at the facilities, the micro balance reactor, ISMA, could not be used.

As this master thesis became a part of the TOMOCAT project, which investigates the deactivation of zeolites, the scope of the work was changed to testing and characterizing the homemade ZSM – 5 zeolites. As a contribution to the TOMOCAT project, the homemade

zeolites will be compared with a total of seven commercial zeolites and evaluated, whether they are suitable for further studies for catalyst deactivation or not.

The TOMOCAT project is about tracking of the deactivation of shaped zeolite catalysts in time and space using x – ray diffraction topology. The motivation for the project is to enable technology for the transition from a fossil - based society to a renewable-based scenario. Zeolites are foreseen to play a pivotal role in the production of fuels and chemicals. The objective for the project is to provide insight that might pave the way for a more efficient utilization of these materials (27).

The main purpose of this work is hence, to investigate these zeolite's catalytic properties and usability in industrial catalytical processes.

The redefined new goal of this work is to characterize the zeolites by use of basic characterization methods and to evaluate if the commercial extrudates are suitable for further studies for catalyst deactivation.

The goal will be achieved by synthesizing three ZSM - 5 zeolites, characterizing the homemade ZSM - 5 zeolites and three commercial ZSM – 5 zeolites, studying catalyst activity in MTH conversion, characterization of deactivated catalysts that include temperature programmed oxidation (TPO) by synchrotron (carried out by external lab) and use of XRD-descriptor on zeolite extrudates that contain both zeolite and alumina, as well as pure zeolite materials to evaluate the degree of deactivation of the materials.

One of the commercial ZSM - 5 zeolites will be used (MFI - 27) to compare with the homemade materials for XRD, TGA and SEM. MFI - 27 was synthesized by Daniel Rojo-Gama and characterized several years ago (28). To ensure that there were no impurities and the material was on proton form, deionization and calcination of the zeolite was required, before it could be used in this study. The second commercial ZSM – 5 zeolite was extrudates from ACS Materials and a third commercial ZSM – 5 zeolite (CBV 8014) will also be used for potentiometric titration.

In addition to the ZSM – 5 zeolites, four commercial Beta zeolites will also be tested for MTH conversion, to increase the experience with the technique and prepare the materials for further catalytic characterization by others in the TOMOCAT project (which include synchrotron studies).

Since zeolites is used in the industry as catalysts, the motivation for this work is to get a better understanding of deactivation of zeolites when coking is the reason for the deactivation. The approach will be by use of basic characterization methods such as powder XRD (PXRD), capillary XRD, thermogravimetric analysis (TGA), N_2 adsorption, scanning electron microscopy (SEM) with energy dispersed x - ray (EDX), microwave plasma atomic emission spectrometer (MP – AES) for element analysis (EA), methanol to hydrocarbons conversion (MTH) and potentiometric titration.

XRD was used to identify the crystallinity of the materials that was used during this work. TGA was used to find out how much the material contain that is not zeolite, N_2 adsorption was used to estimate a specific surface area of the materials. SEM was used to get a better understanding of the materials' morphology, EA (EDX and MP - AES) was used to evaluate the element composition for the materials, MTH was used to investigate the catalytic activity for the materials and potentiometric titration was used to calculate a number of acid sites for the materials.

Characterization of the deactivated materials will be in focus, as it might make it possible to determine the degree of deactivation for the materials. If the homemade and commercial zeolites appear to have high catalytic activity, more resources can be invested for further investigation of the materials. The foundation for further studies will be laid down by the preparation of the Beta zeolites, which will be tested for MTH conversion for further catalytic characterization in the future.

3 Instrumental and apparatus theory

3.1 Solvothermal synthesis

Solvothermal synthesis is a method to prepare materials. The process involves the use of a solvent at moderate to high temperatures. If water is the solvent, the method is called hydrothermal synthesis.

An autoclave is a closed vessel that can be used to perform experiments with solvothermal conditions to study chemical reactions during high pressure at relatively high temperatures. Experiments are usually performed under waters supercritical temperature of 374°C (29, 30). When a liquid is supercritical, it can diffuse through solids like a gas and dissolve materials like a liquid. Figure 3-1 illustrates the conditions of vapor pressure of water as function of temperature during hydrothermal synthesis.

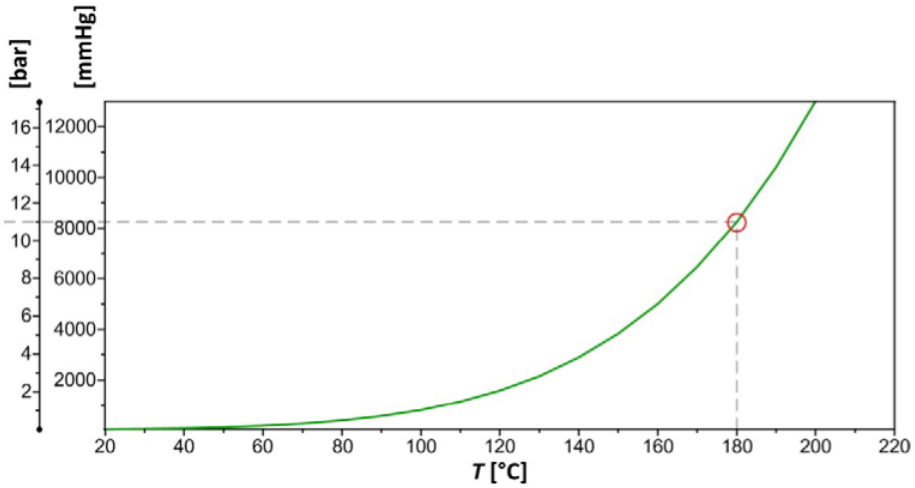

Figure 3-1: The water vapor pressure as function of temperature as an approximation of the conditions during hydrothermal synthesis. Adapted from (31).

By use of autoclave, it is possible to do experiments at other conditions than otherwise possible, since the reactants otherwise would have decomposed. When working with autoclaves it is important to investigate the physical and chemical properties of the solvent and reaction to ensure that the autoclave can manage the conditions during the experiment. The conditions must be investigated, since it is a closed system, which will have a vapor pressure during heating. The content for autoclaves is kept in Teflon liners during the growth of zeolites.

3.2 Powder x - ray diffraction

Powder x - ray diffraction (PXRD) is an analysis method for characterization of crystal structure, by use of x - ray radiation on a sample in powder form. The radiation is sent out from a radiation source. When it hits the sample, the radiation is diffracted before it is detected by the detector, which gives a diffractogram. A diffraction pattern is a product of a material's unique crystalline structure (32). The XRD pattern is dependent of the atomic arrangement of a material and its unit cell, which is the basic repeating unit that defines the crystal structure. The position of peaks corresponds to the size of the unit cell and the peak intensity depends on the relative position of atoms in the unit cell (33).

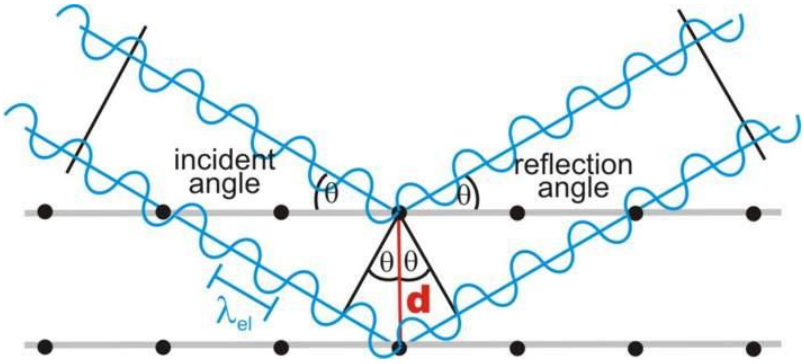

Figure 3-2: An illustrated example, where a plate is hit by x - ray radiation and diffracted of by an angle θ. Adapted from (34).

The phenomenon illustrated in Figure 3-2 can be described by Bragg's equation, which is:

$$n\lambda = 2dsin\theta \qquad \text{(eq 5)}$$

Where λ is the wavelength of the x - ray source, θ is the diffraction angle and d is the lattice distance.

There are two types of interference for x – ray diffraction that is dependent on how the waves overlap. The types are constructive interference and destructive interference. Constructive interference occurs when diffracted beams composed of large number of scattered rays are moving in phase and reinforce each other. Destructive interference is when the scattered rays are not moving in phase and reduces the amplitude of the signal (35). An illustration of the phenomenon is shown in Figure 3-3.

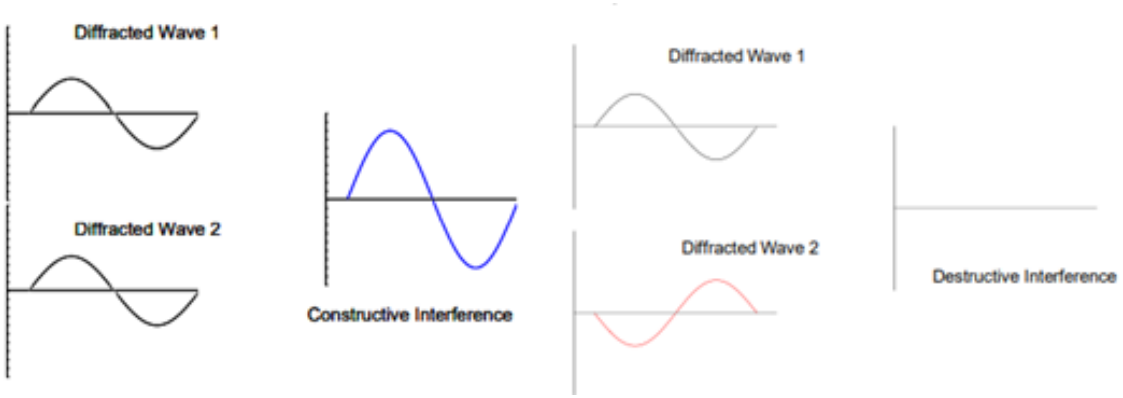

Figure 3-3: Illustrates the concept of constructive and destructive interference in x – ray diffraction. Adapted from (35).

By knowing the exact content of the unit cell, the whole crystal can be imagined. From the crystallography, an image of the electron density that surrounds the molecules in an average unit cell in a crystal can be obtained. With this information all the atoms in a unit cell may be located and a full 3 – dimensional unit cell may be acquired.

The angle of diffraction is inversely related to the interplanar spacing (eq 6). The interplanar is the distance between parallel planes of atoms or ions and spacing can be evaluated in terms of the parameters and each of the formulas for different crystal systems. An illustration of a cubic and an orthorhombic unit cell is given in Figure 3-4 and 3-5 (illustrations for the same data for all the crystal systems is given in Figure 8-1 and Figure 8-2 in appendix 8.1).

Interplanar spacing implies that large unit cells with large spacing, will have small angle of diffraction. Likewise, small unit cells give large angles of diffraction and produces fewer measurable reflections (36). The number of measurable reflections determines how much information that is possible to gather from a unit cell. The more atoms in a unit cell, the more information is possible to gather from it and a larger unit cell is likely to contain more atoms than a small unit cell. Every atom that is present contributes to every reflection in a diffraction pattern.

XRD can be used to determine a crystal's unit cell parameters. Based on that the peak intensities from a diffractogram determines position of atoms within a unit cell, the relative peak intensity of diffraction is determined by atom types present in a unit cell and which phases, site occupation and thermal parameters they have.

The Miller indices are a group of three numbers that is used to specify the orientation of a plane or a set of planes of atoms in a crystal (37). h, k, l is common notations for Miller indices in crystallography. The electron density on the set of planes (hkl) produces the reflection hkl of the diffraction pattern. Each set of parallel planes produces one reflection or describes the electron density within a unit cell (32). The intensity of that reflection depends on the electron distribution along the planes that produce the reflection.

The angle of the diffraction peaks is determined by the distance between parallel planes of atoms in the crystals. There exist several databases with reference data on d - values as well as relative height of the peaks for a wide range of crystal minerals, like the international Centre for diffraction data (ICDD) database. It is possible to identify phases in a sample by comparing with reference patterns (38) from these diffraction databases.

d in Bragg's equation (eq 5) is a product of the a, b and c lattice parameters from the equation of interplanar spaces (32):

$$d = \frac{1}{|ha+kb+lc|^2} \qquad \text{(eq 6)}$$

Where: $|ha + kb + lc|^2 =$

$$h^2a^2+k^2b^2+l^2c^2 + 2klbc \times cosa + 2lhc\alpha \times cos\beta + 2hka \times b \times cos\gamma \qquad \text{(eq 7)}$$

Where:

α is the angle between the lattice vectors b and c, β is the angle between the lattice vectors a and c and γ is the angle between the lattice vectors a and b. h, k and l are dimensional parameters for the plane hkl.

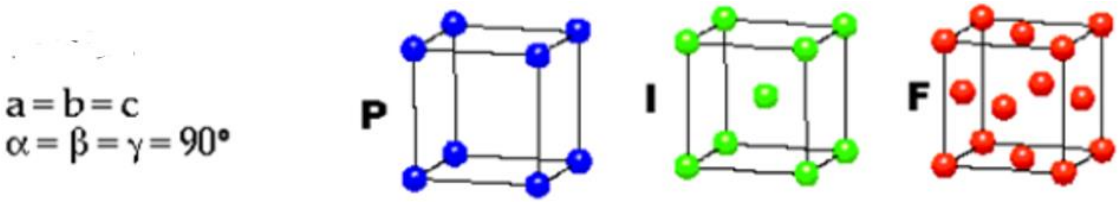

Figure 3-4: Describes unit cell for the cubic crystal structure. The parameters (as indicated in Figure 1-9) are given for the crystal system. P, I, and F are abbreviations for the lattices primitive, body centered and face centered respectively. Adapted from (39, 40).

Equation 8 shows the formula for interplanar spacing for a cubic crystal (as illustrated in Figure 3-4).

$$\frac{1}{d^2} = \frac{h^2+k^2+l^2}{a^2} \quad \text{(eq 8)}$$

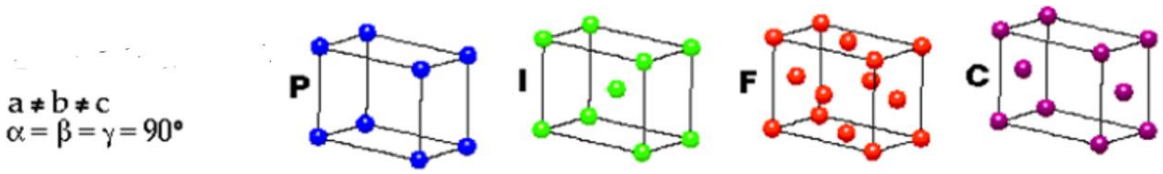

Figure 3-5: Describes unit cell for the cubic crystal structure. The parameters (as indicated in Figure 1-9) are given for the crystal system. P, I, F and C are abbreviations for the lattices primitive, body centered, face centered and side centered respectively. Adapted from (39, 40).

The formula for interplanar spacing for an orthorhombic crystal (as illustrated in Figure 3-5) is given in equation 9.

$$\frac{1}{d^2} = \frac{h^2}{a^2} + \frac{k^2}{b^2} + \frac{l^2}{c^2} \quad \text{(eq 9)}$$

Peak width is due to crystal's lattice strain and crystallite size. The lattice can be affected by compressive strain, tensile strain and non - uniform strain, which impacts the peaks position. A crystals disorder can be estimated by the Scherrer equation by defining a coherency length (41):

$$d = \frac{K\lambda}{\beta cos\theta}, \quad \text{(eq 10)}$$

where:

K is a constant (usually 0.9),

λ is the wavelength,

θ is half of the corresponding peak angle 2θ and β is the full width at half maximum (FWHM) of the peak.

When XRD are performed on powder, the powder is usually kept on a XRD – plate or in a capillary (illustrated in Figure 4-1 and 4-2). There exist various plates and sample holders for

use with XRD, which is intended for varying amounts of sample. Powder can be placed on plates by suspending it in solvent such as isopropanol or covering the plate with plastic foil to keep the powder in place.

Normally one aim to prepare a powder so the grain is randomly ordered. However, in some cases this can be difficult due to the form of some crystals and so-called preferred orientation appears. This may occur in cases where the crystals consist of plate or needle like shape that may make it harder to get random orientation on the plate. If this happens, it can be solved by using a capillary XRD instead. A capillary will solve the issue with preferred orientation because the capillary is rotated 360°, which results in that the detector will be able to measure all angles around the capillary, while the material in a plate will be in one plane for the whole measurement (42).

The intensities for diffractograms of randomly oriented and preferred oriented crystals can be completely different. Intensity ratios can be greatly distorted if the crystals pack as a flat surface where not all areas of the crystals' surface can be reflected (43).

Rietveld refinement is a technique used in characterization of crystalline materials, which involves the fitting of a complete experimental diffraction pattern with calculated profiles and background (44). The method uses a least square to refine a theoretical pattern until a best match with the measured profile is obtained. The technique can deal with overlapping peaks.

XRD has been used in this work to determine the crystallinity, effects of coke and for determination of lattice parameters of materials used in this work.

3.3 Thermogravimetric analysis

Thermogravimetric analysis (TGA) is a characterization method that may be used to determine the concentration of defects and amount of organic material in a sample. This is done by heating a sample to several hundred degrees Celsius, with defined atmospheric conditions where mass losses are recorded during the analysis. For precise measurements, it is important that the sample holder is inert and does not react with the sample or the atmosphere (unless it is desired). The sample holder can consist of Pt, Al, Al_2O_3 and SiO_2. Figure 3-6 shows a scheme of the TGA set up, that includes the instrument with sample holders and a computer system.

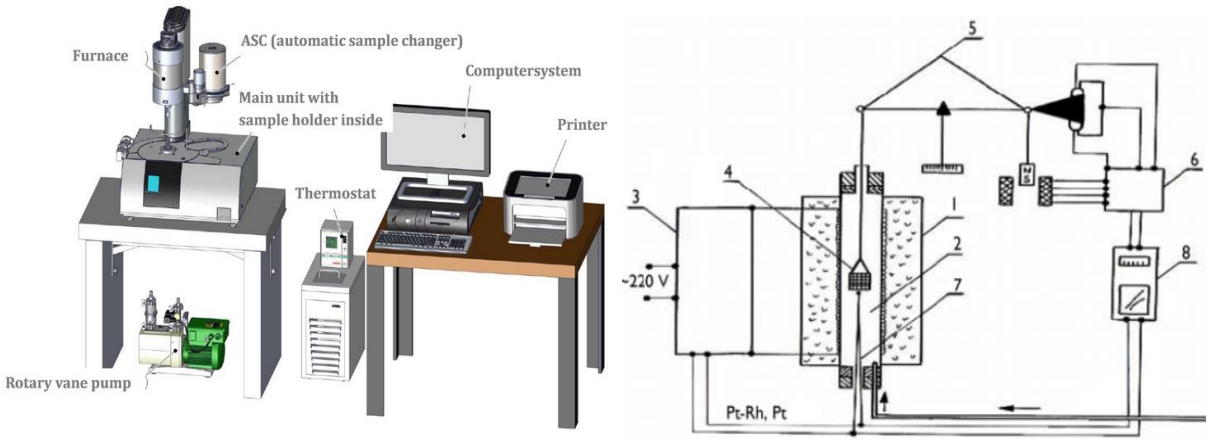

Figure 3-6: A schematic set up of the TGA on the left, that includes the TGA instrument and a computer system and a scheme of the inside of the furnace on the right. The scheme on the right includes a balance with sample at the point marked 4 and it has gas flow introduced from the bottom of the furnace. Adapted from (45).

Zeolites are usually stable by the temperature range used for TGA measurements and do not decompose during analysis conditions (46). The thermal stability of zeolites generally increases with higher Si/Al ratio (6).

TGA – curves are often indicated with two y – axises (illustrated in Figure 3-7). One that shows weight loss and one that shows differential scanning calorimetry (DSC). For a DSC, heat is supplied into the sample and the reference, where the heat flow is proportional to the heat difference between the sample holders of the sample and the reference. If endothermic or exothermic reactions occur for the sample, the system supplies heat to keep the temperature constant. By calibrating the standard material, thermal measurements can be achieved (47). DSC tells whether a reaction at a given temperature, is exothermic or endothermic (if the curve goes up or down). The information from the DSC, can be taken to account together with the overview of weight loss to get a better understanding of what happens with the sample during a TGA analysis.

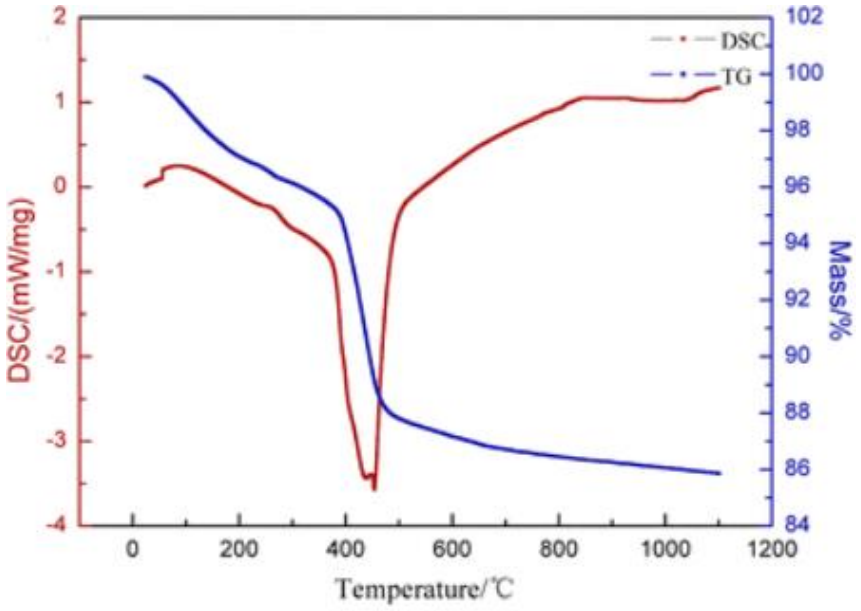

Figure 3-7: An example of a TGA – curve of an as - synthesized ZSM – 5 zeolite. Adapted from (48).

For the work in this thesis TGA has been used to get an overview of the amount of water, organic template and coke content for different samples.

3.4 Scanning electron microscopy

A scanning electron microscope (SEM) is a microscope that uses an electron beam instead of a light source to generate images for studies. The way a SEM function, is that it emits a focused beam of electrons across a sample's surface that is placed in the instrument, which produces an image of the sample. The image is created after electrons from the beam has interacted with atoms from the sample's surface, secondary electrons are emitted from the surface and received by the detector. The data, the detector receives from the emitted electrons contain information about the sample's surface topology. This microscope can zoom in on a sample to the nanometer scale. Some SEMs can achieve resolution better than 1 nanometer (21). By being able to achieve resolution to the nanometer scale it is possible to visually see a sample's morphology through the instrument. The electrons, which is sent out from the beam will over time interact with the sample and expose it to too much force. This can over time cause it to decompose.

Backscattering of electrons (BSE) has high energy, which occurs by backscattered electrons from the electron beam to the detector and gives extra information of particle morphology (19).

Secondary electrons (SE) originate from samples' surface or the near – surface regions of the sample. They occur due to inelastic interactions between the primary electron beam and the sample. These electrons contain lower energy than those from backscattering (49). A SEM – instrument can also be configurated with an energy dispersion x - ray (EDX) detector, which allows it to function to do an EDX analysis and thus elemental composition can be determined. How information is gathered from BSE and SE is illustrated in Figure 3-8.

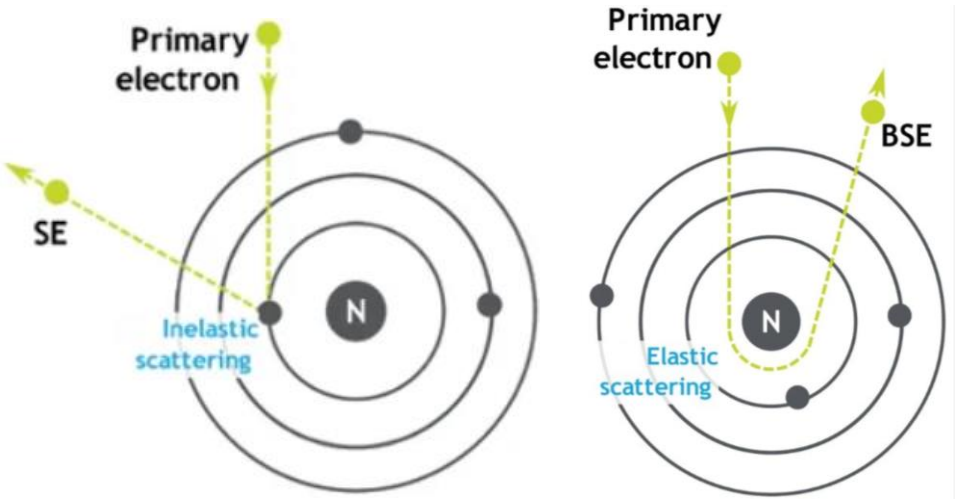

Figure 3-8: Scheme of secondary electron on the left (where inelastic scattering = secondary electron scattering) and an electron being back scatted after interaction with an atom nucleus on the right. Adapted from (49).

SEM microscope was used in this work to gather information about the morphology of materials used in this work.

3.5 Microwave plasma atomic emission spectrometer

Microwave plasma atomic emission spectrometer (MP - AES) is a technique, that is used to determine and quantify the elemental composition of a sample (50). The spectrometer employs microwave energy to produce a plasma discharge using nitrogen supplied from a gas cylinder. Microwave plasma source has a self – sustainable atmospheric pressure of nitrogen, where a

fraction of the gas is converted to plasma while the remaining gas serves to keep the plasma away from the walls of the torch. The MP – AES technique has relatively good detection and multi element capability (51, 52). The sample introduction for the instrument is like an inductively coupled plasma atomic emission spectrometry (ICP – AES) instrument (53). The atomized samples pass through the plasma and electrons are promoted to the exited state. Light emitted from electrons returning to its ground state is separated into a spectrum and the intensity of each emission line is measured by the detector. It consists of a standard torch, a spray chamber, and a glass concentric nebulizer. Since MP – AES is a solution technique. This means that solid samples must be dissolved and made into solutions before an analysis can be performed, while liquid samples can be analyzed directly. Based on several studies, the MP – AES method provides highly accurate and precise data. The precision and accuracy of MP - AES has been tested by comparing its performance with ICP – OES (51, 54).

MP – AES was used in this work to do elemental analysis of materials for comparison with the results from EDX analysis of the same materials.

3.6 Energy dispersion x - ray analysis

An energy dispersion x - ray analysis (EDX) is an analysis that can provide element concentrations. In this work it is used in combination with a SEM instrument as described in section 3.4. By having the EDX mounted to a SEM it is possible to perform a EDX analysis through the SEM instrument. An EDX can be used to determine the presence of elements (elemental analysis) and the concentration of them, that are present. In this case, the presence of elements in a SEM – picture can be determined.

When using an EDX, frequencies occur when a focused electron beam is sent into a sample, that will emit x – ray radiation when electrons from the sample are exited after hit by the electron beam (illustrated in Figure 3-9). The principle for a EDX – analysis is based on, that each element has a unique atomic structure, that gives rise to a unique set of peaks on its electromagnetic emission spectrum. The peak positions are predicted by Moseley's law (55), which is:

$$v = A \times (Z - b)^2 \qquad \text{(eq 11)}$$

Where:

v is the frequency of the observed x – ray emission,

A and b are constants that depend on the type of line (K_α, L_β, etc.) and

Z is the atomic number.

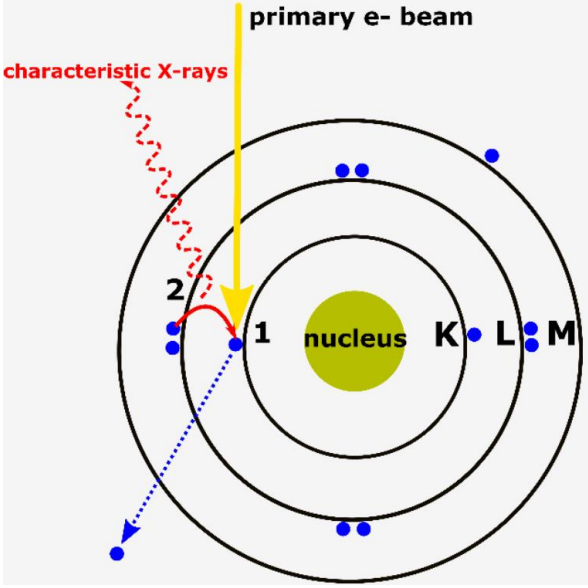

Figure 3-9: Illustration of x – ray emission from an atom, where energy transferred to the atomic electron, knocks it out of the shell and leaves an available position for additional atomic electrons. When the position is filled by another electron, a characteristic is emitted. Adopted from (56).

EDX analysis was used in this work to do elemental analysis of small areas for materials and compare the results with results from MP – AES for the same materials.

3.7 N_2 adsorption

N_2 adsorption is a method to determine surface area by measuring the amount of N_2 molecules that adsorbs onto the surface of interest (7). N_2 is used in BET (Brunauer Emmet Teller) surface area analysis, because of its availability in high purity and its suitable interaction with most solids (57). N_2 adsorption is analyzed by use of BET – theory, which is a theory for multi layered surfaces and gives an estimate of a sample's surface area. BET - theory is a continuation of Langmuir - theory, which is based on single layer surfaces. It is most common to use nitrogen

gas for measuring of surface area for BET. A catalyst's surface is important due to its reactivity. When a catalyst is used, the number of active sites for a catalyst will be reduced, due to blocking when a catalyst is deactivated it must be replaced. The equation for the BET isotherm is (58):

$$\frac{n_{ads}}{n_{mono}} = \frac{v_{ads}}{v_{mono}} = \frac{c \times p_{rel}}{(1-p_{rel})[1+(c-1)p_{rel}]} \quad \text{(eq 12)}$$

Where:

p is pressure,

$p_{rel} = \frac{p}{p_0}$, where p is the measured pressure and p_0 is the standard pressure,

c is the BET constant,

v_{ads} is the volume of adsorbed gas,

v_{mono} is the volume of adsorbed gas at monolayer adsorption,

n_{ads} are number of moles adsorbed and

n_{mono} is mole for a monolayer.

The BET plot is a transformation of the adsorption isotherm. The monolayer volume (v_{mono}) and BET constant c is calculated from the slope and intercept of the BET plot. The specific surface area for BET (S_{BET}) can be obtained from v_{mono} by the following relation (59):

$$S_{BET} = \frac{v_m \times N_A \times A_{CS}}{V_m \times m} \quad \text{(eq 13)}$$

Where:

N_A is Avogadro's number,

V_m is the molar volume of a gas (22.4 m^3/mol),

A_{CS} is the surface occupied by one molecule of N_2 (16.2×10^{-20} m^2) and

m is mass of adsorbent.

There are 5 main types of adsorption isotherms, (illustrated in Figure 3-9). Type I corresponds to the formation of one single absorbate layer and is typical for a situation of strong interaction

between the adsorbate and the adsorbent. Since this isotherm type is a single layer, it may be called a pseudo - Langmuir isotherm. Type II and IV represent a situation where several adsorbate layers are formed, and where the first layer is different in energy than the following layer. Because of this, the BET isotherm describes these two isotherms well. Isotherm II and IV look similar, because they represent two similar situations. Isotherm III and V are typical of weak adsorbent and adsorbate interactions. Type I, VI and V are the most common adsorption isotherms for zeolites (57).

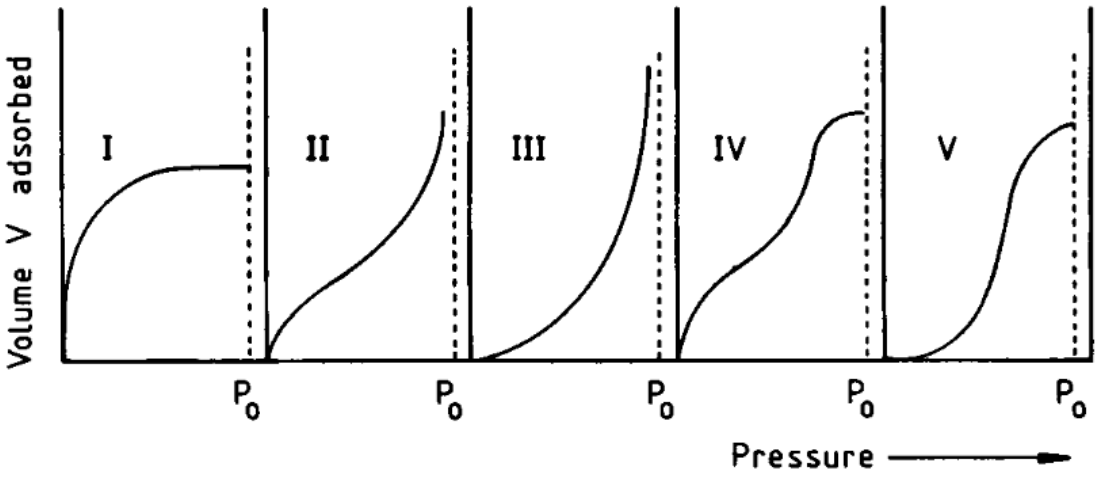

Figure 3-10: Illustrates what typical BET isotherms look like and their numbering. Adapted from (60).

Adsorption and desorption isotherms may branch and a phenomenon called a hysteresis loop occurs. A hysteresis loop is the visual difference for the adsorption and desorption isotherms cycle when adsorption and desorption are not identical. A hysteresis loop is usually seen when a layer is filled and emptied by capillary condensation. N_2 is typically adsorbed at 77 K, due to its melting point (61). Hysteresis in zeolites isotherms is an indication, that it has mesopores (62).

N_2 adsorption was used in this work to calculate the specific surface area and to study the pores of materials.

3.8 Reactors for catalytic testing

Many different reactors for catalytic testing exist. There are three main reactor types, that are used for heterogenous catalysis, which are fixed bed reactor, fluidized bed reactor and stirred tank reactor.

The reactor used for the testing in this work was a fixed bed reactor, which is illustrated in Figure 3-10. A fixed bed reactor has the catalyst resting on a bed, while the reactant gases pass through the bed from the top. It is a simple reactor that is commonly used in lab experiments (63) and it is used because the catalyst on the top of the bed will be more exposed to the reactant (coming from the inlet from the top) than the catalyst on the bottom. Based on this, it is possible to get catalyst that is gradually deactivated from inlet to outlet. By making multiple beds in the reactor, the result after a test can be multiple layers, where the beds have different amounts of coke. A stirred tank reactor has stirring, which therefore leads to homogeneity and can therefore not give the same effect as with beds. A fluidized bed reactor is more complex and expensive, which makes it less suitable to use for lab scale experiments.

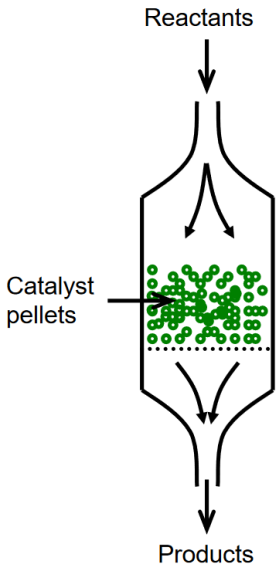

Figure 3-11: A scheme of a fixed bed reactor. Adapted from (64).

The ideal reactor for the testing is a plug flow reactor with fixed residence time. It is the ideal reactor because of assumptions such as steady state, changes in temperature, pressure and density of the flow can be ignored when this reactor is used. Reaction kinetics and deactivation for a plug flow reactor are decoupled (65). A plug flow reactor was not used, because it is

difficult to operate when it comes to particles. A scheme of a plug flow reactor is shown in Figure 3-11.

Figure 3-12: Scheme of a plug flow reactor, where the flow is indicated as 3 grey lines. Adapted from (66).

The fixed bed reactor was used in this work to contain sample for methanol to hydrocarbon conversion in a homemade Co – feed test rig at UiO, where the samples were used until they were deactivated (lost catalytic performance).

3.9 Potentiometric acid - base titration

Potentiometric titration is a much used technique for determination of acid and base strength of materials. For determination of acid strength typically a solution of NaOH is used as a titrant, which is then added to a test solution until the acid is neutralized. The volume used to reach the equivalence point is than used to calculate the acid strength of the test solution. In earlier days the equivalence point was determined by use of indicators, which nowadays the equivalence point is determined potentiometric by use of a pH electrode. A digital burette is also used, which control and record the corresponding added volume. An equivalence point can be determined for a titration when there is a rapid change in pH. The equivalence point is where the slope of the titration curve is steepest. This may be determined by looking at the derivative ($\frac{dpH}{dV}$) of the titration curve, where dpH is the change in pH and dV is the change in volume (67).

Zeolites have acidic sites inside their pores. It is important to know how much of a zeolite's acid sites/active sites that are available, since this is where the material's reactions occur**.** As mentioned, potentiometric titration makes it possible to determine the amount of acid sites in zeolites pores. During titration, OH^- can penetrate through a zeolite's pore channels, which makes it possible to determine both acid sites on the surface and in the zeolite's pores. By determining the amount of acid sites, the catalyst's catalytic activity will be clearer. From this, the density of acid sites (μmol/g) and the accessibility of acid sites (%) can be determined. The density of acid sites can be calculated for materials, based on the amount of base that was

required to reach the equivalence point. The density of acid sites can thereafter be calculated from the accessibility of acid sites.

$$Accessibillity\ of\ acid\ sites = \frac{n_{OH^-}}{n_{total\ acid\ sites}} \times 100\% \quad \text{(eq 14)}$$

The method is a useful technique to characterize porous materials, since it is an accurate and reproduceable technique that is quick to perform.

In this work potentiometric titration was used to determine the acidity of porous zeolites.

3.10 Temperature programmed oxidation

Temperature programmed oxidation (TPO) is a material characterization process, which is a type of a thermogravimetric analysis that is carried out in an oxidizing environment (68). The apparatus heats a sample, then it establishes oxidation during thermal influence. With an integrated mass spectrometer (shown in section 4.7) and a heating element, it can analyze any catalytic activity in real time as a gas flow passes through the sample during a measurement (69). A catharometer or a TC (thermal conductivity) detector is often used in the TPO method. A catharometer is a detector that serves for measuring the difference in thermal conductivity between reference gas and the mixture of carrier gas reactant that flows through the sample. The data obtained from a TPO experiment are presented as a variation of the signal intensity as a function of time or temperature (70). If an advanced diffractometer is mounted (which is the case for the apparatus at ESRF) to the TPO set up a XRD diffractogram can be acquired at any time during an experiment.

An apparatus for TPO measurements (illustrated in Figure 3-12) can often also do temperature programmed reduction (TPR) measurements, which uses the same technique for characterization, but with reducing conditions (for instance by H_2) (70).

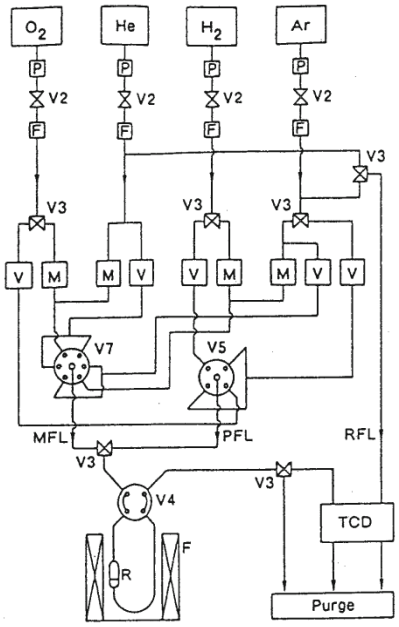

Figure 3-13: Scheme of a typical TPO apparatus, where P is pressure controller, F is purification stage, M is mass flow controller, V, V2, V3, V4, V5, V6 and V7 are valves, R is reactor, and PFL, RFLK and MFL are pretreatment flow line, reference flow line and measure flow line respectively. Adapted from (70).

TPO is typically used to investigate the oxidation of organic and inorganic compounds. The heating element of a TPO apparatus can be heated up to 1000°C during an experiment. This technique provides dynamic and accurate data, which makes it an important technique (69). The method uses oxygen as a reactant and the advantage for the method is that it allows for monitoring of the oxygen uptake directly (71).

During a TPO analysis several products are formed (which include H_2O, CO and CO_2) where the main reaction for TPO and TPR is illustrated in equation 15 and 16 (70). It is important to remove all undesired gases that can interfere with the signal output. A suitable pretreatment of sample is therefore necessary (72).

TPO: $$M_xO_{y(s)} + 2H_{2(g)} = M_{x(s)} + H_2O_{(g)}$$ (eq 15)

TPR: $$xM_{(s)} + y/2O_{2(g)} = M_xO_{y(s)}$$ (eq 16)

Where M is a metal atom and x and y are amount of moles of M and O respectively.

An example of a typical TPO and TPR profile for a sample where oxygen consumption is analyzed is illustrated in Figure 3-13.

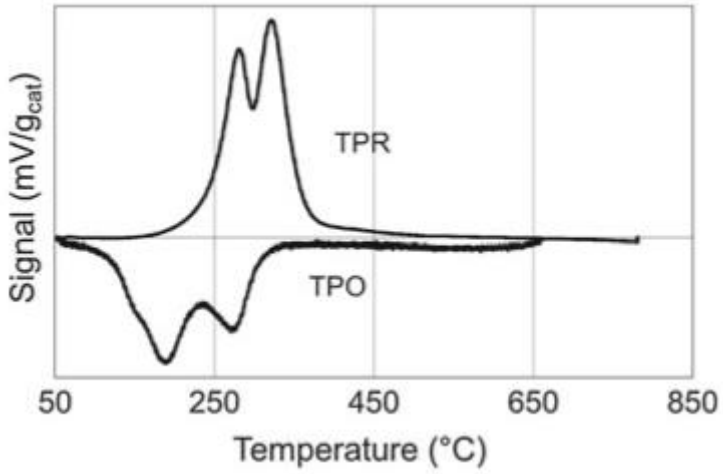

Figure 3-14: Example of a typical TPO profile for a sample. Adapted from (69).

TPO was used in this work to study the change in the a and b unit cell parameters during heating and cooling of the homemade material HM02 for further information on the material.

4 Experimental

4.1 Synthesis of ZSM – 5 zeolites

The synthesis of ZSM – 5 zeolite was done according to the procedure given in the article '*Methanol to gasoline over zeolite H – ZSM - 5: Improved catalyst performance by treatment with NaOH'* by Bjørgen (25).

The first step in the synthesis was to make two solutions. They will be called solution A and solution B to easier keep track of which is which. Solution A consisted of 20 g tetra propyl ammonium bromide (TPABr) dissolved in 20 g de - ionized water and 25 g Ludox 30% (colloidal silica). Solution B consisted of 0.25 g $Al(OH)_3$, 0.11 g NaOH and 0.41 g KOH. Solution B was made with 77 g of water and the hydroxides were dissolved before it was transferred to solution A. The mixture was then adjusted to pH 11 by drop - wise addition of 2M H_2SO_4 during stirring for 2 hours. The mixture was then transferred to a 250 ml Teflon liner, which was placed in an autoclave and placed in an oven at 170°C for 14 days. After 14 days the content was filtrated (filter paper from Hawach scientific with fast filtration speed, 20 μm pore diameter) and washed with distilled water before characterized by the techniques described in section 3. The final molar gel composition was 78 SiO_2: 1.0 Al_2O_3: 2.3 K_2O: 0.86 Na_2O: 47 TPABr: 4000 H_2O (Si/Al ratio 39)

The first sample (HM01) were synthesized by the same procedure as above, except there was used less water, since the amount was not specified in the article. The $Al(OH)_3$ used during the synthesis for this sample was from Fluka (76.5% purity).

A second sample (HM02) was made where $Al(OH)_3$ (0.25 g), NaOH (0.11 g) and KOH (0.41 g) was dissolved in 77 g de - ionized H_2O with $Al(OH)_3$ crystal source from Fluka (same aluminum source as for HM01).

A third sample (HM03) were also made, where a different less crystalline $Al(OH)_3$ was used, which was from Aldrich (50 - 57% purity).

The samples were calcinated and ion exchanged to remove absorbates, templates and impurities and make sure the zeolite is in proton form. The calcination was done in static air at 550°C for 6 hours in a Nabertherm oven. Calcination was done both before and after ion exchange for the synthesized samples.

The ion exchange procedure was performed by suspending the sample in 1 M NH_4NO_3 in a 125 ml plastic bottle and placed in a heating bath with water at 70°C for 2 hours. After 2 hours the bottle was centrifuged with a counterweight and as much as possible of the NH_4NO_3 – solution was decanted off. The bottle was then refilled with NH_4NO_3 and the procedure was repeated two times. After the NH_4NO_3 – solution had been removed a third time, the bottle was placed in an oven at 60°C to dry the sample.

4.2 XRD – X - ray diffraction

The PXRD instrument that was used for regular powder - XRD was a Bruker D8 x - ray diffractometer, diff 5 instrument with a Lynxeye detector and 2 kW Cu K-alpha-1 radiation selected by a Ge (111) Johanessen monochromator. Most of the measurements were done in the 2θ range of 2 - 60°. Most of the measurements was done with a timescale of 1 (19.20s per step). Before use of the instrument, the samples were prepared by placing the sample on a plate (illustrated in Figure 4-1). For a simple plate (noted as glass plate), approximately 50 mg of sample was used and covered with plastic foil. When a full plate (sample plate with 1 mm depth) was used approximately 1 g of sample was placed on the plate and then covered with plastic foil.

Figure 4-1: Powder XRD plates, where the XRD plate to the left is a full plate (1 mm depth) and the plate to the right is a glass plate.

The RECX - 1 instrument (Bruker D8-A25 instrument with Ge (111) Johanssen monochromator, Lynxeye detector and Cu K-alpha-1 radiation) at the department of chemistry was used for capillary XRD. Capillary tubes with 0.5 mm diameter of quartz were used and mounted to a station like illustrated in Figure 4-2. Approximately 50 mm of the tube is required to be filled with material to cover the area where the x – ray beam passes the tube.

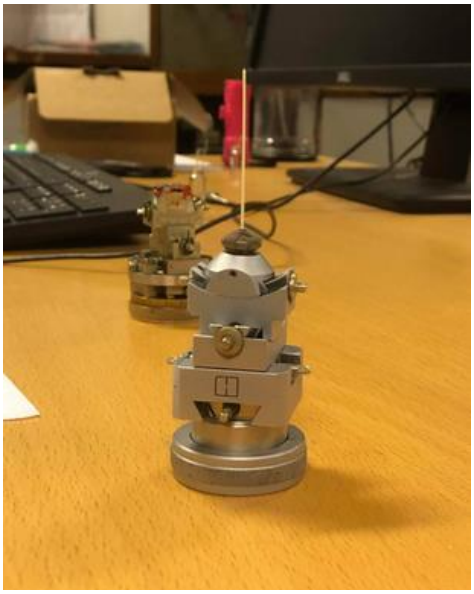

Figure 4-2: Illustration of how a capillary tube with sample is mounted on a station for capillary XRD.

A XRD pattern of sample of HM02 on proton form was gathered on BM01 from the European Synchrotron Radiation Facility (ESRF) in oct. 2020. The sample was sent to Grenoble to get additional data for the crystal structure of the material. The measurement was performed by local staff, where the capillaries were measure at 25°C and the sample was heated to 600°C.

The data from the XRD instruments was treated in the softwares Origin or Diffrac.EVA. The computed crystallinity was performed for patterns in Diffrac.EVA to calculate the %-crystallinity. Diffrac.EVA uses the furmulas in equation 17 and 18 to calculate the %-crystallinity (73):

$$\% - Amorphous = \frac{Global\ area - Reduced\ area}{Global\ area} \times 100\% \quad \text{(eq 17)}$$

$$\% - Crystallinity = 100 - \% - Amorphous \quad \text{(eq 18)}$$

The data retrieved from XRD was used to compare with literature patterns for the zeolites, from Treacy and Higgins's collection: *Collection of simulated XRD powder patterns for zeolites* (38) to get knowledge about the materials crystallinity and purity. Additional analysis has been done by Nico König.

4.3 TGA – Thermogravimetric analysis

The TGA instrument that was used was a STA 449 F3 thermogravimeter from Netzsch, where the used atmosphere was 80% nitrogen and 20% oxygen except for the ACS extrudates, which had 40% nitrogen and 60% oxygen. The instrument has a robot installed, which handles the sample holders. The TGA has 19 slots for sample holders, where one of them are for reference sample holder and 18 of them are for sample analysis. There were used at least 10 mg of sample for every measurement to get precise measurements, which was weighted out in an alumina crucible. The samples were ramped up to 800 or 900 ℃ with 5 ℃ increase per minute. TGA was done for both synthesized samples, samples on proton form and samples that had been tested on the Co - feed rig test rig (deactivated samples).

Samples on proton form was expected to not show much change after an analysis since most zeolites are still stable at the temperature range used for the analysis (53). For the synthesized and deactivated samples there should be a weight change after the analysis. For the synthesized samples, there should be a change due to removal of template and impurities. For the deactivated samples there should be a change in weight due to removal of coke from the catalytic testing.

4.4 SEM – Scanning electron microscopy

The SEM - instrument used, was a SU8230 ultra high-resolution cold FE-SEM microscope from Hitachi with Bruker system. A multi sample holder, which could take up to 6 samples at a time was used. The samples were dispersed over carbon tape which were attached to the sample holders. Small amounts of sample were required and the excess were removed by blowing pressurized air onto the tape. The high current mode was used when taking pictures to see the morphology of the crystalline samples. Secondary electron (SE) detector and backscattering electron (BSE) detector was used during use of the microscope.

4.5 MP – AES - Microwave plasma atomic emission spectrometer

The MP – AES used for the analysis was an Agilent 4100 MP-AES spectrometer. The instrument has an Agilent SPS 3 auto-sampler and a charge coupled device (CCD) detector. The instrument is controlled by MP Expert software installed on a nearby computer.

The instrument was calibrated before use with one blank and 6 standard solutions of Si and Al (250, 216, 168, 114, 80 and 49 mg/L of Si and 2, 6, 12, 22, 30 and 34 mg/L of Al).

Approximately 25 mg of sample is used for a measurement with a MP - AES. Since samples for analysis must be in liquid phase, 1 ml 25% hydrogen fluoride (HF) was used to ensure complete dissolution before the solutions was added boric acid to neutralize the acid and diluted to 1 mg sample per ml. The sample solution is introduced by a peristaltic pump into the spray chamber, where it is formed into an aerosol, heated to emit light which is then detected by the detector.

A hazard that users should be aware of when working with HF, is that HF easily penetrates through skin and muscles and bonds strongly with Ca in skeletons.

The MP – AES analysis for the materials in this work was done by Sebastian Prodinger at UiO.

4.6 EDX - Energy dispersion x - ray analysis

The EDX analysis was performed in a SU8230 SEM microscope (described in section 4.4). For EDX analysis, the samples were placed directly on the multi sample holder with no preparation of the samples and held on the sample holder by carbon tape. The acceleration voltage was set to 10 kV.

4.7 N_2 adsorption

A BelSorp miniX gas adsorption instrument from MicrotracBEL was used to determine samples of zeolites' surface area, pore size distribution sorption capacity by N_2 adsorption. The samples were introduced to the instrument by use of a sample cell. The sample cell was weighted before and after adding the sample. Approximately 30 mg of sample was used for one measurement. When the sample cells have been filled with sample, they were ready for pretreatment. The

conditions for the pretreatment were performed at 300°C and vacuum for 8 hours. Figure 4-3 shows a picture of the pretreatment instrument for N_2 adsorption, which is used to remove water, other adsorbates and to make sure there is vacuum in the sample cells. Number 1 in Figure 4-3, marks the temperature controller, number 2, 3 and 4 are switches for vacuum, purge, and heat respectively. Number 5 marks the oven on the instrument, number 6 marks position for sample cell holders and number 7 marks ports on the instrument.

After the pretreatment a bath of liquid N_2 was fitted to the instrument to facilitate the adsorption of N_2 in the zeolites. The sample's surface area was now measured. After the measurement, the sample cell was weighted again to determine the change in mass and determine the specific surface area (m^2/g). The shape of the isotherm could then be determined.

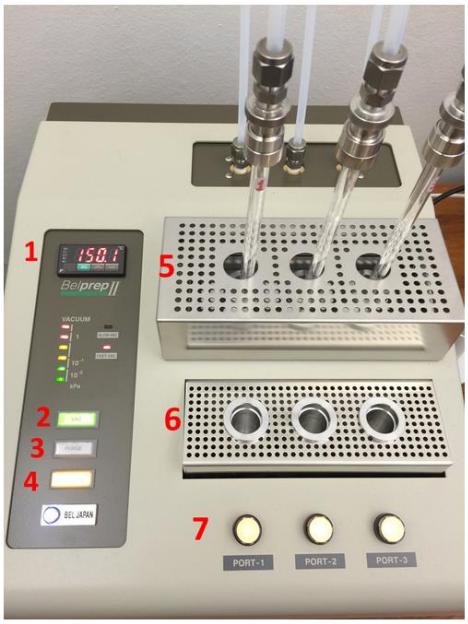

Figure 4-3: A picture of the instrument used for pretreatment for N_2 adsorption.

4.8 Test rig for methanol to hydrocarbons conversion

The test rig used in this work is called a Co - feed rig, which is an apparatus made at UiO. This apparatus is specifically designed for testing on zeotype catalysts for methanol to hydrocarbons (MTH) conversion. This apparatus is capable of exposing the catalyst to both reducing and oxidizing conditions. The system includes three heated saturators, several mass flow controllers, a pneumatically operated stream, multiple loop system and an MS detector. In addition, a combined GC - MS are connected to the test rig. The MS allows for determination of isotopic composition and identification of products from the testing.

The apparatus introduces gas stream to the sample through a fixed bed reactor, where the sample is placed. The reactor is a 'U' shaped quartz reactor with a 6 mm internal diameter. In the bottom of the reactor there is quartz wool, which is the bed. The sample is made into three layers, where each layer is separated with a 3 mm height bed of quartz wool. Each layer of sample consists of approximately 70 mg. The three layers will be referred to as top, middle and bottom, which corresponds to the order of layer, with the top layer being on side of the reactor inlet.

After the reactor has been filled with the sample, a stopper was fitted on the top with a position for a thermometer. After this the reactor was placed in a heating mantel and covered with quartz wool to isolate it. All glass connections were lubricated with grease to avoid leaks.

The samples are separated into layers in the reactor as illustrated in Figure 4-4, to make it possible to have catalysts with different degrees of deactivation and thereby determine an eventual difference in deactivation between the layers. Differences in deactivation between the layers may be determined by calculating the amount of carbon content in the layers (by using TGA). There may also be a visual difference between layers, where the layer with more coke content is darker than the layers with less coke.

Figure 4-4: Picture of how three layers of sample is separated by quartz wool in a reactor, were there is increasing coke content from bottom to top. Adapted from (23).

When all connectors were set and the set up was covered with quartz wool, a leak test was done to check if there were any leaks in the system. The leak test was performed by closing the system and applying some pressure. If the system was leaking, then it was necessary to remove

the quartz wool and check the connectors, before trying again. If there were no leaks, the system's temperature was increased to 400°C over 40 minutes. After this, the parameters must be adjusted in the control panel as illustrated in Figure 4-7.

Experiments in this work were performed at atmospheric pressure. The catalyst was activated with an initial heating ramp of 5°C min^{-1} under 20% oxygen in helium to 550°C and the temperature was kept at 550°C for 1 hour under 100% oxygen. Then the catalysts were cooled down to reaction temperature at 5°C min^{-1} under 100% helium atmosphere. The deactivation of the materials took place at 307 mbar of partial pressure of MeOH at 400°C balanced with helium (5.0 purity). The total flow was 26 ml min^{-1} (8 ml min^{-1} MeOH and 16 ml min^{-1} He) and giving a weight hour space velocity (WHSV) of 2.95 $g_{MeOH}\, g_{catalyst}^{-1}\, h^{-1}$. The partial pressure of MeOH was controlled by a condenser set at 37°C. The eluent from the reactor was analyzed after two minutes of reaction and subsequently every 77 minutes by the GC - MS. In Figure 4-5 a picture of the test rig is shown and a schematic illustration of the system is given in Figure 4-6.

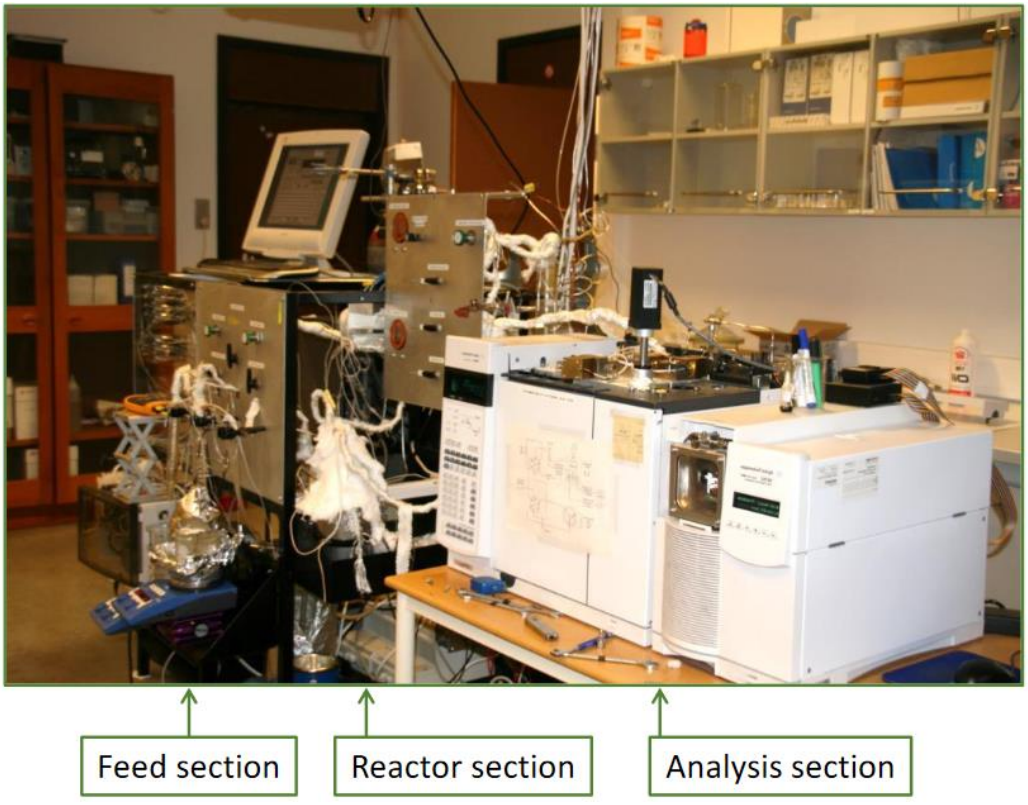

Figure 4-5: Set up for Co – feed test rig. Adapted from (66).

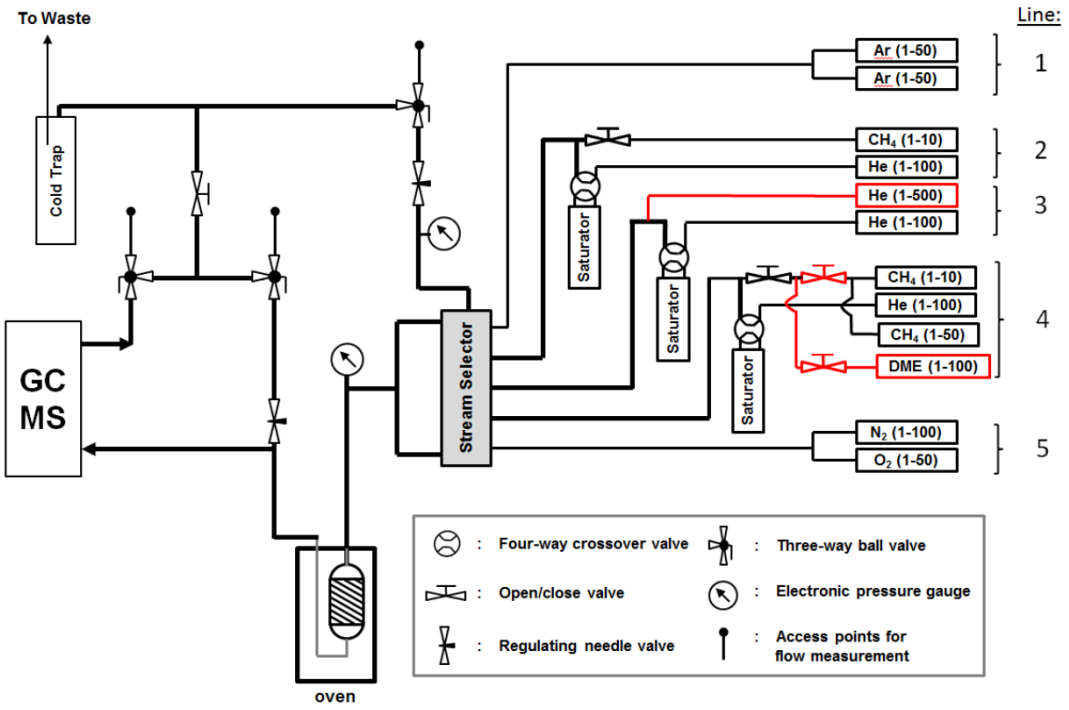

Figure 4-6: Schematic illustration of the system for the Co - feed test rig. Adapted from (74).

Figure 4-6 shows a scheme of the system for the test rig. The system consists of 12 mass flow controllers for introducing gas. These are divided into 5 groups. These are labelled line 1 – 5. Line 1 and 5 are used to introduce inert gas. Line 2 and 4 introduces CH_4, DME and helium. Line 3 consists of two helium mass flow controllers. All 5 lines go through a stream selector, which consists of one valve block for each line and two end blocks, that collects the lines into a feed line and a bypass line. After the stream selector, the bypass line goes through a needle valve, which is used to adjust the overpressure. The stream valves are controlled in an own control panel, which is shown in Figure 4-7.

Most of the materials used on the Co – feed test rig for testing of catalytic activity was part of the TOMOCAT project. Their sample labeling is listed in Table 4-1.

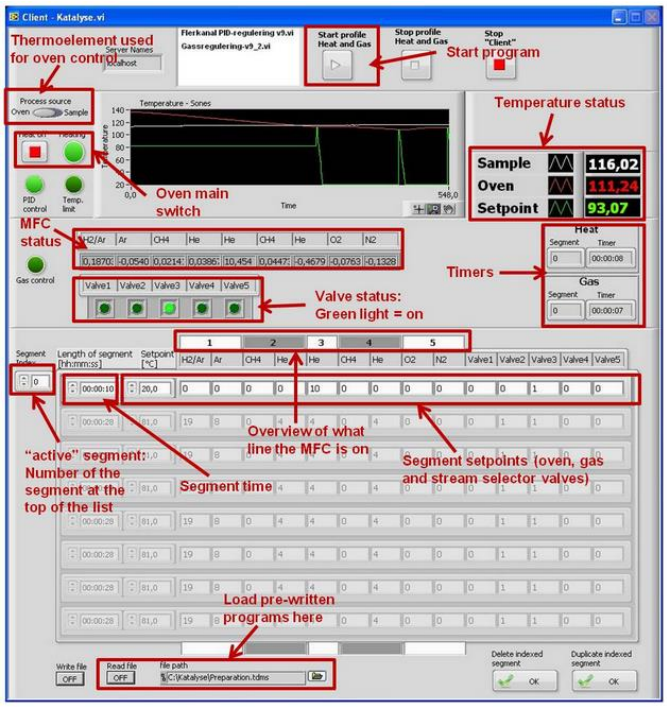

Figure 4-7: The panel which controls the stream valves. Adapted from (74).

Table 4-1: An overview of all the materials that were used on the Co - feed test rig for catalytic testing. Including the type of zeolite, the material's Si/Al ratio and referenced specific surface area.

TOMO no.	Name of material	Type of zeolite	Si/Al ratio	Reference surface area (m^2/g)
TOMO001	ACS extrudates	ZSM – 5	19	Above 250 (15)
TOMO002	09-00243/1	Beta	13.5	560 (75)
TOMO003	HM02	ZSM – 5	28.4 (determined in this work)	318 (determined in this work)
TOMO004	SK_CP814C	Beta	19	710 (75)
TOMO005	CP806B-25	Beta	27	677 (76)
TOMO007	CP811BL-25	Beta	13	620 (75)
	HM03	ZSM – 5	41.6 (determined in this work)	321 (determined in this work)

Before a catalyst test with the apparatus, it is necessary to have particles in a certain size range to make sure the particles stay in the reactor in the correct way to avoid pressure build up in the reactor. Therefore, the sample was pressed, grinded with mortar and sieved to filter away particles that have the wrong size. The desired particle size is 250 – 420 μm. A hydraulic pellet press from Specac Graseby was used to press the samples and the powder was pressed with a force up to 5 tons.

The gas chromatography's (GC) connected to the test rig was an Agilent 5975C gas chromatograph – mass spectrometer. The main parts of the GC – MS are an injector, two columns and a detector, as shown in Figure 4-8. The injector injects sample through the column. This GC – MS injects samples automatically. The GC – MS had three detectors: mass spectrometer (MS) detector, flame ionization detector (FID detector) and TC detector. The columns used were Restek rtx-DHA-150 columns. Hydrogen (Praxair, purity 6.0) was used as the carrier gas. The gas chromatograph separates species based on their affinity with the stationary phase in the capillary column and the detector detects species coming out of the column and the intensities can be viewed on the connected computer.

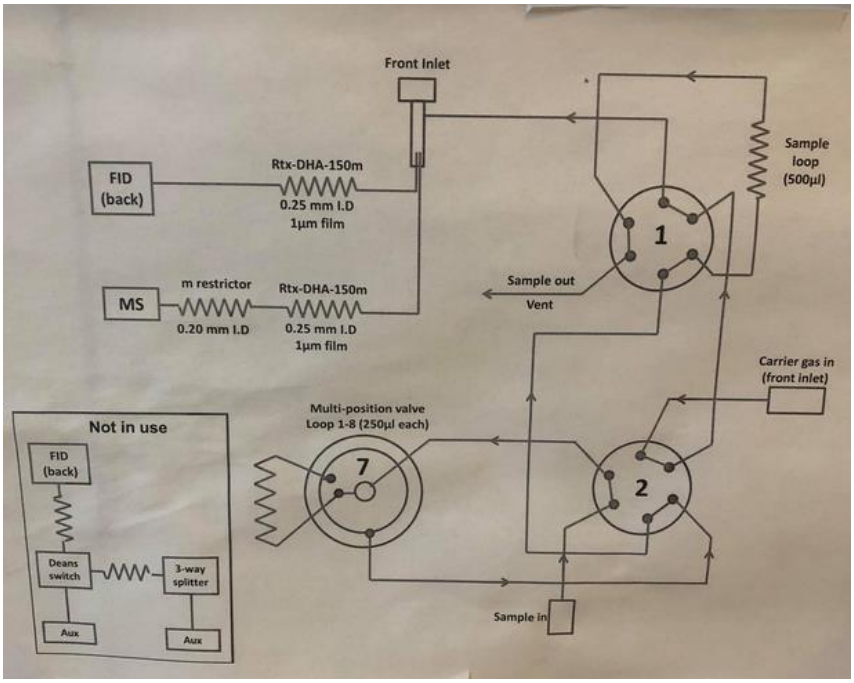

Figure 4-8: Scheme of the combined GC – MS.

4.9 Potentiometric acid – base titration

The set up for the potentiometric titration is illustrated in Figure 4-9. There has been made a procedure for the titration instrument to follow by Sushant Kumar as described in *'Potentiometric acid - base titration as a tool to characterize porous solid acids'* (12). The procedure was followed during the titrations. The procedure starts by rinsing the system with NaOH – solution (0.1 M) that will be used during the titration. The apparatus will rinse the systems 3 times by its own. After the rinsing, the pH - electrode must be calibrated. This is done by introducing the system to four standard solutions (with pH 2, 4, 7 and 10). Next a method must be chosen for the measurement. The method chosen was set to stir the sample for 1 minute and add 0.5 ml of base per minute and the stop condition was set to either when 10 ml of base had been added or the solution reaches pH 12. Typical around 500 mg of sample was used.

Before a measurement with a zeolite, the sample must go through a pretreatment, where it was added into a titration sample - cup with 60 ml of $NaNO_3$ – solution and stirred overnight.

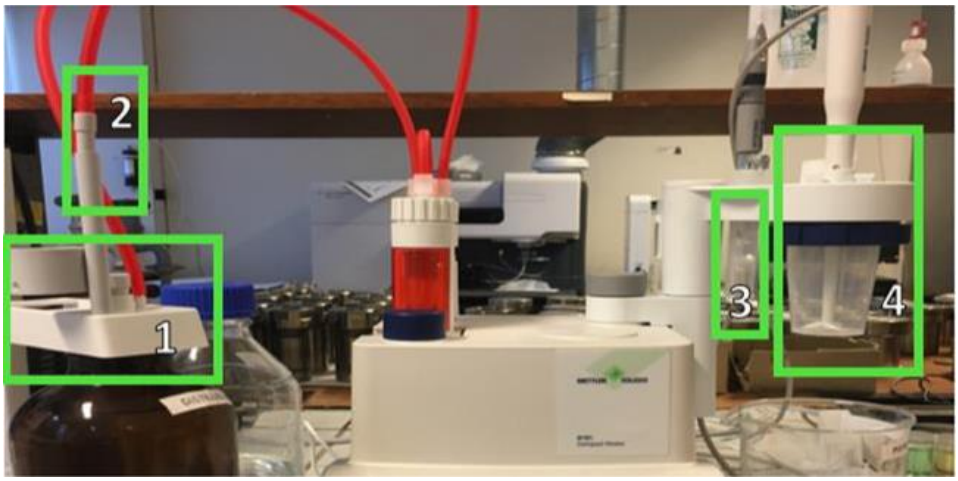

Figure 4-9: Illustration of set up for the potentiometer, where 1 is burette feed, 2 is burette tip, 3 is pH – electrode in stand with 3 M KCl – solution and 4 is the titration stand. Adapted from (12).

4.10 TPO – Temperature programmed oxidation

A temperature programmed oxidation (TPO) experiment was performed on HM02 in Grenoble in oct. 2020. The sample was sent together with the rest of the samples that required use of facilities at ESRF, where the experiment was completed by local staff. The experiment was started at room temperature, increased to 550°C and cooled down back to room temperature. The apparatus used was the Swiss - Norwegian Beamline (BM01) at operando conditions (under reaction conditions where reaction products are measured). The analysis was handled by Nico König and Nicolai Haber Junge.

Figure 4-10 shows a picture of the TPO apparatus and a capillary ready for a measurement. In the picture the reactor, reactor inlet, reactor outlet, the beam and the heating blower are indicated. The reactor is mounted horizontally on a Huber station. The reactor was connected with one side to the gas system, used as reactor inlet and the other side was connected to the end of the system leading to the MS, which is therefore used as reactor outlet.

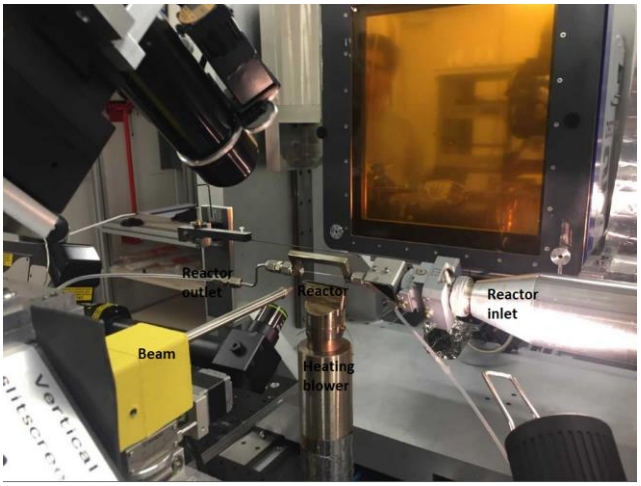

Figure 4-10: Picture of a TPO apparatus with sample in a capillary.

5 Results

In this section the results gathered from the various characterization techniques will be given for the zeolite materials used in this work.

5.1 X – ray diffraction

XRD was performed on ZSM – 5 and Beta zeolite samples to determine their crystallinity and thereby making sure that the samples are the materials they are supposed to be. Their XRD patterns were compared with literature to see if they matched the crystallinity they were supposed to and if they were without impurities. Peak lists retrieved from Diffrac.EVA has been added for most of the XRD patterns.

For HM01, only XRD for the as – synthesized form of the material was performed. For the other two homemade materials (HM02 and HM03), XRD was performed on as – synthesized, protonic and coke containing forms of the materials. XRD was also performed on protonic form of the ACS extrudates, MFI - 27 and 4 Beta zeolites (09-00243/1, SK_CP814C, CP806B-25 and CP811BL-25).

5.1.1 HM01

A XRD diffractogram of HM01 is given in Figure 5-1, which was not added enough H_2O during the synthesis. A list with the angle, d value, intensity and relative intensity of the peaks in Figure 5-1 is given in Table 5-1. This resulted in that the sample did not have the required amounts of H_2O to be able to crystalize properly and it was therefore not successful. It is quite visible in the figure, that the crystallinity is not as it should be, because it has its first visible signal after 10° and it has a broad signal between 20° and 30°, which is an indication that the material is amorphous. Figure 5-2 is an example of how it should have looked like. The sample was therefore set aside and not investigated any further. According to the computed crystallinity of the raw. file for the pattern in Diffrac.EVA, it has a 50.1% crystallinity and is 49.9% amorphous.

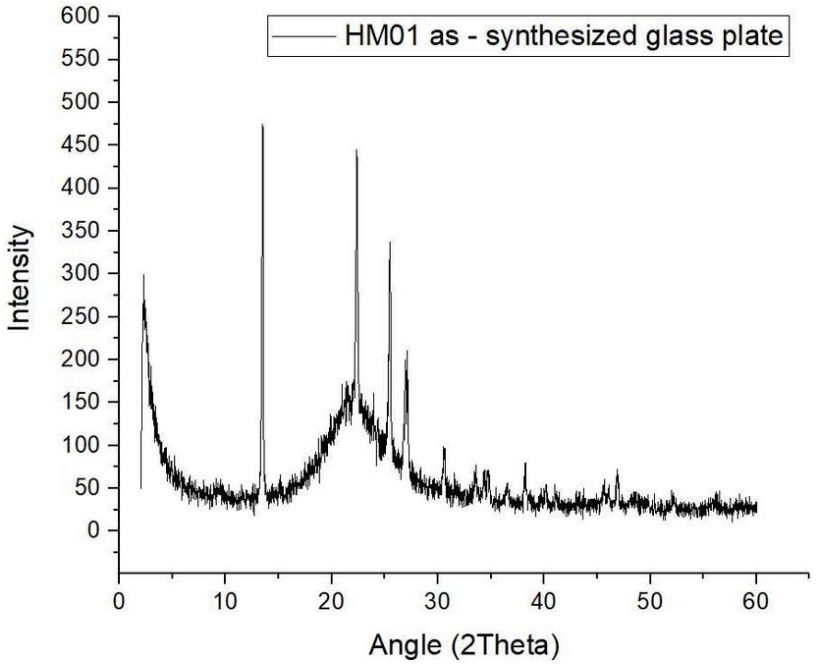

Figure 5-1: Recorded XRD diffraction pattern of as - synthesized HM01measured on a glass plate.

Table 5-1: Peak list for HM01 as – synthesized glass plate XRD.

angle (° 2θ)	d value (Å)	Intensity (counts)	Rel. Int. (%)	angle (° 2θ)	d value (Å)	Intensity (counts)	Rel. Int. (%)
2.35	37.615	106.7	36.1	33.56	2.668	34.9	11.8
2.48	35.640	106.3	36.0	34.29	2.613	25.7	8.7
2.98	29.590	49.6	16.8	34.73	2.581	24.1	8.1
13.49	6.559	295.5	100.0	36.51	2.459	15.1	5.1
22.37	3.971	246.0	83.3	38.25	2.351	35.1	11.9
25.46	3.496	163.8	55.4	40.15	2.244	20.2	6.8
26.94	3.306	82.7	28.0	45.59	1.988	16.4	5.6
27.02	3.297	30.3	10.3	46.90	1.936	36.4	12.3
30.58	2.921	36.7	12.4	58.03	1.588	11.6	3.9
31.59	2.830	13.9	4.7				

5.1.2 HM02

Two other samples (HM02 and HM03) were synthesized successfully afterwards. These two samples were synthesized with the same conditions, except that it was used different $Al(OH)_3$ sources during the synthesis. The obtained XRD diffractogram of protonic HM02 in a capillary is shown in Figure 5-2.

A reference XRD pattern for ZSM – 5 from '*Collection of simulated XRD powder patterns for zeolites'* (38) is attached in Figure 8-3 in appendix 8.2.

A plate XRD diffractogram of as - synthesized HM02 with preferred orientation is shown in Figure 8-4 in appendix 8.2. A list with the angle, d value, intensity and relative intensity of the peaks in Figure 5-2 is given in Table 5-2.

Figure 8-4 in appendix 8.2 shows a glass plate XRD of HM02, which do not look like an ordinary XRD pattern for a ZSM - 5 zeolite. Specially the two peaks before 10° are different from the reference. Where in the reference, the first peak at 7.9° is higher than the second peak at 9.1°. In Figure 8-4, it is visible that the second peak at 9.11° has several times (approximately 5 times) higher intensity than the first peak at 8.15°. The first peak is supposed to have higher intensity than the second as illustrated in the reference pattern. The peaks at 18.0°, 27.1°, 36.0° and 45.7° does also have stronger intensities relatively to the rest of the peaks than it is supposed to. A list with the angle, d value, intensity and relative intensity of the peaks in Figure 8-4 is given in Table 8-2.

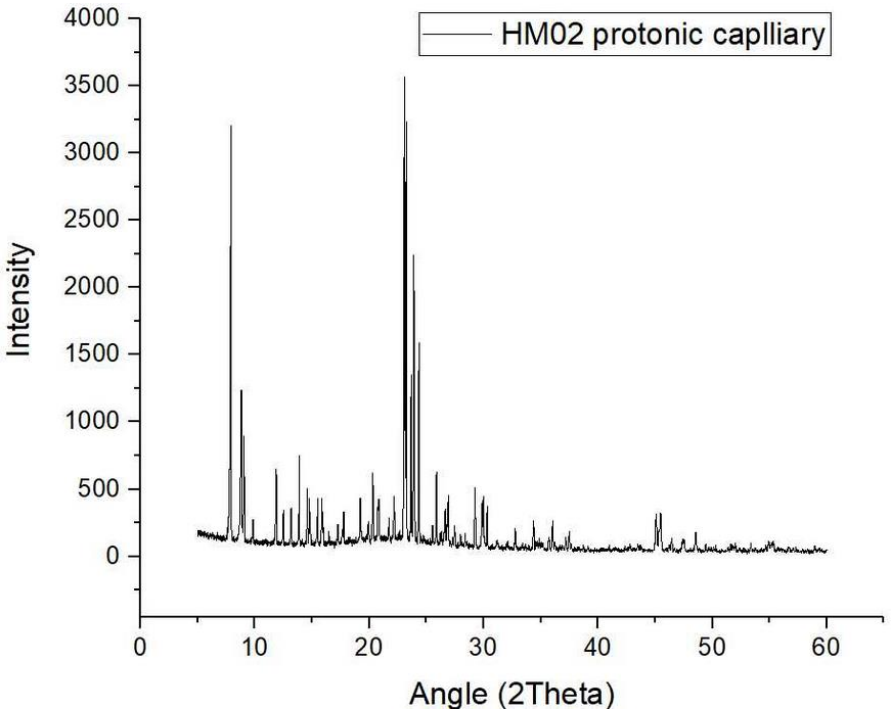

Figure 5-2: Obtained XRD pattern of a capillary with protonic HM02.

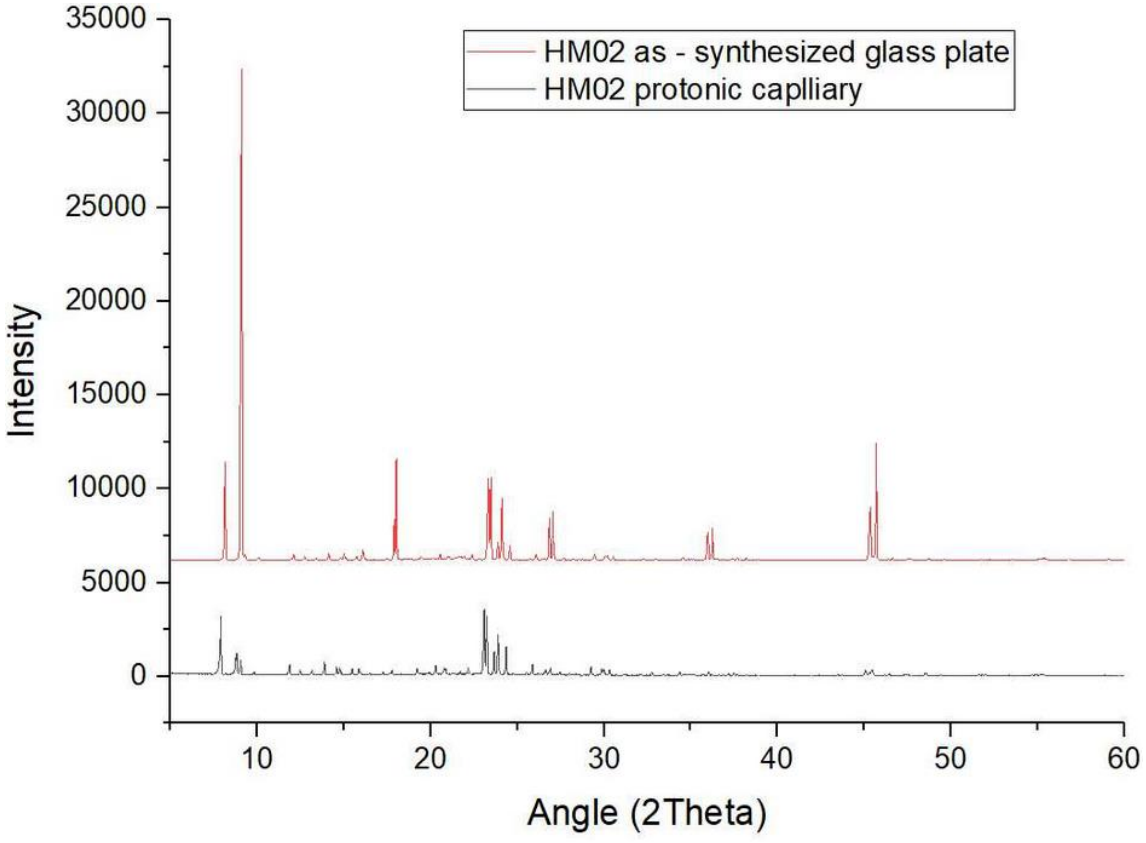

Figure 5-3: XRD pattern of HM02 as – synthesized and protonic capillary in the same plot.

Table 5-2: Peak list for HM02 protonic capillary XRD that include angle in 2θ range, d value, intensity and relative intensity of peaks.

angle (° 2θ)	d value (Å)	Intensity (counts)	Rel. Int. (%)	angle (° 2θ)	d value (Å)	Intensity (counts)	Rel. Int. (%)	angle (° 2θ)	d value (Å)	Intensity (counts)	Rel. int. (%)
7.91	11.171	2261.4	76.1	28.56	3.123	39.3	1.3	49.89	1.826	22.3	0.8
8.81	10.027	512.5	17.2	29.25	3.051	424.7	14.3	50.14	1.818	31.6	1.1
9.06	9.754	614.8	20.7	29.87	2.989	271.7	9.1	50.31	1.812	18.8	0.6
9.84	8.986	119.1	4.0	30.00	2.977	320.9	10.8	51.35	1.778	22.7	0.8
10.98	8.048	50.3	1.7	30.33	2.945	277.3	9.3	51.64	1.769	60.8	2.0
11.88	7.443	410.8	13.8	31.21	2.864	36.0	1.2	52.01	1.757	57.8	1.9
12.49	7.081	186.9	6.3	32.11	2.785	47.1	1.6	52.42	1.744	18.8	0.6
13.17	6.719	229.7	7.7	32.77	2.731	132.9	4.5	52.74	1.734	21.0	0.7
13.89	6.371	551.3	18.5	33.41	2.680	35.9	1.2	53.37	1.715	25.4	0.9
14.59	6.068	315.9	10.6	33.67	2.660	22.5	0.8	53.77	1.703	22.3	0.7
14.76	5.995	282.4	9.5	34.37	2.607	198.9	6.7	54.64	1.678	43.4	1.5
15.50	5.714	285.4	9.6	34.68	2.584	41.8	1.4	54.91	1.671	49.0	1.6
15.88	5.577	260.9	8.8	34.85	2.573	80.1	2.7	55.16	1.664	59.0	2.0
16.49	5.372	65.1	2.2	35.19	2.548	38.2	1.3	55.32	1.659	49.2	1.7
17.26	5.134	105.7	3.6	35.72	2.512	59.5	2.0	56.67	1.623	26.2	0.9
17.65	5.021	67.2	2.3	36.04	2.490	172.9	5.8	57.08	1.612	28.1	0.9
17.77	4.986	223.5	7.5	36.24	2.477	91.5	3.1	58.94	1.566	22.8	0.8
19.22	4.614	273.8	9.2	36.64	2.451	28.9	1.0	60.94	1.519	27.0	0.9
19.94	4.449	82.1	2.8	36.90	2.434	12.7	0.4	62.31	1.489	59.8	2.0
20.31	4.369	444.1	14.9	37.20	2.415	79.6	2.7	63.37	1.467	25.3	0.8
20.81	4.264	155.3	5.2	37.51	2.396	97.7	3.3	63.71	1.460	92.7	3.1
21.72	4.089	121.7	4.1	37.67	2.386	44.0	1.5	63.98	1.454	68.0	2.3
22.17	4.006	267.9	9.0	38.71	2.324	29.8	1.0	64.36	1.446	124.7	4.2
22.62	3.927	49.2	1.7	39.12	2.301	26.4	0.9	65.07	1.432	65.6	2.2
23.09	3.850	2923.0	98.3	40.96	2.202	36.4	1.2	65.55	1.423	78.8	2.7
23.25	3.823	2973.4	100.0	42.78	2.112	18.6	0.6	65.98	1.415	55.3	1.9
23.67	3.756	1173.0	39.4	43.48	2.079	62.5	2.1	66.33	1.408	27.4	0.9
23.89	3.721	1937.5	65.2	45.08	2.010	245.4	8.3	66.96	1.396	58.8	2.0
24.36	3.651	1495.2	50.3	45.33	1.999	158.0	5.3	67.39	1.388	61.6	2.1
24.77	3.591	60.1	2.0	45.48	1.993	229.7	7.7	67.72	1.383	24.9	0.8
25.54	3.485	143.6	4.8	46.24	1.962	62.6	2.1	68.78	1.364	20.0	0.7
25.87	3.441	487.5	16.4	46.45	1.953	99.2	3.3	69.90	1.345	22.4	0.8
26.21	3.398	26.3	0.9	47.38	1.917	60.0	2.0	73.50	1.287	29.2	1.0
26.35	3.380	84.4	2.8	47.42	1.916	59.9	2.0	74.74	1.269	37.3	1.3
26.66	3.342	223.8	7.5	47.51	1.912	36.9	1.2	77.86	1.226	33.2	1.1
26.91	3.310	358.5	12.1	48.55	1.874	123.6	4.2	78.90	1.212	66.9	2.3
27.46	3.245	141.9	4.8	48.82	1.864	55.6	1.9	81.07	1.185	16.3	0.5
28.00	3.184	83.1	2.8	49.39	1.844	44.2	1.5	82.63	1.167	10.3	0.3
28.39	3.141	85.9	2.9	49.66	1.834	34.8	1.2	85.96	1.130	18.1	0.6

A diffractogram showing protonic HM02 performed on a glass plate with preferred orientation is also illustrated in appendix 8.2, in Figure 8-5. For the proton form of HM02, the peak at 9.18° has approximately double of the intensity of the peak at 8.26°.

The reason the diffractogram looks different from an ordinary XRD pattern of a ZSM - 5 zeolite is due to that the sample has preferred orientation. Preferred orientation is explained in section 3.2 as a case where the crystals orientate in a non – random distribution on a surface. To minimize the effects of preferred orientation, the sample was reanalyzed using capillary XRD. The capillary XRD of HM02 is shown in Figure 5-2, where the effects of preferred orientation are gone and thereby showing a XRD pattern that is characteristic of a ZSM - 5 zeolite. The XRD pattern is characteristic of a ZSM – 5 by for example the major double peak at 7.91° and 8.81°, the peaks between 13° and 18° and the characteristic double peak at 45.08° and 45.48°. By comparing these peaks with literature, it is concluded that the material is a ZSM – 5 zeolite.

The pattern of and protonic capillary of HM02 is shown together with as – synthesized glass plate on the same x - axis in Figure 5-3. According to the computed crystallinity of the raw. file for the pattern of HM02 as – synthesized in Diffrac.EVA, it has a 95.3% crystallinity and is 4.7% amorphous and 81.2% crystallinity and 18.8% amorphous for the capillary of HM02 and the pattern of HM02 protonic with preferred orientation (see Figure 8-5) has a 95.4% crystallinity and 4.6% amorphous.

A XRD pattern of a sample of HM02 on proton form was measured on BM01 synchrotron at ESRF in Grenoble is shown in appendix 8.2, in Figure 8-6. The measurement was performed in oct. 2020. A Rietveld refinement with the ZSM - 5 framework (illustrated in Figure 5-4) was analyzed by Nico König and the refinement resulted in a quite bad fit with R_{wp} (weighted profile residual) > 30%, which estimated a, b and c vectors of 20.074 Å, 19.924 Å and 13.419 Å respectively. Particularly the relative intensity was off. Addition of dummy carbons improves the fit to R_{wp} 20% (18.7%). The mismatch might originate from water that had adsorbed into the material's pores. A Pawley refinement was also conducted on the data (77), which estimated a, b and c vectors of 20.073 Å, 19.923 Å and 13.417 Å respectively, which is very similar to the Rietveld refinement. The Pawley refinement gave basically identical results, but a lower R_{wp} (9%). The results from the Rietveld and Pawley refinement are summarized in Table 5-3. The data in Figure 5-4 was from a HM02 sample measured in a capillary. The capillary was not rotated during the experiment. Because of this it seems that not all of the effects from preferred

orientation have been removed, which could explain the bad fit for Rietveld and Pawley refinement.

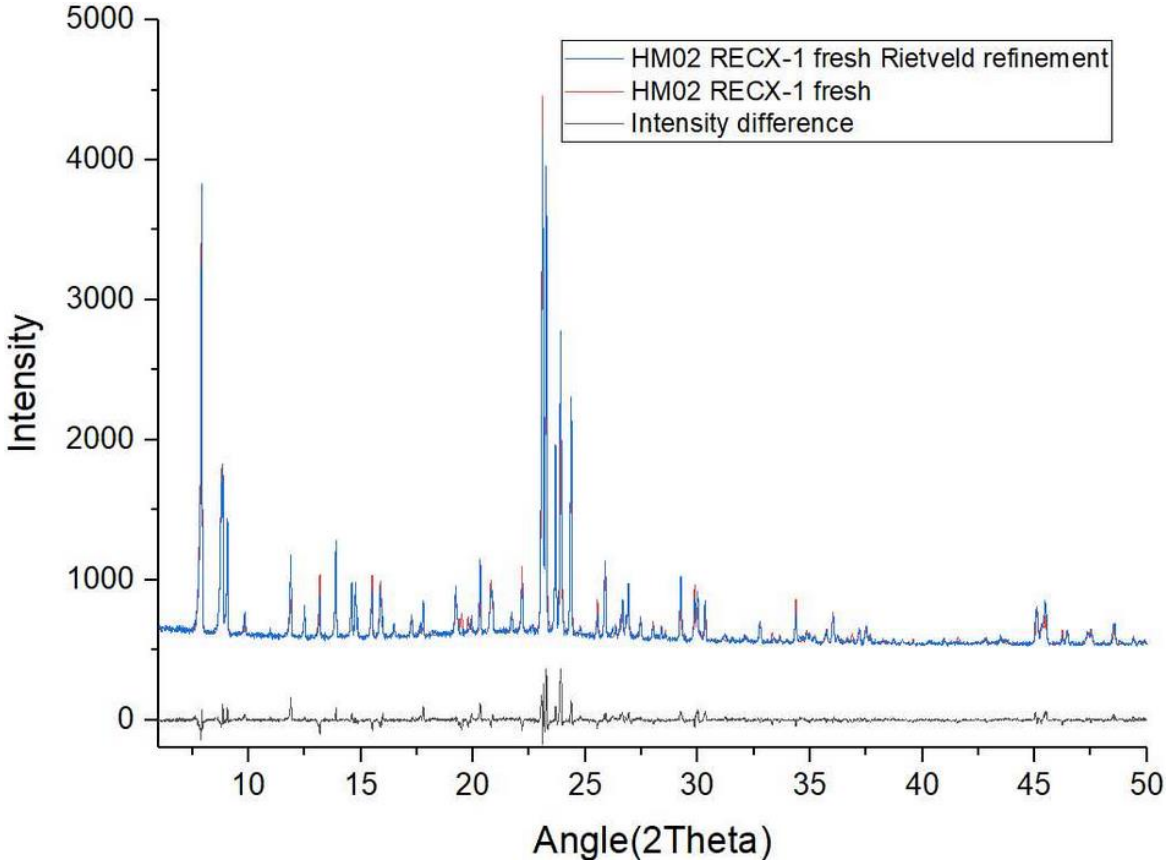

Figure 5-4: XRD diffractogram of HM02 (in blue) with a Rietveld refinement to the data (in red). Differences in intensity between the pattern and the refinement is indicated in black.

Table 5-3: Summary of a Rietveld and Pawley refinement for the diffractogram in Figure 5-4.

Quantity	Rietveld	Pawley
a (Å)	20.074	20.073
b (Å)	19.924	19.923
c (Å)	13.419	13.417
R_{wp} (%)	18.7	9.0

5.1.3 HM03

A XRD diffractogram of as - synthesized HM03 is illustrated in Figure 5-5 and Figure 5-6 shows a XRD pattern of protonic HM03 from a full plate.

Figure 5-5 shows a plate XRD diffractogram of as – synthesized HM03, which in contrast to HM02, do not show preferred orientation for the crystals. A list with the angle, d value, intensity and relative intensity of the peaks in Figure 5-5 is given in Table 5-4. The XRD pattern is characteristic of a ZSM – 5 by for example the major double peaks at 8.19° and 9.12°, the peaks between 13° and 18° and the characteristic double peak at 45.31° and 45.62°. By comparing these peaks with literature, it is concluded that the material is a ZSM – 5 zeolite. This XRD therefore looks like a typical XRD pattern for a ZSM - 5 zeolite.

The HM03 sample shown in Figure 5-6 was only calcined and ion exchanged before the XRD was taken and is very similar to the pattern in Figure 5-5. The only major difference is the relative intensity of the peak at 23.37° for as - synthesized and 22.99° for the protonic form. The angle, d value, intensity and relative intensity of the peaks in Figure 5-6 is given in Table 5-5. The pattern of as – synthesized glass plate and protonic full plate HM03 is shown on the same x - axis in Figure 5-7. According to the computed crystallinity of the raw. file for the pattern of HM03 as – synthesized in Diffrac.EVA, it has a 72.0% crystallinity and is 28.0% amorphous. According to the computed crystallinity for the raw. file for the pattern of HM03 protonic in Diffrac.EVA, it is 78.8% crystalline and is 21.2% amorphous.

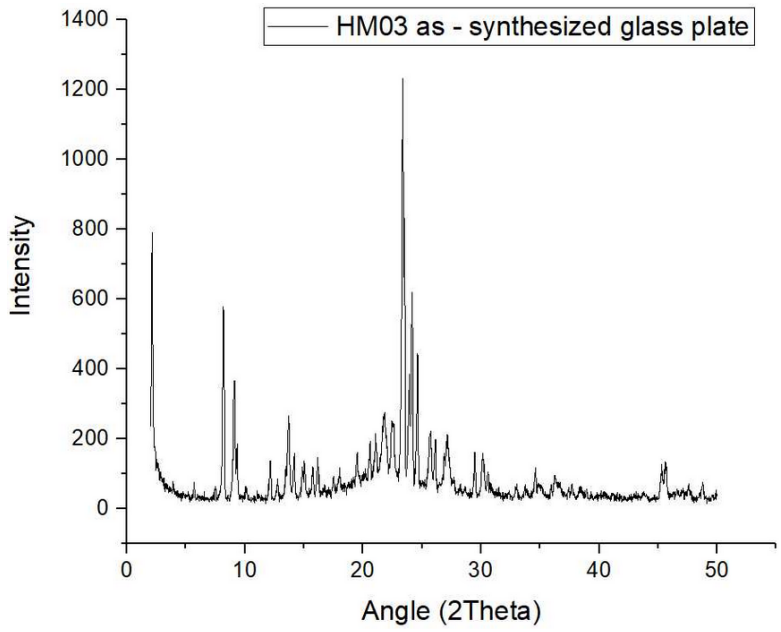

Figure 5-5: A glass plate XRD of as - synthesized HM03.

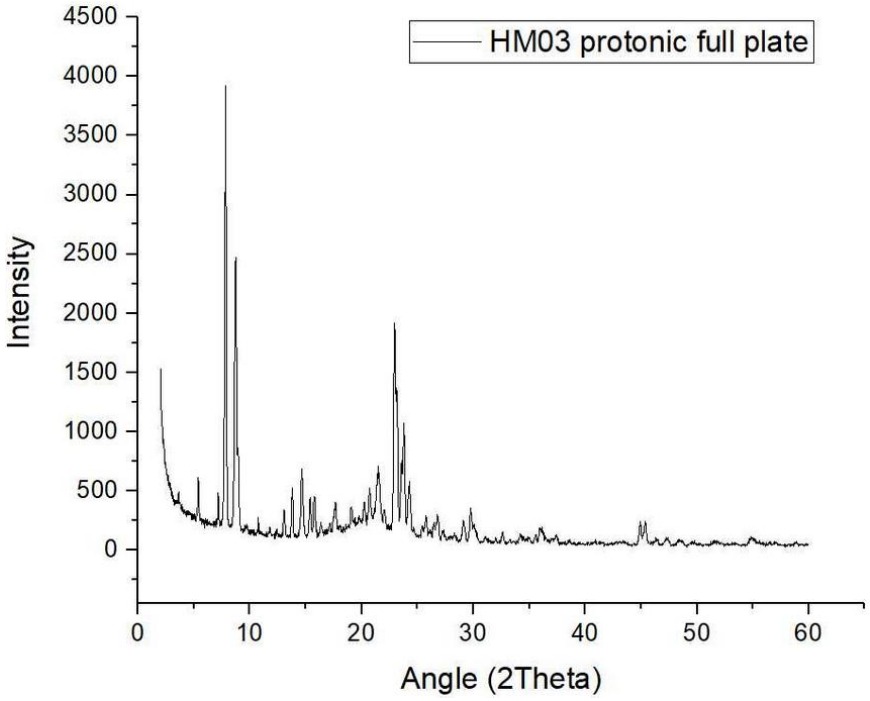

Figure 5-6: A full plate XRD of protonic HM03.

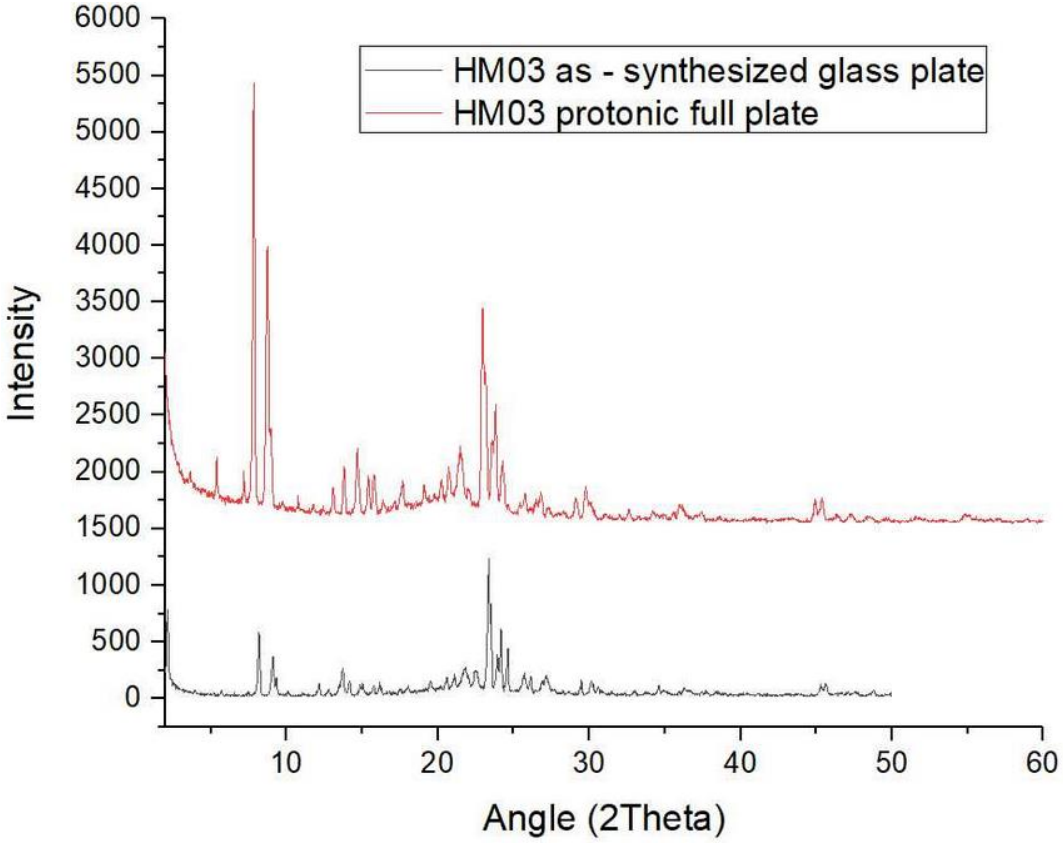

Figure 5-7: XRD pattern of HM03 as – synthesized glass plate and protonic full plate in the same plot.

Table 5-4: Peak list for HM03 as – synthesized glass plate XRD.

angle (° 2θ)	d value (Å)	Intensity (counts)	Rel. int. (%)	angle (° 2θ)	d value (Å)	Intensity (counts)	Rel. int (%)
5.70	15.483	25.2	3.2	24.16	3.681	409.3	51.9
7.49	11.791	26.4	3.4	24.63	3.612	286.1	36.2
8.19	10.789	342.7	43.4	25.69	3.464	102.0	12.9
9.12	9.690	212.4	26.9	26.13	3.408	86.5	11.0
9.35	9.456	106.8	13.5	27.15	3.282	109.1	13.8
10.10	8.749	26.5	3.4	27.59	3.230	17.6	2.2
12.15	7.277	77.1	9.8	28.25	3.156	22.3	2.8
12.77	6.924	31.2	4.0	29.48	3.027	86.7	11.0
13.71	6.454	145.5	18.4	30.15	2.962	88.3	11.2
14.17	6.245	76.9	9.7	30.59	2.921	48.4	6.1
15.05	5.883	49.6	6.3	33.03	2.710	29.5	3.7
15.76	5.619	58.4	7.4	34.60	2.590	61.5	7.8
16.16	5.479	73.6	9.3	35.97	2.495	18.0	2.3
16.76	5.285	16.9	2.1	36.31	2.472	36.7	4.7
17.53	5.055	21.7	2.7	36.60	2.453	23.4	3.0
17.99	4.928	27.6	3.5	37.71	2.384	27.3	3.5
19.50	4.548	58.6	7.4	38.41	2.342	15.7	2.0
20.57	4.315	59.7	7.6	38.94	2.311	25.0	3.2
21.10	4.208	57.2	7.2	45.31	2.000	73.3	9.3
21.81	4.072	97.5	12.4	45.62	1.987	83.3	10.6
22.55	3.939	101.6	12.9	47.59	1.909	32.0	4.1
23.37	3.804	789.4	100.0	48.77	1.866	38.8	4.9
23.93	3.716	227.5	28.8				

Table 5-5: Peak list for HM03 protonic full plate XRD.

angle (° 2θ)	d value (Å)	Intensity (counts)	Rel. Int. (%)	Angle (° 2θ)	d value (Å)	Intensity (counts)	Rel. Int. (%)	angle (° 2θ)	d value (Å)	Intensity (counts)	Rel. Int. (%)
5.40	16.353	209.6	8.4	22.04	4.030	86.7	3.5	35.56	2.523	40.4	1.6
7.18	12.297	173.3	7.0	22.99	3.865	944.9	38.0	35.98	2.494	79.4	3.2
7.84	11.273	2487.0	100.0	23.12	3.844	837.8	33.7	36.18	2.481	69.9	2.8
8.73	10.118	1534.1	61.7	23.60	3.767	382.1	15.4	37.40	2.402	48.5	2.0
9.73	9.081	42.5	1.7	23.79	3.737	599.6	24.1	38.60	2.330	24.5	1.0
10.76	8.218	88.5	3.6	24.28	3.663	277.9	11.2	40.82	2.209	17.0	0.7
11.80	7.496	43.1	1.7	24.65	3.609	45.8	1.8	44.94	2.016	127.7	5.1
12.41	7.126	50.9	2.0	25.43	3.499	56.2	2.3	45.37	1.997	151.6	6.1
13.08	6.765	146.5	5.9	25.76	3.456	124.6	5.0	46.38	1.956	21.4	0.9
13.81	6.408	276.1	11.1	26.51	3.360	70.5	2.8	47.29	1.921	34.4	1.4
14.67	6.034	362.9	14.6	26.80	3.324	148.2	6.0	48.44	1.878	28.6	1.1
15.40	5.749	227.4	9.1	27.29	3.265	38.4	1.5	54.88	1.672	43.1	1.7
15.78	5.610	191.6	7.7	28.29	3.152	49.2	2.0	56.46	1.628	15.1	0.6
16.38	5.408	63.4	2.6	29.13	3.063	91.6	3.7	60.82	1.522	18.7	0.8
17.14	5.169	35.4	1.4	29.77	2.999	192.8	7.8	62.34	1.488	26.6	1.1
17.64	5.024	129.9	5.2	30.06	2.970	83.3	3.3	63.45	1.465	52.5	2.1
19.08	4.648	135.3	5.4	31.09	2.875	30.5	1.2	64.24	1.449	39.0	1.6
19.75	4.491	41.2	1.7	31.99	2.796	17.5	0.7	66.93	1.397	44.3	1.8
20.22	4.387	135.0	5.4	32.62	2.743	64.7	2.6	73.51	1.287	19.1	0.8
20.71	4.285	212.9	8.6	34.21	2.619	53.2	2.1	78.78	1.214	30.3	1.2
21.46	4.136	338.5	13.6	34.92	2.568	23.4	0.9				

5.1.4 ACS extrudates

Figure 5-8 consists of a XRD diffractogram of the ACS extrudates on proton form. A list with the angle, d value, intensity and relative intensity of the peaks in Figure 5-8 is given in Table 5-6. The XRD pattern is characteristic of a ZSM – 5 with the major double peak at 8.22° and 9.09°, the peaks between 13° and 18° and the characteristic double peak at 45.26° and 45.71°. Since these peaks are characteristic for a ZSM - 5 zeolite, it is concluded that the material has correct crystallinity (55). However as described by Wragg et al. (78), the signal at 67° is alumina, which means that the zeolite was not the only phase present in the sample. According to the computed crystallinity of the raw. file for the pattern in Diffrac.EVA, it has an 80.3% crystallinity and is 19.7% amorphous.

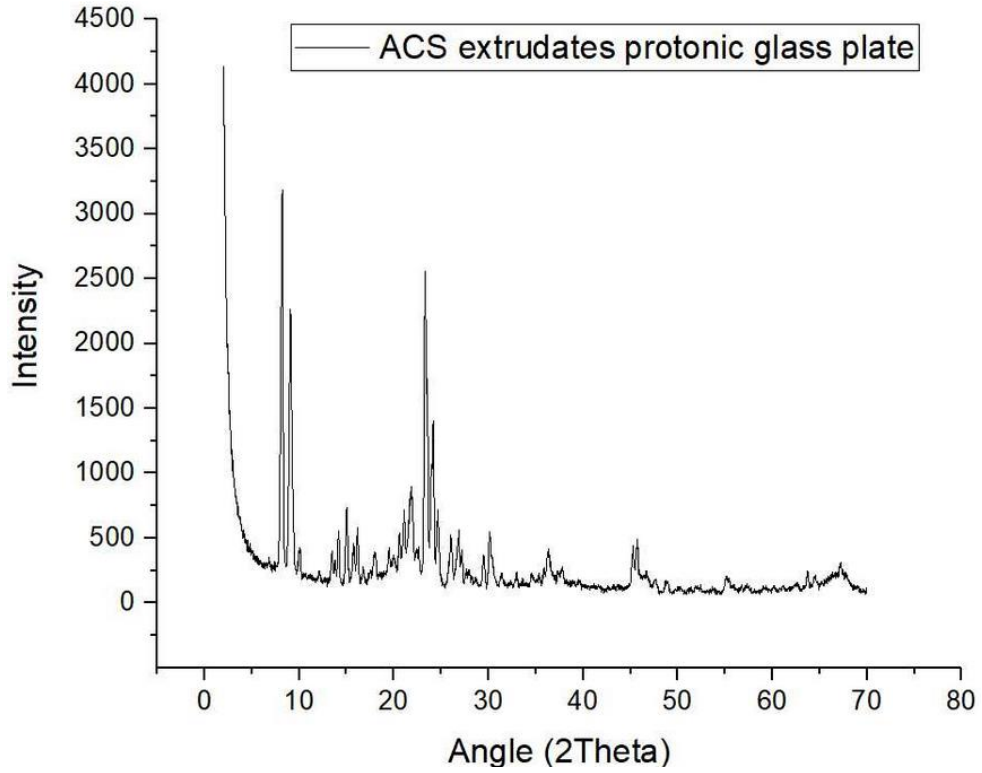

Figure 5-8: XRD diffractogram of protonic ACS extrudates measured om a glass plate.

Table 5-6: Peak list for ACS extrudates glass plate XRD.

angle (° 2θ)	d value (Å)	Intensity (counts)	Rel. int. (%)	angle (° 2θ)	d value (Å)	Intensity (counts)	Rel. int. (%)	angle (° 2θ)	d value (Å)	Intensity (counts)	Rel. int. (%)
8.22	10.748	2930.0	100.0	23.31	3.812	2413.1	82.4	35.87	2.501	151.1	5.2
9.09	9.724	2032.1	69.4	23.52	3.780	1457.4	49.7	36.33	2.471	256.5	8.8
10.02	8.819	149.3	5.1	24.17	3.680	1271.3	43.4	36.21	2.479	221.7	7.6
12.11	7.302	79.3	2.7	24.64	3.610	603.3	20.6	37.42	2.401	46.8	1.6
12.76	6.934	46.8	1.6	26.03	3.421	373.9	12.8	37.74	2.381	98.4	3.4
13.41	6.597	221.9	7.6	26.85	3.318	431.9	14.7	45.26	2.002	326.0	11.1
13.77	6.426	177.6	6.1	27.18	3.278	258.8	8.8	45.71	1.983	383.4	13.1
14.16	6.248	397.3	13.6	27.65	3.223	117.3	4.0	46.63	1.946	137.8	4.7
15.02	5.896	605.4	20.7	27.94	3.190	124.8	4.3	47.64	1.907	94.5	3.2
15.77	5.616	303.5	10.4	28.24	3.158	67.7	2.3	48.81	1.864	83.2	2.8
16.16	5.482	403.0	13.8	28.65	3.113	66.8	2.3	55.14	1.664	112.9	3.9
16.75	5.288	96.1	3.3	29.51	3.024	214.8	7.3	55.37	1.658	94.3	3.2
17.98	4.929	213.5	7.3	30.10	2.967	464.0	15.8	56.75	1.621	44.5	1.5
19.48	4.553	195.7	6.7	30.38	2.940	226.3	7.7	60.13	1.538	32.5	1.1
19.95	4.447	124.5	4.3	31.42	2.845	101.1	3.4	61.11	1.515	47.3	1.6
20.61	4.307	326.8	11.2	32.37	2.764	51.6	1.8	63.72	1.459	135.6	4.6
21.11	4.206	431.4	14.7	32.97	2.715	107.8	3.7	64.44	1.445	137.3	4.7
21.86	4.063	597.3	20.4	34.57	2.592	69.0	2.4	67.20	1.392	167.0	5.7
22.58	3.934	192.5	6.6	35.33	2.539	72.9	2.5				

5.1.5 MFI - 27

Figure 5-9 consists of a XRD diffractogram of MFI – 27 material on proton form. A list with the angle, d value, intensity and relative intensity of the peaks in Figure 5-9 is given in Table 5-7. The XRD pattern is characteristic of a ZSM – 5 with the major double peak at 8.06° and 8.99°, the peaks between 13° and 18° and the characteristic double peak at 45.13° and 45.57°. By comparing these peaks with literature from '*Collection of simulated XRD powder patterns for zeolites'* (38), it is concluded that the material is a ZSM – 5 zeolite. A picture of a reference x – ray pattern is attached in appendix 8.2 in Figure 8-3. According to the computed crystallinity of the raw. file for the pattern in Diffrac.EVA, it has an 82.8% crystallinity and is 17.2% amorphous.

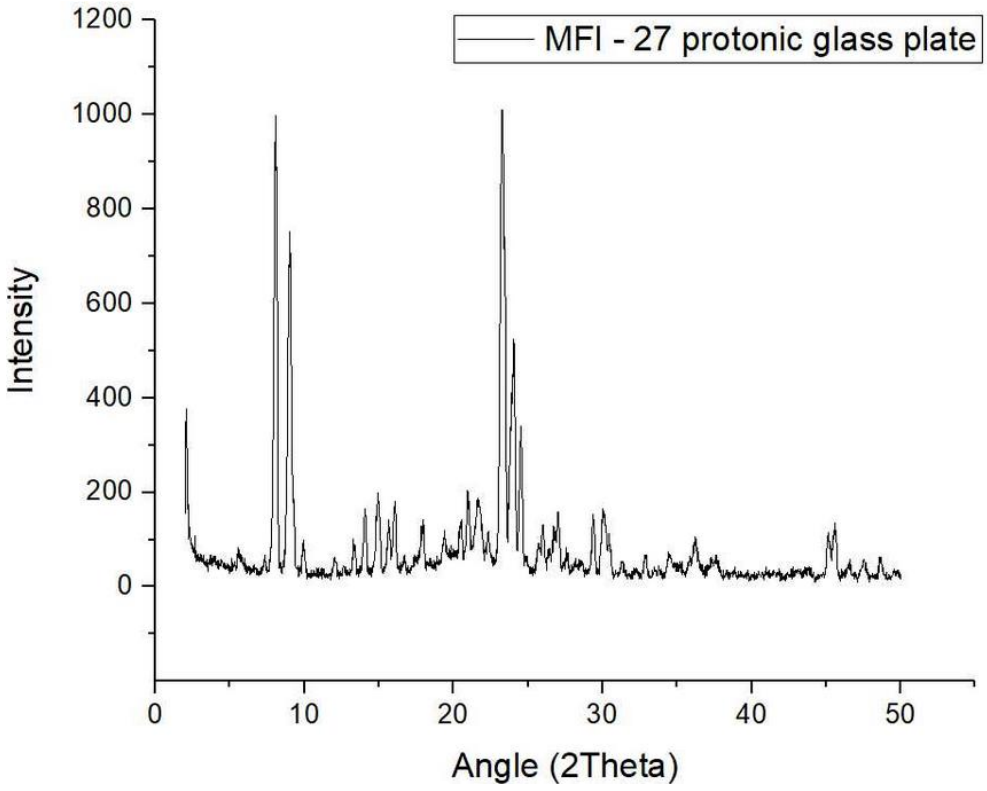

Figure 5-9: XRD diffractogram of the protonic form of the commercial material, MFI – 27 measured on a glass plate.

Table 5-7: Peak list for MFI – 27 glass plate XRD.

angle (° 2θ)	d value (Å)	Intensity (counts)	Rel. int. (%)	angle (° 2θ)	d value (Å)	Intensity (counts)	Rel. int. (%)
5.64	15.662	22.4	3.5	24.52	3.628	214.2	33.2
7.34	12.035	16.2	2.5	24.87	3.577	18.2	2.8
8.06	10.962	644.3	100.0	25.74	3.458	37.0	5.7
8.99	9.824	502.7	78.0	26.00	3.425	51.1	7.9
9.95	8.880	30.9	4.8	26.76	3.329	73.9	11.5
12.04	7.342	19.0	2.9	27.03	3.296	72.9	11.3
12.62	7.007	11.5	1.8	27.58	3.231	22.2	3.4
13.33	6.639	29.6	4.6	28.53	3.127	20.0	3.1
14.07	6.291	81.7	12.7	29.38	3.038	77.3	12.0
14.93	5.929	102.6	15.9	30.08	2.969	86.4	13.4
15.68	5.648	77.8	12.1	30.43	2.935	62.2	9.7
16.07	5.512	101.1	15.7	31.29	2.857	22.3	3.5
16.67	5.313	18.7	2.9	32.23	2.775	15.0	2.3
17.97	4.933	52.6	8.2	32.87	2.722	27.6	4.3
19.39	4.573	46.7	7.2	34.50	2.598	23.7	3.7
20.48	4.334	50.3	7.8	36.24	2.477	60.4	9.4
20.99	4.230	84.1	13.0	45.13	2.007	64.6	10.0
21.67	4.097	65.4	10.2	45.57	1.989	75.0	11.6
22.33	3.977	31.4	4.9	46.53	1.950	26.5	4.1
23.27	3.820	635.6	98.6	47.53	1.911	30.8	4.8
24.00	3.705	270.9	42.0	48.66	1.870	35.1	5.4

5.1.6 Beta zeolites

The XRD patterns of the Beta zeolites had the expected crystallinity, since they were commercial materials and they had all good matches with literature (79). The XRD diffractograms of the Beta materials used for catalytic testing are given in appendix 8.2 in Figure 8-7 to 8-10 and the peaks are listed in Table 8-4 to 8-7. According to the computed crystallinity of the raw. file for the patterns in Diffrac.EVA, 09-00243/1 has a 67.4% crystallinity and is 32.6% amorphous, SK_CP814C has 69.7% crystallinity and is 30.3% amorphous, CP806B-25 has 69.9% crystallinity and is 30.1% amorphous and CP811BL-25 has 52.8% crystallinity and is 47.2% amorphous.

5.2 Thermogravimetric analysis

TGA was performed on as – synthesized form, protonic form and deactivated samples that had been used on the Co - feed test rig of the materials HM02 and HM03. TGA was also performed on protonic form of the commercial MFI – 27 material, as well as the protonic form and deactivated form of the ACS extrudates. The data gathered from the analysis was used to get a better understanding of the materials' composition by determining the amount of template, water and coke in the materials.

From as - synthesized samples, the amount of template compared to zeolite was identified. For ZSM – 5 zeolites with TPA as SDA, it is known that the maximum of incorporated TPA ions per unit cell of the MFI framework is about four (80). From protonic samples, there is not expected to be much change for the samples during a TGA analysis. TGA was performed on protonic samples to investigate the amount of water that is present in the material and to verify that there were no remaining template, adsorbents or impurities present in the material. From a TGA analysis of samples that had been used on the Co – feed test rig, it is visible how much coke the sample contains after a catalytic test, which is the main interest from TGA analysis from the deactivated samples. The TGA of the samples with coke content are focused on in section 5.9.

5.2.1 HM02

The TGA analysis of as – synthesized HM02 (see Figure 5-10) shows that the sample contains 14 wt.% total of template and impurities (indicated as the difference between the red and blue dashed line). It has a little mass loss at 200°C with 0.7 wt.%, which correspond to the removal of adsorbed water from the material (the drop from temperature at time 0 to 200°C). The bigger drop from 300 – 700°C (12.1 wt.%), corresponds to the decomposition of template and impurities (81).

The TGA analysis of protonic HM02 (see Figure 5-11) shows a mass drop until approximately 100°C equal to 1.6 wt.%, which corresponds to removal of water in the structure of the sample.

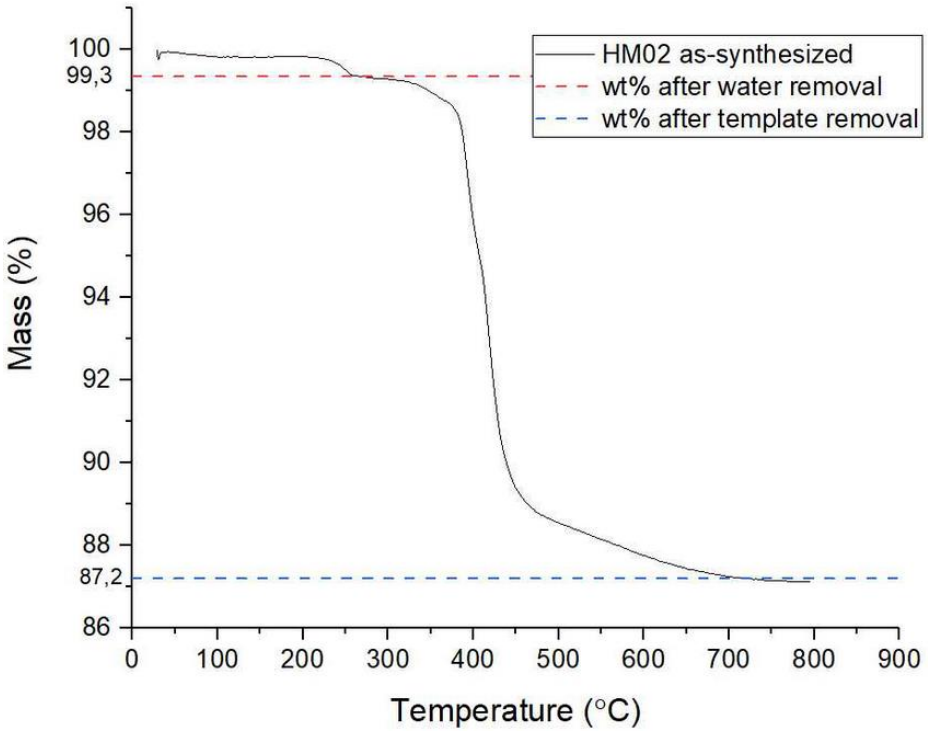

Figure 5-10: TGA analysis of as - synthesized HM02, where the material is heated from room temperature to 800°C, with an atmosphere of 20% oxygen and 80% nitrogen.

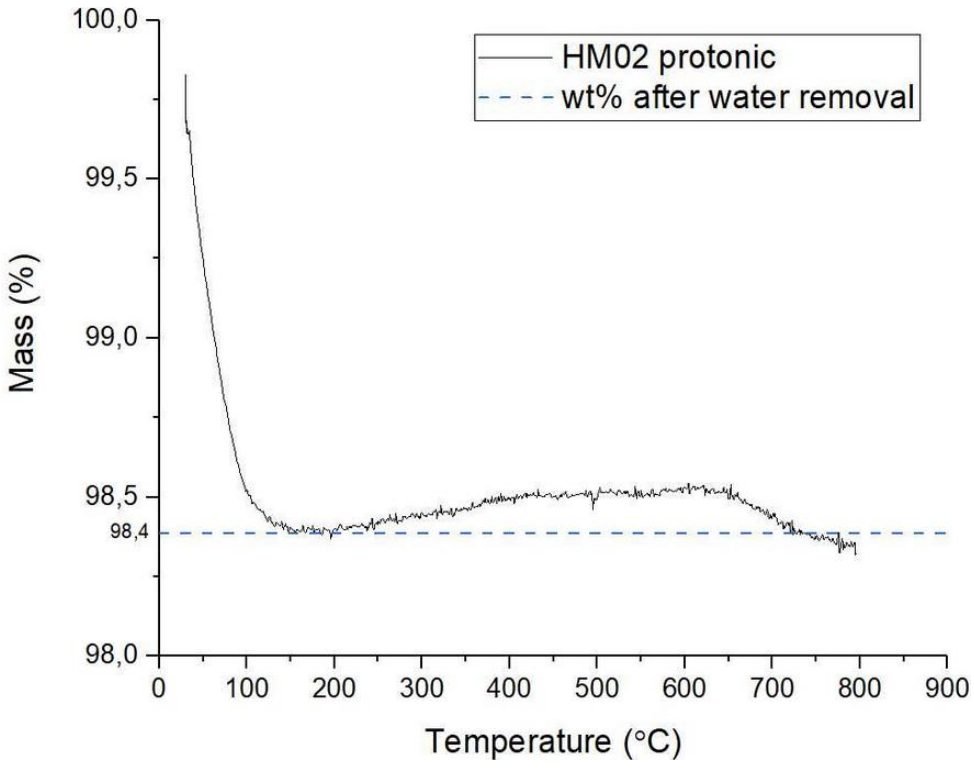

Figure 5-11: TGA analysis of protonic HM02, where the material is heated from room temperature to 800°C, with an atmosphere of 20% oxygen and 80% nitrogen.

5.2.2 HM03

The TGA analysis in Figure 5-12 shows that as - synthesized HM03 contains a total of 25 wt.% of other material than actual zeolite, which is mostly template and impurities. It has a mass loss at 200°C (approximately 17 wt.%), which might correspond to the removal water and impurities and a drop from 300 – 700°C corresponding to 8 wt.% (drop from red to blue dashed line), which corresponds to the decomposition of template and impurities in the sample. It is uncertain as of why the drop for HM03 at 200°C is as big as it is.

The TGA analysis of protonic HM03 (see Figure 5-12) shows a mass drop in the beginning equal to 2.8 wt.%, which corresponds to removal of water in the structure of the sample.

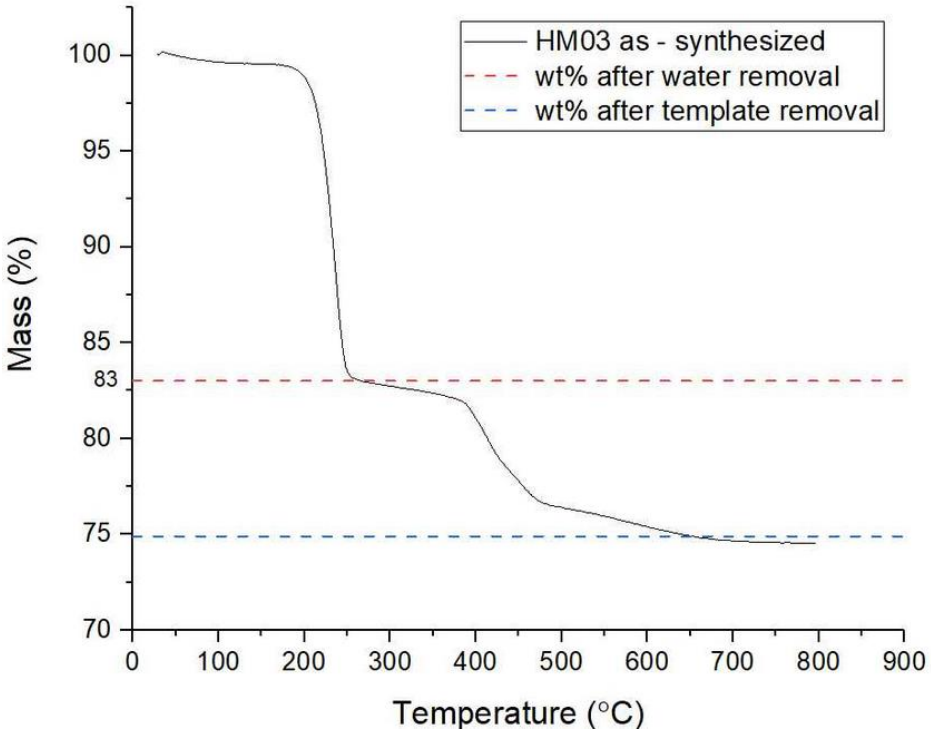

Figure 5-12: TGA analysis of as - synthesized HM03, where the material is heated from room temperature to 800°C, with an atmosphere of 20% oxygen and 80% nitrogen.

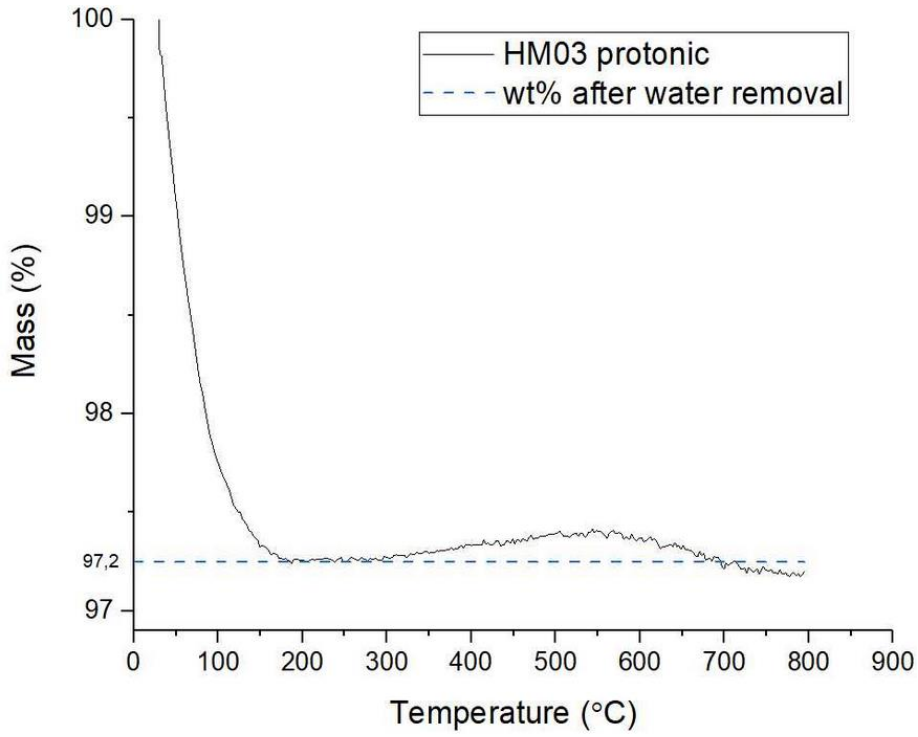

Figure 5-13: TGA analysis of protonic HM03, where the material is heated from room temperature to 800°C, with an atmosphere of 20% oxygen and 80% nitrogen.

Except for the drop until 100°C for the TGA analysis of protonic HM02 and HM03 (see Figure 5-11 and 5-13), which is removal of water, no significant mass changes during the two analyses are observed. HM02 has 1.6 wt.% of water (indicated as the drop to the blue dashed line), that is present in its protonic form and HM03 has 2.8 wt.% of water that is present (indicated as the drop to the blue dashed line). The water amount that is estimated in a TGA, is water molecules that is bonded to zeolites active sites. The amount of water adsorbed by a zeolite is dependent on atmospheric conditions. The expected observed weight loss due to water for a protonic zeolite, is 5 – 10% according to '*The hygroscopic nature of H-ZSM—5, zeolites'* (81), which is higher than the weight loss for both HM02 and HM03 due to the removal of water. This is an indication that both materials have fewer active sites than a usual ZSM – 5 zeolite.

5.2.3 ACS extrudates

A TGA analysis of the ACS extrudates on proton form is illustrated in Figure 5-14. The analysis illustrates that the sample has a weight loss in the beginning, which is because of the removal of water. The water content for the material is expected to correspond to the drop until 200°C

(indicated by blue dashed line), which is equal to 4 wt.%. The residual weight loss after 200°C is expected to be additional impurities. ACS extrudates is similar as HM02 and HM03 in the way that it has less water in its structure than what is usual for a ZSM – 5 zeolite, but since 30% of the material is alumina, it is reasonable that the material has fewer active sites than a usual zeolite to absorb water.

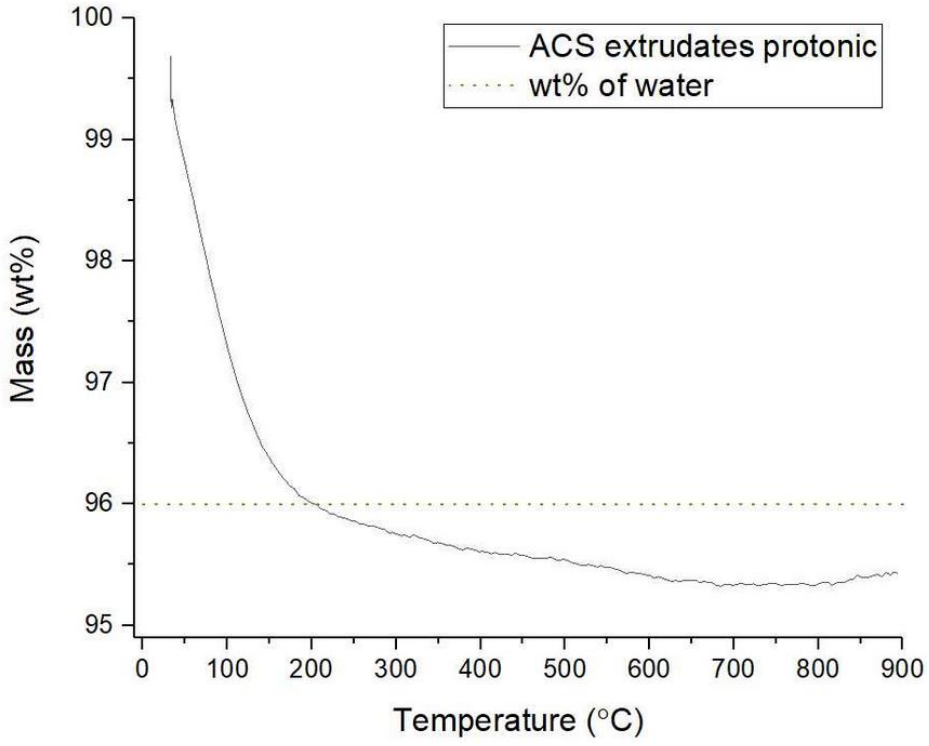

Figure 5-14: TGA analysis of protonic HM03, where the material is heated from room temperature to 900°C, with an atmosphere of 60% oxygen and 40% nitrogen.

5.2.4 MFI - 27

A TGA analysis of protonic MFI – 27 is illustrated in Figure 5-15. There is a drop in weight for the sample until 150°C, which is removal of water (indicated by red dashed line). According to the analysis, the material has 6.5 wt.% of water, that is present in the structure of the material. The instrument was unstable at the time of the TGA analysis for this material (although the analysis was repeated), which can be an explanation for the mass increase at high temperature.

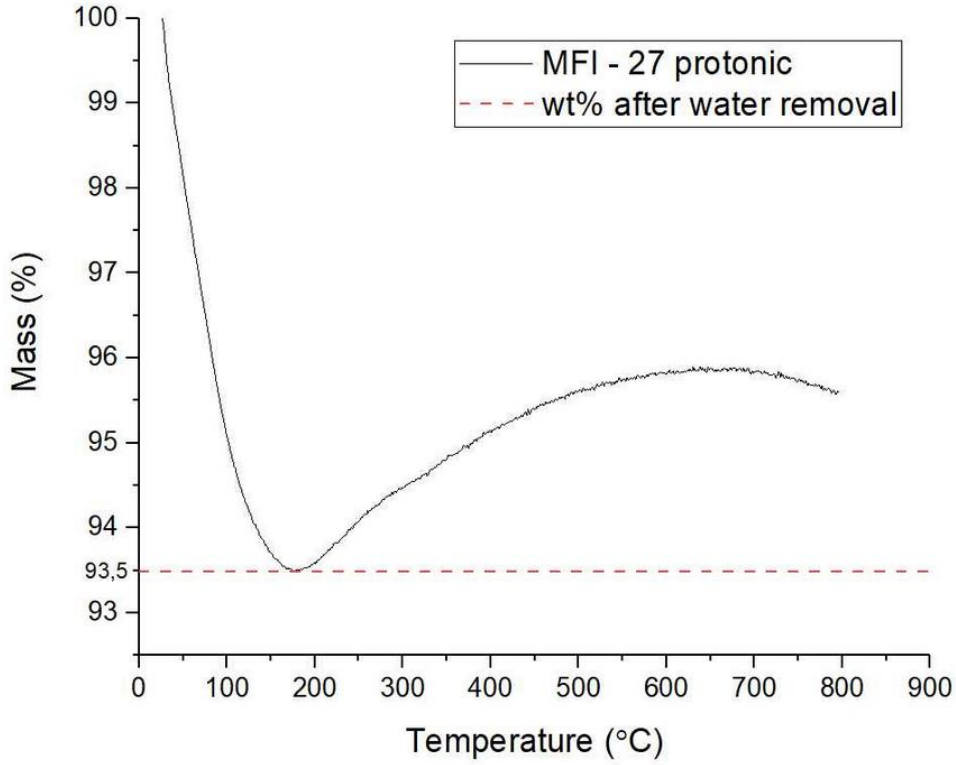

Figure 5-15: TGA analysis of the commercial zeolite MFI – 27 on proton form, where the material is heated from room temperature to 800°C, with an atmosphere of 20% oxygen and 80% nitrogen.

5.2.5 Summarized results

The results for the TGA analysis of as – synthesized and protonic materials are summarized in Table 5-8 and Table 5-9.

Table 5-8: Summary of TGA analysis for as – synthesized materials.

Material name	Sample weight (mg)	First mass drop (%)	Second mass drop (%)
HM02 as – synthesized	22.4	0.7	12.1
HM03 as – synthesized	16.2	17.0	8.0

Table 5-9: Summary of TGA analysis for protonic materials.

Material name	Sample weight (mg)	Amount of water (%)
HM02 protonic	42.5	1.6
HM03 protonic	17.4	2.8
ACS extrudates protonic	13.3	4.0
MFI - 27 protonic	30.0	6.5

5.3 Scanning electron microscope

SEM was performed to understand the materials morphology. The zeolites morphology was compared with materials from literature. SEM was used to investigate the morphology of the two homemade ZSM – 5 zeolites HM02 and HM03 and the commercial MFI – 27 zeolite material.

5.3.1 HM02

Two images of HM02 from a SEM microscope is shown in Figure 5-16, where the image on the left shows a picture that is focused on 2 crystals and the image on the right shows a picture of multiple packed crystals. All crystals appear to be at the same size and very similar to typical crystal shape of MFI. The average crystal size of the particle for HM02 is 35 µm × 16 µm. The crystal shape of HM02 is similar to the crystal shape of the parent sample from *Applied catalysis, 'Methanol to gasoline over zeolite H-ZSM-5: improved catalyst performance by treatment with NaOH' (2008)* (25). The crystals for HM02 are according to Koegler et al. and Maarten et al. (82, 83), crystals that have intergrown crystals. According to the article, the crystals also have central defects.

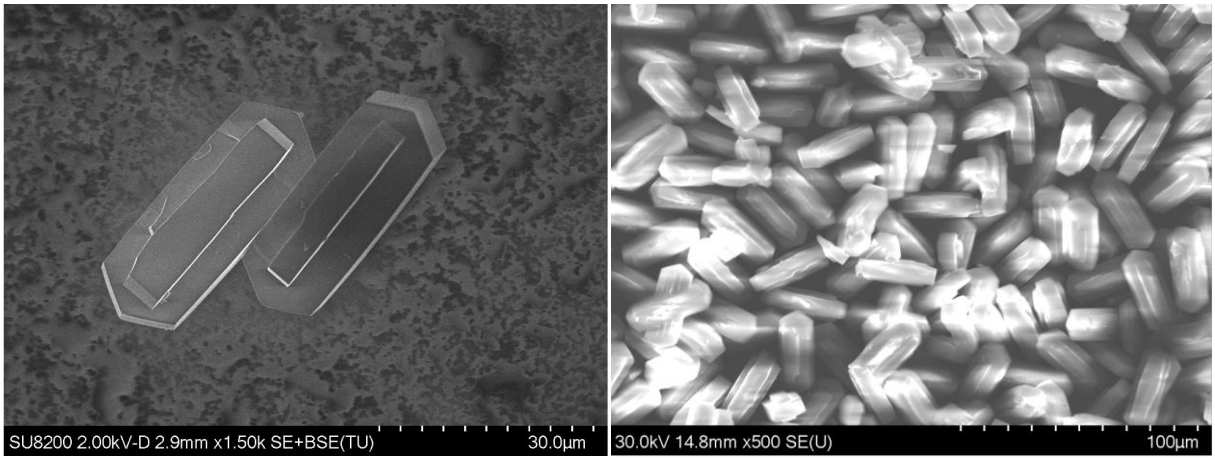

Figure 5-16: SEM images of HM02 with 1.5k and 500 magnification, using a SE detector and BSE detector for the left image and SE detector for the image on the right.

The SEM image of HM02 in Figure 5-17 shows some crystals of the material, that is packed around each other.

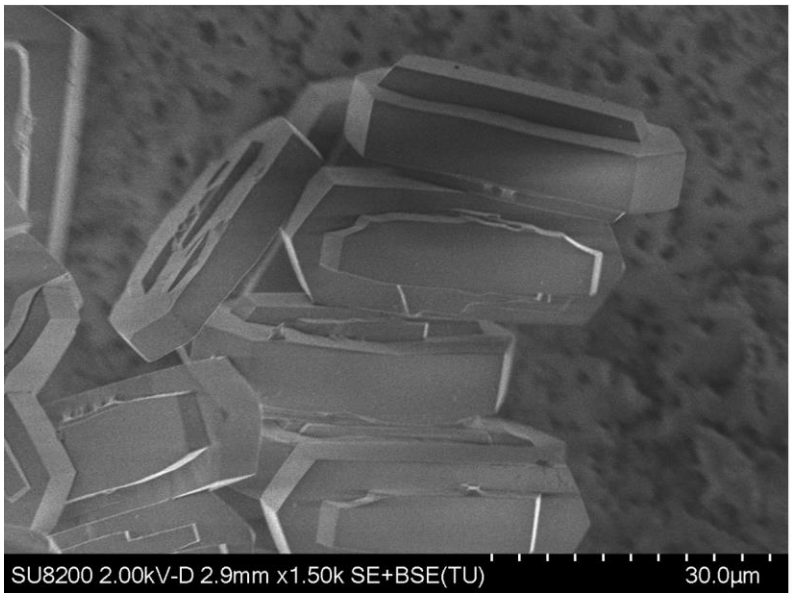

Figure 5-17: An additional SEM image of HM02 with 1.5 k magnification, using a SE and BSE detector.

5.3.2 HM03

Figure 5-18 shows two SEM pictures of HM03, which seems to have variety in morphology, in both size and shape. There are crystals in the same shape as HM02 and the materials from *Applied catalysis, 'Methanol to gasoline over zeolite H-ZSM-5: improved catalyst performance by treatment with NaOH' (2008)* (25) in clusters, but also crystals in other shapes. The crystal size varies in length from 15 μm to 60 μm (measured manually). Additional SEM pictures of HM03 are given in appendix 8.4, in Figure 8-13 to 8-15.

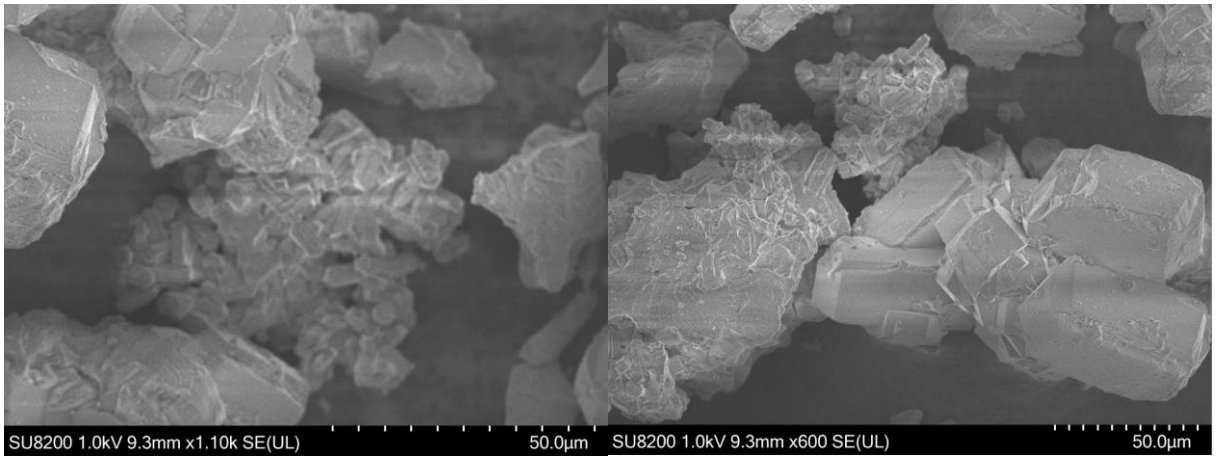

Figure 5-18: Two SEM pictures of HM03 with 1.1k and 600 magnification, using a SE detector.

5.3.3 MFI - 27

Two SEM pictures of the MFI – 27 material is shown in Figure 5-19, which seems to have variety in morphology, in both size and shape. The crystal size varies in length from 2 μm to 50 μm. The small crystals are as Koegler et al. and Maarten et al. (82, 83) described as a ramp. The ramps described is small defects in the morphology of the crystals, that is formed like ramps. Maarten et al. suggests that these ramps are small, 90° intergrown sections with well-developed crystal faces. The crystals of MFI – 27 resembles the same morphology of the material in Figure 2c from the article (83).

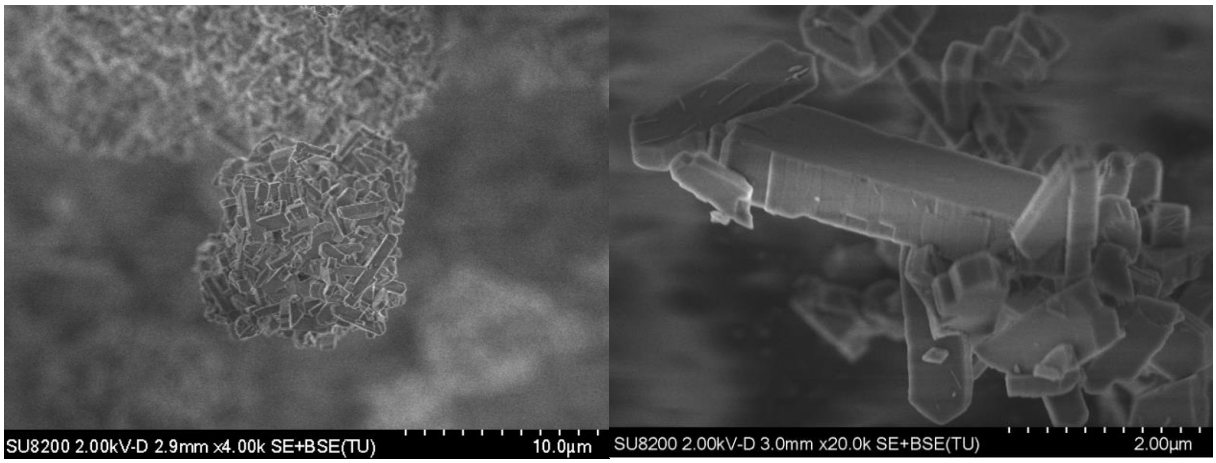

Figure5-19: Two SEM pictures of the commercial MFI - 27 with 4k magnification for the image on the left and a magnification of 20k for the image on the right. The detectors used for both images were a SE and BSE detector.

5.4 Microwave atomic emission spectrometer

MP – AES was performed to get data for an elemental analysis. This was used to calculate Si/Al distribution of complete samples dispersed in solution. The MP – AES analysis was measured once for the HM02 and HM03 materials. The measurements were performed by Sebastian Prodinger and the data from the MP – AES analysis is summarized in Table 5-10.

Table 5-10: Obtained Si and Al results from the MP – AES analysis performed on the two samples HM02 and HM03. Calculated Si/Al ratio based on amount of Si and Al is also given.

Material	Si (mg/L)	Al (mg/L)	Si/Al ratio
HM02	216.0	7.6	28
HM03	216.3	5.2	41

5.5 Energy dispersion x – ray analysis

For an EDX analysis, the instrument scans specific areas of sample when doing an analysis. The method was used to perform elemental analysis of samples and get better understanding of samples elemental composition. It was Si and Al that was the elements of interest in the zeolite materials that was analyzed. The concentrations of Si and Al was analyzed so that the Si/Al distribution could be calculated. EDX analysis was performed on the two ZSM – 5 zeolites HM02 and HM03 with assistance from Sebastian Prodinger.

The data for the EDX analysis of HM02 and HM03 is given in Table 5-11 and Table 5-12 respectively.

Table 5-11: Obtained Si/Al distribution from EDX analysis of HM02 over 3 separate areas and its average, where norm. C is the normalized concentration. The uncertainty is measured by the instrument based of particle size and size distribution.

Scan	Si (norm. C, %)	Al (norm. C, %)	Si/Al ratio
Scan 1	96.9±1.7	3.1±0.1	31
Scan 2	96.6±1.9	3.4±0.1	28
Scan 3	96.3±1.9	3.7±0.1	25
Average	96.6	3.4	28

From Table 5-11 we see that Si/Al ratios was 31, 28 and 25 respectively for the three scans, which is quite similar. The difference from highest to lowest Si/Al ratio is 6.

Another SEM picture of HM02 is shown in Figure 5-20, where there is an exception in the Si/Al distribution in the middle of Figure 5-20, where there is a bigger collection of Al. Except for this there seems to be a uniform distribution of Si and Al in the area of the image. The exception for Si/Al distribution in the image, looks to either be a high Al amount that is packed in that area or maybe that one side of a crystal with Al is pointed directly at the beam.

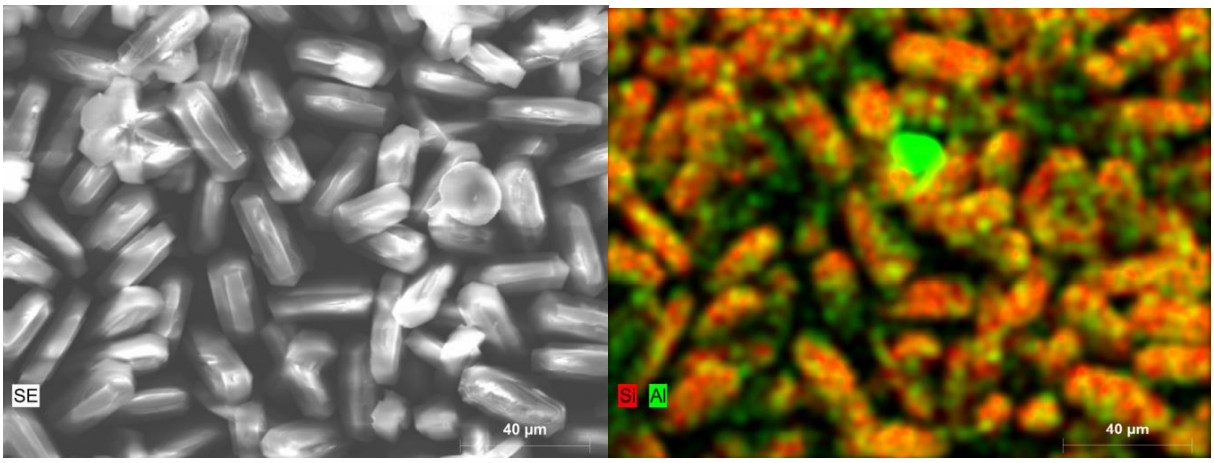

Figure5-20: A SEM image of HM02 (left) and Si/Al distribution for a scan of the area (right). For the right picture Si is indicated in red and Al in green.

A summary of the EDX analysis for HM03 is shown in Table 5-12. Where the amount of Si and Al is given separately in percentage. The Si/Al ratio for each scan is also given in the table. Table 5-12 include scans with Si/Al ratios of 41, 30 and 25.

Table 5-12: Obtained Si/Al distribution for HM03 for three separate areas determined with EDX analysis (similar as for HM02).

Scan	Si (norm. C, %)	Al (norm. C, %)	Si/Al ratio
Scan 1	97.7±1.4	2.3±0.1	41
Scan 2	96.9±1.9	3.1±0.1	30
Scan 3	96.2±1.6	3.8±0.1	25
Average	96.9	3.1	32

In this case there is a relatively large difference between the lowest and highest ratio (difference of 16). The amount of Si for the EDX analysis doesn't change much for the six scans of HM02 and HM03. All amounts of Si are between 96% and 97% except for the first scan of HM03. This means that there should be less alumina particles for the first scan of HM03 and that the Si/Al distribution varies within the material. However, since there is overlap between the uncertainties for the scans it is not possible to conclude whether they are different or not.

The complete EDX analysis for both HM02 and HM03 is given in appendix 8.5, in Figure 8-16 to 8-21.

5.6 N_2 adsorption

N_2 adsorption was performed on ACS extrudates, HM02 and HM03, with one measurement on all samples. The measurement of HM02 and HM03 was performed with assistance of Nicolai Haber Junge and the measurement of the ACS extrudates was performed by Nicolai Haber Junge. It was performed to get an understanding of the zeolites pores and surface and thereafter calculating a surface area from measured adsorption isotherm. The surface area was compared with the surface area of the ZSM - 5 and Beta zeolites used for catalytic testing. The BET method was used for the analysis with p/p_0 range from 0 – 0.15. The data from the N_2 adsorption of the three materials is summarized in Table 5-16.

5.6.1 HM02

The result from the N_2 adsorption experiment for HM02 is shown graphically in Figure 5-21. According to Figure 5-21, HM02 has a hysteresis loop for its adsorption and desorption isotherms at low p/p_0. The Surface area of HM02 from BET measurements of the data from N_2 adsorption is 318 m^2/g (see Figure 5-21). The data for the linearization of the BET plot is given in Table 5-13.

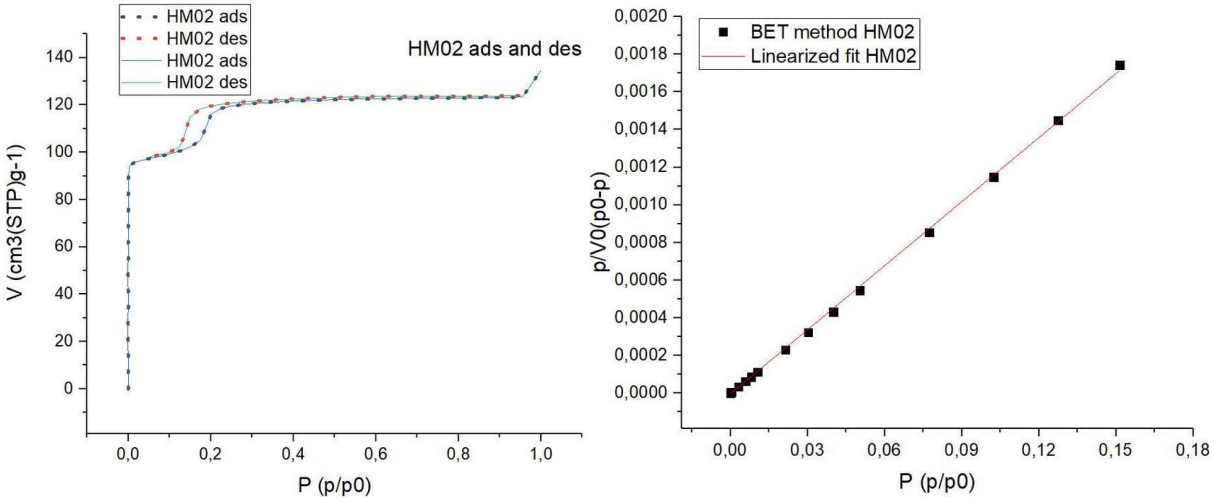

Figure 5-21: Measured adsorption and desorption isotherms of HM02 on the left and a linearized BET plot on the right.

Table 5-13: Data for linearized BET plot for HM02.

Equation	y =a+b*x
Plot	$p/(V_0(p_0-p))$
Intercept	-3.6305E-6±2.13E-5
Slope	0.0113±4.70E-5
Residual sum of squares	2.98E-09
Pearson's r	0.9998
R-square (COD)	0.9995
Adj. R-square	0.9995

5.6.2 HM03

The result from the N_2 adsorption experiment for HM03 is shown graphically in Figure 5-22. According to Figure 5-22, HM03 has a hysteresis loop for its adsorption and desorption isotherms at high p/p_0. The hysteresis loop for HM03 is associated with condensation between particles of the material. The Surface area of HM03 from BET measurements of the data from N_2 adsorption is 321 m^2/g (see Figure 5-22). The data for the linearization of the BET plot is given in Table 5-14.

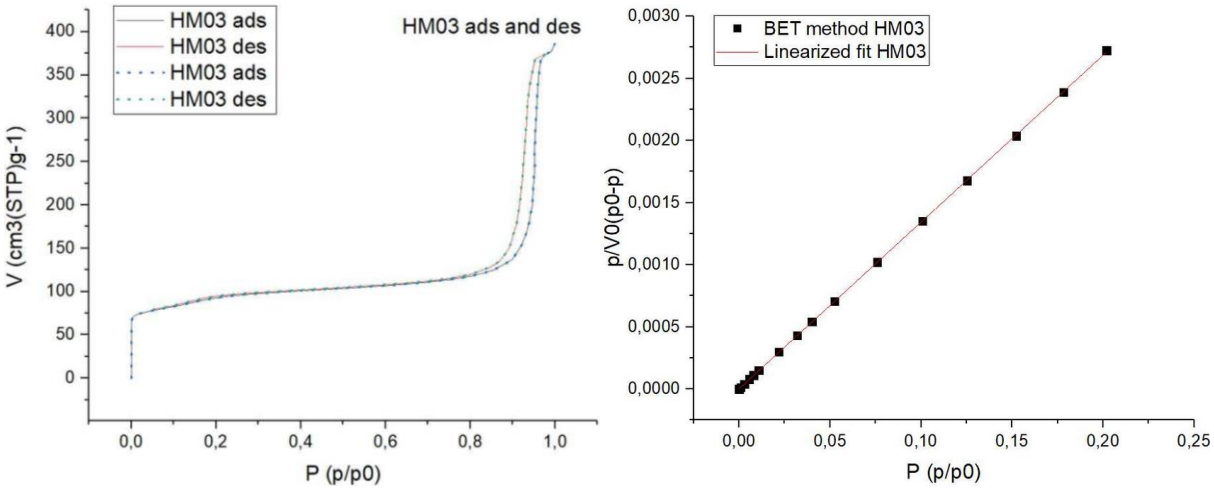

Figure 5-22: Measured adsorption and desorption isotherms of HM03 on the left and a linearized BET – plot for HM03 on the right.

Table 5-14: Data for linearized BET plot for HM03.

Equation	y=a+b*x
Plot	$p/(V_0(p_0-p))$
Intercept	1.8E-6±8.74E-7
Slope	0.0134±1.24E-5
Residual sum of squares	3.70E-10
Pearson's r	0.9999
R-square (COD)	1.0000
Adj. R-square	1.0000

5.6.3 ACS extrudates

The result from the N_2 adsorption experiment for the ACS extrudates (30% alumina) is shown graphically in Figure 5-23. According to Figure 5-23, ACS extrudates has a hysteresis loop for its adsorption and desorption isotherms. The hysteresis loop for the ACS extrudates is characteristic of filling and emptying of mesopores by capillary condensation, according to '*Characterization of micro/mesoporous materials by physisorption: Concepts and case studies'* (78). The surface area of ACS extrudates is according to the N_2 adsorption in Figure 5-23 306 m^2/g. The data for the linearization of the BET plot is given in Table 5-15.

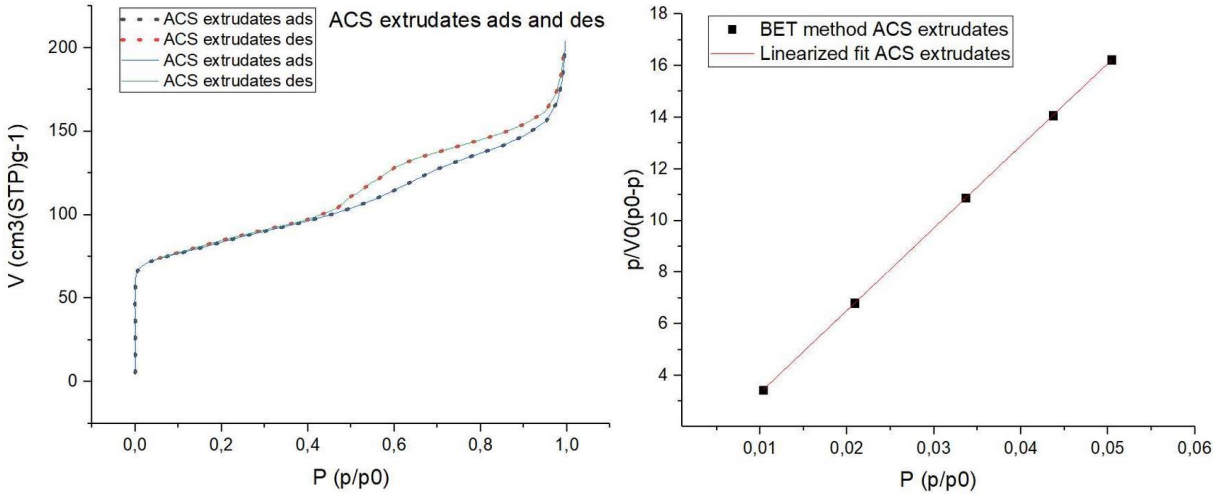

Figure 5-23: Measured N_2 adsorption for ACS extrudates on the left and a linearization of the BET - data for ACS extrudates on the right.

Table 5-15: Data for linearized BET plot of the ACS extrudates.

Equation	y =a+b*x
Plot	$p/(V_0(p_0-p))$
Intercept	0.15±0.01
Slope	318.88±0.17
Residual sum of squares	9.72E-05
Pearson's r	1.0000
R-square (COD)	1.0000
Adj. R-square	1.0000

5.6.4 Summarized results

The results from N_2 adsorption are summarized in Table 5-16.

Table 5-16: Determined surface area and reference surface area for the ZSM – 5 zeolites ACS extrudates, HM02 and HM03.

Material	Surface area (m^2/g)	Reference surface area (m^2/g)
ACS extrudates	306	above 250 (15)
HM02	318	313 (25)
HM03	321	313 (25)

As indicated in Table 5-16, according to the N_2 adsorption, the surface area for HM02 and HM03 are similar, with a difference of 3 m^2/g. The value for the surface area of the ACS extrudates is also close to HM02 and HM03, with a difference of 12 m^2/g between HM02 and the ACS extrudates. The measured surface area of the three zeolites is somewhat different from the literature value listed in Table 5-16. ACS extrudates has a measured surface area 56 m^2/g higher than the literature, HM02 has 5 m^2/g higher than the literature and HM03 has 8 m^2/g higher than the value from the literature.

Data for T – method and full BET – plots for both HM02, HM03 and ACS extrudates are given in appendix 8.6, in Figure 8-22 to Figure 8-26.

5.7 Acid – base titration

Acid – base titration was performed on the ZSM - 5 zeolites that was used for catalytic testing on the Co - feed test rig (sample ACS extrudates, HM02 and HM03 on proton form). It was performed on the materials to get information on the degree of active sites that is available for reaction and what the density of acid sites is in the material. The density of acid sites was calculated based on how much base that was required to get to the measured equivalents point for each material. When the density of acid sites had be calculated, the accessibility of acid sites could also be calculated. Calculations for density of acid sites and accessibility of acid sites is given in appendix 8.7.3.

In the beginning, the method was tested with reference samples before doing the measurements (test titrations are given in appendix 8.7.1 and calculations for density of acid sites and accessibility of acid sites are given in appendix 8.7.3). The test titrations were done, because each titration required 500 mg of sample, which is a considerable amount compared to other catalytic characterization techniques. A sample of ZSM – 5 CBV 8014 zeolite (Si/Al = 40), was used as a test sample for titrations. The three ZSM - 5 zeolites were suspended in 1M solution of $NaNO_3$. The data from acid – base titration of the three characterized materials and the CBV 8014 is summarized in Table 5-17 and the titration curves are given in Figure 8-27–8-29 in appendix 8.7.1 and Figure 8-34 in appendix 8.7.2.

Table 5-17: Summary of potentiometric titrations.

Material name	Sample weight (mg)	C_{NaOH} (M)	V_{NaOH} equivalence point (ml)	pH equivalence point	Acid density (µmol/g)
CBV 8014	500	0.0855	2.30	5.2	401
ACS extrudates	500	0.0967	0.36	8.4	69
HM02	500	0.0967	0.15	8.6	29
HM03	500	0.0967	0.68	8.0	132

The acid – base titration curve for ACS extrudates, suspended in 1M $NaNO_3$ – solution is shown in Figure 8-27. According to the titration data, the sample had a density of acid sites of 69 µmol/g and an accessibility of acid sites of 8% (calculated in appendix 8.7.3).

The acid – base titration curve for HM02, suspended in 1M $NaNO_3$ – solution is shown in Figure 8-28. According to the titration data, the sample had density of acid sites of 29 μmol/g and an accessibility of acid sites of 5%.

The acid – base titration curve for HM03, suspended in 1M $NaNO_3$ – solution is shown in Figure 8-29. According to the titration data, the sample had a density of acid sites of 132 μmol/g and an accessibility of acid sites of 34%.

The titration curves in Figure 5-24 contain the same data as in Figure 8-27 to 8-29 put together in the same plot. It clarifies the differences between the three datasets. The figure makes it clear that the ACS extrudates and HM02 starts at around the same pH (approximately pH 5), but HM03 starts at a lower pH (approximately pH 4). Although the ACS extrudates and HM02 starts at around the same pH, HM02 reaches pH 12 (and ends the titration) earlier than the ACS extrudates.

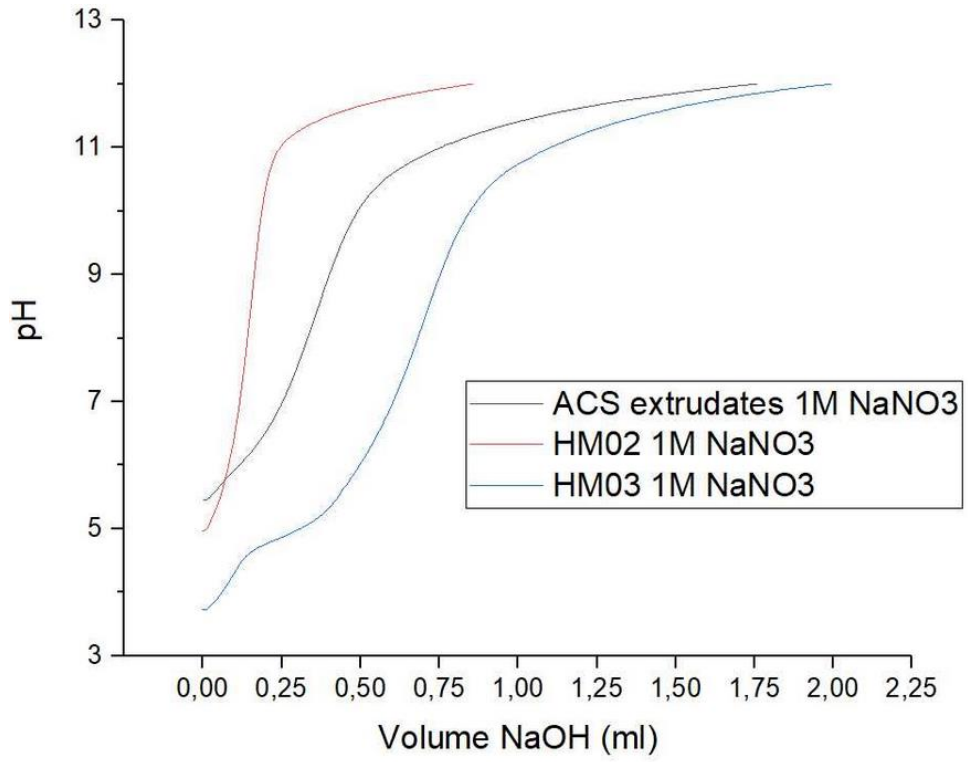

Figure 5-24: The titration curves of ACS extrudates, HM02 and HM03 for acid – base titration together in the same plot.

Table 5-18: Calculated accessibility of acid sites and density of acid sites for CBV 8014, ACS extrudates, HM02 and HM03. The Si/Al ratio used from titration data in the calculations for HM02 and HM03 is the ratio measured from MP - AES. The accessibility of acid sites was based on the theoretically highest possible accessibility of acid sites the materials could have and is calculated from the materials composition.

Material	Accessibility of acid sites (%)	Density of acid sites (μmol/g)
CBV 8014	99	401
ACS extrudates	8	69
HM02	5	29
HM03	34	132

As indicated in Table 5-18, both the accessibility of acid sites and density of acid sites are low. The accessibility of acid sites for the ZSM – 5 materials in Kumar's study (12) was between 60 – 70%, so it was expected that these materials would have similar numbers. The values of HM02 are especially low. The density of acid sites is much lower for all three samples compared to Kumar's investigation at the same conditions (12). HM03, which had the highest density of acid sites out of ACS extrudates, HM02 and HM03, still had ten times less μmol/g than from Kumar, S. *'Potentiometric acid-base titration as a tool to characterize porous solid acids'*, 2020 (12). The data for CBV 8014 tells that the material has a high degree of accessible acid sites and higher than the other materials. Based on all the results for the titration the ACS extrudates, HM02 and HM03 has low accessibility of acid sites compared to CBV 8014.

Additional titration curves are given in appendix 8.7.1 and calculations for the titration data are given in appendix 8.7.3.

5.8 Methanol to hydrocarbon conversion

MTH conversion was performed to see how well a zeolite performed as a catalyst in methanol to hydrocarbons conversion. The ZSM – 5 and Beta zeolites was deactivated during time on stream (TOS) and the deactivation of the zeolites occurred when coke (carbon) started occupying the materials active sites. MTH conversion data was collected in cooperation with Georgios Kalantzopolous and Nicolai Haber Junge for three ZSM – 5 zeolites (ACS extrudates,

HM02 and HM03) and four Beta zeolites (09-00243/1, SK_CP814C, CP806B-25 and CP811BL-25).

5.8.1 ZSM – 5 zeolites

ACS extrudates

The conversion shown in Figure 5-25 is the sum of converted DME and MeOH, which is the starting materials for the catalytic testing. The figure shows that the total selectivity of the products is stable as the conversion for the material decreases. As is illustrated in the figure, the selectivity of the products is at 10 – 15% for $C_1 + C_2$, 38% for $C_3 + C_4$ and 48 - 50% for C_{5+}. The testing of the material ended at 10% yield.

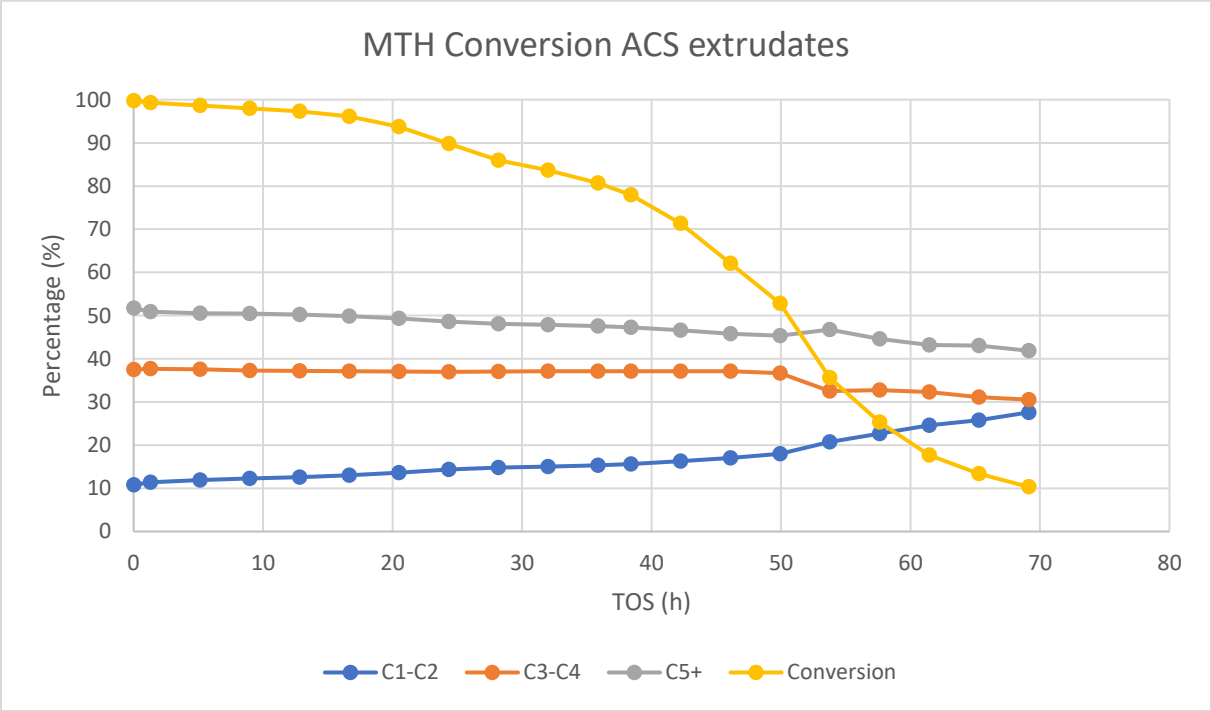

Figure 5-25: Plot of both yield and product selectivity for ACS extrudates, versus time on stream at 400°C with WHSV of 2.95 $g_{MeOH}\, g_{catalyst}^{-1}\, h^{-1}$. Conversion is the sum of converted DME and MeOH.

HM02

The conversion shown in Figure 5-26 is the sum of converted DME and MeOH, which is the starting materials for the catalytic testing. For this material, the conversion does not start at 100%, but 90%. The figure shows that the total selectivity of the products is stable as the conversion for the material decreases. As is illustrated in the figure, the selectivity of the products is at 9 – 11% for $C_1 + C_2$, 46 - 50% for $C_3 + C_4$ and 40 - 45% for C_{5+}. The testing of the material ended at 14% yield.

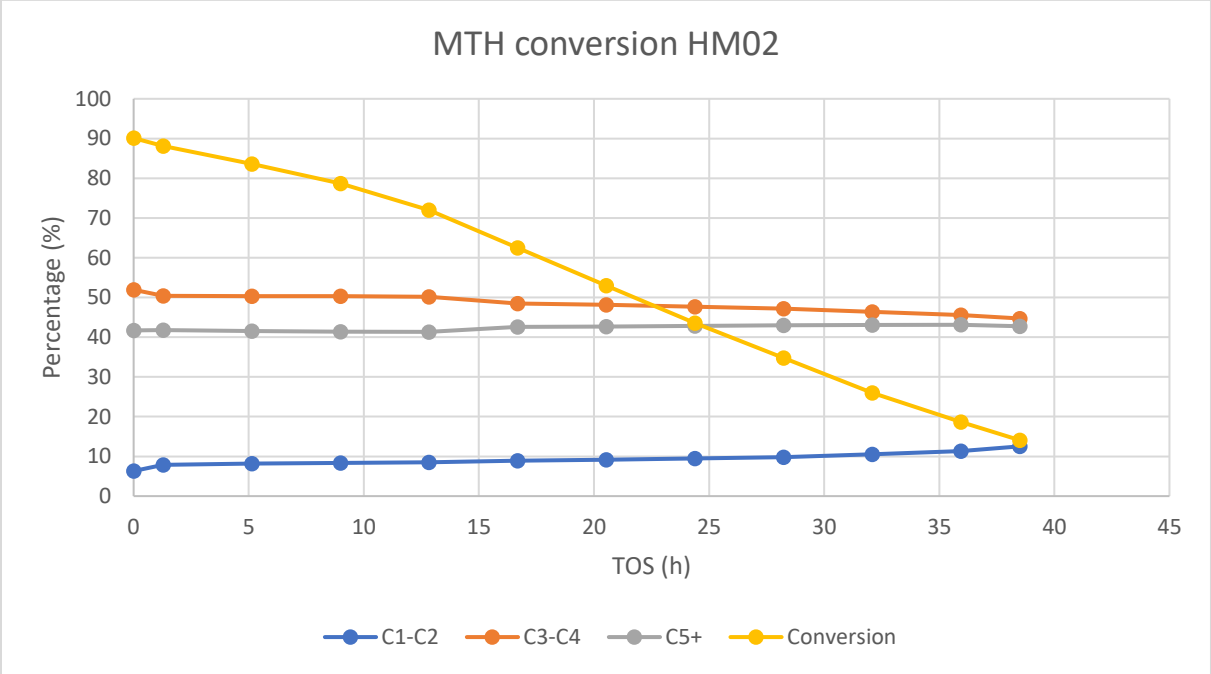

Figure 5-26: Plot of both yield and product selectivity for HM02, for time on stream at 400°C with WHSV of 2.95 $g_{MeOH}\, g_{catalyst}^{-1}\, h^{-1}$. Yield is the sum of converted DME and MeOH.

HM03

The conversion shown in Figure 5-27 is the sum of converted DME and MeOH, which is the starting materials for the catalytic testing. The figure shows that the total selectivity of most the products slowly decreases as the conversion for the material decreases. As is illustrated in the figure, the selectivity of the products is at 10% for $C_1 + C_2$, 20 - 50% for $C_3 + C_4$ and 10 - 25% for C_{5+}. The testing of the material ended at 51% yield.

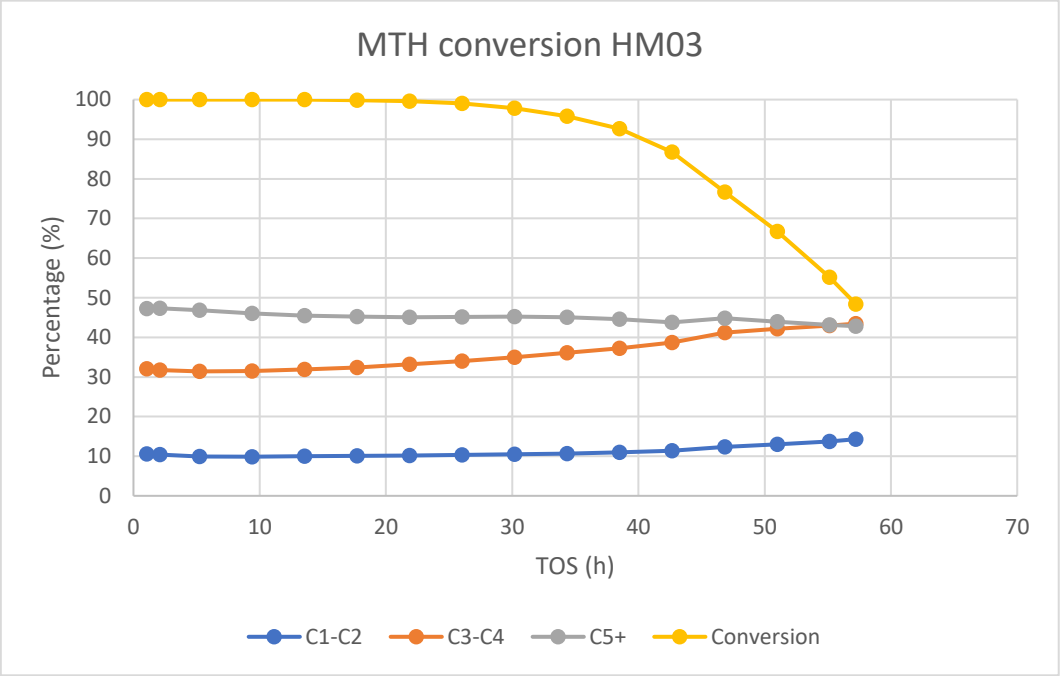

Figure 5-27: Plot of both yield and product selectivity for HM03, for time on stream at 400°C with WHSV of 2.95 $g_{MeOH}\, g_{catalyst}^{-1}\, h^{-1}$. Yield is the sum of converted DME and MeOH.

The MTH conversion of HM02 illustrated in Figure 5-26 shows many similarities with the MTH conversion of the parent sample from *Applied catalysis, 'Methanol to gasoline over zeolite H-ZSM-5: improved catalyst performance by treatment with NaOH' (2008)* (25). The similarities between the two materials were that both had less than 100% conversion at time zero and the conversion of the two materials decreased similarly. As both gradually decreased in conversion until the test ended at 35 – 40 hours, where both had approximately 10% conversion.

The conversion for the three ZSM - 5 zeolites that were tested on the Co - feed test rig is shown together in Figure 5-28. From the figure it is clear to say that HM03 is more active over time than the other two and HM02 is the least active. Something else can be observed from the figure

is that HM02 starts at a conversion lower than 100%. The two curves in the middle is ACS extrudates and partially deactivated ACS extrudates. Since the data collections of the curves in the middle is the same material, they should have very similar curves, which they are. The fact that the two datasets for ACS extrudates are very similar indicates that the data from the testing is reproduceable.

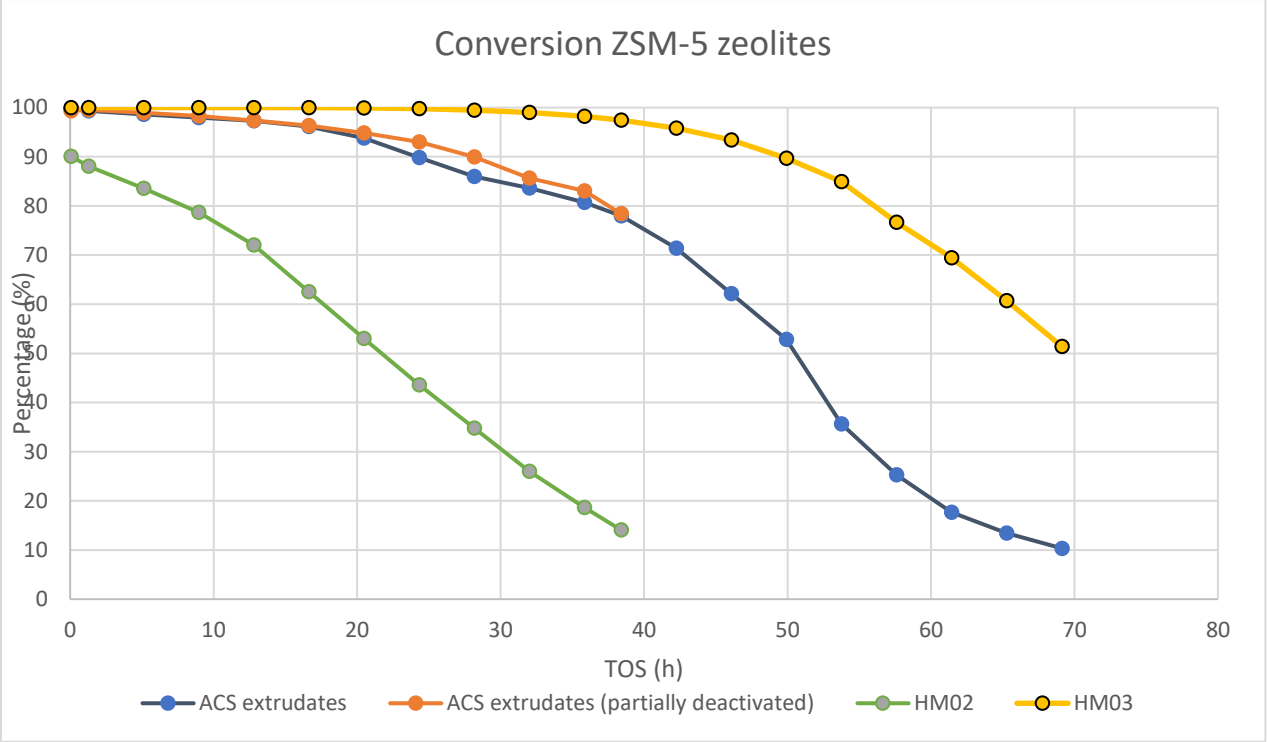

Figure 5-28: Change in yield over time at 400°C, for the three ZSM - 5 zeolite materials ACS extrudates, HM02 and HM03.

The initial product selectivity for ZSM – 5 zeolites used on the Co – feed test rig is given in Figure 5-29. Generally, the materials had high selectivity towards aromatics (C_{6+}) and selectivity towards C_1. ACS extrudates and HM03 had similarities in their initial product selectivity, where the major differences were that the extrudates had higher selectivity towards C_{6+} and lower selectivity towards C_3. For ACS extrudates, the most abundant product was carbon products of C_{6+} (39%) followed by C_4 products. The most abundant product for HM02 was C_3 (30%) with C_{6+} (29%) right below. For HM03 was the most abundant product C_{6+} (32%).

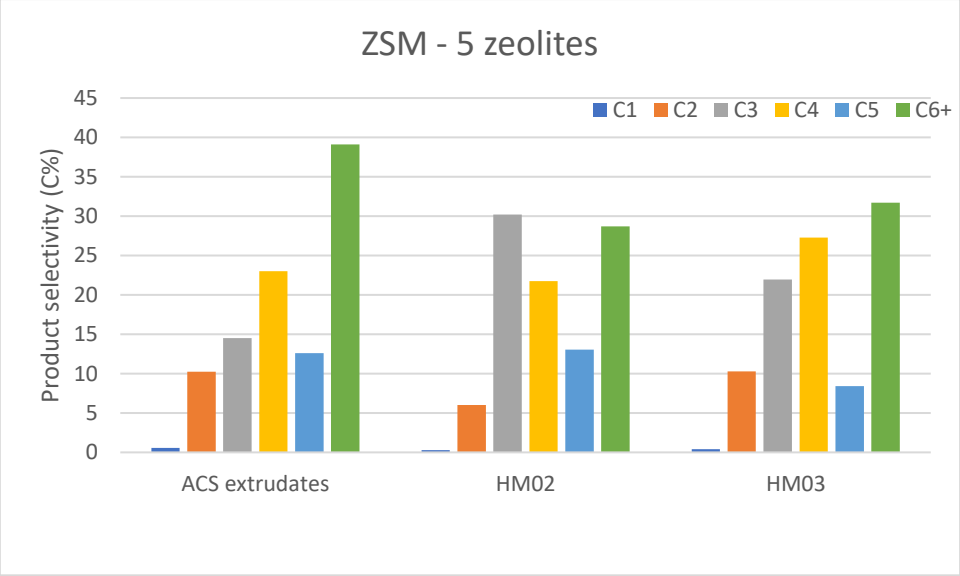

Figure 5-29: Product selectivity at initial conversion at 400°C for the three ZSM – 5 zeolites that was tested for catalytic activity.

The initial product selectivity for the replicated testing of the ACS extrudates material, that was partially deactivated before the test was ended, is given in Figure 8-41 in appendix 8.8.

5.8.2 Beta zeolites

Figure 5-30 shows data for the Beta zeolites' conversion, which illustrates that all of them decreases fast in conversion. SK_CP814C, CP806B-25 and CP811BL-25 end their test at approximately zero conversion and 09-00243/1 ends at less than 20% conversion. This means that all the Beta zeolites have basically all their active site on their surface covered with coke and are thereby completely deactivated. For the Beta zeolites the material that was most active

is 09-00243/1. The material that was the fastest to deactivated and therefore was the least active material was CP806B-25.

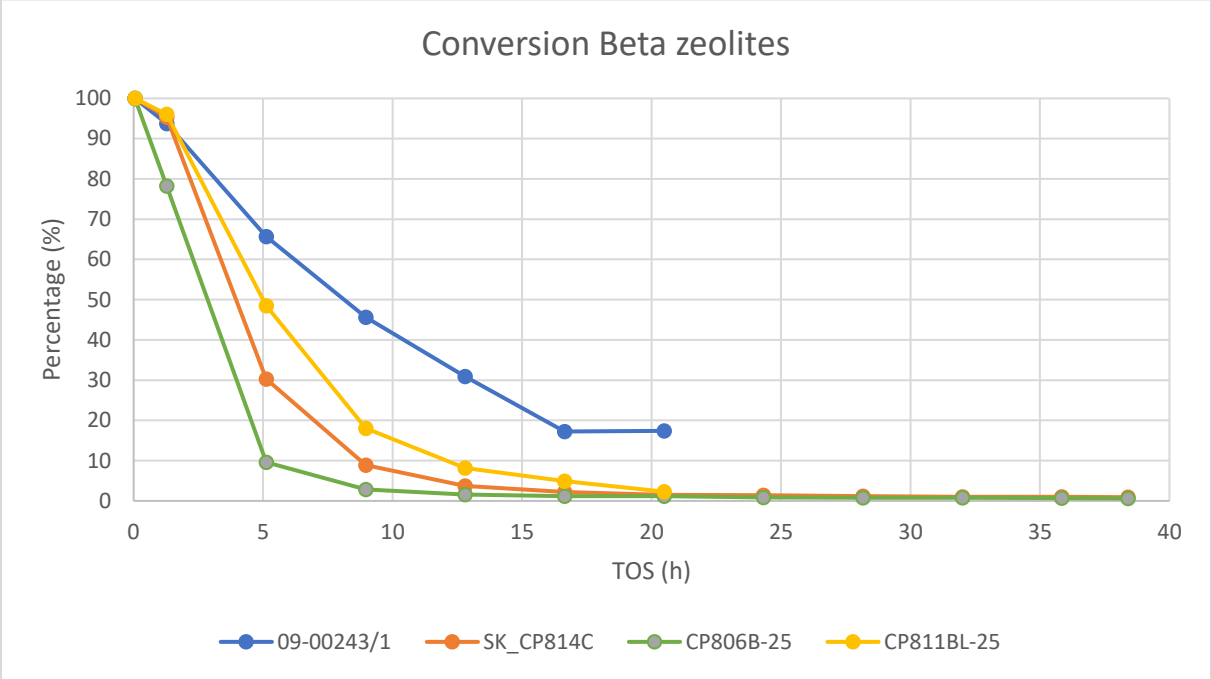

Figure 5-30: Conversion over time as time on stream, for the Beta zeolites 09-00243/1, SK_CP814C, CP806B-25 and CP811BL-25. The temperature for time on stream was 400°C with WHSV of 2.95 $g_{MeOH}\, g_{catalyst}^{-1}\, h^{-1}$.

The initial product selectivity for Beta zeolites used on the Co – feed test rig is given in Figure 5-31. Generally, the materials had high selectivity towards Isobutane (C_4) and low selectivity towards C_1 and C_2. There were many similarities in their initial product selectivity. The most abundant product for all four zeolites was C_3. The catalyst that stood out for its initial product selectivity was 09-00243-1, which had lower selectivity towards C_3 and higher selectivity towards C_{6+} than the rest. Minor amounts of C_1 were detected for all catalyst used for catalytic testing. Based on data from GC – analysis, the C_1 product was mainly methane.

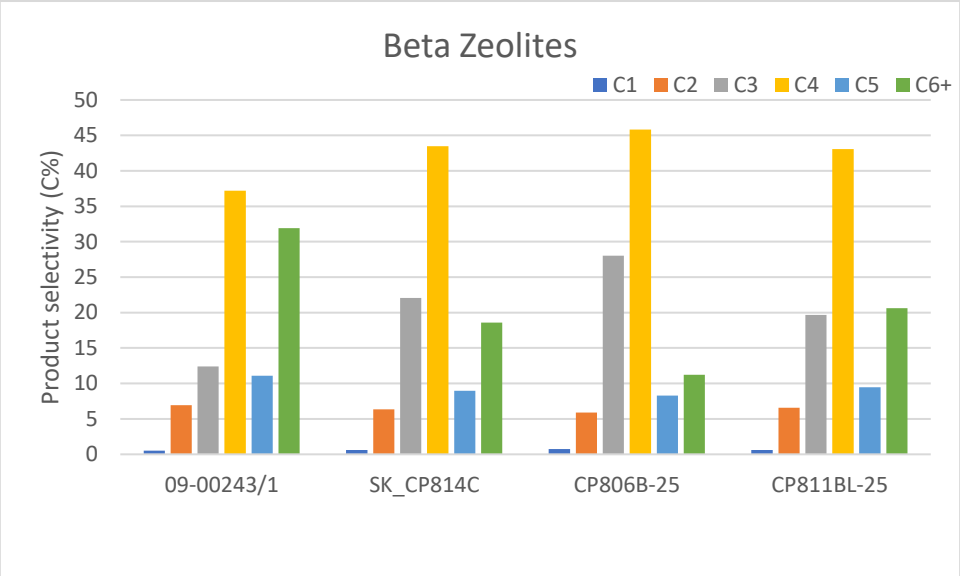

Figure 5-31: Product selectivity at initial conversion at 400°C for the four Beta zeolites that was tested for catalytic activity.

The catalytic test data for selectivity of the partially deactivated ACS extrudates and Beta zeolites is shown in Figure 8-36 to 8-41 in appendix 8.8.

5.9 Analysis of deactivated zeolites

5.9.1 Thermogravimetric analysis

TGA was performed on HM02 and HM03 to investigate how much coke the materials contained after they had been used for MTH conversion. TGA was done on the top layer for both materials. TGA was also performed by Nicolai Junge at UiO on the top, middle and bottom layer of fully deactivated ACS extrudates.

The TGA analysis of the deactivated top layer of HM02, from the MTH conversion is shown in Figure 5-32, where the first drop to 100°C is due to H_2O removal and the second drop is due to coke removal (the difference between the red and blue dashed line). The coke content for the material is low (1.3%).

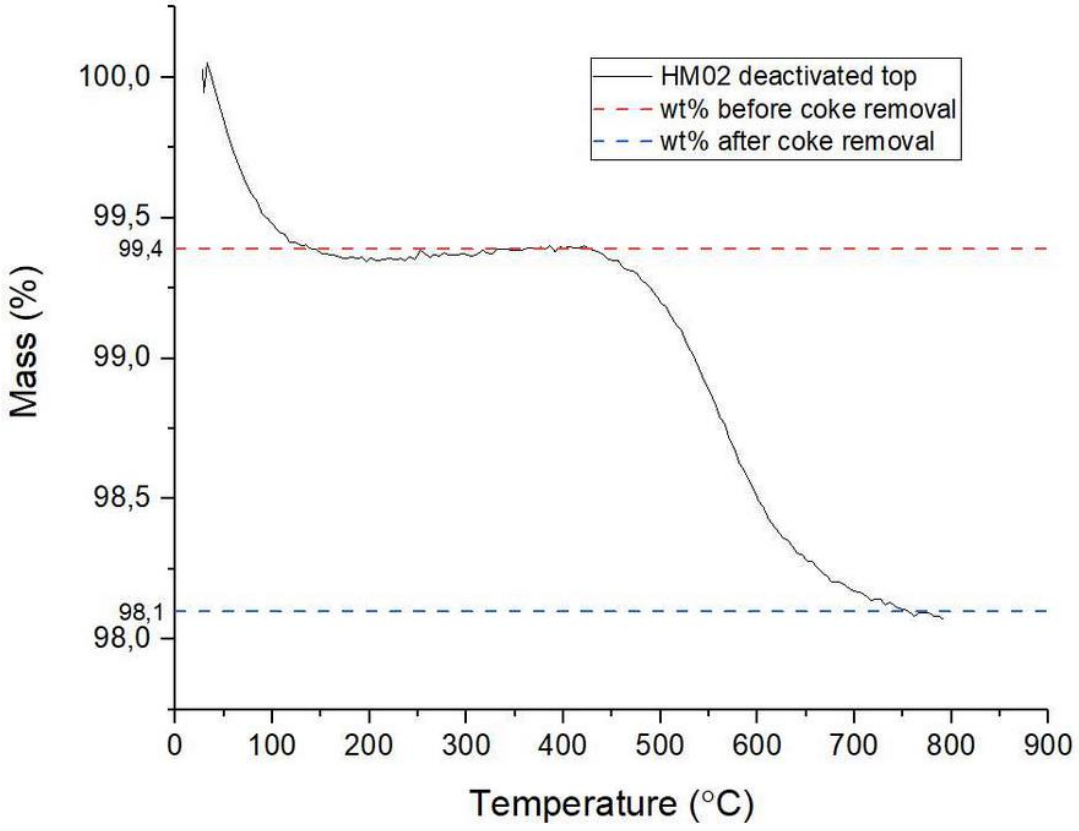

Figure 5-32**:** TGA analysis for the top layer of deactivated HM02, where the material is heated from room temperature to 800°C, with an atmosphere of 20% oxygen and 80% nitrogen. The material has coke content in its structure.

The DSC result for the TGA analysis of deactivated HM02 in Figure 5-32 is given in appendix 8.3, in Figure 8-11.

A TGA analysis of the deactivated top layer of HM03, from the MTH conversion is given in Figure 5-33, where the first drop before 100°C is due to H_2O removal and the second drop is due to coke combustion (drop between red and blue dashed line). The corresponding DSC for this analysis (see Figure 5-34) has a peak at 600°C, which is an exothermic reaction that corresponds to the 6.1 wt.% drop in the TGA curve.

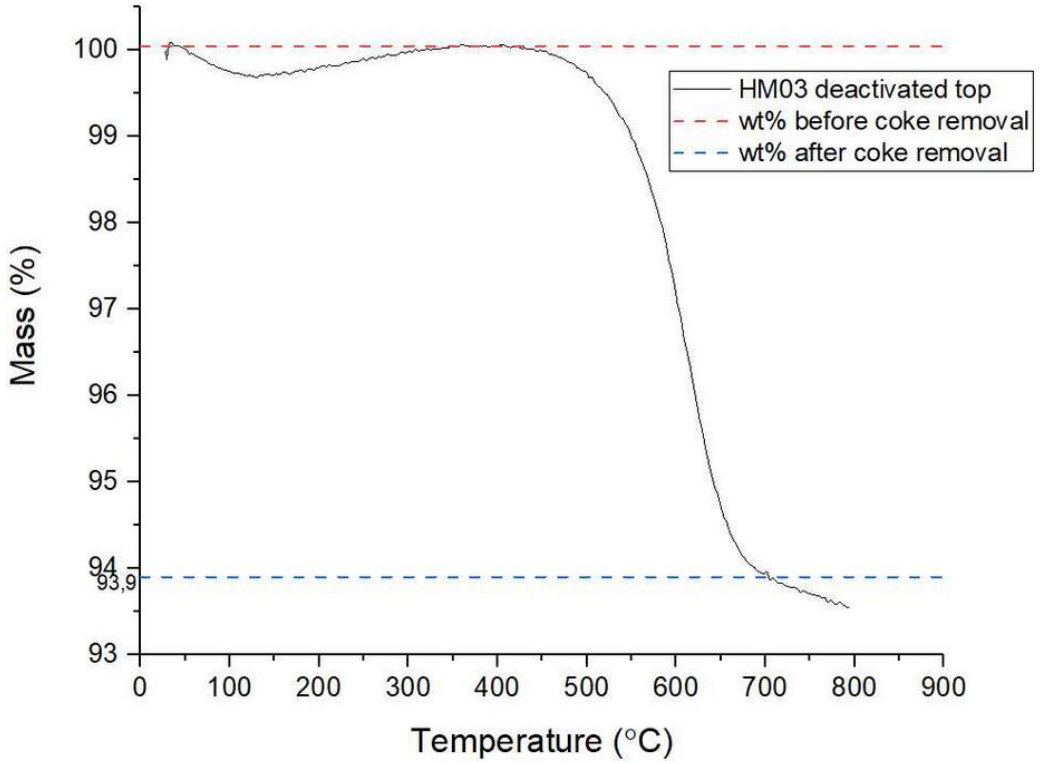

Figure 5-33: TGA ananlysis of the top layer of deactivated HM03. The material was heated from room temperature to 800°C, with an atmosphere of 20% oxygen and 80% nitrogen.

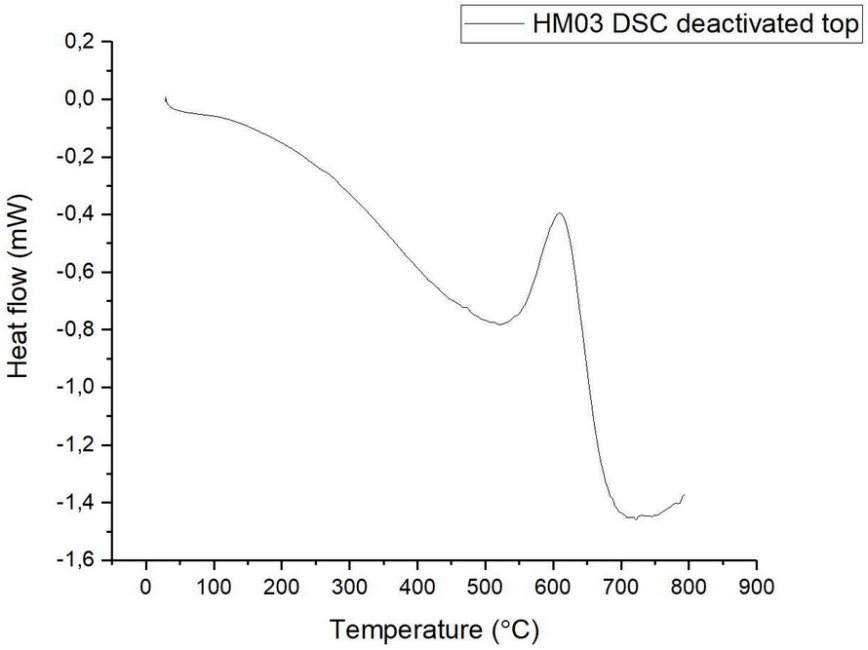

Figure 5-34: The corresponding DSC result of the top layer of deactivated HM03 of the TGA analysis.

A TGA analysis of the ACS extrudates for the deactivated version of the material was performed by Nicolai Haber Junge at UiO. Result for the top, middle and bottom layer is shown in Figure 5-35. There are two plateaus for the TGA, where the first drop before 100°C is due to H_2O removal and the second drop is due to coke removal. It shows that the amount of coke is different between the layers and that the amount gradually increases from bottom to top. The bottom layer has 6.2 wt.% of coke, the middle layer has 7.2 wt.% and the top layer has 9.3 wt.% of coke.

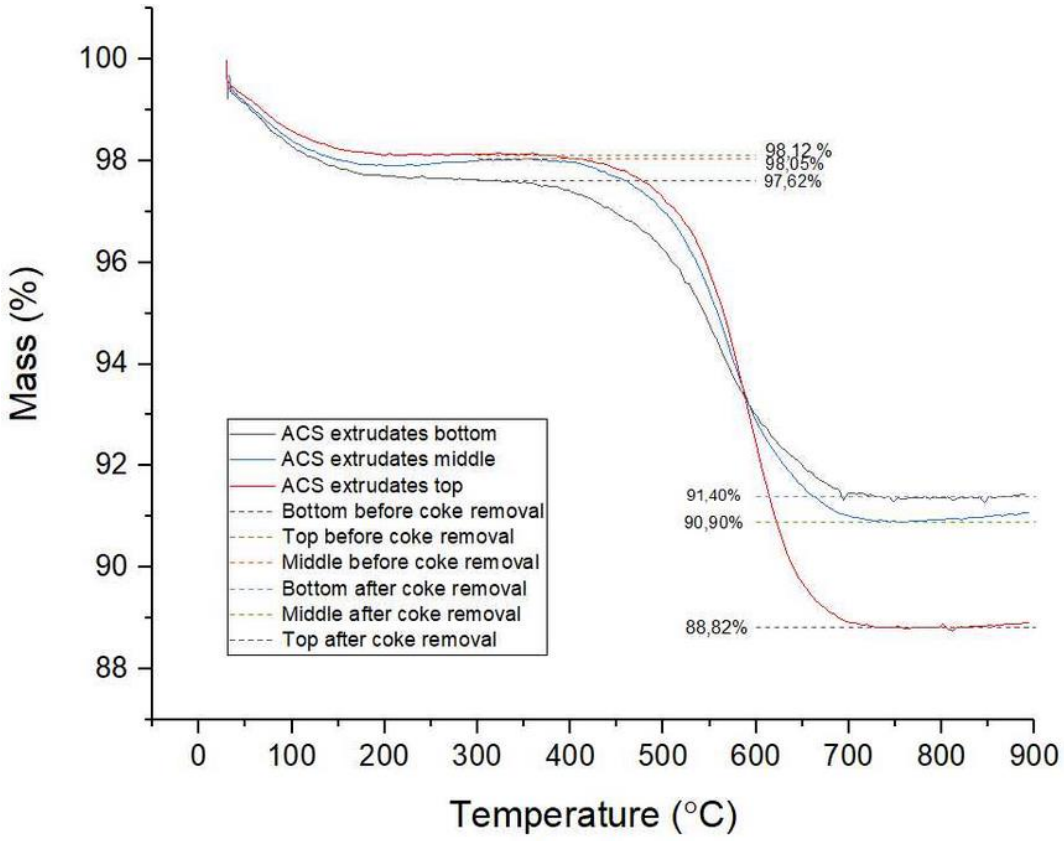

Figure 5-35: TGA analysis of the top, middle and bottom layer of the ACS extrudates, used for MTH analysis. The material is heated from room temperature to 900°C, with an atmosphere of 60% oxygen and 40% nitrogen.

The DSC results for the TGA analysis of the ACS extrudates in Figure 5-35 is given in appendix 8.3, in Figure 8-12.

The mass drop for the TGA analysis of the deactivated materials is given in Table 5-19.

Table 5-19: summary of TGA results for deactivated materials.

Sample name	Sample weight (mg)	Mass drop, coke removal (%)
HM02 top	23.0	1.3
HM03 top	22.6	6.1
ACS extrudates top	12.0	9.3
ACS extrudates middle	14.3	7.2
ACS extrudates bottom	10.0	6.2

5.9.2 X – ray diffraction analysis

XRD was performed on deactivated zeolites to investigate if it was possible to determine any difference between the XRD pattern of a material with coke in its pores and a material that did not have coke in its pores. For HM02, XRD was performed on the middle layer from the reactor and for HM03 XRD was performed on the top layer from the reactor.

Figure 5-36 shows XRD diffractogram of HM02 for the middle layer from the reactor that was used during the catalytic testing of the material. A list with the angle, d value, intensity and relative intensity of the peaks in Figure 5-36 is given in Table 5-20. The coke content is the cause of the deactivation and the middle layer is the layer that is expected to have the second most coke content. Since the material was at 14% yield when the experiment ended, it is not expected that there is much difference between the top and middle layer for the material. A plot showing the pattern of protonic capillary and deactivated middle of HM02 is given in Figure 5-37. According to the computed crystallinity of the raw. file for the pattern of HM02 deactivated middle in Diffrac.EVA, it has an 82.9% crystallinity and is 17.1% amorphous.

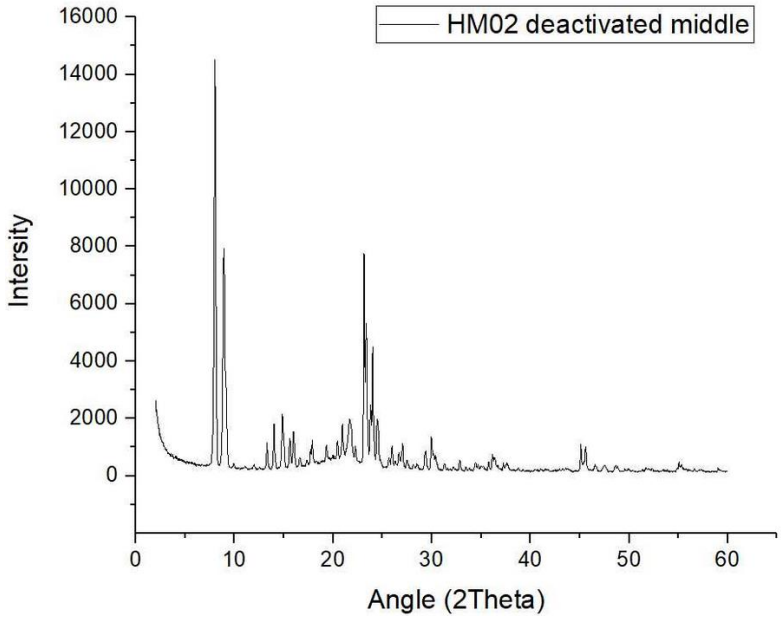

Figure 5-36: Pattern of a glass plate XRD of the middle layer of after MTH conversion.

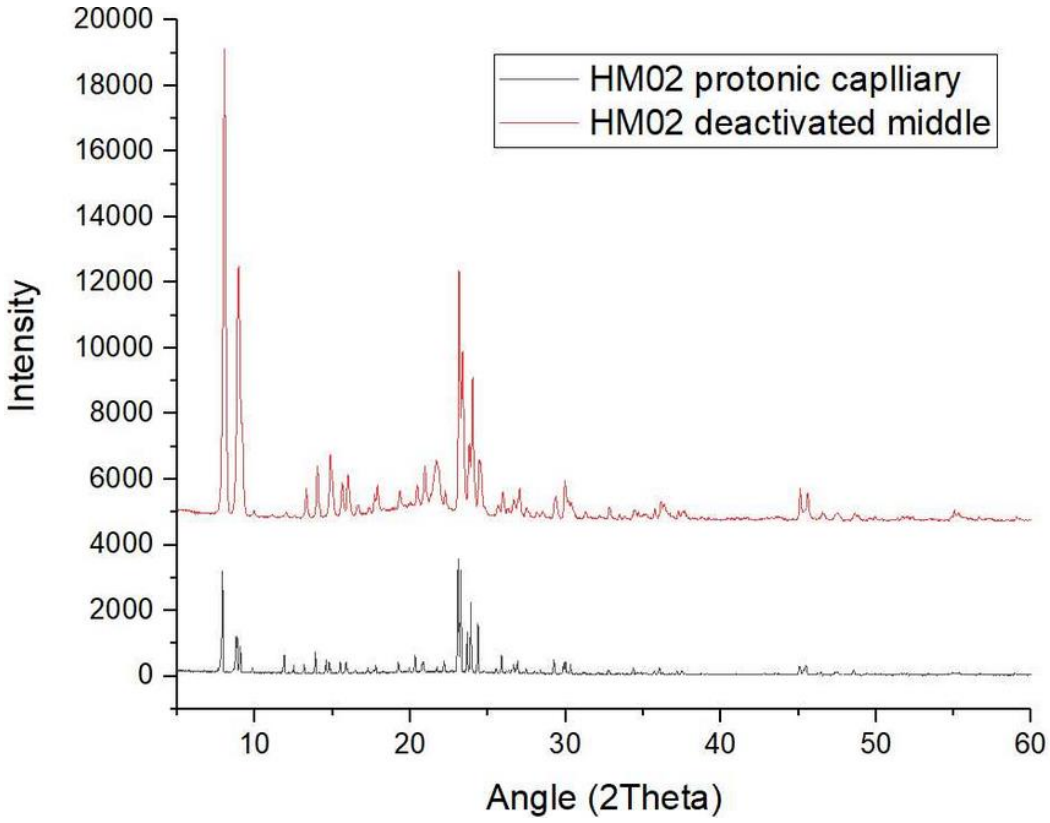

Figure 5-37: XRD pattern of HM02 protonic capillary and deactivated middle in the same plot.

Table 5-20: Peak list for HM02 deactivated middle glass plate XRD.

angle (° 2θ)	d value (Å)	Intensity (counts)	Rel. Int. (%)	Angle (° 2θ)	d value (Å)	Intensity (counts)	Rel. Int. (%)	Angle (° 2θ)	d value (Å)	Intensity (counts)	Rel. Int. (%)
8.03	11.004	9488.0	100.0	24.01	3.704	3118.5	32.9	37.25	2.412	229.8	2.4
8.94	9.889	5121.0	54.0	24.50	3.631	923.6	9.7	37.59	2.391	143.4	1.5
9.92	8.908	95.9	1.0	25.65	3.470	213.8	2.3	38.77	2.320	78.9	0.8
11.09	7.968	60.0	0.6	25.98	3.427	498.0	5.2	39.25	2.293	48.4	0.5
12.01	7.364	118.4	1.2	26.27	3.389	148.2	1.6	40.46	2.228	42.1	0.4
12.56	7.040	42.4	0.4	26.66	3.341	380.0	4.0	41.08	2.196	48.9	0.5
13.30	6.651	636.3	6.7	27.04	3.295	633.9	6.7	41.70	2.164	40.6	0.4
14.02	6.314	1073.6	11.3	27.52	3.239	145.2	1.5	42.96	2.104	64.8	0.7
14.90	5.942	890.4	9.4	28.14	3.168	113.1	1.2	43.72	2.069	66.5	0.7
15.61	5.671	681.2	7.2	28.49	3.131	119.1	1.3	45.11	2.008	877.9	9.3
15.99	5.539	827.9	8.7	29.37	3.039	383.9	4.0	45.60	1.988	743.6	7.8
16.63	5.325	184.2	1.9	29.96	2.980	895.0	9.4	46.59	1.948	123.0	1.3
17.35	5.108	130.5	1.4	30.38	2.939	314.4	3.3	47.49	1.913	136.0	1.4
17.71	5.004	372.2	3.9	31.31	2.855	155.5	1.6	48.64	1.871	167.8	1.8
17.89	4.954	604.8	6.4	32.22	2.776	60.8	0.6	48.85	1.863	139.1	1.5
18.24	4.860	78.8	0.8	32.84	2.725	254.8	2.7	49.61	1.836	33.8	0.4
19.33	4.589	415.4	4.4	33.47	2.675	102.8	1.1	49.92	1.825	93.2	1.0
19.99	4.437	159.3	1.7	33.81	2.649	79.5	0.8	51.37	1.777	73.3	0.8
20.44	4.341	500.1	5.3	34.43	2.603	204.7	2.2	51.77	1.765	52.7	0.6
20.94	4.239	908.5	9.6	34.70	2.583	181.2	1.9	52.31	1.747	63.4	0.7
21.68	4.095	1030.4	10.9	35.14	2.552	56.7	0.6	55.05	1.667	269.7	2.8
22.24	3.993	362.4	3.8	35.75	2.509	257.9	2.7	55.26	1.661	141.8	1.5
23.21	3.830	1388.0	14.6	36.21	2.479	187.8	2.0	56.63	1.624	108.3	1.1
23.37	3.804	3279.0	34.6	36.35	2.469	341.3	3.6	57.24	1.608	43.8	0.5
23.79	3.737	1404.8	14.8	36.91	2.433	43.2	0.5	59.02	1.564	94.8	1.0

In Figure 5-38 the pattern of protonic HM02 is highlighted in the 2θ range 45-46°. Similarly, the same range is highlighted for the pattern of the middle layer in Figure 5-39. As can be seen the patterns are quite similar.

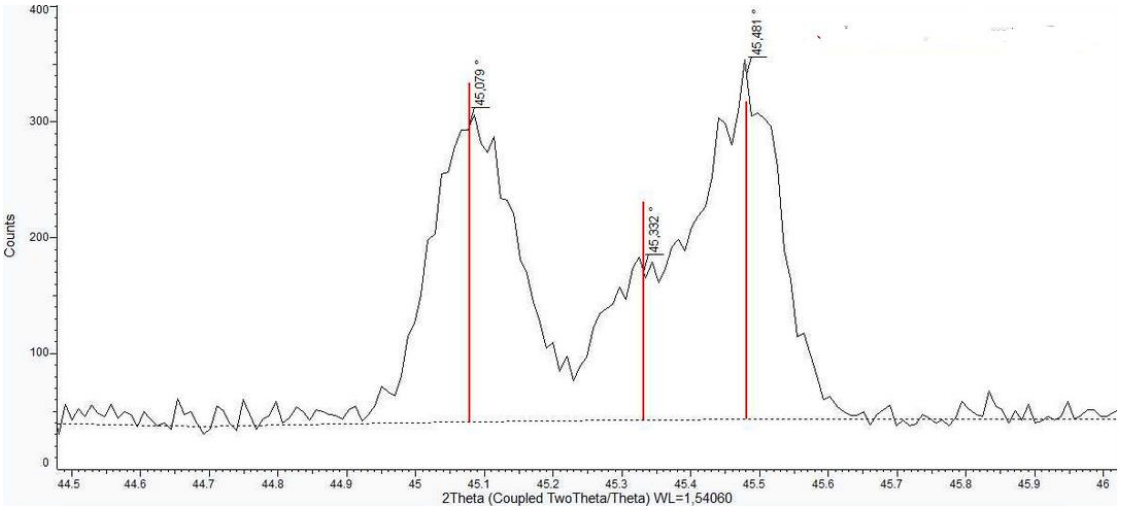

Figure 5-38: XRD pattern of protonic HM02 by capillary from Diffrac.EVA, zoomed in on the peaks between 45° and 46°.

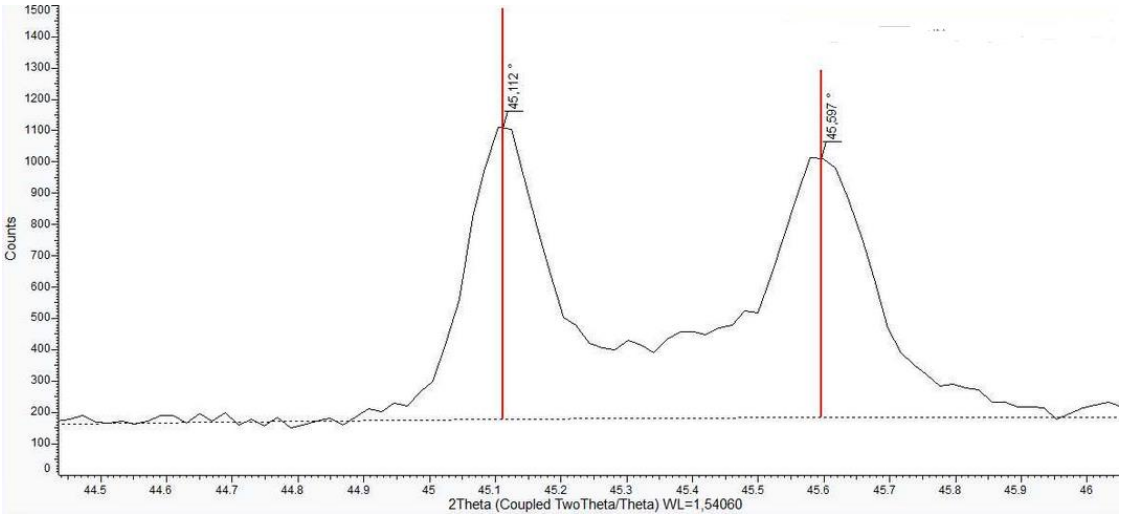

Figure 5-39: XRD pattern of the middle layer from the catalytic testing of HM02 measured on a glass plate. The data was analyzed in Diffrac.EVA, where it was zoomed in on the peaks between 45° and 46°.

Figure 5-40 shows a XRD diffractogram of HM03 for the top layer from the reactor that was used during the catalytic test on the Co - feed test rig. The coke content is the cause of the deactivation and the top layer is the layer containing the most coke out of the three layers. The angle, d value, intensity and relative intensity of the peaks in Figure 5-40 is given in Table 5-21. A plot is given in Figure 5-41, where the pattern for protonic full plate and deactivated top

for HM03 is plotted on the same x – axis. According to the computed crystallinity of the raw. file for the pattern of HM03 deactivated top in Diffrac.EVA, it has an 74.2% crystallinity and is 25.8% amorphous.

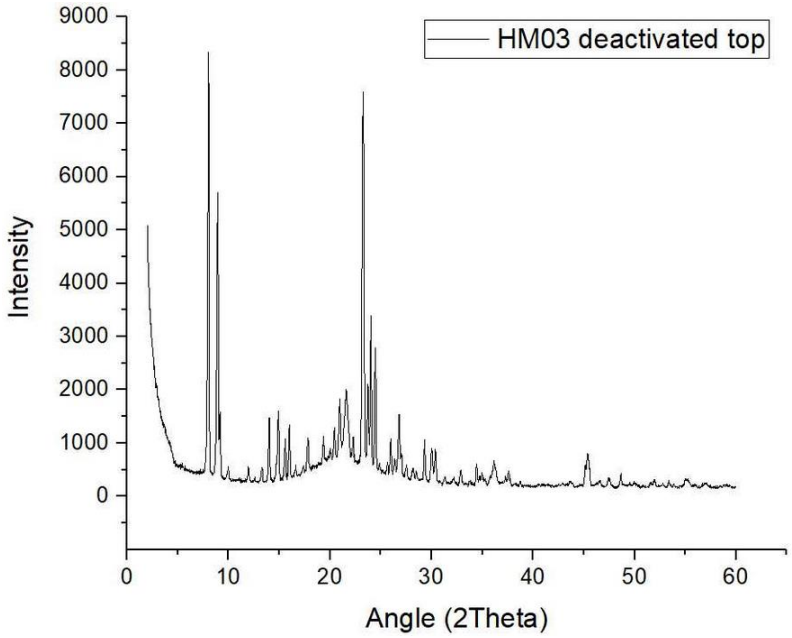

Figure 5-40: Glass plate XRD of the top layer of HM03 after MTH conversion.

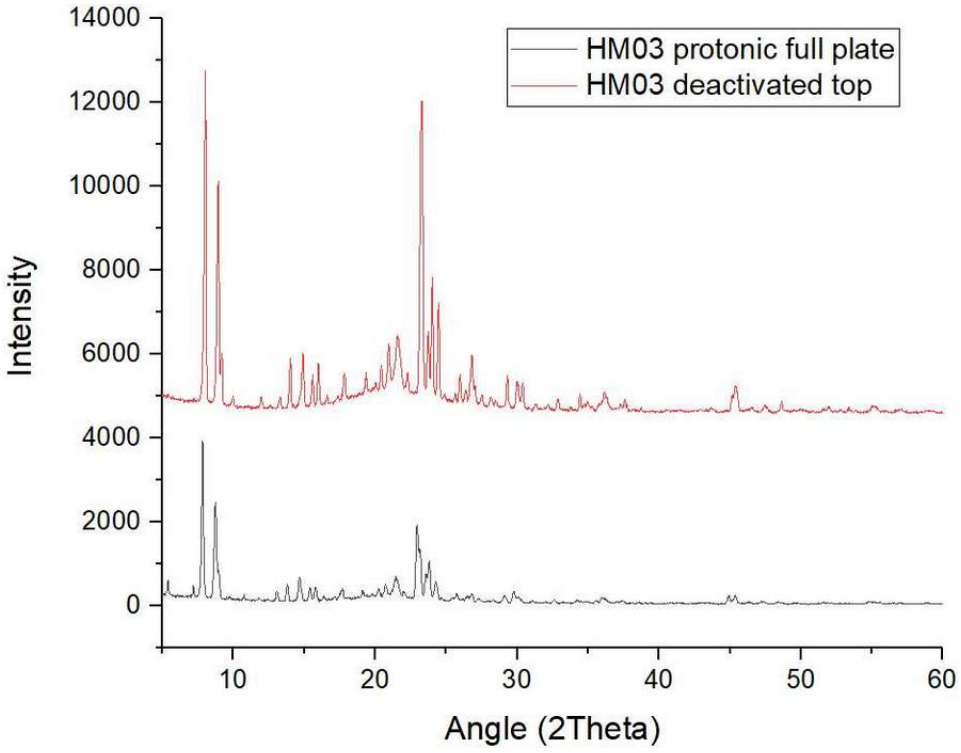

Figure 5-41: XRD pattern of protonic full plate HM03 and deactivated top in the same plot.

Table 5-21: Peak list for HM03 deactivated top glass plate XRD.

angle (° 2θ)	d value (Å)	Intensity (counts)	Rel. int. (%)	angle (° 2θ)	d value (Å)	Intensity (counts)	Rel. int. (%)	angle (° 2θ)	d value (Å)	Intensity (counts)	Rel. int. (%)
8.03	11.001	5315.4	100.0	25.98	3.426	442.5	8.3	45.38	1.997	487.9	9.2
8.94	9.886	3549.9	66.8	26.36	3.378	224.2	4.2	46.54	1.950	88.5	1.7
9.18	9.625	831.4	15.6	26.81	3.323	834.6	15.7	47.42	1.915	134.7	2.5
9.98	8.859	142.9	2.7	27.04	3.295	302.4	5.7	48.66	1.870	215.0	4.0
11.97	7.385	166.7	3.1	27.50	3.240	191.6	3.6	49.53	1.839	57.4	1.1
12.60	7.019	62.6	1.2	28.15	3.168	161.5	3.0	49.98	1.823	67.1	1.3
13.31	6.649	168.7	3.2	28.49	3.130	96.9	1.8	51.62	1.769	29.7	0.6
14.02	6.313	839.6	15.8	29.32	3.044	561.0	10.6	51.96	1.759	126.6	2.4
14.90	5.940	885.4	16.7	30.00	2.976	452.5	8.5	52.77	1.733	66.4	1.2
15.59	5.679	536.2	10.1	30.38	2.940	466.0	8.8	53.37	1.715	91.7	1.7
16.00	5.534	694.0	13.1	31.34	2.852	72.9	1.4	53.87	1.701	56.9	1.1
16.62	5.330	163.5	3.1	32.19	2.778	91.9	1.7	55.08	1.666	103.7	2.0
17.37	5.103	92.0	1.7	32.86	2.723	207.5	3.9	55.99	1.641	44.8	0.8
17.83	4.971	426.2	8.0	33.80	2.650	41.6	0.8	56.70	1.622	56.3	1.1
19.35	4.584	402.0	7.6	34.44	2.602	319.8	6.0	57.00	1.614	58.2	1.1
20.03	4.429	219.0	4.1	34.96	2.564	162.1	3.0	61.02	1.517	22.8	0.4
20.43	4.343	512.4	9.6	35.75	2.509	92.5	1.7	62.33	1.488	105.2	2.0
20.96	4.235	826.0	15.5	36.15	2.483	343.3	6.5	63.71	1.460	43.9	0.8
21.59	4.113	943.5	17.8	37.28	2.410	128.7	2.4	64.13	1.451	99.3	1.9
22.27	3.989	380.2	7.2	37.59	2.391	215.4	4.1	64.32	1.447	113.8	2.1
23.29	3.817	4666.4	87.8	38.25	2.351	30.8	0.6	65.66	1.421	140.0	2.6
23.73	3.746	1132.9	21.3	38.74	2.323	75.4	1.4	67.11	1.394	86.6	1.6
24.03	3.701	2090.9	39.3	42.90	2.107	53.7	1.0	67.82	1.381	47.7	0.9
24.46	3.636	1651.5	31.1	43.66	2.072	59.3	1.1	68.75	1.364	50.2	0.9
24.87	3.577	94.2	1.8	45.16	2.006	323.1	6.1	69.07	1.359	58.5	1.1
25.65	3.470	161.6	3.0								

Differences in the patterns in Figure 5-41 is the relative intensity of peaks and the form of the peaks. Change in peaks intensity is visible for peaks such as the peaks below 10° as well as the peaks around 23°. For the peak at 22.99° for protonic and 23.29° for deactivated top, the relative intensity increases for the peaks around 23° compared to the peaks below 10° from protonic to the deactivated sample. The relative peak intensity changes from as - synthesized to protonic as well (shown in Figure 5-7), where the peak decreases when the sample has been turned to proton form. This change is not visible for HM02.

Figure 5-42 shows the data for Figure 5-40 where the 2θ range 45° - 46° is highlighted. Similarly, the same range is highlighted for the pattern of the top layer in Figure 5-43. These peaks are the same peaks as illustrated in Figure 1-10, From these two patterns there is an evident visual difference between the two peaks, where the peaks in Figure 5-42 is a double

peak and the peaks in Figure 5-43 resembles more a single peak. The change for the peaks is due to filling of the pores causing the unit cell of the crystals to become more of tetragonal than orthorhombic structure (23).

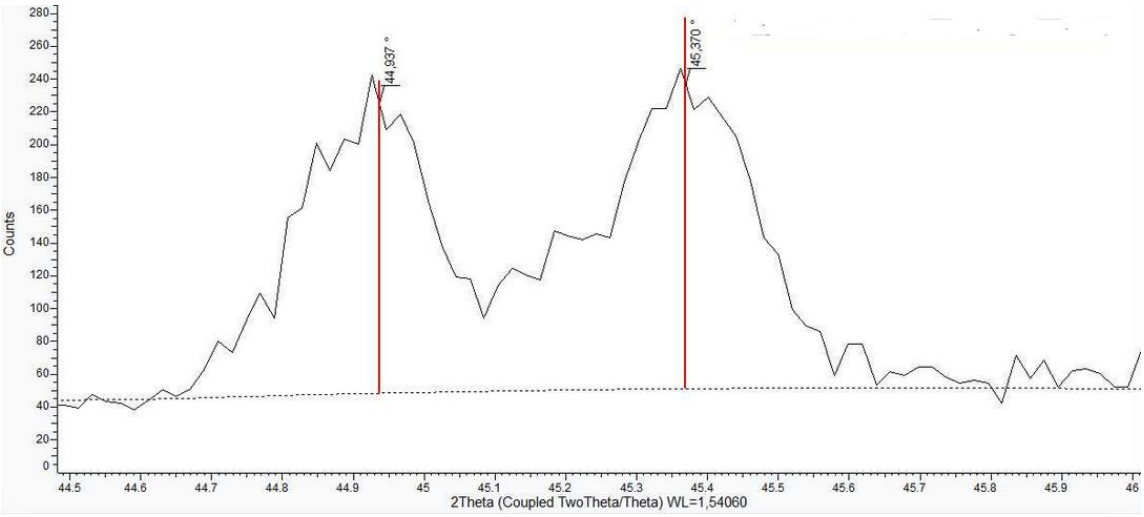

Figure 5-42: A XRD pattern of protonic HM03 measured on a full plate. The data was analyzed in Diffrac.EVA, where it was zoomed in on the peaks between 45° and 46°.

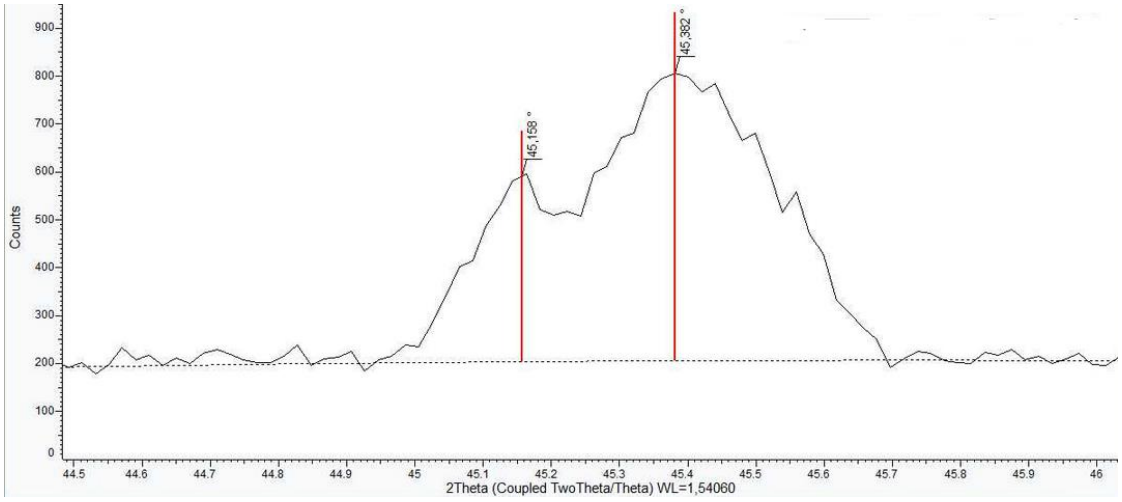

Figure 5-43: A XRD pattern of the top layer from the catalytic testing of HM03 measured on a glass plate. The data was analyzed in Diffrac.EVA, where it was zoomed in on the peaks between 45° and 46°.

5.10 Temperature programmed oxidation

TPO was performed during operando conditions to investigate the oxidation and thereby also investigate the coke content of the ZSM – 5 zeolite HM02 synthesized in this work.

The TPO experiment in Figure 5-44 shows how the difference between the a and b parameters of the unit cell of HM02 with coke content changes over time. The experiment is performed during heating from room temperature and cooling back to room temperature. A Pawley and Rietveld refinement was performed on the data, where both refinements showed very similar results. A curve of the Pawley refinement is included in the plot. The Pawley refinement (the analysis is made by Nico König) is summarized in Table 5-22.

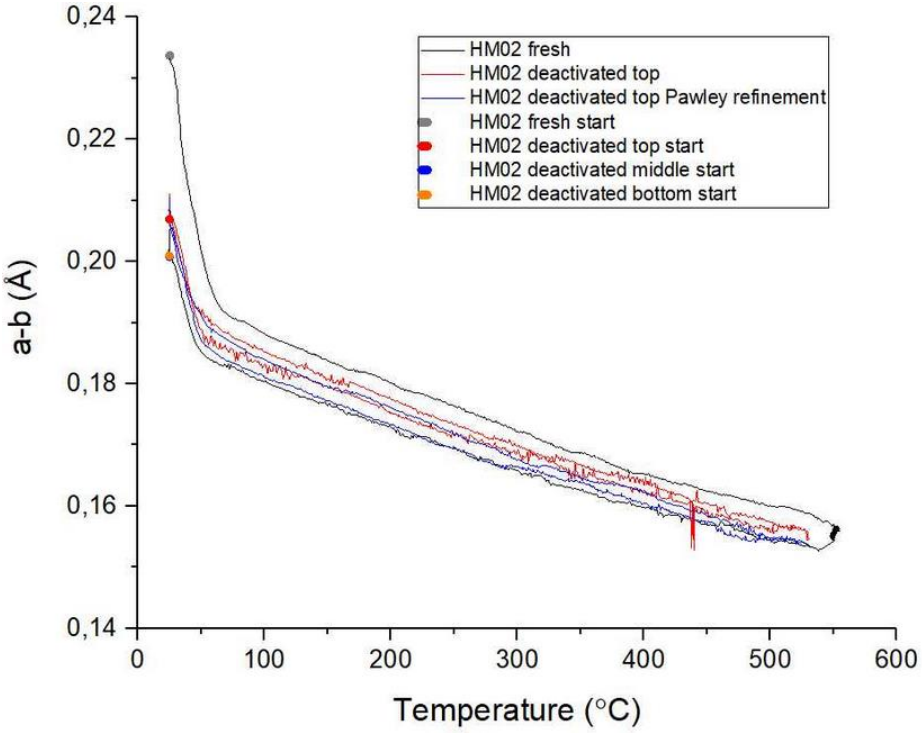

Figure 5-44: TPO experiment of HM02 performed in a capillary at 25°C of fresh, top, middle and bottom layer used in the reactor during the catalytic testing. The starting vector for fresh, top, middle and bottom is marked as a grey (0.23368 Å), red (0.20691 Å), blue (0.20078) and orange (0.20095 Å) dot respectively.

Table 5-22: Summary of the parameters for a Pawley refinement of the data from the diffractogram in Figure 5-44.

Quantity	Fresh	Top	Middle	Bottom
a (Å)	20.111	20.109	20.110	20.109
b (Å)	19.877	19.902	19.909	19.908
c (Å)	13.387	13.392	13.394	13.394
R_{wp} (%)	16.7	10.2	7.1	9.1

The initial drop in Figure 5-44, is due to the removal of water from the material. The air that is introduced to the sample is dry, which results in that the water is removed before 100°C. The rest of the decrease during the heating is because of coke removal and the strain the sample is taking from the thermal influence. After the removal of water for the fresh sample, it acts almost identical for both, during heating and cooling as the deactivated layers, which means that the sample doesn't contain much coke. The main effects that is visible on the sample, during the experiment should than be caused by temperature.

The change in the difference between a and b from start to end for the experiment says something about the amount of coke in the sample and according to the figure, there seems to be almost no coke in the sample (approximately 0.5 wt.% from TGA). The data for the top, middle and bottom layer are very similar, with not much difference and with overlap for the experimental data. All three datasets are between the dataset for the fresh material (in gray) in the figure. The change in the difference between the a and b parameters during the whole experiment is approximately 0.08, which is lower than usual and what has been reported earlier (Rojo-Gama had a difference of 0.16 in his Ph.D. thesis (28)).

6 Discussion

In this section, data from the result section will be discussed and compared to each other and to literature. The results that will be mainly focused on, is the results from XRD, TGA and MTH conversion. The MP – AES and EDX analysis will be discussed together in terms of the elemental analysis.

The only difference in the synthesis of HM02 and HM03 was the alumina source that was used, where an alumina source from Fluka was used for HM02 and one from Aldrich was used for HM03. The gathered results from the characterization methods indicates that the alumina source from Aldrich is better than the alumina source from Fluka for crystallizing ZSM – 5 for zeolite synthesis. The gathered results include that HM03 had higher Si/Al ratio, more accessible acid sites, higher specific surface area and higher catalytic activity than HM02.

6.1 X – ray diffraction

6.1.1 Non deactivated zeolites

There are small differences in peak positions for the materials (e.g., peak at 8.90°2θ for protonic ACS extrudates and 8.89°2θ for the reference pattern). If the difference is not caused by instrumental error or sample preparation, then it is caused by differences in the unit cell compared to the literature.

As mentioned in section 5.1, HM01 was evaluated to be amorphous and did not have the required crystallinity of a ZSM – 5 material. It was identified as amorph by the broad peak from approximately 15°2θ to 30°2θ, and according to the calculated crystallinity of the pattern, it was 50% amorphous. Additionally, the material did not have the correct crystallinity based on that there were missing characteristic signal, such as the two peaks at 8°2θ and 9°2θ. The reference pattern (see Figure 8-3) had its first signal at 7.95°2θ and HM01 had its first peak at 13.49°2θ. The rest of the materials was evaluated to be of the correct zeolite material.

Both the XRD diffractogram of as - synthesized and protonic HM02 done with glass plate, showed preferred orientation (illustrated in Figure 8-4 and 8-6 in appendix 8.2) and they differ somewhat from a regular XRD pattern for a ZSM – 5 material. This is not uncommon for materials with preferred orientation. These two XRD patterns are not identical either. As

mentioned in section 5.1, the peak intensity for the signals at 8.15°2θ and 9.11°2θ has a 2 times difference for the as - synthesized HM02 and a 5 times difference for the peaks at 8.26°2θ and 9.18°2θ for protonic form. The difference in relative intensity is assumed to be caused by the change to proton form, where the electron density is decreased. The difference in relative intensity is supported by refinements (Rietveld and Pawley) of pattern for HM02, that showed that although the peaks matched well with literature, it still had deviations in peak intensities.

There are differences between the relative intensity of signals for the pattern with preferred orientation and the one without preferred orientation (see Figure 5-3). Examples for this is the peaks at 9.11°2θ, 18.03°2θ, 27.06°2θ, 36.26°2θ and the double peak at 45.36°2θ and 45.70°2θ. For all these signals, the relative intensity is higher for the pattern with preferred orientation.

Another change in the XRD pattern of HM02 (with preferred orientation) in proton form is the relative intensity between the peaks approximately at 8°2θ and 23°2θ. For the XRD pattern of the as - synthesized version the two peaks are at equal intensity, but for the proton form, the peak at 8.26°2θ has approximately 3 times higher intensity than the peak at 23.25°2θ. This change is similar for HM03. The change in the XRD patterns is thereby probably caused by the removal of template since it was the only treatment of the material between analysis of the diffractograms.

The capillary XRD of HM02 was the first pattern of HM02 that did not show preferred orientation (see Figure 8-2). The relative intensity for the first two peaks for this pattern was 76.1% and 17.2% respectively, where the first peak was slightly higher than the reference (at 68.4%) and the second peak was slightly lower than the reference (at 36.8%) (see Table 8-1). Otherwise, the pattern matches well with the reference confirming that the material is indeed a high crystalline ZSM - 5.

The as – synthesized HM03 has a relative intensity of 43.4% and 26.9% respectively for its first two peaks. This is lower than for the reference (see Table 8-1). The difference in relative intensity may be due to that the signal at 23.37°2θ (peak with highest intensity) has a slightly higher intensity than the reference and becomes the peak with highest intensity in the pattern. It is possible that what is the cause of the abnormal high drop for the drop at 200°C in the TGA analysis of the as – synthesized HM03 is involved in influencing the relative intensity of the peak at 23°2θ in the XRD pattern, giving it higher intensity than it should.

The XRD pattern of as – synthesized HM03 and the protonic form of HM03 (illustrated in Figure 5-5 and Figure 5-6) agrees with what is given in '*Collection of simulated XRD powder patterns for zeolites'* (55) and is thereby confirmed to be of a high crystalline ZSM - 5. The relative peak intensity of the signals at approximately 8°2θ and 23°2θ differs for the two forms of the material. This is due to that the electron density changes.

The XRD of protonic ACS extrudates showed that the first two characteristic peaks have a relative intensity of 100% and 69.4% respectively and the peak at 23.31°2θ has a relative intensity of 82.4%. The reference pattern in the zeolite collection (38) for protonic ZSM – 5 has a relative intensity of 100% and 52% for the peaks at 7.94°2θ and 8.90°2θ respectively and 45% for the peak at 23.10°2θ, which means that the ACS extrudates has a higher intensity for these peaks**.** Otherwise, the pattern matches well with the reference confirming that the material is indeed a high crystalline ZSM - 5.

The XRD of protonic MFI – 27 showed that the first two characteristic peaks at 8.06°2θ and 8.99°2θ have a relative intensity of 100% and 78% respectively and the peak at 23.27°2θ has a relative intensity of 98.6%. Compared to the reference pattern (mentioned above) the second peak for MFI – 27 has a relative intensity 26% higher and the peak at 23.27°2θ has a relative intensity 53.6% higher than the reference pattern. Otherwise, the pattern for MFI – 27 is a good match to the reference pattern confirming that the material is indeed a high crystalline ZSM – 5.

All four Beta zeolites showed similar XRD patterns, which show resemblance to literature pattern of zeolite beta (79). They showed characteristic peaks that includes a peak with high intensity at 8°2θ and a peak with high intensity at 23°2θ, as well as small peaks at 14°2θ, 15°2θ and 44°2θ. For TOMO007, it is barely possible to register the peak at 14°2θ and there is no significant peak at 15°2θ.

6.1.2 Deactivated zeolites

The XRD patterns of protonic and deactivated version of HM02 and HM03 was investigated and compared to each other by use of the program Diffrac.EVA, to compare shape of peaks and relative peak intensities.

As shown in the XRD diffractogram in Figure 5-38, protonic HM02 has a double peak at 45.08°2θ and 45.48°2θ. The peak for the deactivated version of HM02 has a signal at 45.11°2θ

and 45.60°2θ, which still resembles a double peak. This is illustrated in Figure 5-39 (full XRD diffractograms are shown in Figure 5-2 and Figure 5-36).

For Figure 5-2 and Figure 5-36, there is also one other thing to notice, which is that the relative intensity for the peaks at approximately 8°2θ and 23°2θ has not changed as much for HM02 as for HM03. For HM02, the peaks at 8°2θ and 23°2θ is at the same hight as can be seen in Figure 5-2 and Figure 5-36. As for HM03 the peak at 23°2θ is higher than the peak at 8°2θ in Figure 5-40 (deactivated top layer), compared to the peak in Figure 5-6 (protonic). This is an indication that the electron density for HM03 has increased more than the electron density for HM02 due to buildup of coke during the process of the MTH conversion. This is expected since HM03 showed higher catalytic performance than HM02.

The XRD of the middle layer of HM02 was done on a glass plate and not in a capillary. Something to recognize, is that the XRD pattern do not show preferred orientation, as the XRD pattern compares well with reference. Based on that the sample of HM02 without coke had preferred orientation and the sample with coke did not, the coke on the sample might prevent the effect of preferred orientation to occur, by changing the structure so that the particles cannot stack in layers.

HM03 was the catalyst that had the highest activity over the longest time of the ZSM - 5 zeolites tested and was still quite active by the time the test was stopped at 57 hours (approximately 50% conversion). HM03 had approximately 8% weight loss during the TGA analysis that corresponds to coke content.

Since HM03 has more coke content in its structure than HM02 and based on that a unit cell may change upon deactivation (section 1.7). It is thereby expected to be easier to identify differences in the XRD pattern for HM03 with coke content than HM02.

There was a clear difference for the signal between 45°2θ and 46°2θ for HM02 and HM03 after the MTH conversion. For HM02, which had low catalytic activity, still had a clear double peak at this analysis, while the double peak was not that clear for HM03 (had more characteristics of a single peak). The change in the peak characteristics is due to coke produced from the MTH conversion which fills the pores of the zeolite and thereby changes the unit cell of the material. The degree of how much coke that is in the zeolite's pores is visible by for example how much the signal between 45°2θ and 46°2θ is characteristic of a single peak. This is also something Rojo-Gama investigated in his PhD (28), where he also had peaks between

45°2θ and 46°2θ that changed from double peaks towards a single peak as the material got more deactivated.

The fact that there is such a big difference in the shape of the peaks between 45°2θ and 46°2θ for HM02 and HM03, indicates that HM03 contains a higher coke content than HM02. This is also indicated from the TGA analysis and MTH conversion for these two materials.

Out of all the zeolites that were measured by XRD, HM02 was the material that showed the highest degree of crystallinity (95.4%) and HM01 was the material with the lowest (50.1%).

6.2 Thermogravimetric analysis

The TGA analysis of as – synthesized HM03 (shown in Figure 5-12) has a massive drop at 200°C (17 wt.%), which is unexpected. The drop for as – synthesized HM02 at the same temperature is minimal compared to HM03 (0.7 wt.%). The drop at that temperature is usually due to the removal of water from the materials, but since the drop is so large for HM03, it might indicate that there are other impurities in the material.

The drop for as – synthesized materials should not have any impact on the materials' further characterization since all later work with the materials was with the materials after calcination, where impurities are removed. The TGA analysis for the protonic form (calcinated version) of the materials did not indicate presence of any impurities.

Both the TGA of as – synthesized HM02 and HM03 showed reasonable amounts of template present, which was removed during the analysis. The template bonded to the zeolites, combusted at approximately 400°C. HM02 had 12.1 wt.% of template and HM03 had 8 wt.% of template removed from its structure.

It is expected that the wt.% of template for a ZSM – 5 zeolite to be approximately 11% of the total weight. This is based on that the theoretical amount of template should be 11.4 wt.% (as is calculated in appendix 8.1), because of the average weight of template in its unit cell. The weight loss for template removal for HM03 was slightly lower than the theoretical amount. This indicates that the material consists of less template than intended (consist of less than four templates per unit cell). However, the low amount of template observed may also be due to the abnormal amount of weight loss at 200°C, which affected the wt.% for the drop at 400°C. This means that both materials can still have approximately 11% template compared to the amount of zeolite (four templates per unit cell). By relating the mass percent to the final weight of the

TGA analysis (where there is only zeolite), the drop for template removal for HM03 as - synthesized (at 83.2 wt.%) equals 9.9% of the total weight, which is 1,5 wt.% lower than the theoretical value, which is an acceptable deviation.

Both the TGA analysis of protonic HM02 and HM03 (illustrated in Figure 5-11 and Figure 5-13) showed that they had low weight loss due to removal of water in their structure. The expected weight loss for a ZSM – 5 zeolite on proton form is as stated in section 5.2, between 5 and 10 wt.%. Based on that the water molecules are adsorbed on a zeolite's active sites, the number of active sites a zeolite has in its structure will determine the amount of water that will be adsorbed. Since the wt.% for removal of water for the two materials are lower than expected, the materials seem to have fewer active sites in their structure than what is usual.

The TGA analysis for the protonic form of MFI – 27 shows a mass loss of more than 5 wt.% (6.5 wt.%) due to the removal of water (illustrated in Figure 5-15), which is more than for both HM02 and HM03. However, the mass loss for MFI - 27 is also within the expected range of mass loss for a ZSM – 5 zeolite on proton form. Therefore, the structure of MFI – 27 is a normal ZSM – 5 zeolite.

The TGA analysis of deactivated HM02 and HM03 (illustrated in Figure 5-32 and Figure 5-33) indicates that there is a major difference in coke content in the top layer for the two materials. HM02 has a weight loss of 1.3% due to removal of coke and HM03 has a weight loss of 8%. This means that there is a difference in weight loss due to coke removal around 7% between the two materials. The difference in coke content between the two materials indicates that HM03 was more active as a catalyst for MTH conversion.

The weight loss of deactivated HM02 is low compared to what is given in '*A straightforward descriptor for the deactivation of zeolite catalyst H-ZSM-5'* (23), where the lowest wt.% after MTH for the top layer of tested materials was 9% and the highest was 21.6%. A possible reason for this may be due to that the crystals are quite large, and the coke blocks the entrances of the pores so that most of the crystals stays 'clean' and thus not much coke can be observed in the XRD or TGA. Additionally, the 1.3 wt.% obtained from TGA might partially be external coke, which does not sit inside the pores. This may further reduce the coke that are detectable in the XRD analysis.

According to the data from the MTH conversion for HM03, the material still had 51% yield when the experiment ended, which was 34% more than for HM02. This means that if HM03 was tested until it was fully deactivated or at least until it had the same yield as HM02, it should

have higher coke content in its structure at that point. The difference in coke content between HM02 and HM03 at end of the testing was 6.7%. It is expected that if the testing was continued for HM03, the difference in coke content would increase to more than 6.7% between HM02 and HM03. If the MTH conversion was continued for HM03, it is expected that the XRD pattern would also change, so that the double peak at 45.16°2θ and 45.38°2θ would be more like a single peak.

All layers of the deactivated ACS extrudates had a higher coke content than both HM02 and HM03, but the ACS extrudates was fully deactivated while HM02 and HM03 was not. As mentioned earlier, HM03 had 6.1 wt.% of coke for its top layer when the material still had 51% yield when it was ended. If the testing was continued for HM03, it might have had higher coke content than the bottom and middle layer of the ACS extrudates and maybe higher than the top layer as well.

The DSC analysis of the ACS extrudates (given in Figure 8-12) shows that there is a difference at which temperature the layers have peaks at and these peaks gradually shifts along the x – axis as the material takes on more coke. The bottom layer has two peaks, one at 398°C and one at 548°C, the middle layer has two peaks, one at 403°C and one at 567°C and the top layer has one peak at 587°C. The peaks from the layers are both exothermic and is due to coke removal. The temperature the peaks occurs at implies that there are two different types of carbon (or carbon that is bonded to the zeolite in different ways) that is removed. What type of carbon that is removed is hard to tell, but they are different in some way. The fact that the top layer only has one peak implies that the layer contains one type of carbon.

6.3 Scanning electron microscope

The SEM studies of the materials shows that there are differences in morphology for the materials. Differences were observed both in shapes and particle size between the materials. The pictures from the SEM microscope showed that the crystals for HM02 (illustrated in Figure 5-16 and Figure 5-17) were uniform and had the boat - like shape as is also described by Koegler et al. (82) and Maarten et al. (83). HM02 had crystals with intergrown crystals and central defects. HM03 had crystals like HM02 as well (illustrated in Figure 5-18), but also crystals with different size and shape. Even though the two materials are synthesized in a very similar way, their morphology are quite different. The difference in morphology for the two materials is expected to be a consequence of the use of different alumina sources.

6.4 Elemental analysis

The Si/Al ratio for HM03 from the MP - AES is close (closer than HM02) to the theoretical Si/Al ratio for the synthesis, with 41.5 measured from MP - AES and 39 is the theoretical value. Based on the Si/Al ratio gathered from the MP – AES, the Si/Al ratio of HM03 is higher than the theoretical value. This could be a consequence of that some of the alumina was not incorporated in the structure during the synthesis. HM02 on the other hand has a lower Si/Al ratio than the theoretical value, (a Si/Al ratio of 28). The low Si/Al ratio for HM02 indicates that there is more alumina or less silicon present in the analyzed sample. A short summary of all the data for the elemental analysis from EDX and MP – AES analysis is given in Table 6-1.

Table 6-1: Summary of the elemental analysis for both the MP - AES analysis and EDX analysis of HM02 and HM03, where the average of the EDX scans is given.

Material	EDX Si/Al ratio	MP-AES Si/Al ratio	Si/Al ratio from synthesis gel
HM02	28	28	39
HM03	32	41	39

It is visible that there are local variations in Si and Al distribution for the materials from both EDX analysis and SEM images of the materials. The EDX indicates the variations from differences in the calculated Si/Al ratio, whereas mentioned in section 5.5, the difference between the highest and lowest Si/Al ratio for HM02 is 6.3 and 16.1 for HM03. This means that for the three scans, HM02 has less variations than HM03. The SEM analysis shows that there are local variations in the SI/Al distribution, as is illustrated in Figure 5.19.

The EDX and MP – AES techniques is different in the way that an EDX does an analysis directly on a sample without any adjustment of the sample, but for a MP – AES the sample is prepared before the analysis by dissolving a sample in solution. An EDX also analyses a very small area at a time, whereas a MP – AES analyses bulk of sample for one analysis.

Both the data from the EDX and MP – AES analysis shows that HM03 has higher Si/Al ratio than HM02. However, there is not good agreement on the actual ratio between the two techniques. The second scan of HM02 is close to the ratio from the MP – AES.

6.5 Accessibility of acid sites and acid density

It is difficult to handle the gathered data, because of the very low accessibility of acid sites and density of acid sites for the zeolites, but it was possible by use of a test sample. In hindsight of the low amount of acid sites, a lower base concentration should have been used instead.

Based on the data from TGA analysis, which is that the protonic form of the materials has less water in their structure than normal ZSM – 5 zeolites, it is reasonable to conclude that the tested materials do not have many available acid sites. The fact that HM02 has lower accessibility of acid sites than HM03 (even though it had more alumina present for the elemental analysis) confirms that the material has alumina present that does not give rise to any acid sites.

As illustrated in Table 6-2, which shows the calculated accessibility of acid sites from the EDX and MP – AES analysis, the accessibility of acid sites is dependent on the Si/Al ratio of a zeolite. The accessibility of acid sites is identical for HM02 from EDX and MP – AES analysis, but for HM03, the value from MP – AES is higher than for the EDX analysis. The value for HM03 is lower for the EDX analysis because it had a spread in lower Si/Al ratios. The accessibility of acid sites increases for the materials when the Si/Al ratio is increased. The accessibility of acid sites shown in Table 6-2 is calculated in the same way as is calculated in appendix 8.7.3. Out of EDX and MP – AES, the numbers from the MP – AES should be the most trustworthy, since the technique is based on a bulk analysis instead of specific areas.

Table 6-2: Accessibility of active sites from measured Si/Al ratio of HM02 and HM03 from MP – AES and EDX. The number for the EDX analysis is the average number from the three measured scans of each material. Calculations for MP – AES is shown in appendix 8.7.3.

Material	Average EDX (%)	MP – AES (%)
HM02	5	5
HM03	26	34

There is still some uncertainty related to the potentiometric titration technique because it is relatively little used for zeolite characterization, which means that some validation is required for the technique. Validation of the technique was started by testing CBV8014, which showed good results with 99% accessibility of acid sites.

6.6 N_2 adsorption

For the N_2 adsorption, the value for the specific surface area of HM02 and HM03 was similar 318 m^2/g and 321 m^2/g respectively. This similarity is reasonable since they were synthesized with only a difference in an alumina source.

Both HM02, HM03 and ACS extrudates had hysteresis, which is an indication that they are mesoporous, which means that they have pores bigger than 2 nm. They did however have the hysteresis loops at different times in their adsorption and desorption. HM02 had a small hysteresis loop in the beginning ($p/p_0 = 0.1$) of the adsorption and HM03 had a bigger hysteresis loop in the end ($p/p_0 = 0.9$) of its adsorption. The ACS extrudates had its hysteresis loop from $p/p_0 = 0.5$ to 0.95. The hysteresis loop for the ACS extrudates resembles a type IV hysteresis loop (84) and is caused by capillary condensation when the mesopores are filled and emptied. The hysteresis for HM03 resembles a type I hysteresis loop (78, 84) and is caused by condensation between particles. The pressure area for where the hysteresis was visible is determined by the size of the materials mesopores. The bigger the pores, the later the hysteresis will occur. Mesoporosity may lead to improved diffusion conditions but may also be related to defects in the crystal structure (85).

The specific surface area of all the ZSM – 5 zeolites are as expected lower than the specific surface area of the Beta materials since the numbers were stated to be lower in the literature (86). However, the determined surface area of HM02 and HM03 was also somewhat lower than a typical ZSM – 5 zeolite. Pinilla-Herrero et al. (87) determined the specific surface area to be 400 m^2/g for ZSM – 5 zeolites with similar Si/Al ratio as in this work.

6.7 Methanol to hydrocarbon conversion

The yield of the ZSM – 5 zeolites during MTH conversion was clearly highest for the HM03 material compared to the other ZSM – 5 materials (illustrated in Figure 5-28). Reasons for the major difference in catalytic activity between the ZSM – 5 materials in this work should be because of properties that separates them such as differences in morphology, Si/Al ratio and pores. Different properties for the materials that might affect the catalytic activity for the materials, was acquired during TGA, SEM, MP – AES, titration and N_2 adsorption.

The TGA, MP – AES and titration gave results that indicate the number of active sites the materials had. The SEM analysis showed that HM02 and HM03 had different morphology (see

section 6.3), which might be a reason for difference in active sites available for catalytic activity. The N_2 adsorption showed that the specific surface area of the three ZSM – 5 materials were similar, but the pores were different as shown in Figure 5-21 to Figure 5-23. All three materials showed hysteresis loops, but with different characteristics (as described in section 6.6). This difference in adsorption properties between the materials, will mean that the form of their pores is different in size or shape.

According to the MP – AES analysis and the titration data, HM03 was the material that had the highest Si/Al ratio and most acid sites. Based on these results, the increase in catalytic activity for the material should be because more of the alumina that is present give rise to acid sites for the material. The catalytic activity presumably increases as well when the specific surface area and number of active sites of the material are increased.

The results of product selectivity for the zeolites during MTH conversion showed that the ACS extrudates had highest selectivity towards C_{6+}, HM02 had highest selectivity towards C_3 and HM03 had highest selectivity towards C_4. This might be partially caused by differences in Si/Al ratio of the materials (as is listed in Table 4-1 in the experimental section). For the ZSM – 5 zeolites, HM03 showed highest Si/Al ratio and it was the material that clearly had the highest activity during the MTH conversion.

An explanation for that the Si/Al ratio might affect the catalytic properties of a ZSM – 5 zeolite may be that this causes a change of active sites. For the zeolites in this work, it appears that the number of active sites increases with increasing Si/Al ratio. The determined acidity of the ZSM – 5 zeolites by titration seems also to support this. This is somewhat unexpected since normally active sites is on the alumina in the structure (but the reason for this observation seems to be because of alumina that is present but is not giving any active sites).

The product selectivity for the ZSM – 5 zeolites is high towards aromatics (C_{6+}) and low towards C_1 and C_2, which in agreement with literature such as Rojo-Gama et al. (76). As mentioned earlier ACS extrudates is the ZSM – 5 zeolites with the lowest Si/Al ratio (Si/Al ratio = 19). For the initial product selectivity (Figure 5-29), there is one major difference between the ACS extrudates compared to HM02 and HM03. The major difference is that the ACS extrudates has a much higher selectivity towards C_{6+} and a lower selectivity towards C_3 compared to the other two materials. The difference in selectivity between the materials may be caused by the difference in density of acid sites for the materials.

All the Beta zeolites deactivated relatively fast, which was expected based on literature (as illustrated in Figure 5-30) (88). For the Beta's the most active material was 09-00243/1 with a Si/Al ratio of 13.5 and the least active material was CP806B-25 with a Si/Al ratio of 27.

This is in contrast to ZSM – 5, since the Beta zeolites' least active material was the material with the highest Si/Al ratio, while for the ZSM – 5 zeolites it was opposite.

As mentioned, 09-00243/1 was the Beta zeolite with the highest catalytic activity and the initial product selectivity for the Beta zeolites indicate that this material has lower C_4 selectivity and higher C_3 selectivity than the rest of the materials (see Figure 5-31). The results showed that CP806B-25 had the highest product selectivity towards C_3 and C_4 of the Beta zeolites and this may be due to that this material have the highest Si/Al ratio. Compared to '*The methanol-to-hydrocarbons reaction: Influence of acid strength on the mechanism of olefin formation', 2010* (89) the Beta zeolites had very different product selectivity. The Beta zeolites in this work had high selectivity towards C_4 while those of Erichsen (89) had low selectivity towards C_4. The high C_4 and C_{6+} selectivity for the Beta zeolites could be expected based on literature (for example in Bjørgen et al. (90)).

6.8 Temperature programmed oxidation

The TPO measurement for HM02 (as shown in Figure 5-44) indicates that even the most deactivated version of the material (top layer) does not contain much coke, since the a and b vector of the unit cell does not change much during the experiment. The a and b vector change in a similar way as for the fresh version of the material, which is only changing due to thermal strain. The data points for the deactivated versions of HM02 is at all times within the area for the fresh version of the material. This means that during heating, the vectors for the deactivated versions are smaller than the fresh version and the vectors are larger during cooling.

The estimated difference between the a and b vector is almost identical for the bottom and middle layer at time 0 for the experiment (see Figure 5-44) (the points are on top of each other in the plot (marked as blue and orange dot) with a difference of 1.7×10^{-4} Å). That HM02 contains low amount of coke agrees well with the results for the material discussed previously.

In retrospective HM02 seems not the best material to be sent to Grenoble for analysis due to its poor catalytic performance. HM03 would have been a better choice. Unfortunately, the material

was not characterized at the time when the selection was done and thus it was not possible to know this.

7 Conclusion and further work

In this work a total of three homemade zeolites were synthesized and they are denoted HM01, HM02 and HM03. Two of them (HM02 and HM03) was identified as crystalline ZSM-5 zeolites. From XRD analysis HM01 was found to be amorphous and was therefore not evaluated further. The two homemade ZSM-5 materials and seven commercial zeolites was characterized and tested for MTH conversion.

The two homemade materials HM02 and HM03 were characterized by PXRD, TGA, SEM, MP – AES, EDX, N_2 adsorption, potentiometric titration and MTH conversion. A TPO experiment was also performed on HM02. Besides that, N_2 adsorption was performed on an ACS extrudate material, as well as PXRD and MTH conversion on the ACS extrudates and four Beta zeolites. Lastly potentiometric titration was performed on the ACS extrudates and CBV 8014 together with HM02 and HM03.

From the TGA of as - synthesized HM02 and HM03, HM03 had more total weight loss than HM02, where HM02 had 12.8% weight loss and HM03 had 25% weight loss. This indicates that HM03 has more impurities in its structure.

The major difference between the synthesis of HM02 and HM03 was the alumina source. This may be the reason that differences in properties between the two zeolites was observed. The properties being such as HM02 having specific orientation and HM03 do not, HM02 having a very clear crystal structure (uniform boat – like crystals) but are not as active as a catalyst as HM03.

From the SEM pictures from the microscope, it appears that HM02 and HM03 has different morphology in both shape and size. HM02 has an average particle size of $35\ \mu m \times 16\ \mu m$ and HM03 varies in length from 15 μm to 60 μm. The cause for this difference could be the different alumina source used during synthesis of the two zeolites.

According to the data from N_2 adsorption, there is hysteresis in the three zeolites ACS extrudates, HM02 and HM03. The hysteresis hints towards that the zeolites are mesoporous materials, which means that they have pores bigger than 2 nm.

For the ACS extrudates, the catalytic activity was found to be lower than expected (they decreased in MTH conversion immediately) and thus evaluated to not be a good catalyst. The material is thereby not recommended to be studied further.

After all the data had been gathered from the characterization methods used for this thesis, it appears that HM02 doesn't have many active sites. This is indicated from TGA as well as for the titration and is visible in Table 5-18, where there is not much signal from the instrument (5% accessibility). That HM02 has low activity is also indicated from experiment in the test rig, where it had less than 100% conversion from time zero and deactivated fast.

According to both TGA and TPO, HM02 did not contain much coke, where from TGA the coke content of the material is estimated to be approximately 1.5% and the TPO the coke on the surface of the material is estimated to be approximately 0.5%.

The results from the catalytic testing of the zeolites indicates that HM03 has the most catalytic activity and especially more than HM02, since HM03 ended at 51% conversion after 69 hours and HM02 started at 90% conversion and deactivated fast.

In section 6.1, it was showed that it could be possible to use XRD patterns to identify the degree of coke that is present in a materials' unit cells, based on changes in the XRD patterns, before and after catalytic testing. HM02 had low coke content and the XRD pattern did not show much change after MTH conversion. HM03 on the other hand, had higher coke content and its XRD pattern had evident change due to coke in the material.

The method for potentiometric titration was tested during Kumar's thesis (12), but it is still not ready for routine characterization. The method therefore requires further validation before it can be used as a routine method for catalyst characterization. The technique can be validated by testing it on further zeolites with other properties, such as different Si/Al ratios to get a better overview of the technique. The technique should be a very useful technique for zeolites characterization in the future.

Deactivated samples of the Beta zeolites and the ACS extrudates were delivered for further characterization by others in the TOMOCAT project.

From this work it is concluded that HM03 and MFI – 27, can be used for future studies of catalyst deactivation, since HM03 was the material with the highest catalytic activity and there has been done previous studies on MFI – 27 which can be continued.

Deactivation of zeolites is still a topic which is investigated and since the materials in this thesis was part of the TOMOCAT project (which investigates the deactivation of zeolites), further work in correlation of this project will be continued in the future.

An example for further study related to this work, could be to investigate the reasons for differences in properties between HM02 and HM03.

8 Appendix

8.1 Calculations for XRD and TGA

Calculations related to equation 7:

$$\left|ha + kb + lc\right|^2 = h^2a^2 + k^2b^2 + l^2c^2 + 2klbc \times cosa + 2lhc\alpha \times cos\beta + 2hka \times b \times cos\gamma$$

$$\left|ha + kb + lc\right|^2 = (ha + kb + lc)(ha + kb + lc)$$

$$= h^2a^2 + k^2b^2 + l^2c^2 + 2klbc + 2hlca + 2khab$$

$$= h^2a^2 + k^2b^2 + l^2c^2 + 2klbc \times cosa + 2lhc\alpha \times cos\beta + 2hka \times b \times cos\gamma$$

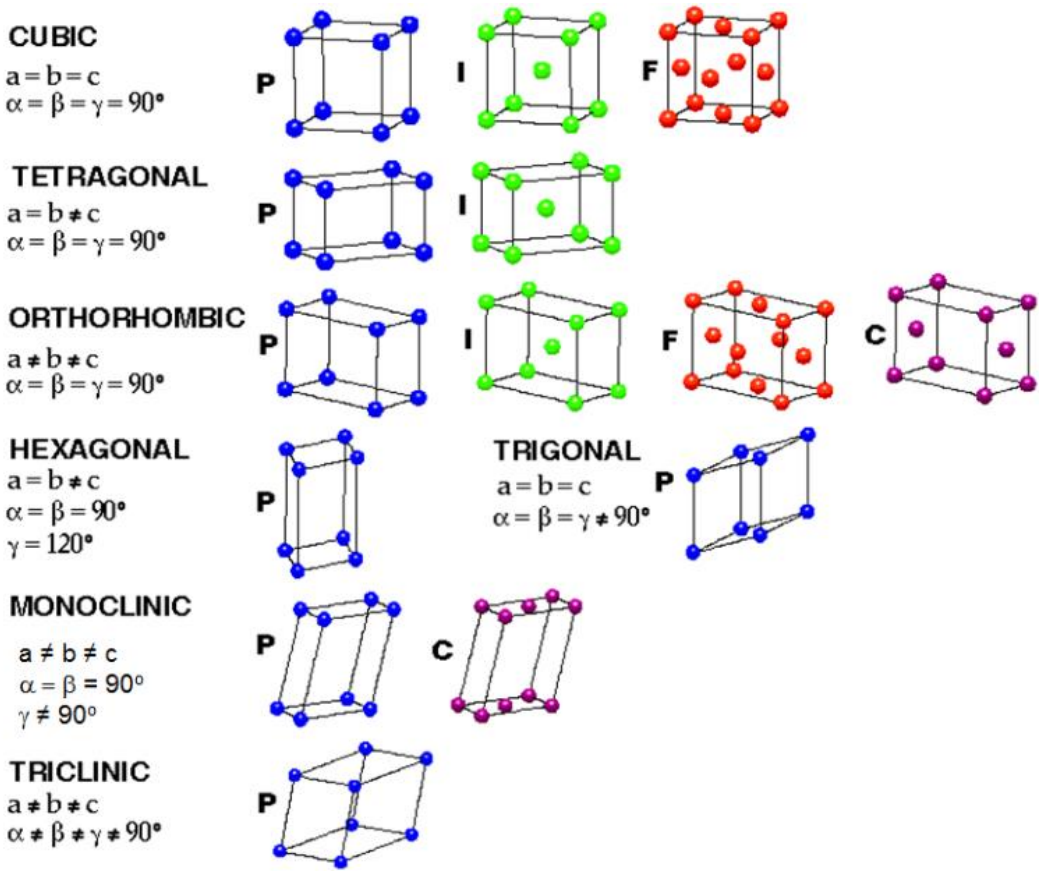

Figure 8-1: Describes unit cells of crystal structures for cubic, tetragonal, orthorhombic, hexagonal, monoclinic, triclinic and trigonal. The parameters (as indicated in Figure 1-9) are given for each crystal system. P, I, F, C by the crystal structures are abbreviations for the lattices primitive, body centered, face centered and side centered respectively. Adapted from (39).

Cubic:

$$\frac{1}{d^2} = \frac{h^2 + k^2 + l^2}{a^2}$$

Tetragonal:

$$\frac{1}{d^2} = \frac{h^2 + k^2}{a^2} + \frac{l^2}{c^2}$$

Hexagonal:

$$\frac{1}{d^2} = \frac{4}{3}\left(\frac{h^2 + hk + k^2}{a^2}\right) + \frac{l^2}{c^2}$$

Rhombohedral:

$$\frac{1}{d^2} = \frac{(h^2 + k^2 + l^2)\sin^2\alpha + 2(hk + kl + hl)(\cos^2\alpha - \cos\alpha)}{a^2(1 - 3\cos^2\alpha + 2\cos^3\alpha)}$$

Orthorhombic:

$$\frac{1}{d^2} = \frac{h^2}{a^2} + \frac{k^2}{b^2} + \frac{l^2}{c^2}$$

Monoclinic:

$$\frac{1}{d^2} = \frac{1}{\sin^2\beta}\left(\frac{h^2}{a^2} + \frac{k^2\sin^2\beta}{b^2} + \frac{l^2}{c^2} - \frac{2hl\cos\beta}{ac}\right)$$

Triclinic:

$$\frac{1}{d^2} = \frac{1}{V^2}(S_{11}h^2 + S_{22}k^2 + S_{33}l^2 + 2S_{12}hk + 2S_{23}kl + 2S_{13}hl)$$

In the equation for triclinic crystals,

$$V = abc\sqrt{1 - \cos^2\alpha - \cos^2\beta - \cos^2\gamma + 2\cos\alpha\cos\beta\cos\gamma}$$

$$S_{11} = b^2c^2\sin^2\alpha,$$

$$S_{22} = a^2c^2\sin^2\beta,$$

$$S_{33} = a^2b^2\sin^2\gamma,$$

$$S_{12} = abc^2(\cos\alpha\cos\beta - \cos\gamma),$$

$$S_{23} = a^2bc(\cos\beta\cos\gamma - \cos\alpha),$$

$$S_{13} = ab^2c(\cos\gamma\cos\alpha - \cos\beta).$$

Figure 8-2: List of Formulas for interplanar spacing that corresponds to the crystal structures in Figure 8-1 (rhombohedral = lattice system of trigonal). Adapted from (40).

Calculation of theoretical amount of template in a unit cell of a zeolite:

The molar mass is calculated for one TPA molecule and one MFI unit before the molar mass of one MFI unit is put together with 4 TPA units.

$$H = 1.008\ g/mol$$

$$C = 12.010\ g/mol$$

$$N = 14.007\ g/mol$$

$$O = 15.999\ g/mol$$

$$Si = 28.085\ g/mol$$

$$1\,TPA = 186.351\ g/mol$$

$$4\,TPA = \ 745.404\ g/mol$$

$$MFI = 5767.968\ g/mol$$

$$4\,TPA + MFI = 6513.372\ g/mol$$

Then the percentage of TPA in the total unit ($4\,TPA + MFI$) was calculated:

$$\frac{745.404}{6513.372}\frac{g}{mol} \times 100\% = 11.4\%$$

8.2 X – ray diffraction

This section contains additional XRD diffractograms, which is not shown in the result section. The additional XRD diffractograms include XRD diffractograms of full non - capillary XRD of HM02 and XRD diffractograms of the Beta zeolites from this work.

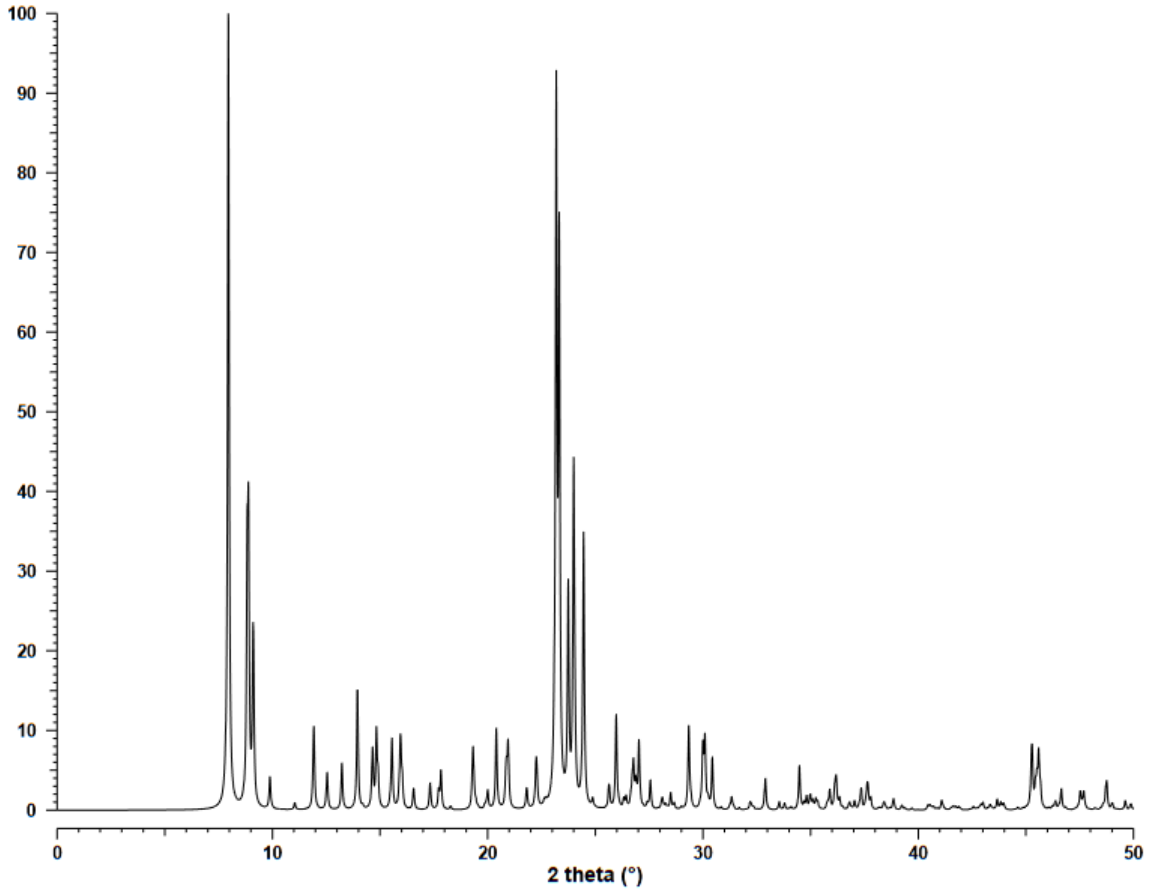

Figure 8-3: Reference x – ray diffraction pattern for ZSM – 5 from '*Collection of simulated XRD powder patterns for zeolites'*. Adapted from (38).

Table 8-1: List of XRD data for the reference pattern of ZSM – 5 in Figure 8-3 from '*Collection of simulated XRD powder patterns for zeolites'*. Adapted from (38).

h	k	l	2θ	d	M	I_{rel}	h	k	l	2θ	d	M	I_{rel}	h	k	l	2θ	d	M	I_{rel}
1	0	1	7.95	11.126	4	68.4	0	5	1	23.32	3.815	4	78.7	6	5	0	35.09	2.557	4	1.0
0	1	1	7.96	11.105	4	50.3	1	5	1	23.74	3.747	8	31.0	5	1	4	35.24	2.546	8	1.4
2	0	0	8.83	10.011	2	31.3	3	0	3	23.99	3.709	4	47.7	1	5	4	35.33	2.540	8	1.0
0	2	0	8.89	9.950	2	36.8	0	3	3	24.04	3.702	4	4.0	5	6	1	35.79	2.509	8	0.5
1	1	1	9.11	9.711	8	25.4	2	5	0	24.06	3.698	4	1.8	8	0	0	35.88	2.503	2	2.6
2	1	0	9.89	8.943	4	4.7	1	3	3	24.45	3.640	8	39.7	0	8	0	36.11	2.487	2	1.9
2	0	1	11.04	8.016	4	1.0	5	2	1	24.87	3.579	8	1.2	3	0	5	36.16	2.484	4	1.9
2	1	1	11.90	7.436	8	2.8	3	2	3	25.63	3.475	8	3.0	0	3	5	36.19	2.482	4	2.1
1	2	1	11.93	7.417	8	10.4	2	3	3	25.66	3.472	8	0.6	2	5	4	36.20	2.481	8	1.0
2	2	0	12.54	7.057	4	5.4	4	3	2	25.97	3.430	8	13.6	3	6	3	36.34	2.472	8	0.6
0	0	2	13.23	6.692	2	6.8	5	1	2	26.32	3.386	8	1.3	4	7	0	36.34	2.472	4	0.9
1	0	2	13.95	6.346	4	17.4	1	5	2	26.43	3.372	8	1.6	8	1	1	36.81	2.442	8	0.9
1	1	2	14.65	6.046	8	8.6	0	0	4	26.64	3.346	2	1.2	8	2	0	37.04	2.427	4	1.0
3	0	1	14.83	5.973	4	10.9	6	0	0	26.71	3.337	2	2.7	2	8	0	37.25	2.414	4	0.5
0	3	1	14.91	5.943	4	4.1	4	0	3	26.77	3.330	4	5.9	7	0	3	37.35	2.408	4	2.7
3	1	1	15.49	5.720	8	0.8	0	6	0	26.88	3.316	2	2.9	5	3	4	37.56	2.394	8	0.8
1	3	1	15.55	5.697	8	10.0	1	0	4	27.02	3.300	4	9.6	3	5	4	37.62	2.391	8	2.3
2	0	2	15.93	5.563	4	6.2	1	1	4	27.40	3.256	8	0.7	6	5	2	37.66	2.389	8	2.1
0	2	2	15.96	5.553	4	5.6	6	0	1	27.55	3.238	4	0.7	1	7	3	37.79	2.380	8	1.6
2	3	0	16.03	5.529	4	3.5	3	3	3	27.55	3.237	8	1.6	8	0	2	38.40	2.344	4	0.9
2	1	2	16.55	5.358	8	1.8	2	5	2	27.56	3.237	8	2.1	4	7	2	38.84	2.319	8	1.6
1	2	2	16.57	5.351	8	1.5	1	6	1	28.07	3.178	8	0.7	0	0	6	40.44	2.230	2	0.6
3	2	1	17.32	5.121	8	3.5	2	0	4	28.12	3.173	4	1.3	4	8	1	41.08	2.197	8	1.3
2	3	1	17.35	5.110	8	0.5	4	2	3	28.26	3.158	8	0.7	3	5	5	42.91	2.107	8	0.6
4	0	0	17.72	5.005	2	2.6	1	2	4	28.50	3.132	8	2.4	3	1	6	43.00	2.104	8	0.8
0	4	0	17.83	4.975	2	5.6	4	5	0	28.66	3.115	4	0.9	6	0	5	43.33	2.088	4	0.5
3	1	2	19.31	4.598	8	8.4	3	5	2	29.34	3.044	8	11.9	8	3	3	43.66	2.073	8	1.5
1	3	2	19.36	4.586	8	2.1	5	4	1	29.40	3.038	8	0.8	8	0	4	45.25	2.004	4	5.7
4	1	1	19.45	4.563	8	0.8	4	5	1	29.44	3.034	8	0.6	10	0	0	45.29	2.002	2	5.8
4	2	0	19.86	4.472	4	0.5	6	3	0	29.97	2.981	4	1.2	0	8	4	45.44	1.996	4	2.6
3	3	1	20.00	4.438	8	2.6	5	0	3	29.99	2.980	4	7.4	4	8	3	45.51	1.993	8	3.2
1	0	3	20.40	4.354	4	4.7	3	4	3	30.05	2.973	8	1.1	0	10	0	45.59	1.990	2	7.5
0	1	3	20.40	4.353	4	7.1	0	5	3	30.09	2.970	4	9.1	1	8	4	45.67	1.986	8	2.4
2	3	2	20.84	4.262	8	3.2	3	1	4	30.22	2.958	8	0.9	1	10	1	46.35	1.959	8	0.6
1	1	3	20.88	4.254	8	3.9	1	5	3	30.43	2.938	8	7.3	2	8	4	46.38	1.958	8	0.7
4	2	1	20.95	4.241	8	8.9	5	2	3	31.33	2.855	8	1.8	4	3	6	46.64	1.948	8	2.9
2	0	3	21.81	4.075	4	3.0	4	0	4	32.18	2.782	4	0.5	8	5	3	47.51	1.914	8	1.6
4	3	0	22.25	3.995	4	5.6	0	4	4	32.24	2.776	4	0.6	3	8	4	47.54	1.912	8	1.2
0	4	2	22.27	3.992	4	0.7	6	3	2	32.89	2.723	8	4.5	0	10	2	47.68	1.907	4	0.6
1	2	3	22.29	3.989	8	1.8	6	0	3	33.54	2.672	4	1.1	9	3	3	47.69	1.907	8	1.9
4	1	2	22.63	3.929	8	0.7	1	0	5	33.78	2.653	4	0.5	5	3	6	48.70	1.870	8	1.8
1	4	2	22.71	3.915	8	0.5	5	5	2	34.48	2.601	8	6.4	3	5	6	48.75	1.868	8	3.4
3	3	2	23.11	3.849	8	4.0	2	0	5	34.69	2.586	4	0.9	3	0	7	49.60	1.838	4	0.7
5	0	1	23.18	3.836	4	100.0	7	3	1	34.81	2.577	8	1.8	0	3	7	49.62	1.837	4	0.7
4	3	1	23.23	3.829	8	0.8	4	3	4	34.98	2.565	8	1.7	8	0	5	49.88	1.828	4	0.6

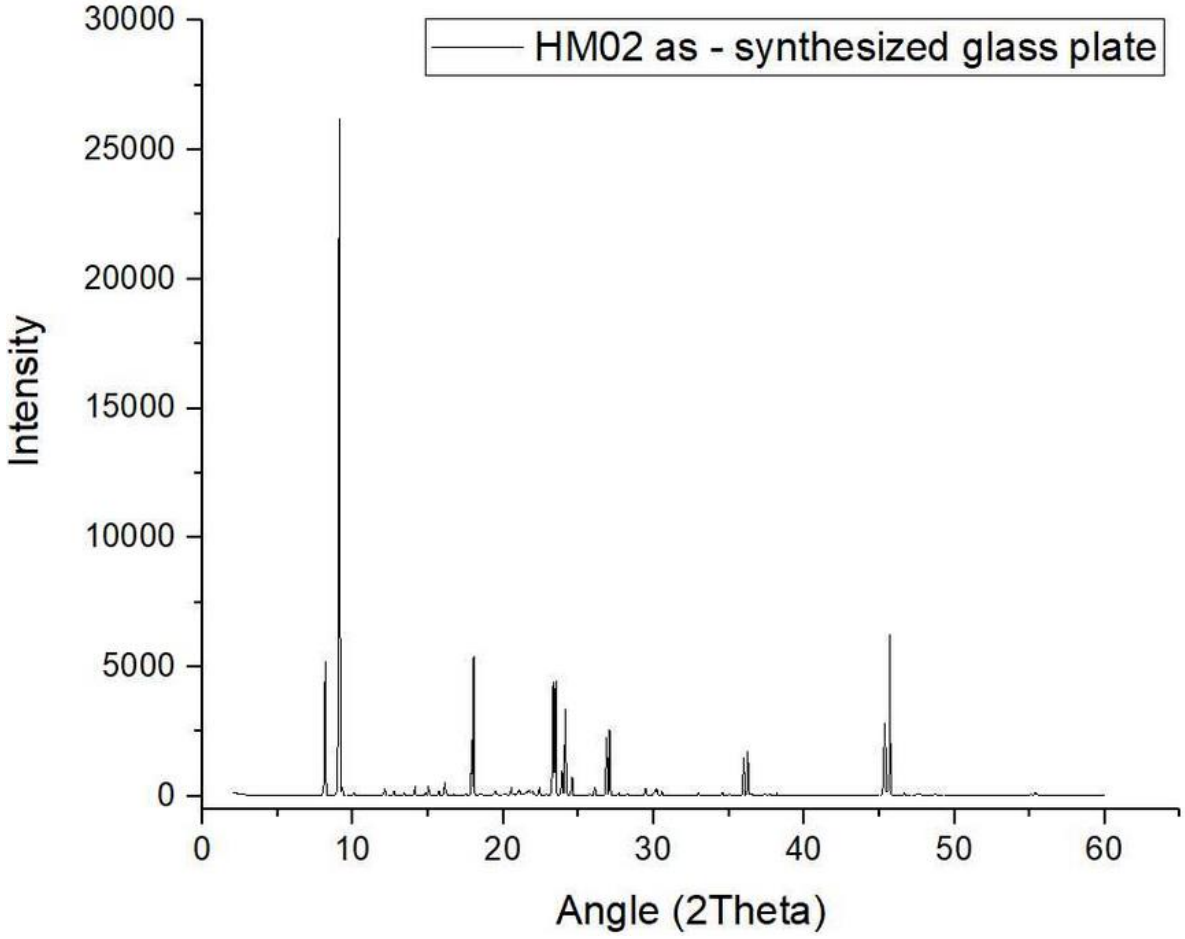

Figure 8-4: Full scale intensity of as - synthesized HM02 with preferred orientation measured on a glass plate.

Table 8-2: Peak list for HM02 as – synthesized glass plate XRD.

angle (° 2θ)	d value (Å)	Intensity (counts)	Rel. Int. (%)	angle (° 2θ)	d value (Å)	Intensity (counts)	Rel. Int. (%)	angle (° 2θ)	d value (Å)	Intensity (counts)	Rel. Int. (%)
8.15	10.843	3584.2	18.3	23.89	3.722	747.7	3.8	37.39	2.403	50.0	0.3
9.11	9.698	19584.3	100.0	24.12	3.687	2768.3	14.1	37.70	2.384	65.3	0.3
10.08	8.770	100.0	0.5	24.58	3.619	599.9	3.1	38.21	2.354	117.4	0.6
11.24	7.864	10.4	0.1	24.99	3.561	27.7	0.1	38.90	2.313	24.0	0.1
12.11	7.303	187.3	1.0	25.74	3.458	46.6	0.2	39.32	2.289	18.5	0.1
12.73	6.949	128.0	0.7	26.09	3.413	239.8	1.2	41.18	2.191	24.9	0.1
13.41	6.599	92.8	0.5	26.50	3.361	11.9	0.1	41.62	2.168	10.7	0.1
14.13	6.263	303.7	1.6	26.86	3.317	1980.1	10.1	42.97	2.103	20.3	0.1
14.81	5.975	89.7	0.5	27.06	3.293	2327.3	11.9	43.70	2.070	25.9	0.1
15.01	5.896	255.5	1.3	27.68	3.221	71.3	0.4	45.36	1.998	2450.5	12.5
15.72	5.631	145.2	0.7	28.24	3.158	49.3	0.3	45.70	1.984	5613.4	28.7
16.10	5.501	374.6	1.9	28.59	3.120	36.3	0.2	46.65	1.946	130.7	0.7
16.70	5.306	36.3	0.2	29.46	3.030	248.1	1.3	47.60	1.909	50.3	0.3
17.48	5.068	43.9	0.2	30.10	2.967	170.1	0.9	48.74	1.867	73.9	0.4
17.90	4.951	1785.9	9.1	30.53	2.925	151.5	0.8	49.60	1.836	32.6	0.2
18.03	4.915	4794.1	24.5	31.38	2.848	23.3	0.1	52.19	1.751	31.3	0.2
18.51	4.789	50.2	0.3	32.30	2.770	32.3	0.2	52.55	1.740	20.7	0.1
19.45	4.560	115.6	0.3	32.98	2.714	66.7	0.3	53.54	1.710	28.4	0.1
20.10	4.413	40.5	0.6	33.62	2.664	19.9	0.1	53.97	1.698	16.4	0.1
20.54	4.321	217.1	0.2	34.56	2.593	116.7	0.6	55.15	1.664	36.2	0.2
21.05	4.216	104.9	1.1	34.87	2.571	13.0	0.1	55.38	1.658	152.5	0.8
21.71	4.089	116.3	0.5	35.05	2.558	36.6	0.2	56.85	1.618	33.3	0.2
21.93	4.049	104.0	0.6	35.98	2.494	1357.5	6.9	57.26	1.608	13.5	0.1
22.40	3.966	201.5	0.5	36.26	2.476	1498.5	7.7	59.10	1.562	31.0	0.2
22.84	3.891	11.8	1.0	36.43	2.464	297.5	1.5				

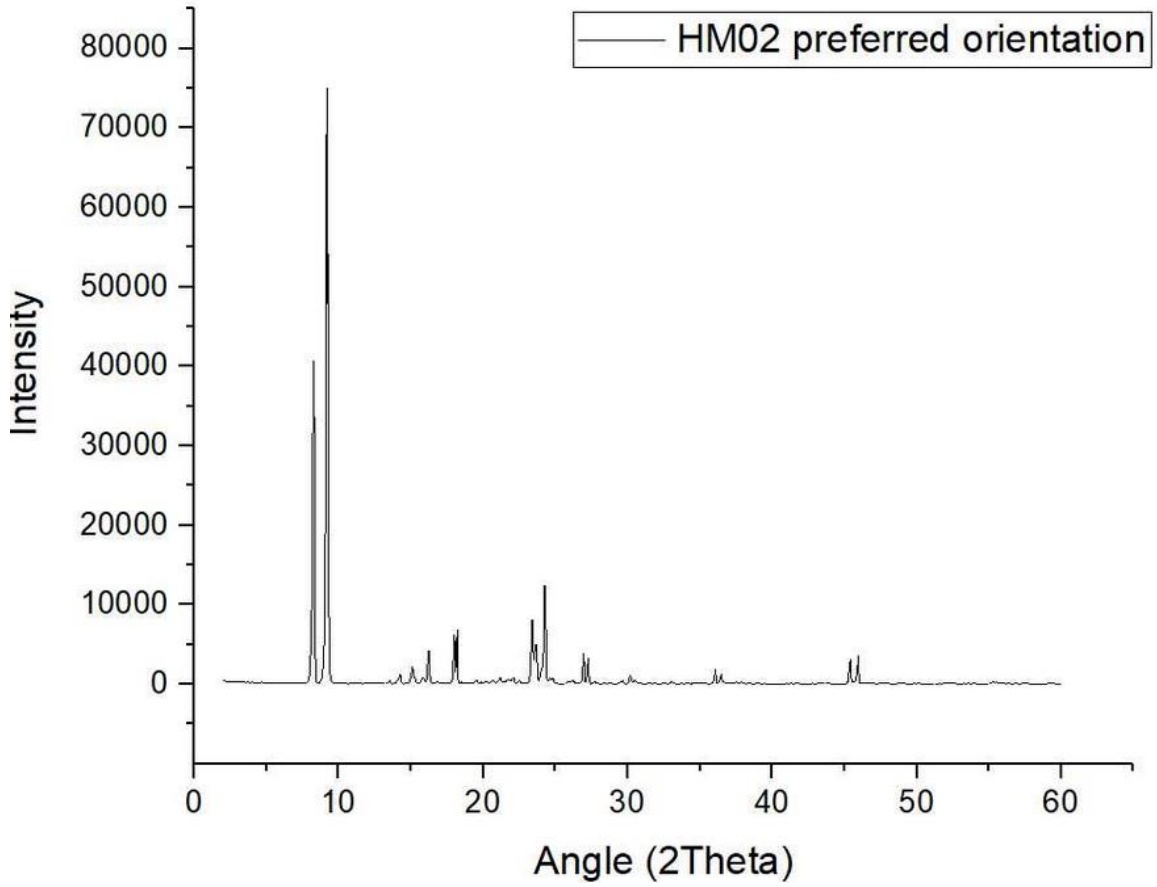

Figure 8-5: Full scale intensity of protonic HM02 with preferred orientation measured on a glass plate.

Table 8-3: Peak list for HM02 protonic glass plate XRD with preferred orientation.

angle (° 2θ)	d value (Å)	Intensity (counts)	Rel. int. (%)	angle (° 2θ)	d value (Å)	Intensity (counts)	Rel. int. (%)	angle (° 2θ)	d value (Å)	Intensity (counts)	Rel. int. (%)
8.26	10.691	26826.1	52.3	26.96	3.305	2772.4	5.4	46.77	1.941	82.6	0.2
9.18	9.624	51260.6	100.0	27.26	3.269	2312.1	4.5	47.74	1.904	100.6	0.2
10.17	8.690	76.7	0.1	27.73	3.215	165.0	0.3	48.78	1.865	135.0	0.3
12.21	7.245	38.8	0.1	28.42	3.138	67.2	0.1	49.11	1.854	81.5	0.2
12.84	6.889	26.7	0.1	28.70	3.108	61.4	0.1	49.86	1.828	39.1	0.1
13.53	6.538	312.0	0.6	29.59	3.017	159.2	0.3	50.20	1.816	51.2	0.1
14.25	6.210	840.0	1.6	30.20	2.957	693.7	1.4	52.04	1.756	56.9	0.1
15.10	5.861	1414.0	2.8	30.49	2.930	294.8	0.6	52.58	1.739	72.7	0.1
15.84	5.592	508.7	1.0	30.84	2.897	70.3	0.1	53.96	1.698	24.3	0.0
16.24	5.455	2693.7	5.3	31.52	2.836	92.7	0.2	55.28	1.660	189.7	0.4
16.85	5.256	104.8	0.2	32.46	2.756	71.8	0.1	55.51	1.654	108.0	0.2
17.57	5.043	63.5	0.1	33.04	2.709	151.0	0.3	55.98	1.641	26.6	0.1
18.02	4.920	4225.4	8.2	33.71	2.657	71.6	0.1	56.85	1.618	95.5	0.2
18.21	4.867	4686.5	9.1	34.04	2.632	31.7	0.1	57.61	1.599	50.6	0.1
18.50	4.791	72.3	0.1	34.65	2.587	74.9	0.1	58.65	1.573	23.0	0.0
19.16	4.628	29.9	0.1	34.94	2.566	92.1	0.2	59.30	1.557	31.9	0.1
19.55	4.537	203.5	0.4	35.39	2.535	50.2	0.1	60.50	1.529	19.1	0.0
20.23	4.385	70.4	0.1	36.06	2.489	1424.2	2.8	61.28	1.512	63.8	0.1
20.68	4.291	294.7	0.6	36.47	2.462	904.2	1.8	61.89	1.498	21.7	0.0
21.16	4.195	436.8	0.9	37.50	2.397	111.1	0.2	62.40	1.487	67.1	0.1
21.75	4.083	310.6	0.6	37.87	2.374	99.1	0.2	62.79	1.479	76.8	0.1
22.09	4.020	430.1	0.8	38.54	2.334	28.5	0.1	63.46	1.465	50.0	0.1
22.48	3.952	240.4	0.5	38.99	2.308	27.7	0.1	63.88	1.456	327.5	0.6
23.39	3.800	5923.5	11.6	38.89	2.314	29.8	0.1	64.69	1.440	180.8	0.4
23.64	3.761	3079.8	6.0	39.47	2.281	16.4	0.0	64.99	1.434	75.7	0.1
24.25	3.667	9498.2	18.5	41.31	2.184	49.6	0.1	65.33	1.427	67.6	0.1
24.72	3.598	253.8	0.5	41.72	2.163	38.4	0.1	65.64	1.421	80.1	0.2
25.06	3.550	73.9	0.1	41.97	2.151	25.0	0.0	66.06	1.413	81.0	0.2
25.84	3.445	116.5	0.2	42.78	2.112	23.7	0.0	66.46	1.406	112.9	0.2
26.18	3.401	221.3	0.4	45.41	1.996	2590.2	5.1	67.45	1.387	212.5	0.4
26.53	3.358	59.0	0.1	45.95	1.974	2852.3	5.6	69.16	1.357	49.8	0.1

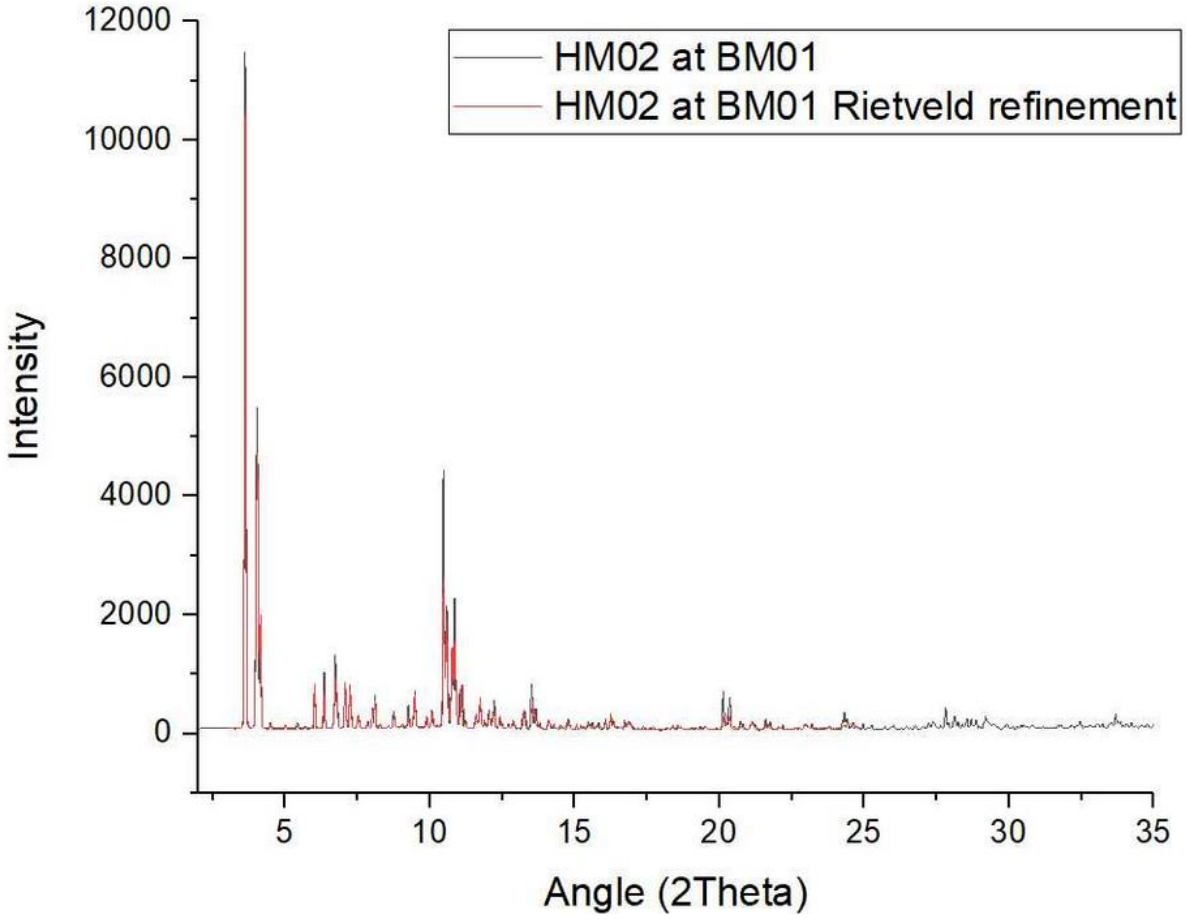

Figure 8-6: PXRD pattern of protonic HM02 from BM01 in Grenoble with a Rietveld refinement.

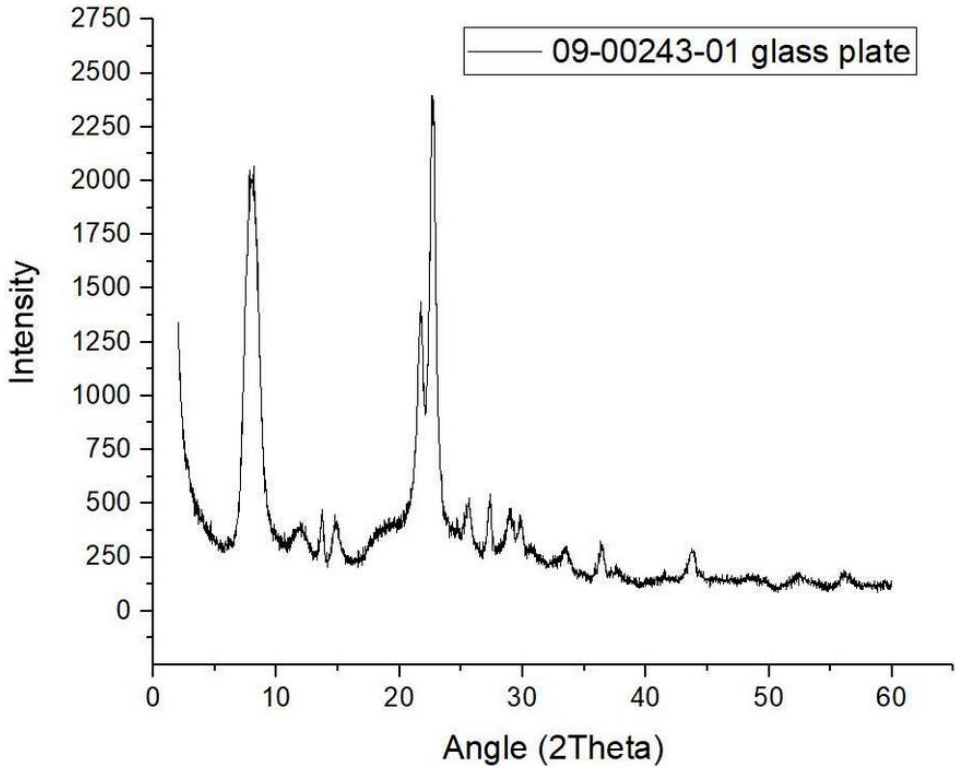

Figure 8-7: XRD diffractogram of protonic Beta zeolite 09-00243-1 measured on a glass plate.

Table 8-4: Peak list for protonic 09-00243-1 glass plate XRD.

angle (° 2θ)	d value (Å)	Intensity (counts)	Rel. int. (%)	angle (° 2θ)	d value (Å)	Intensity (counts)	Rel. int. (%)
7.81	11.314	996.8	72.7	25.57	3.480	135.1	9.9
8.00	11.050	1115.6	81.4	27.31	3.263	154.0	11.2
13.70	6.460	140.9	10.3	28.94	3.082	131.9	9.6
15.00	5.903	102.5	7.5	29.83	2.993	127.4	9.3
14.80	5.980	137.4	10.0	33.51	2.672	78.0	5.7
20.80	4.267	72.5	5.3	36.49	2.460	106.8	7.8
21.73	4.087	706.2	51.5	43.28	2.089	26.7	1.9
22.70	3.914	1371.3	100.0	43.77	2.066	81.4	5.9

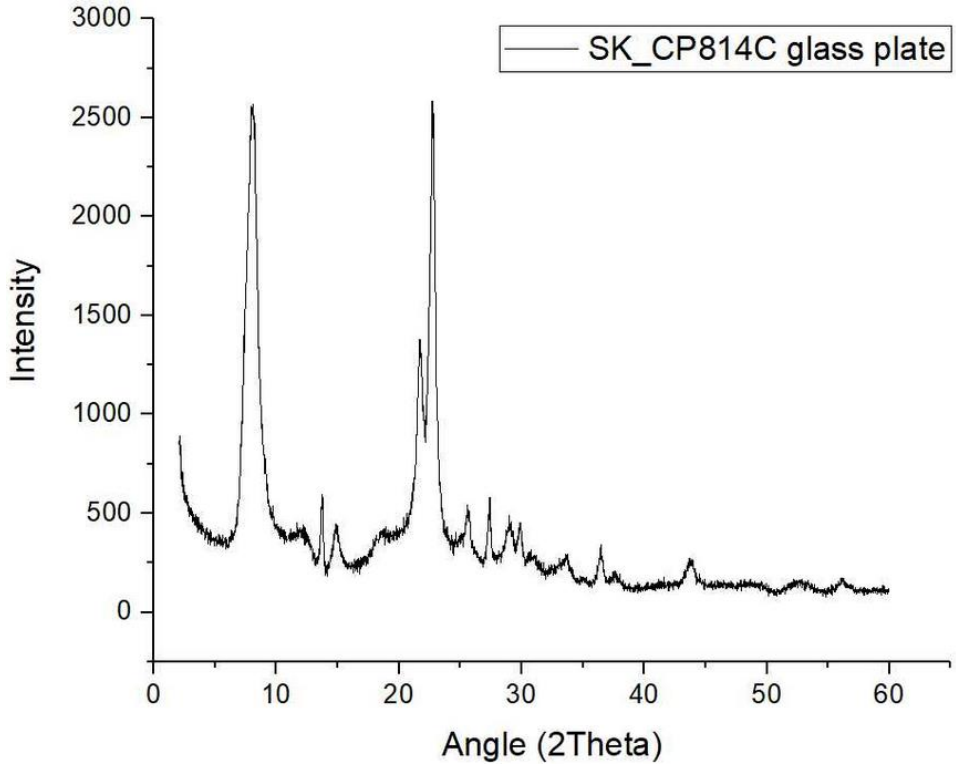

Figure 8-8: XRD diffractogram of protonic Beta zeolite SK_CP814C measured on a glass plate.

Table 8-5: Peak list for protonic SK_CP814C glass plate XRD.

angle (° 2θ)	d value (Å)	Intensity (counts)	Rel. int. (%)	angle (° 2θ)	d value (Å)	Intensity (counts)	Rel. int. (%)
8.00	11.048	1459.0	95.3	29.04	3.072	123.7	8.1
13.72	6.449	224.9	14.7	29.88	2.988	116.6	7.6
14.93	5.929	138.8	9.1	33.65	2.662	68.6	4.5
21.71	4.091	660.4	43.1	36.45	2.463	150.8	9.9
22.75	3.905	1530.5	100.0	37.72	2.383	40.1	2.6
25.61	3.476	165.5	10.8	43.77	2.067	69.8	4.6
27.40	3.253	212.9	13.9	51.74	1.765	29.4	1.9

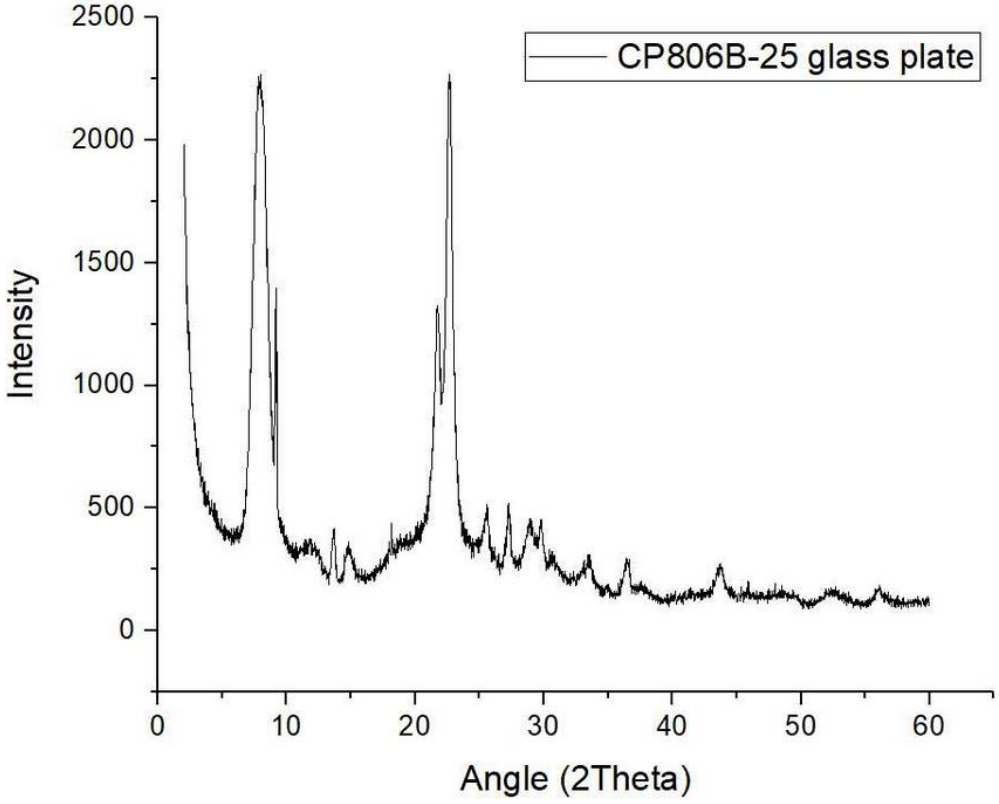

Figure 8-9: XRD diffractogram of protonic Beta zeolite CP806B-25 measured on a glass plate.

Table 8-6: Peak list for protonic CP806B-25 glass plate XRD.

angle (° 2θ)	d value (Å)	Intensity (counts)	Rel. int. (%)	angle (° 2θ)	d value (Å)	Intensity (counts)	Rel. int. (%)
7.92	11.155	1241.6	96.8	27.23	3.272	182.8	14.3
9.14	9.665	609.3	47.5	28.88	3.089	134.2	10.5
11.81	7.486	76.2	5.9	29.05	3.071	112.1	8.7
13.65	6.484	120.7	9.4	29.79	2.996	134.0	10.4
14.85	5.961	102.6	8.0	33.55	2.669	106.7	8.3
21.74	4.085	668.6	52.1	36.51	2.459	68.6	5.3
22.66	3.922	1282.5	100.0	43.76	2.067	81.1	6.3
25.57	3.481	159.9	12.5	45.90	1.976	70.8	5.5

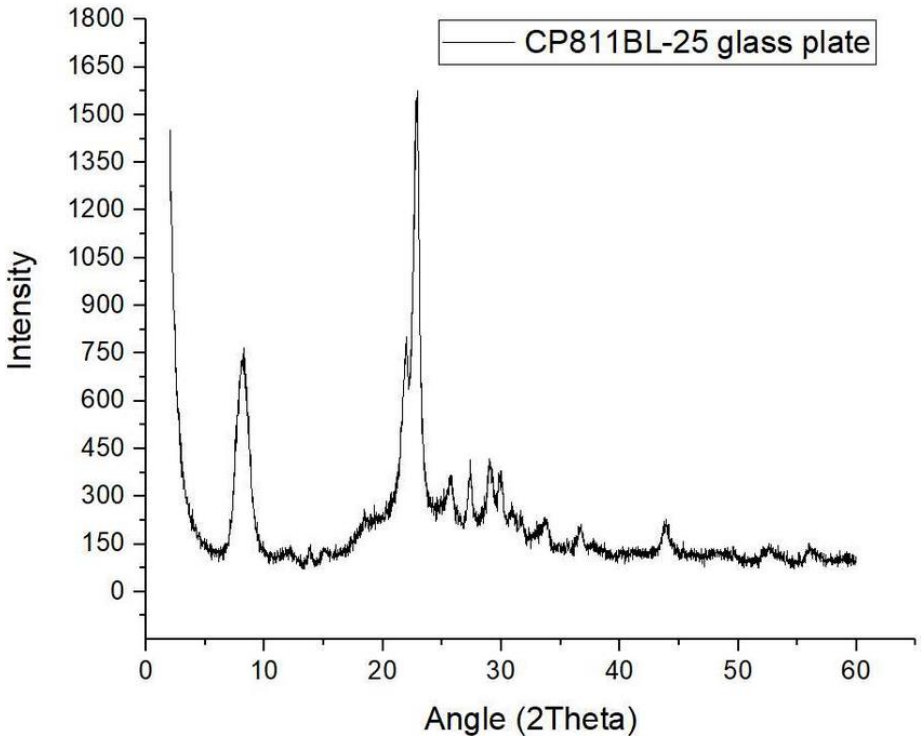

Figure 8-10: XRD diffractogram of protonic Beta zeolite CP811BL-25 measured on a glass plate.

Table 8-7: Peak list for protonic CP811BL-25 glass plate XRD.

angle (° 2θ)	d value (Å)	Intensity (counts)	Rel. int. (%)	angle (° 2θ)	d value (Å)	Intensity (counts)	Rel. int. (%)
7.54	11.709	210.9	26.1	27.37	3.256	119.6	14.8
8.21	10.762	410.8	50.9	29.07	3.070	108.6	13.4
7.90	11.178	332.3	41.1	29.16	3.060	78.5	9.7
8.16	10.825	427.0	52.9	29.93	2.983	117.9	14.6
13.82	6.403	35.5	4.4	30.88	2.894	39.4	4.9
21.99	4.039	364.7	45.2	33.66	2.661	60.7	7.5
22.84	3.890	807.6	100.0	36.70	2.447	56.2	7.0
25.71	3.462	69.5	8.6	43.90	2.061	79.7	9.9

8.3 Thermogravimetric analysis

This section shows additional data from TGA analysis for this work.

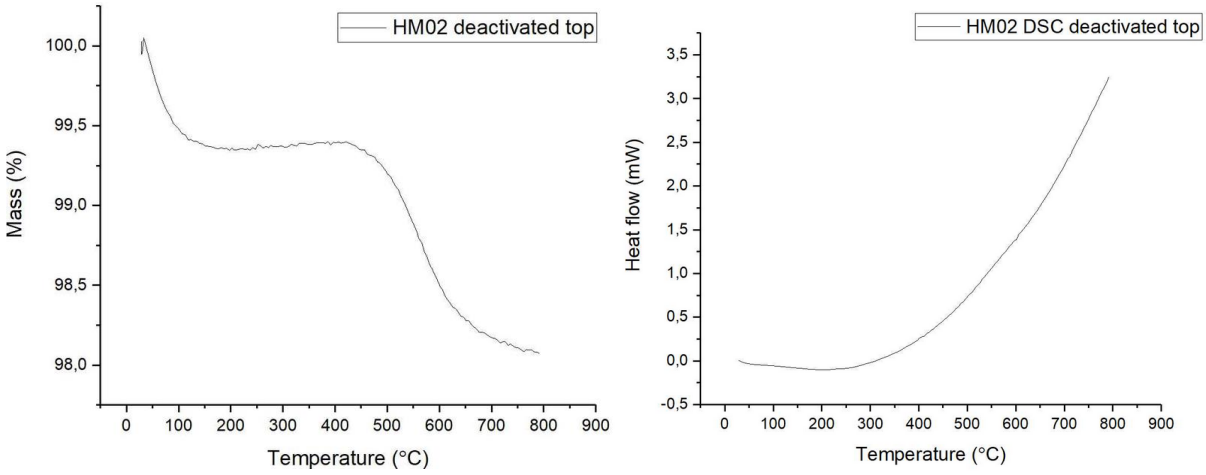

Figure 8-11: TGA HM02 for deactivated top and the correspond DSC profile for the analysis. The material is heated from room temperature to 800°C, with an atmosphere of 20% oxygen and 80% nitrogen.

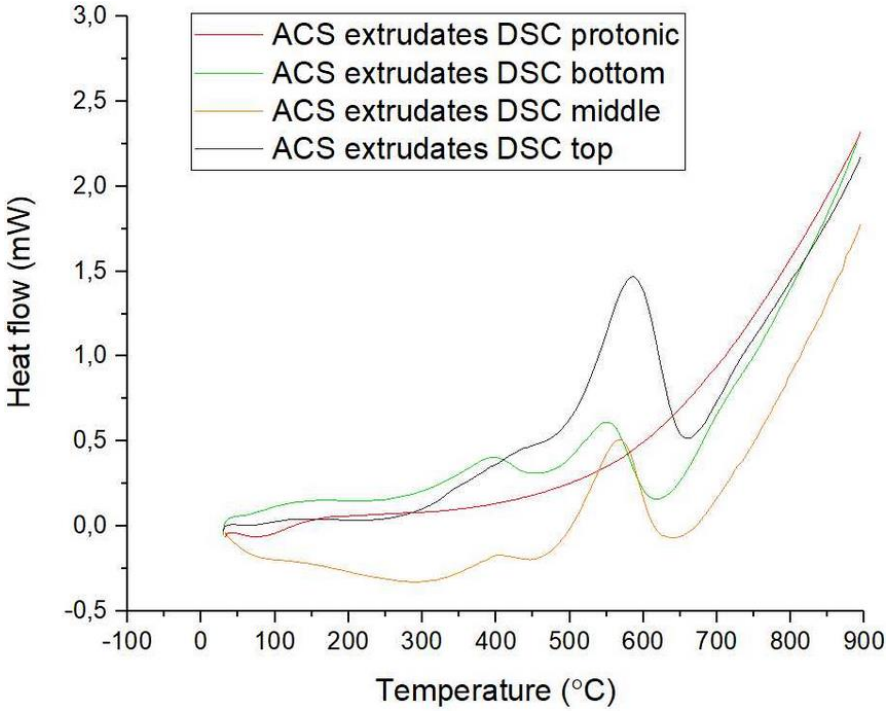

Figure 8-12: The corresponding DSC profile for the TGA analysis for the protonic form ACS extrudates and the top, middle and bottom layer of the material, from the reactor used for MTH conversion. The material is heated from room temperature to 900°C, with an atmosphere of 60% oxygen and 40% nitrogen.

8.4 Scanning electron microscopy

This section includes additional SEM images of the HM03 material from this work.

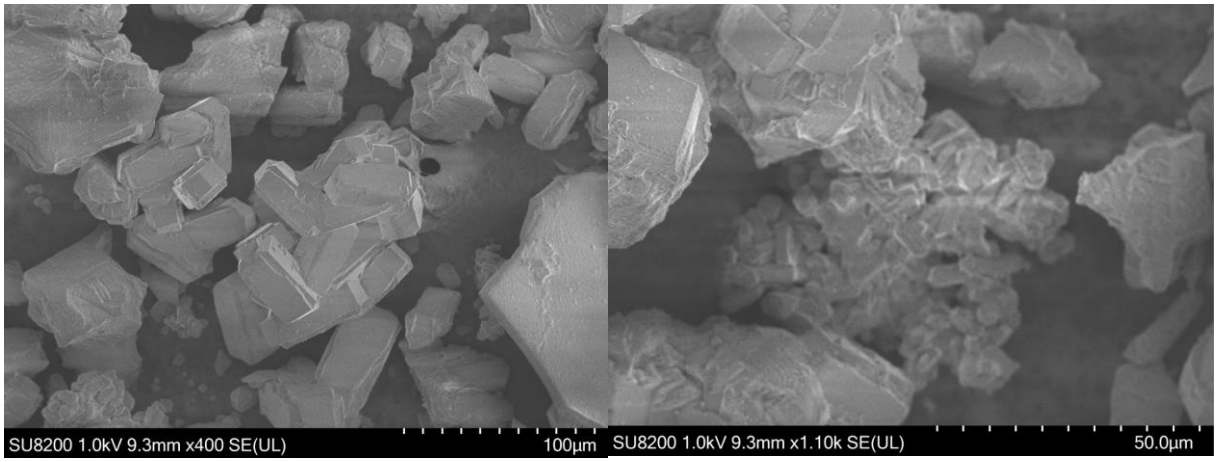

Figure 8-13: Two additional SEM images of HM03 with 1.1k and 400 magnification, using a SE detector.

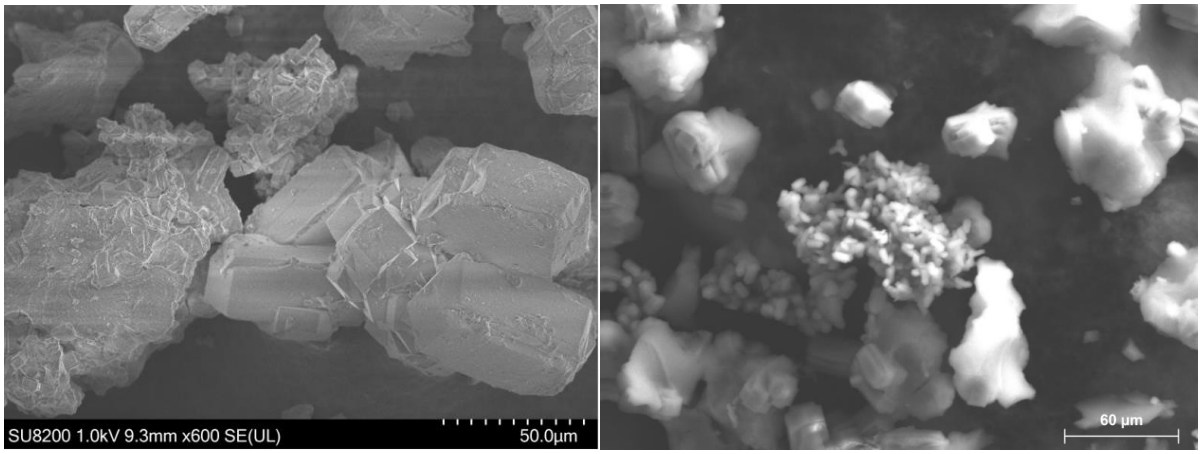

Figure 8-14: Two additional SEM pictures of HM03 where the image on the left has a magnification of 600, using a SE detector.

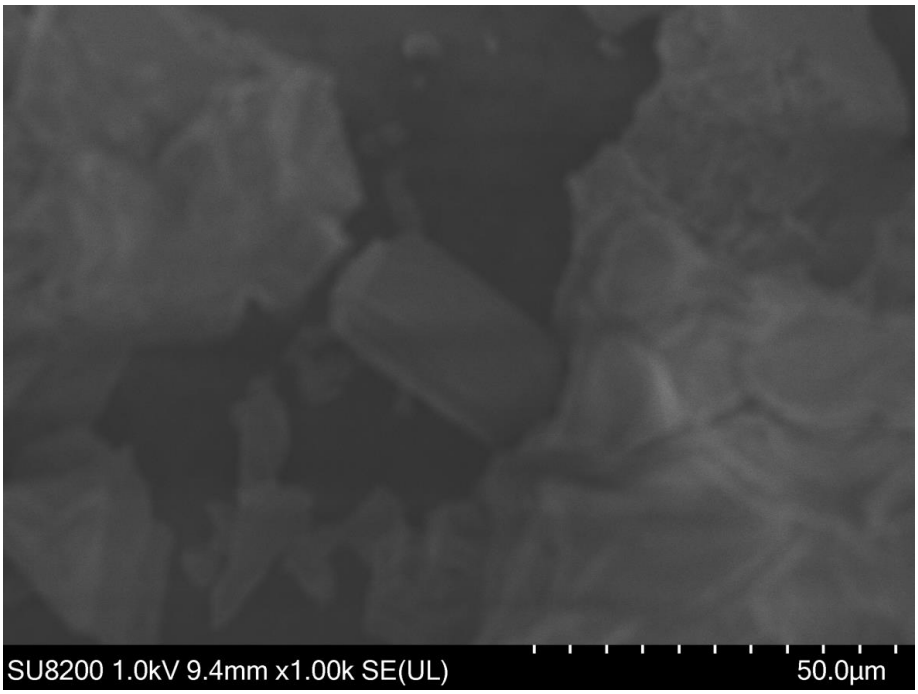

Figure 8-15: Another SEM image of HM03 with 1k magnification, using a SE detector.

8.5 Energy dispersed x - ray analysis

Attached scan reports for HM02 and HM03.

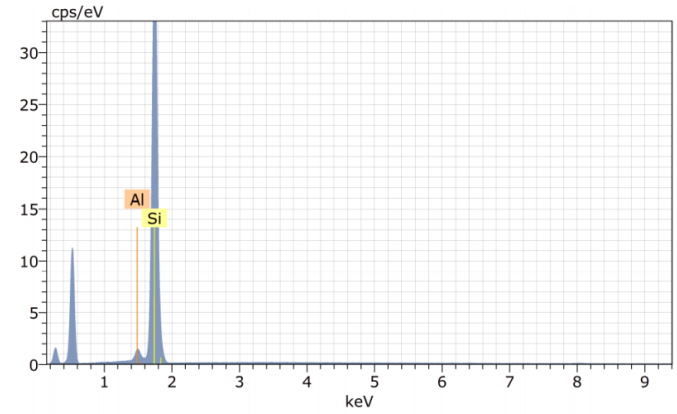

Spectrum: KFG SELVLAGD NR2 TOT 1

El	AN	Series	unn. C [wt.%]	norm. C [wt.%]	Atom. C [at.%]	Error (1 Sigma) [wt.%]
Si	14	K-series	38.02	96.89	96.77	1.72
Al	13	K-series	1.22	3.11	3.23	0.09
		Total:	39.24	100.00	100.00	

Figure 8-16: The first scan of the EDX analysis for an area of HM02, where EL is element, AN is atomic number, Series is characteristic x - ray lines, unn. C [wt. %] is the unnormalized concentration in weight percent of the element, norm. C [wt. %] is the normalized concentration in weight percent of the element, C Atom. [at. %] is the atomic weight percent, C Error (1 Sigma) [wt. %] is error in the weight percent concentration at the 1 sigma level.

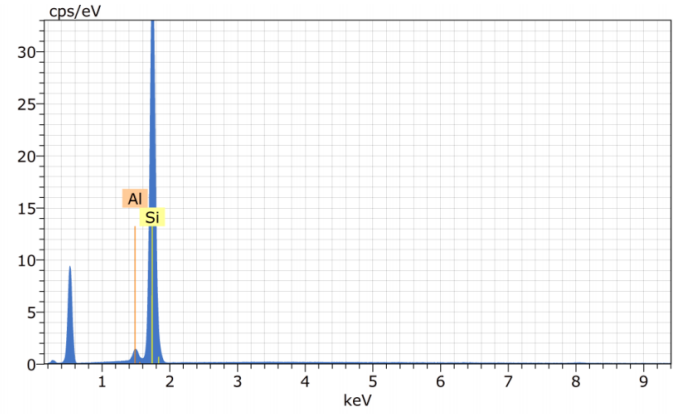

Spectrum: KFG SELVLAGD NR2 TOT 2

El	AN	Series	unn. C [wt.%]	norm. C [wt.%]	Atom. C [at.%]	Error (1 Sigma) [wt.%]
Si	14	K-series	41.52	96.55	96.41	1.87
Al	13	K-series	1.48	3.45	3.59	0.10
		Total:	43.01	100.00	100.00	

Figure 8-17: Second scan of the EDX analysis for an area of HM02, where EL is element, AN is atomic number, Series is characteristic x - ray lines, unn. C [wt. %] is the unnormalized concentration in weight percent of the element, norm. C [wt. %] is the normalized concentration in weight percent of the element, C Atom. [at. %] is the atomic weight percent, C Error (1 Sigma) [wt. %] is error in the weight percent concentration at the 1 sigma level.

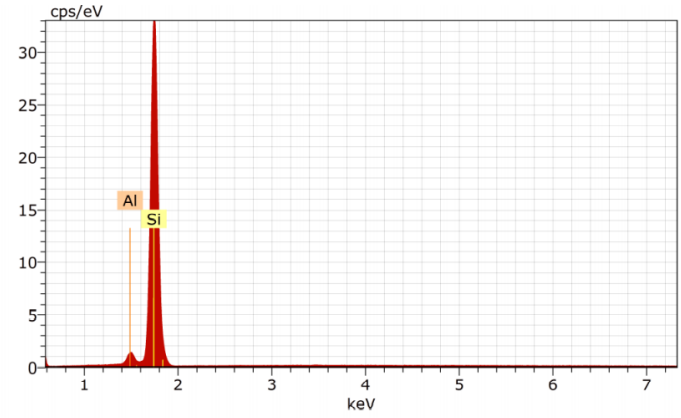

Spectrum: KFG SELVLAGD NR2 TOT 3

El AN	Series	unn. C [wt.%]	norm. C [wt.%]	Atom. C [at.%]	Error (1 Sigma) [wt.%]
Si 14	K-series	41.56	96.28	96.14	1.87
Al 13	K-series	1.60	3.72	3.86	0.11
	Total:	43.16	100.00	100.00	

Figure 8-18: Third scan of the EDX analysis for an area of HM02, where EL is element, AN is atomic number, Series is characteristic x - ray lines, unn. C [wt. %] is the unnormalized concentration in weight percent of the element, norm. C [wt. %] is the normalized concentration in weight percent of the element, C Atom. [at. %] is the atomic weight percent, C Error (1 Sigma) [wt. %] is error in the weight percent concentration at the 1 sigma level.

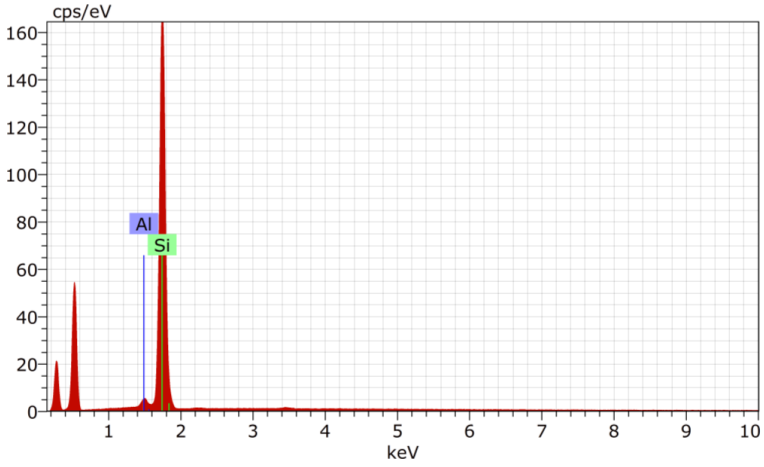

Spectrum: KFG Selvlagd nr3 3

El AN	Series	unn. C [wt.%]	norm. C [wt.%]	Atom. C [at.%]	Error (1 Sigma) [wt.%]
Si 14	K-series	31.69	97.65	97.55	1.43
Al 13	K-series	0.76	2.35	2.45	0.07
	Total:	32.45	100.00	100.00	

Figure 8-19: The first scan of the EDX analysis for an area of HM03, where EL is element, AN is atomic number, Series is characteristic x - ray lines, unn. C [wt. %] is the unnormalized concentration in weight percent of the element, norm. C [wt. %] is the normalized concentration in weight percent of the element, C Atom. [at. %] is the atomic weight percent, C Error (1 Sigma) [wt. %] is error in the weight percent concentration at the 1 sigma level.

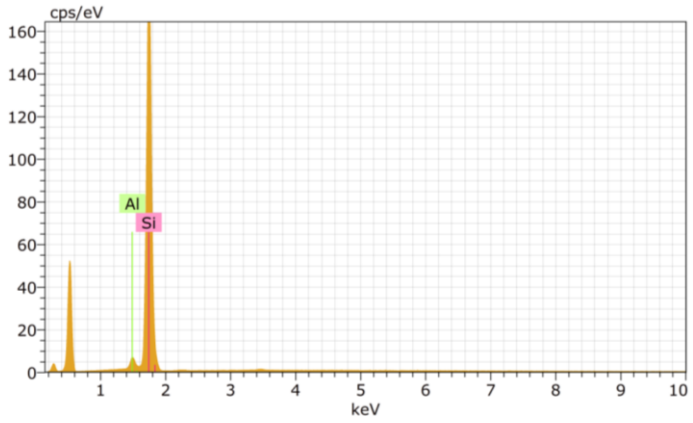

Spectrum: KFG Selvlagd nr3 2

El AN	Series	unn. C [wt.%]	norm. C [wt.%]	Atom. C [at.%]	Error (1 Sigma) [wt.%]
Si 14	K-series	42.51	96.94	96.82	1.91
Al 13	K-series	1.34	3.06	3.18	0.09
	Total:	43.85	100.00	100.00	

Figure 8-20: Second scan of the EDX analysis for an area of HM03, where EL is element, AN is atomic number, Series is characteristic x - ray lines, unn. C [wt. %] is the unnormalized concentration in weight percent of the element, norm. C [wt. %] is the normalized concentration in weight percent of the element, C Atom. [at. %] is the atomic weight percent, C Error (1 Sigma) [wt. %] is error in the weight percent concentration at the 1 sigma level.

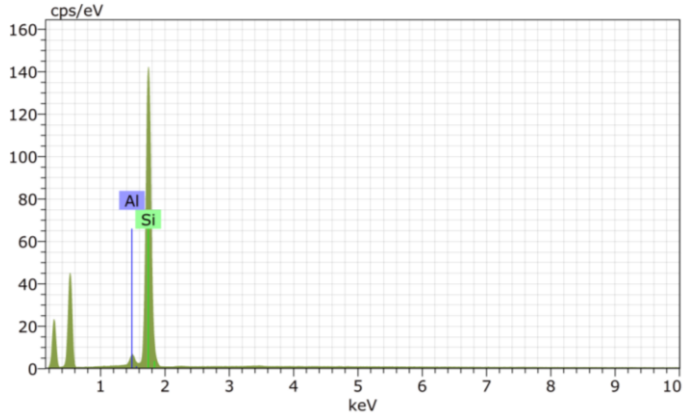

Spectrum: KFG Selvlagd nr3 1

El AN	Series	unn. C [wt.%]	norm. C [wt.%]	Atom. C [at.%]	Error (1 Sigma) [wt.%]
Si 14	K-series	35.34	96.23	96.09	1.60
Al 13	K-series	1.38	3.77	3.91	0.10
	Total:	36.72	100.00	100.00	

Figure 8-21: Third scan of the EDX analysis for an area of HM03, where EL is element, AN is atomic number, Series is characteristic x - ray lines, unn. C [wt. %] is the unnormalized concentration in weight percent of the element, norm. C [wt. %] is the normalized concentration in weight percent of the element, C Atom. [at. %] is the atomic weight percent, C Error (1 Sigma) [wt. %] is error in the weight percent concentration at the 1 sigma level.

8.6 N_2 adsorption

This section includes the t – plot and BET method for HM02 and HM03, as well as the BET method for the ACS extrudates.

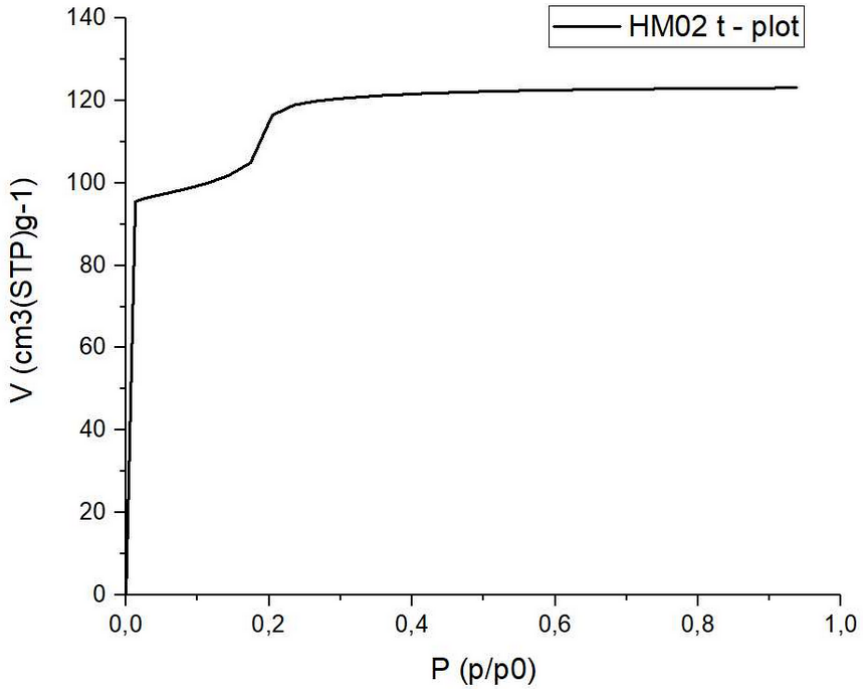

Figure 8-22: Plot for the t – method for HM02.

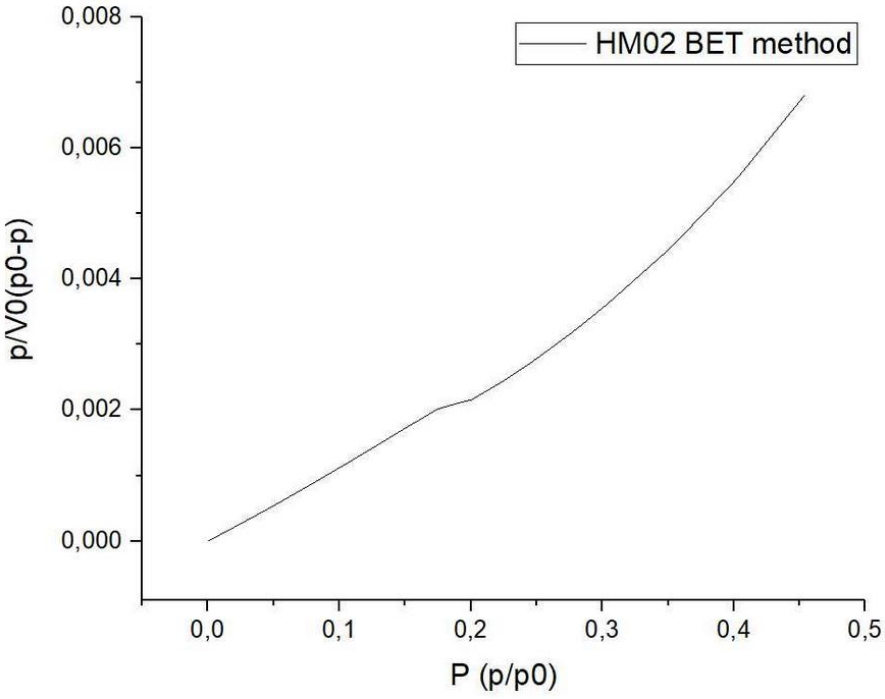

Figure 8-23: Plot of the BET method from N_2 adsorption for HM02.

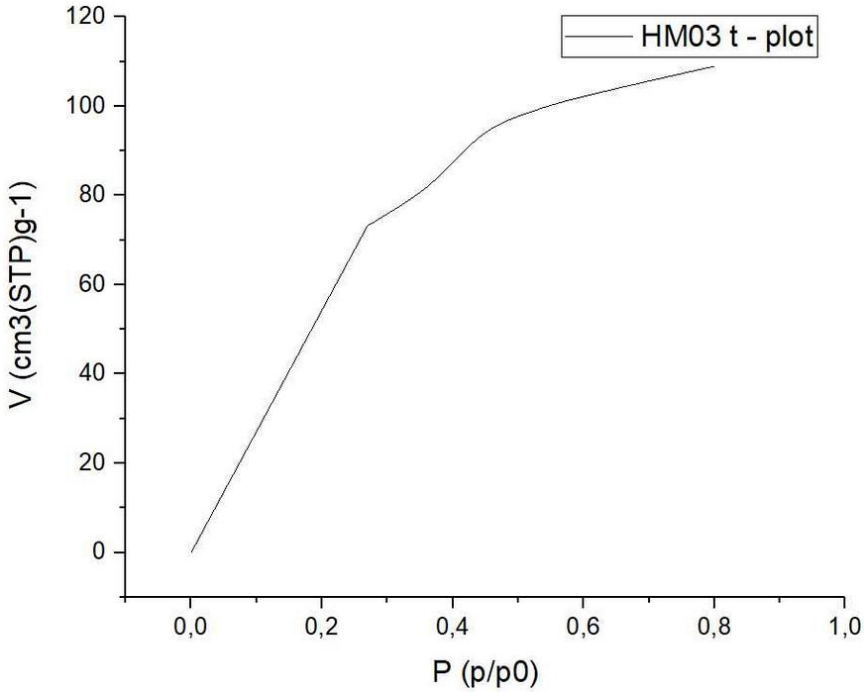

Figure 8-24: Plot of the t – method for HM03.

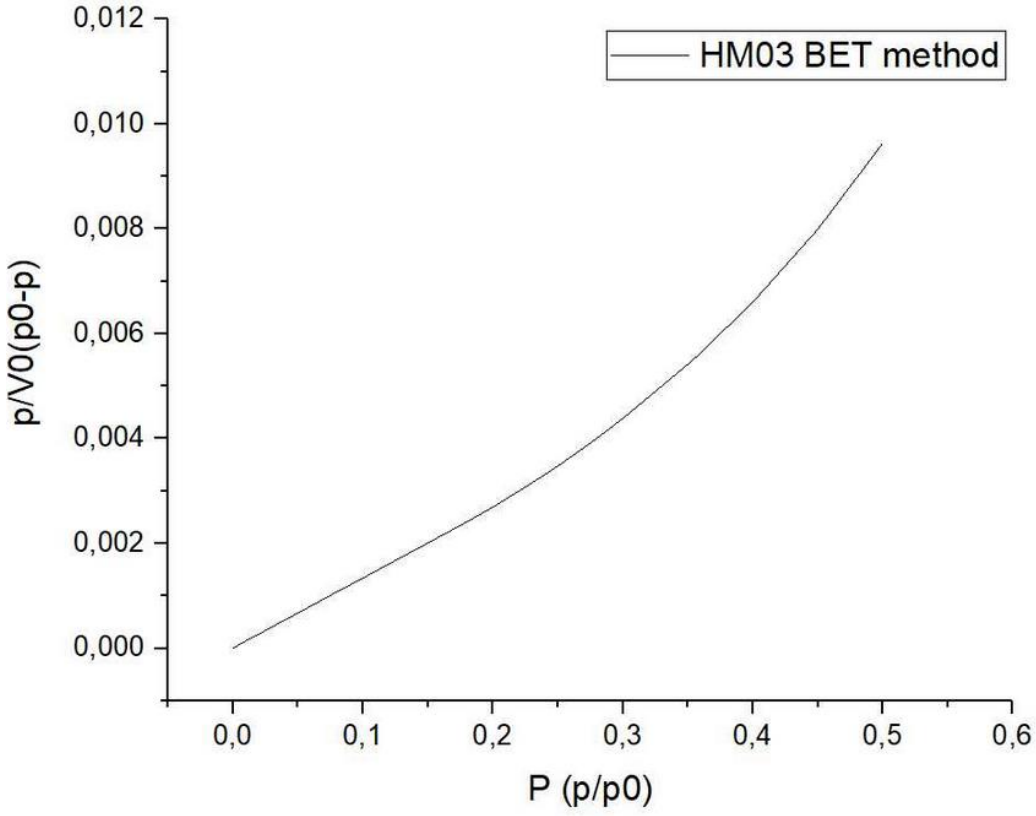

Figure 8-25: Plot of the BET method from N_2 adsorption for HM03.

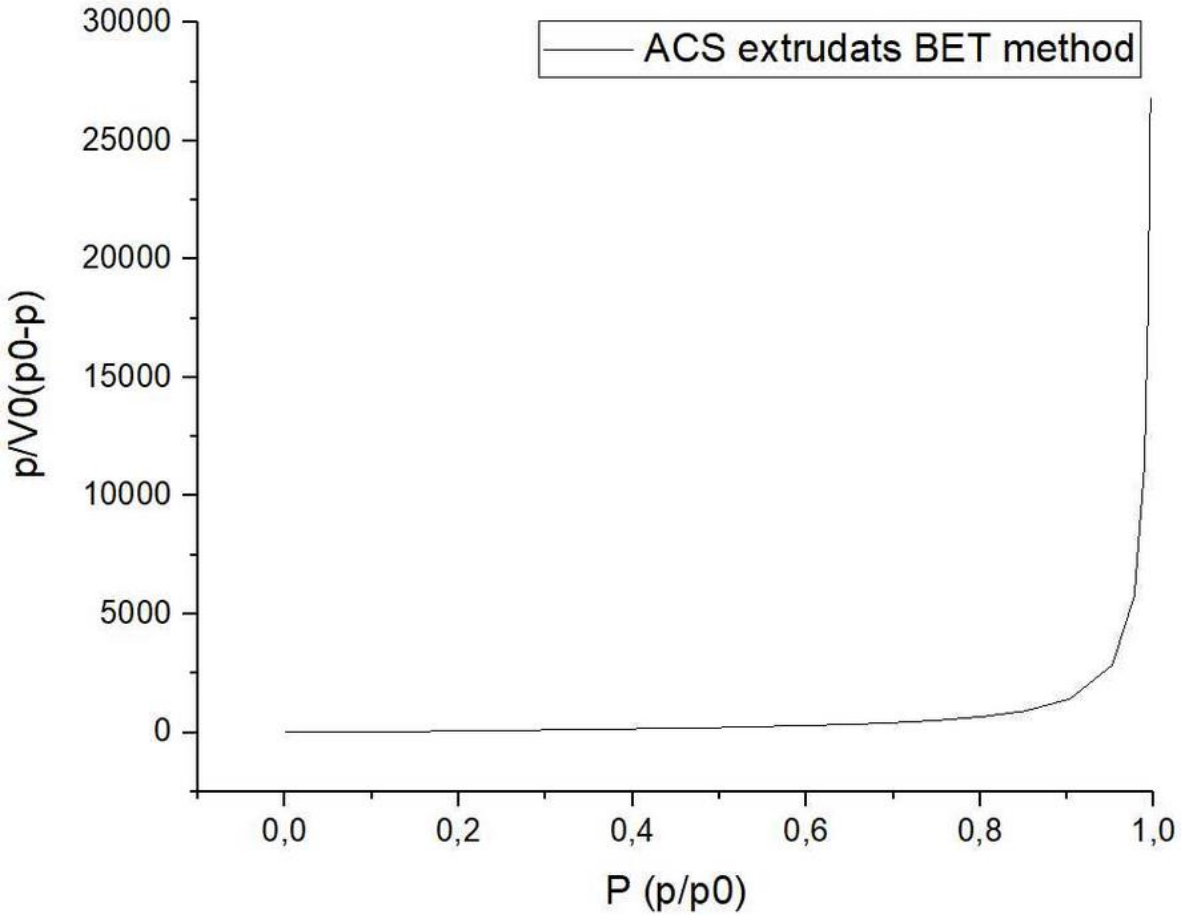

Figure 8-26: Plot of the BET method from N_2 adsorption for the ACS extrudates.

8.7 Acid – base titration

This section includes additional data for the acid – base titrations done in this work.

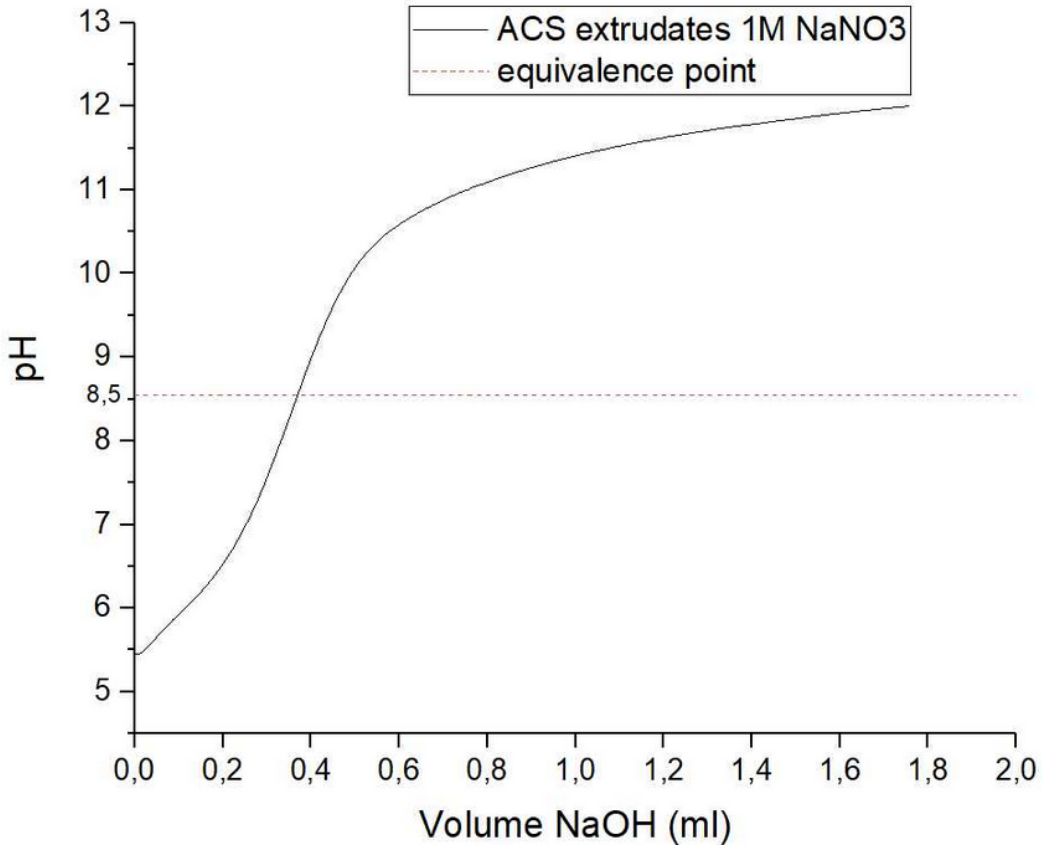

Figure 8-27: Titration curve for the ACS extrudates for acid - base titration.

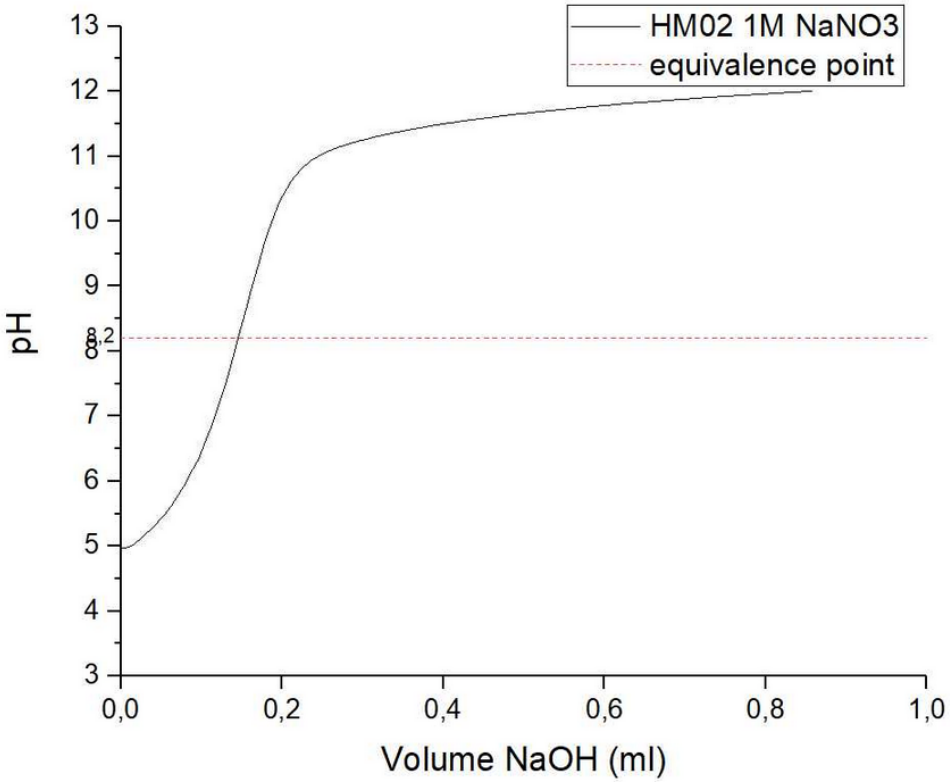

Figure 8-28: Titration curve of HM02 for acid - base titration.

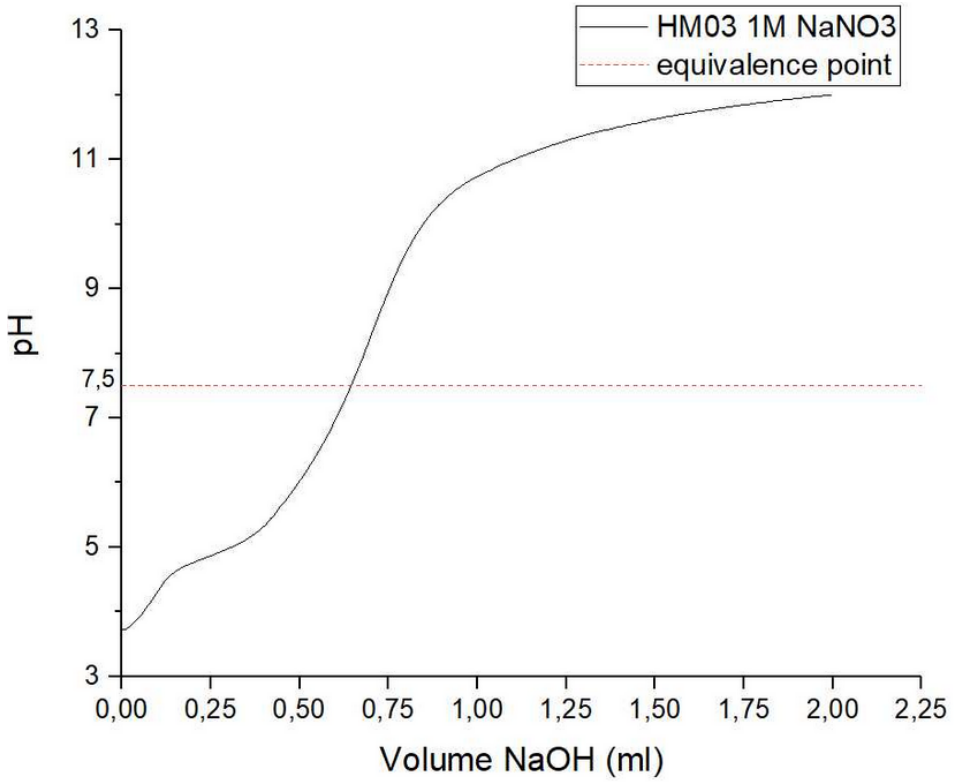

Figure 8-29: Titration curve of HM03 for acid – base titration.

8.7.1 Titration test samples

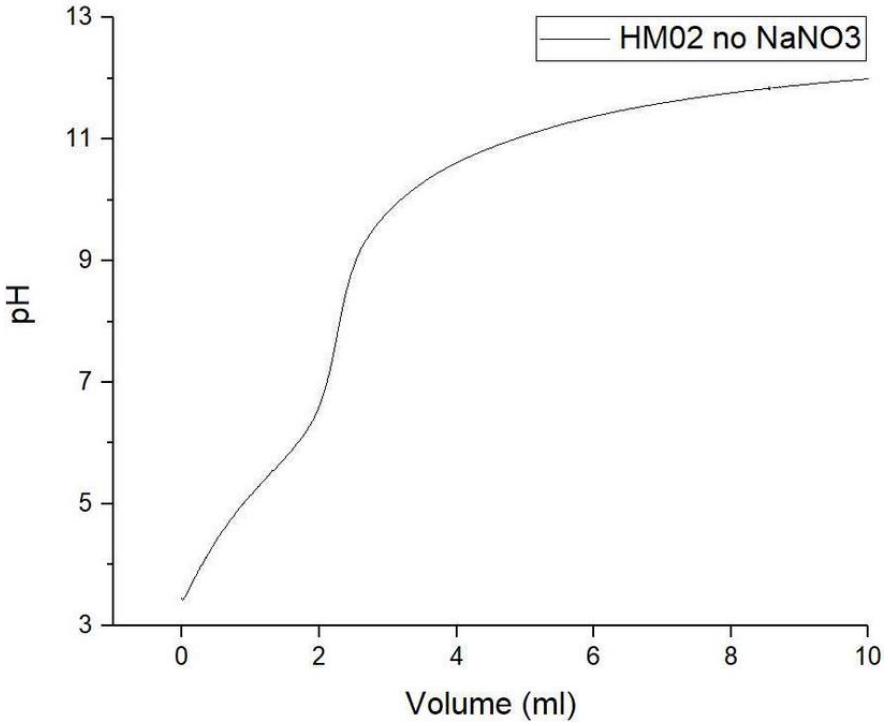

Figure 8-30: Test titration with HM02.

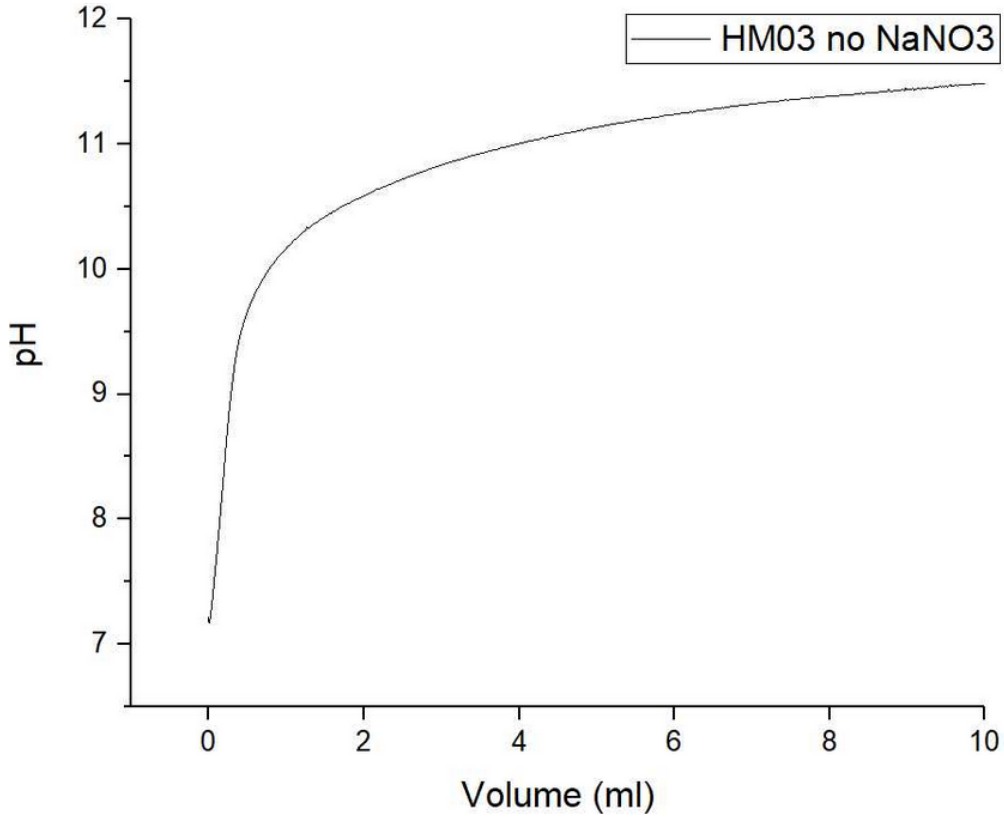

Figure 8-31: Test titration with HM03.

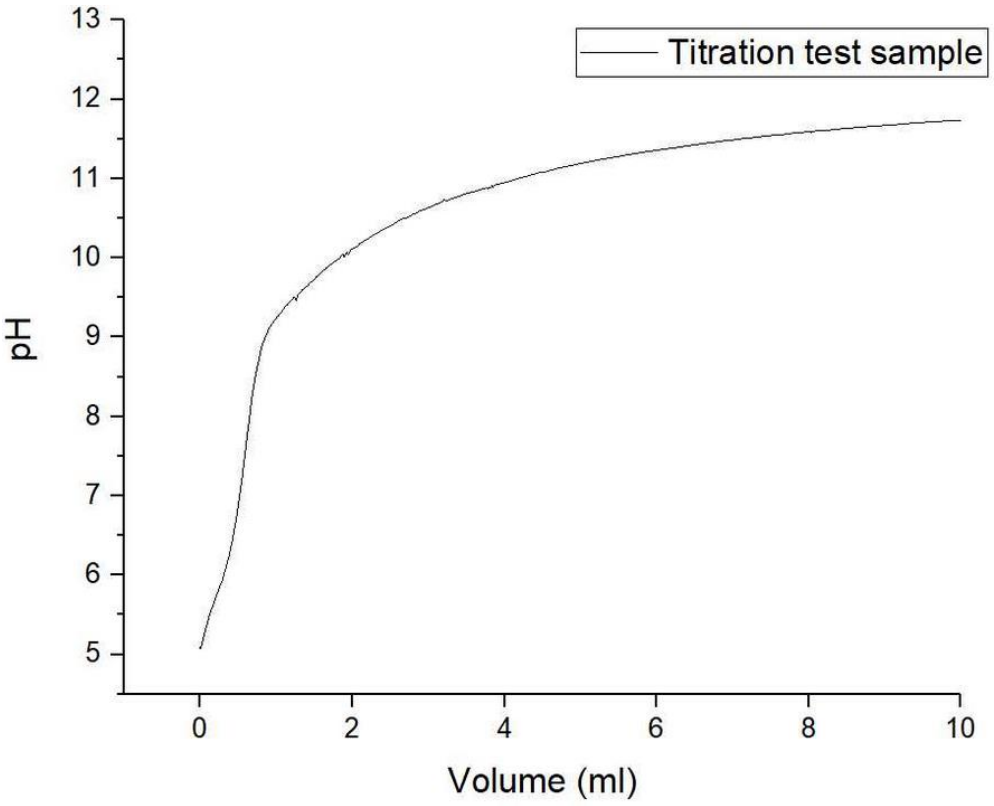

Figure 8-32: The first test titration with the test sample CBV8014.

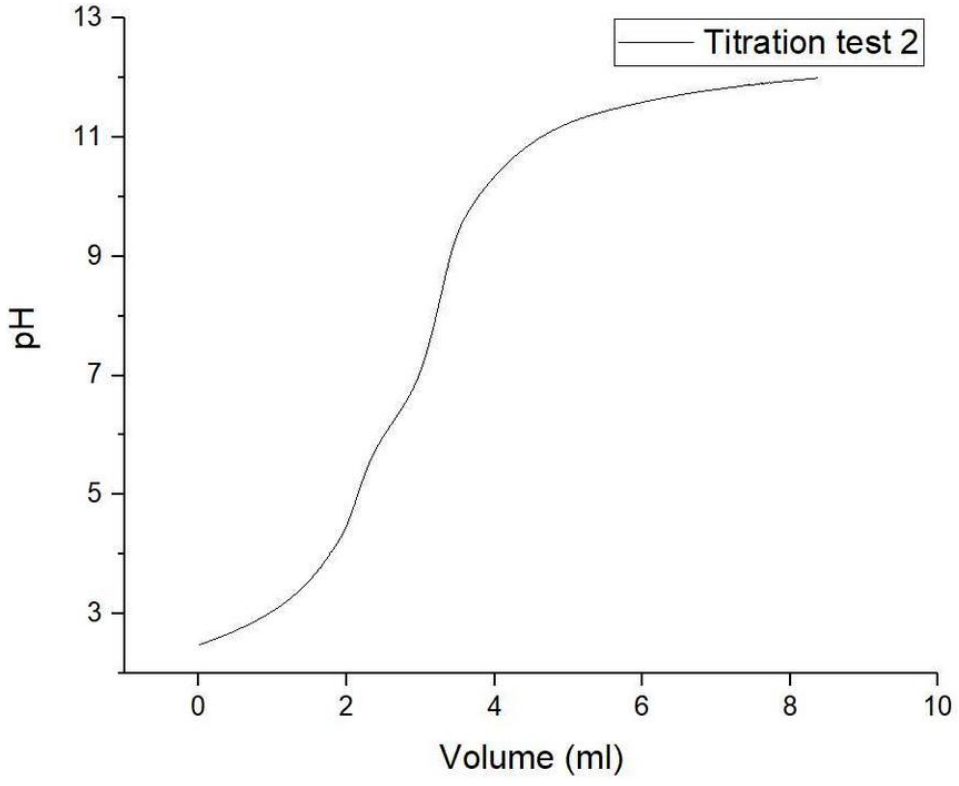

Figure 8-33: Second test titration with the test sample CBV8014.

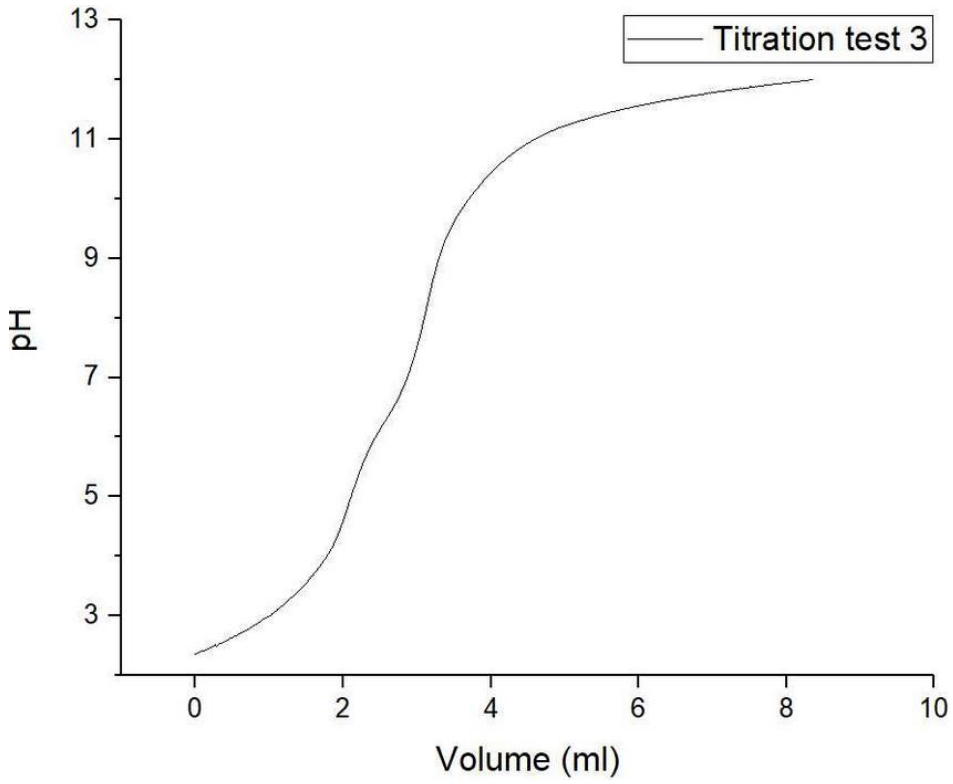

Figure 8-34: Shows the third test titration with the test sample CBV8014.

8.7.2 Titration of benchmark sample

Figure 8-35 shows the titration curve corresponding to the data used for the calculations in section 8.7.3 for the CBV 8014 material.

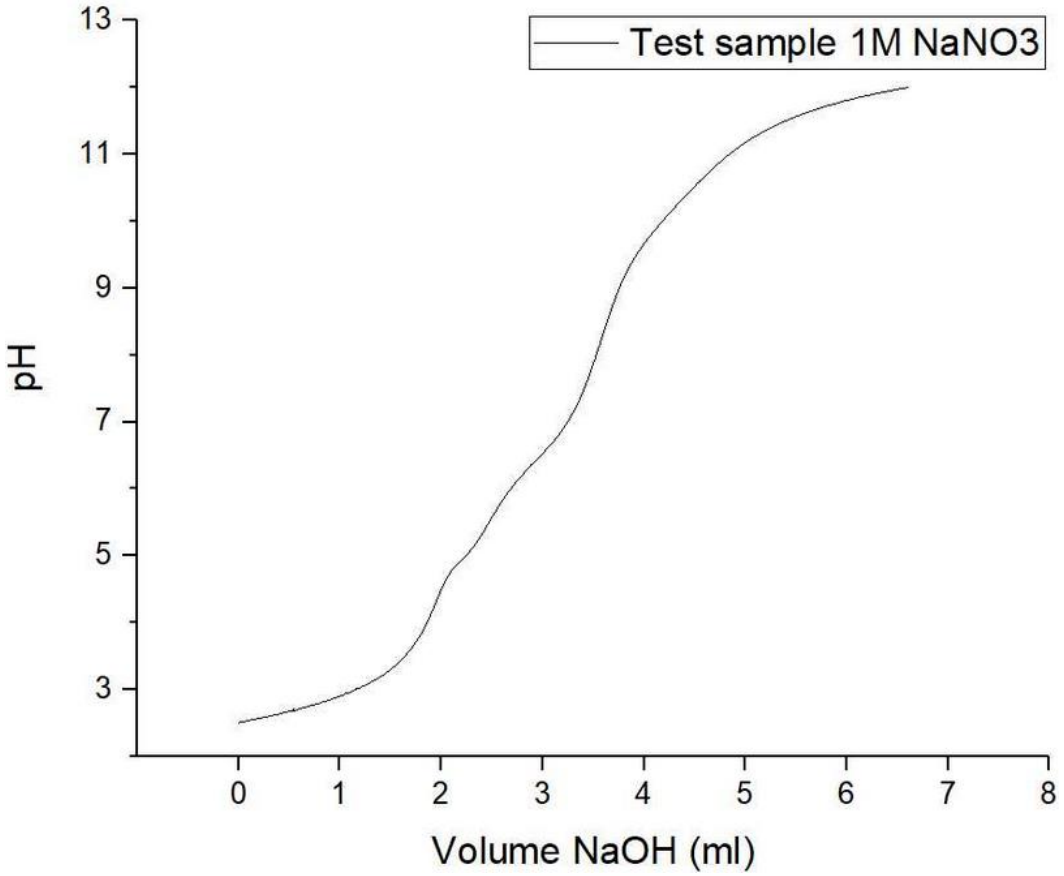

Figure 8-35: Titration of the benchmark sample, CBV8014. The sample was suspended in 1M $NaNO_3$.

8.7.3 Titration analysis

Calculations for CBV 8014:

0.500g was used and 1M $NaNO_3$ was used.

The base concentration measured from back titration using 0.01M HCl as the acid, was 0.0855 M.

The equivalence point was determined to be at 2.345×10^{-3} L.

The CBV 8014 material has a Si/Al ratio of 40 (91), therefore the chemical formula of this zeolite is: $[H]^{+}[Al_1Si_{40}O_{82}]$

Then the molar mass is calculated to be:

$$H = 1.008\ g/mol$$

$$Al = 26.982\ g/mol$$

$$O = 15.999\ g/mol$$

$$Si = 28.085\ g/mol$$

$$Total\ molar\ mass = 2463{,}3\ g/mol$$

Since 0.500g of sample was used during the titration the number of mole H^+ corresponds to:

$$\frac{0.500g}{2463{,}3\ g/mol} = 2.03 \times 10^{-4}\ \text{mol}$$

The moles of OH^- required to reach the equivalence point can be calculated by using the concentration of HCl and the volume required to reach the equivalence point:

$$Moles\ OH^- = 0.855\ M \times 2.345 \times 10^{-4} L = 2.005 \times 10^{-4}\ mol$$

The percentage of accessibility of acid sites can be calculated:

$$Accessibility\ of\ acid\ sites = \frac{2.005 \times 10^{-4}}{2.03 \times 10^{-4}} \times 100\% = 99\%$$

Lastly the density of acid sites can be calculated:

$$2.005 \times 10^{-4}\ mol \times 10^{6} = 200{,}5 \mu mol$$

$$\frac{200{,}5 \mu mol}{0.500\ g} = 401\ \mu mol/g$$

Calculations for ACS extrudates:

0.500g was used and 1M $NaNO_3$ was used.

The base concentration measured from back titration using 0.01M HCl as the acid, was 0.0967 M.

The equivalence point was determined to be at 3.562×10^{-4} L.

The ACS extrudates material has a Si/Al ratio of 19, therefore the chemical formula of this zeolite is: $[H]^{+}[Al_1Si_{19}O_{40}]$

Then the molar mass is calculated to be:

$$H = 1.008\ g/mol$$

$$Al = 26.982\ g/mol$$

$$O = 15.999\ g/mol$$

$$Si = 28.085\ g/mol$$

$$Total\ molar\ mass = 1201.6\ g/mol$$

Since 0.500g of sample was used during the titration the number of mole H^+ corresponds to:

$$\frac{0.500g}{1201.6\ g/mol} = 4.16 \times 10^{-4}\ \text{mol}$$

The moles of OH^- required to reach the equivalence point can be calculated by using the concentration of HCl and the volume required to reach the equivalence point:

$$Moles\ OH^- = 0.967\ M \times 3.562 \times 10^{-4} L = 3.44 \times 10^{-5}\ mol$$

The percentage of accessibility of acid sites can be calculated:

$$Accessibility\ of\ acid\ sites = \frac{3.44 \times 10^{-5}}{4.16 \times 10^{-4}} \times 100\% = 8.3\%$$

Lastly the density of acid sites can be calculated:

$$3.44 \times 10^{-5}\ \times 10^{-4}\ mol \times 10^{6} = 34.4\ \mu mol$$

$$\frac{34.4 \mu mol}{0.500\ g} = \ 68.8\ \mu mol/g$$

Calculations for HM02:

0.500g was used and 1M $NaNO_3$ was used.

The base concentration measured from back titration using 0.01M HCl as the acid, was 0.0967 M.

The equivalence point was determined to be at 1.511×10^{-4} L.

The HM02 material has a Si/Al ratio of 28.4, therefore the chemical formula of this zeolite is: $[H]^{+}[Al_1Si_{28.4}O_{57}]$

Then the molar mass is calculated to be:

$$H = 1.008\ g/mol$$

$$Al = 26.982\ g/mol$$

$$O = 15.999\ g/mol$$

$$Si = 28.085\ g/mol$$

$$Total\ molar\ mass = 1772.3\ g/mol$$

Since 0.500g of sample was used during the titration the number of mole H^+ corresponds to:

$$\frac{0.500g}{1772.3\ g/mol} = 2.82 \times 10^{-4}\ \text{mol}$$

The moles of OH^- required to reach the equivalence point can be calculated by using the concentration of HCl and the volume required to reach the equivalence point:

$$Moles\ OH^- = 0.967\ M \times 1{,}511 \times 10^{-4} L = 1.46 \times 10^{-6}\ mol$$

The percentage of accessibility of acid sites can be calculated:

$$Accessibility\ of\ acid\ sites = \frac{1.46 \times 10^{-6}}{2.82 \times 10^{-4}} \times 100\% = 5.2\%$$

Lastly the density of acid sites can be calculated:

$$1.46 \times 10^{-6}\ mol \times 10^{6} = 14.6\ \mu mol$$

$$\frac{14.6 \mu mol}{0.500\ g} = 29.2\ \mu mol/g$$

Calculations for HM03:

0.500g was used and 1M $NaNO_3$ was used.

The base concentration measured from back titration using 0.01M HCl as the acid, was 0.0967 M.

The equivalence point was determined to be at 6.835×10^{-4} L.

The HM03 material has a Si/Al ratio of 41.5, therefore the chemical formula of this zeolite is: $[H]^{+}[Al_1Si_{41.5}O_{83}]$

Then the molar mass is calculated to be:

$$H = 1.008\ g/mol$$

$$Al = 26.982\ g/mol$$

$$O = 15.999\ g/mol$$

$$Si = 28.085\ g/mol$$

$$Total\ molar\ mass = 2553.4\ g/mol$$

Since 0.500g of sample was used during the titration the number of mole H^+ corresponds to:

$$\frac{0.500g}{2553.4\ g/mol} = 1.96 \times 10^{-4}\ \text{mol}$$

The moles of OH^- required to reach the equivalence point can be calculated by using the concentration of HCl and the volume required to reach the equivalence point:

$$Moles\ OH^- = 0.967\ M \times 6.835 \times 10^{-4} L = 6.11 \times 10^{-5}\ mol$$

The percentage of accessibility of acid sites can be calculated:

$$Accessibility\ of\ acid\ sites = \frac{6.11 \times 10^{-5}}{1.96 \times 10^{-4}} \times 100\% = 34\%$$

Lastly the density of acid sites can be calculated:

$$6.11 \times 10^{-5}\ mol \times 10^{6} = 61.1\ \mu mol$$

$$\frac{61.1 \mu mol}{0.500\ g} = 132.2\ \mu mol/g$$

The Si/Al ratio used for HM02 and HM03 is the measured ratio from MP - AES.

8.8 Co - feed test - rig

This section includes an overview of the MTH conversion that has been done for the four Beta zeolites and the partially deactivated ACS extrudates in this work. The initial product selectivity for the partially deactivated ACS extrudates is included as well.

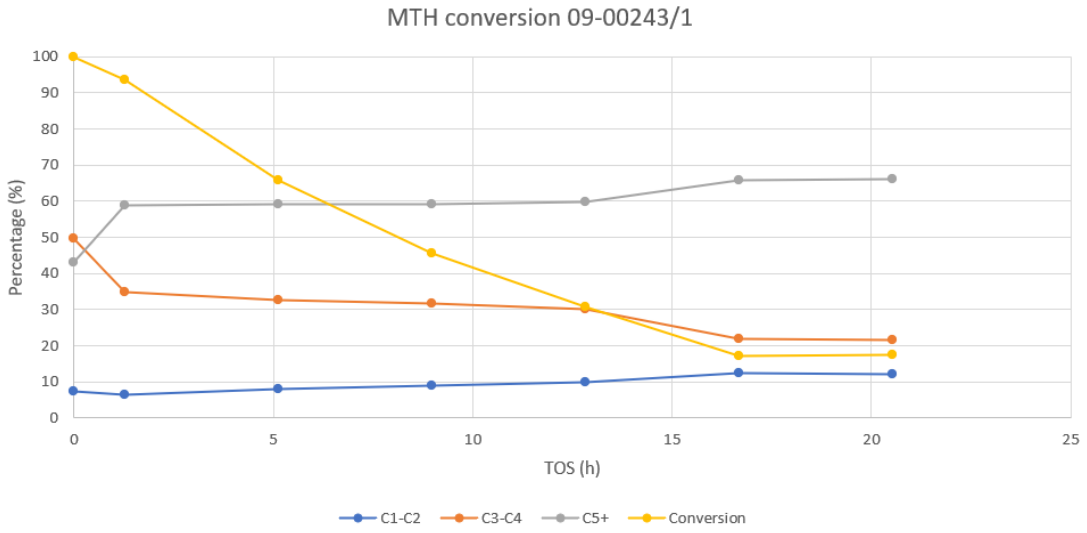

Figure 8-36: Data for both yield and product selectivity for the Beta zeolite 09-00243/1, for time on stream at 400°C with WHSV of 2.95 $g_{MeOH}\, g_{catalyst}^{-1}\, h^{-1}$, where yield is the sum of converted DME and MeOH.

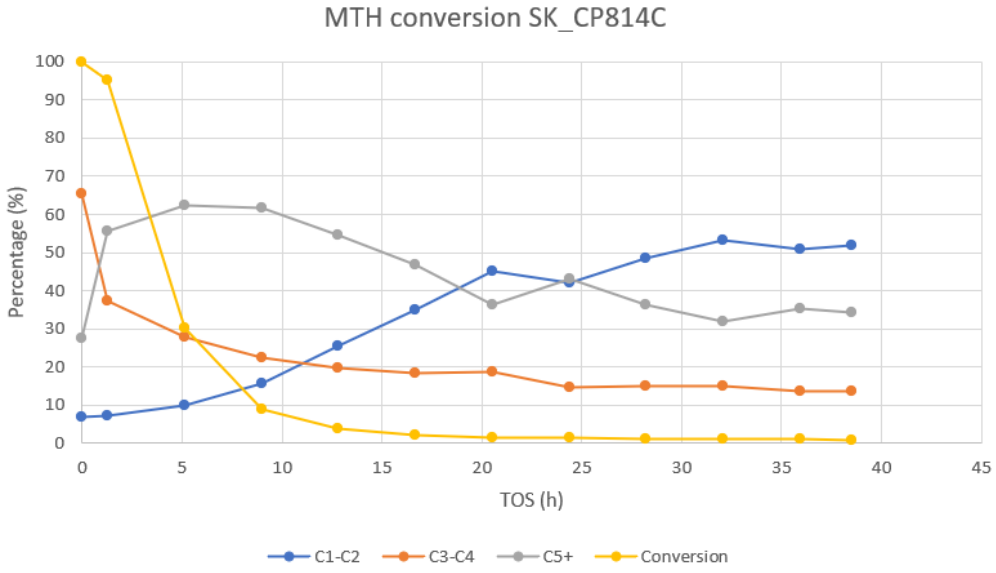

Figure 8-37: Data for both yield and product selectivity for the Beta zeolite SK_CP814C, for time on stream at 400°C WHSV of 2.95 $g_{MeOH}\, g_{catalyst}^{-1}\, h^{-1}$, where yield is the sum of converted DME and MeOH.

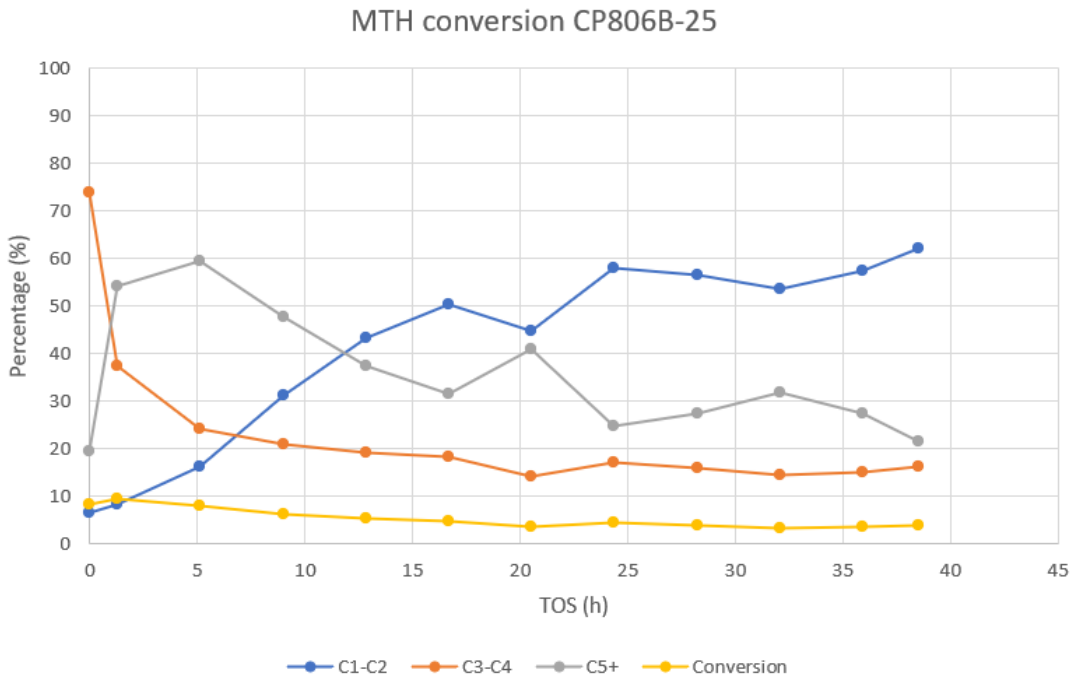

Figure 8-38: Data for both yield and product selectivity for the Beta zeolite CP806B-25, for time on stream at 400°C WHSV of 2.95 $g_{MeOH}\, g_{catalyst}^{-1}\, h^{-1}$, where yield is the sum of converted DME and MeOH.

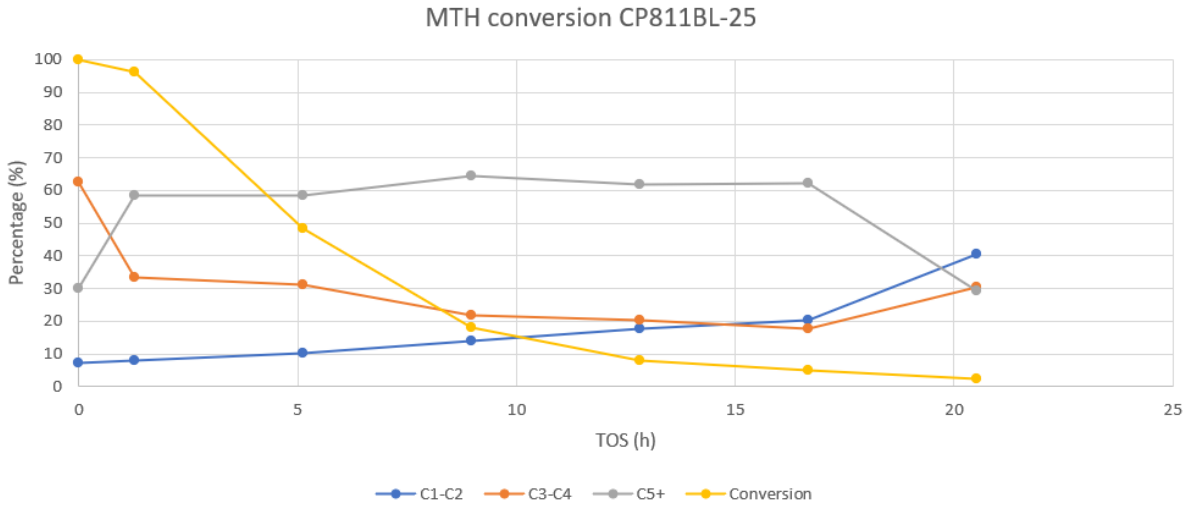

Figure 8-39: Data for both yield and product selectivity for the Beta zeolite CP811BL-25, for time on stream at 400°C with WHSV of 2.95 $g_{MeOH}\, g_{catalyst}^{-1}\, h^{-1}$, where yield is the sum of converted DME and MeOH.

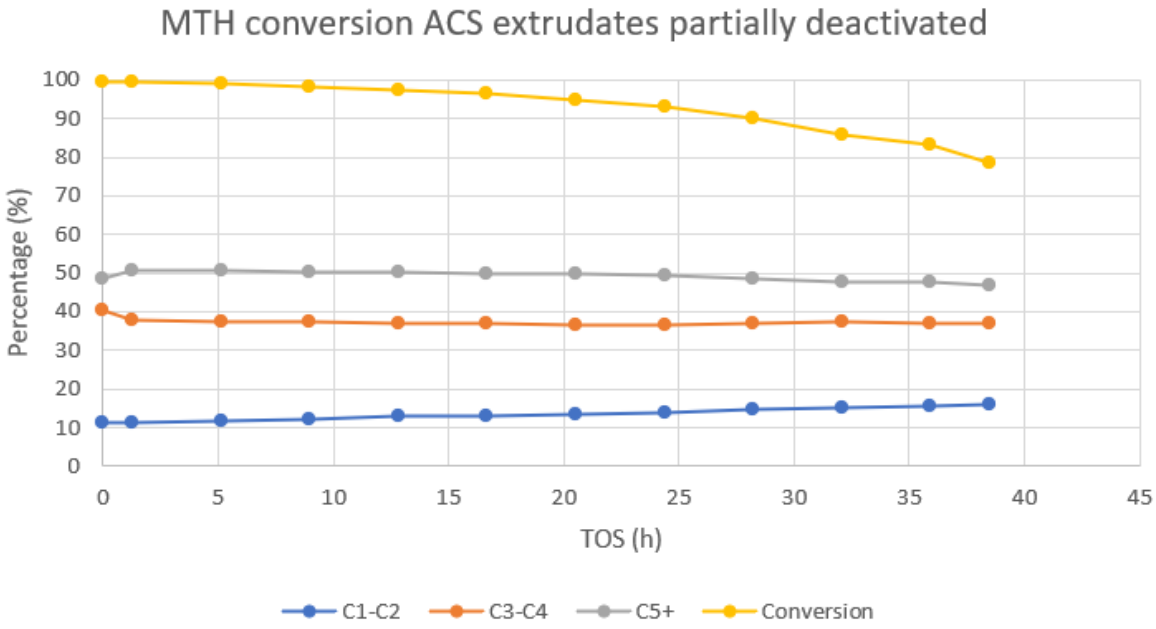

Figure 8-40: Data for both yield and product selectivity for partially deactivated ACS extrudates, for time on stream at 400°C with WHSV of 2.95 $g_{MeOH}\, g_{catalyst}^{-1}\, h^{-1}$, where yield is the sum of converted DME and MeOH.

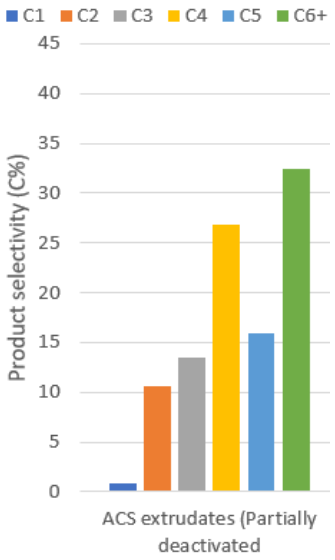

Figure 8-41: Product selectivity at initial conversion at 400°C for the partially deactivated ACS extrudates that was tested for catalytic activity.

9 References

1. Ishida H. Overview and historical background of polybenzoxazine research, Handbook of benzoxazine resins, Hatsuo, I.; Tarek, A. (eds.), Elsevier, 2011, 3-81, DOI: https://doi.org/10.1016/B978-0-444-53790-4.00046-1.

2. Ola Nilsen, Lecture handouts, KJM 5100 Inorganic material synthesis, University of Oslo, Autumn 2019.

3. ZSM-5, Wikipedia, The free encyclopedia, 2020, https://en.wikipedia.org/wiki/ZSM-5, (accessed 2020-03-12).

4. Daniel Firth, Lecture handouts, KJM5810 Heterogenous catalysis, University of Oslo, Spring 2020.

5. Atomic scale design network, zeolites, https://asdn.net/asdn/chemistry/zeolites.php, (accessed 2020-02-18).

6. Xu, D.; Feng, J.; Che, S. An insight into the role of the surfactant CTAB in the formation of microporous molecular sieves, Dalton transactions, 2013, 43, 3612-3617, DOI: https//doi.org/10.1039/c3dt53308e.

7. Busca, G. Acidity and basicity of zeolites: A fundamental approach, Microporous and mesoporous materials, 2017, 254, 3-16, DOI: https://doi.org/10.1016/j.micromeso.2017.04.007.

8. Shan, Y.; Du, J.; Zhang, Y.; Shan, W.; Shi, X.; Yu, Y.; Zhang, R.; Meng, X.; Xiao, F.; He, H. Selective catalytic reduction of NOx with NH3: opportunities and challenges of Cu-based small-pore zeolites, National science review, 2021, 8 (10), 1-20, DOI: https://doi.org/10.1093/nsr/nwab010.

9. Lenntech, library, Zeolite applications, https://www.lenntech.com/library/media-filtration/zeolites-applications.htm, (accessed 2021-12-06).

10. Stian Svelle, Lecture handouts, KJM3810 Catalysis and industrial chemistry, University of Oslo, Autumn 2018.

11. Mozgawa, W.; Król, M.; Barczyk, K. FT-IR studies of zeolites from different structural groups, Chemik, 2011, 65 (7), 667-674.

12. Kumar, S. Potentiometric acid-base titration as a tool to characterize porous solid acids, MSc. thesis, University of Oslo, Oslo, Norway, 2020.

13. International zeolite association, Database of zeolite structures, https://asia.iza-structure.org/IZA-SC/ftc_table.php, (accessed 2020-03-14).

14. International zeolite association, Database of zeolites, Framework type MFI, https://asia.iza-structure.org/IZA-SC/framework.php?STC=MFI, (accessed 2020-03-14).

15. ACS materials, ZSM – 5 catalyst, https://www.acsmaterial.com/zsm-5-catalyst.html, (accessed 2021-08-08).

16. International zeolite association, Database of zeolites, Framework type BEA, https://asia.iza-structure.org/IZA-SC/framework.php?STC=BEA, (accessed 2020-03-14).

17. Čejka J. í.; Morris R.E.; Nachtigall P. Zeolites in catalysis: properties and applications, Royal society of chemistry, 2017, DOI: https://doi.org/10.1039/9781788010610.

18. Cerro, R. L.; Higgins, B. G.; Whitaker, S. Material balances for chemical engineers, 7.2: Multiple reactions - conversion, selectivity and yield, Libretext, 2014, https://eng.libretexts.org/Bookshelves/Chemical_Engineering/Book%3A_Material_Balances_for_Chemical_Engineers_(Cerro_Higgins_and_Whitaker)/07%3A_Material_Balances_for_Complex_Systems/7.02%3A_Multiple_Reactions_-_Conversion_Selectivity_and_Yield, (accessed 2019-05-03).

19. Hjelen, J. Scanning elektron-mikroskopi, 1989.

20. Molino A.; Lukaszuk K. A.; Rojo-Gama D.; Lillerud K. P.; Olsbye U.; Bordiga S.; Svelle S.; Beato P. Conversion of methanol to hydrocarbons over zeolite ZSM-23 (MTT): exceptional effects of particle size on catalyst lifetime, Chemical communications, 2017, 53, 6816-6819, DOI: https://doi.org/10.1039/C6CC10118F.

21. JEOL. Scanning electron microscope A to Z, https://www.jeol.co.jp/en/applications/pdf/sm/sem_atoz_all.pdf, (accessed 2021-09-20).

22. Lee, K.; Kang, M.; Ihm, S. Deactivation by coke deposition on the HZSM-5 catalysts in the methanol-to-hydrocarbon conversion, Journal of physics and chemistry of solids, 2021, 73 (12), 1542-1545, DOI: https://doi.org/10.1016/j.jpcs.2012.09.005.

23. Rojo-Gama D; Nielsen M.; Wragg D. S.; Dyballa M.; Holzinger J.; Falsig H.; Lundegaard L. F.; Beato P.; Brogaard R. Y.; Lillerud K. P.; Olsbye U.; Svelle S. A straightforward descriptor for the deactivation of zeolite catalyst H-ZSM-5, ACS catalysis 2017, 7 (12), 8235-8246, DOI: https//doi.org/10.1021/acscatal.7b02193.

24. Ameh, E. S. A review of basic crystallography and x-ray diffraction applications, Springer, 2019, 105, 3289-3302, DOI: https://doi.org/10.1007/s00170-019-04508-1.

25. Bjørgen M.; Jensen F.; Holm M.; Olsbye U.; Lillerud K. P.; Svelle S. Methanol to gasoline over zeolite H-ZSM-5: improved catalyst performance by treatment with NaOH, Applied catalysis A: General, 2008, 345, 43-50, DOI: https//doi.org/10.1016/j.apcata.2008.04.020.

26. Falcioni M.; Deem M. W. A biased Monte Carlo scheme for zeolite structure solution, Journal of chemical physics, 1999, 110, 1754-1766, DOI: https://doi.org/10.1063/1.477812.

27. University of Oslo home page, Department of chemistry, TOMOCAT, https://www.mn.uio.no/kjemi/english/research/groups/catalysis/research/tomocat.html, (accessed 2021-12-10).

28. Rojo-Gama, D., Investigations of the long term catalytic activity and stability of zeolite-based catalysts in the conversion of methanol-to-hydrocarbons, Ph.D. thesis, Department of chemistry, University of Oslo, Oslo, Norway, 2017, https://www.duo.uio.no/handle/10852/59127, (accessed 2019-01-11).

29. Santanu B.; Soumen D. Chapter 1 - Nucleation and particle growth in solution-processed thin films, Chemical solution synthesis for materials design and thin film device applications, 1st. Ed., Soumen, D.; Sandip, D. (eds.), Elsevier, 2021, 1-27, DOI: https://doi.org/10.1016/C2019-0-00309-3.

30. Boero, M.; Terakura, K.; Ikeshoji, T.; Liew, C.; Parrinello, M. Water at supercritical conditions: A first principles study, The journal of chemical physics, 2001, 115, 2219-2227, DOI: https//doi.org/10.1063/1.1379767.

31. Wojcik P.; Santos L.; Pereira L.; Martins R.; Fortunato E. Supporting information to Tailoring morphology and structure of tungsten oxide nanoparticles for inkjet printed electrochromic devices, RSC nanoscale, 2015, 7 (5) 1696-1708, DOI: https://doi.org/10.1039/C4NR05765A.

32. Kelly, A.; Knowles, K. M. Crystallography and crystal defects, 2nd. Ed., Wiley, 2012, 469-472.

33. Helmer Fjellvåg, Lecture handouts, MENA5020 Nano chemistry, University of Oslo, Automn 2021.

34. Yale University home page, XRD principles, https://ywcmatsci.yale.edu/principle-0, (accessed 2020-01-15).

35. Widjonarko, N. Introduction to advanced x-ray diffraction techniques for polymeric thin films, Coatings, 2016, 6, 54, DOI: https//doi.org/10.3390/coatings6040054.

36. Rhodes, G. Crystallography made crystal clear, 3rd. Ed., Elsevier, 2006, 83-99.

37. Nix, R. Surface science, 1.2: Miller indices, Libretext, 2021, https://chem.libretexts.org/Bookshelves/Physical_and_Theoretical_Chemistry_Textbook_Maps/Book%3A_Surface_Science_(Nix)/01%3A_Structure_of_Solid_Surfaces/1.02%3A_Miller_Indices_(hkl).

38. Treacy M.; Higgins J. Collection of simulated XRD powder patterns for zeolites, 4th. Ed., Elsevier, 2001.

39. Helmer Fjellvåg, Lecture handouts, KJM-MENA 3120 Inorganic chemistry II, University of Oslo, Spring 2019.

40. Introduction x – ray diffraction, http://www.physics.rutgers.edu/~eandrei/389/xrays/missing%20lines.pdf.

41. Savikhin, V.; Toney, M. F. Handbook of organic materials for electronic and photonic devices, 2nd. Ed., Woodhead publishing series in electronic and optical materials, 2019, 489-528, DOI: https://doi.org/10.1016/B978-0-08-102284-9.00015-2.

42. Speakman S. A. Massachusetts institute of technology, Basics of x-ray diffraction, http://prism.mit.edu/xray/documents/1%20Basics%20of%20X-Ray%20Powder%20Diffraction.pdf, (accessed 2020-01-15).

43. Scintag Inc. Chapter 7: Basics of x-ray diffraction, 1999, 7.1-7.25, http://www.geo.umass.edu/courses/geo311/xrdbasics.pdf.

44. Asmi, D.; Manurung, P.; Low, I. M. Advances in ceramic matrix composites, 2nd. Ed., Woodhead publishing series in composites science and engineering, 2018, 121–153, DOI: https://doi.org/10.1016/B978-0-08-102166-8.00006-2.

45. Department of Chemistry, University of Oslo home page, Netzsch TGA, https://www-int.mn.uio.no/kjemi/english/research/groups/catalysis/internal/sop-sja/tga-netzsch.html, (accessed 2020-02-21).

46. Zhdanov, S. P.; Feoktistova, N. N.; Kozlova, N. I.; Polyakova, I. G. Thermal stability of high-silica zeolites of the ZSM-5 family, Bulletin of the academy of sciences of the USSR, Division of chemical science, 1985, 34, 2463–2466, DOI: https://doi.org/10.1007/BF00953006.

47. Hitachi homepage, Principle of differential scanning calorimetry (DSC), https://www.hitachi-hightech.com/global/products/science/tech/ana/thermal/descriptions/dsc.html (accessed 2022-01-17).

48. Zhang, Z.; Li, S.; Bao, S. Sustainable synthesis of ZSM-5 Zeolite from Rice Husk ash without addition of solvents, 2019, 10, 2825-2835, Springer, DOI: https//doi.org/10.1007/s12649-018-0356-0.

49. Azo materials, Different types of SEM imaging – BSE and secondary electron imaging, Azo materials, 2017, https://www.azom.com/article.aspx?ArticleID=14309.

50. Balaram V, Microwave plasma atomic emission spectrometry (MP-AES) and its applications – A critical review, Microchemical journal, 2020, 159, 1-6, DOI: https://doi.org/10.1016/j.microc.2020.105483.

51. Fan M.; Fu F. 1 - Introduction: A perspective – natural fibre composites in construction, Advanced high strength natural fibre composites in construction, Woodhead publishing, 2017, 1-20.

52. Chalyavi, N.; Doidge, P. S.; Morrison, R. J. S.; Partridge, G.B. Fundamental studies of an atmospheric-pressure microwave plasma sustained in nitrogen for atomic emission spectrometry, Journal of analytical atomic spectroscopy, 2017, 32 (10), 1988-2002, DOI: https://doi.org/10.1039/c7ja00159b.

53. CBRNE tech index home page, Microwave plasma atomic emission spectroscopy (MPAES), https://www.cbrnetechindex.com/Chemical-Detection/Technology-CD/Elemental-Analysis-CD-T/Microwave-Plasma-Atomic-Emission-Spectroscopy-CD-EA, (accessed 2021-05-21).

54. Jung M. Y.; Kang H. J.; Choi Y. S.; Lee D. Y.; Lee J. Y.; Park J. S. Analytical features of microwave plasma-atomic emission spectrometry (MP-AES) for the quantitation of manganese (Mn) in wild grape (Vitis coignetiae) red wines: Comparison with inductively coupled plasma-optical emission spectrometry (ICP-OES), Food chemistry, 2019, 274, 20-25, DOI: https://doi.org /10.1016/j.foodchem.2018.08.114.

55. Singh, J.; Shraddhesh, C.; Verma, H. C. IIT JEE PHYSICS, 2018, 1-4.

56. Nanakoudis, A. Thermofisher, EDX analysis with SEM: How does it work?, https://www.thermofisher.com/blog/microscopy/edx-analysis-with-sem-how-does-it-work/ (accessed 2022-01-25).

57. Raja, P. M. V.; Barron, A. R. Physical methods in chemistry and nano science, Rice University, 2012, 185-195.

58. Rouquerol J.; Llewellyn P.; Rouquerol F. Is the bet equation applicable to microporous adsorbents?, Studies in surface science and catalysis, Elsevier, 2007, 160, 49-56, DOI: https//doi.org/10.1016/S0167-2991(07)80008-5

59. Lange, M. F.; Lin, L.; Gascon, J.; Vlugt, T. J. H.; Kapteijn F. Assessing the surface area of porous solids: Limitations, probe molecules, and methods, Langmuir, 2016, 32 (48), 12664-12675, DOI: https://doi.org/10.1021/acs.langmuir.6b03531.

60. Stian Svelle, Lecture handouts, KJM5500 Surface- and nanotechnology, University of Oslo, Spring 2020.

61. Sing K. S. W.; Williams R.T. Physisorption hysteresis loops and the characterization of nanoporous materials, Adsorption science & technology, 2004, 22 (10), 773-782, DOI: https//doi.org/10.1260/0263617053499032.

62. Zhao J.; Yin Y.; Li Y.; Chen W.; Liu B. Synthesis and characterization of mesoporous zeolite Y by using block copolymers as templates, Chemical engineering journal, 2016, 284, 405-411, DOI: https//doi.org/10.1016/j.cej.2015.08.143.

63. Worstell J. Adiabatic fixed-bed reactors, Butterworth-Heinemann, 1st. Ed., Elsevier, 2014, 1-12, https://www.elsevier.com/books/adiabatic-fixed-bed-reactors/worstell/978-0-12-801306-9.

64. Stian Svelle, Lecture handouts, KJM5810 Heterogenous catalysis, University of Oslo, Spring 2020.

65. Wang S.; Davidson D. F.; Hanson, R. K. Chapter 3 - Shock tube techniques for kinetic target data to improve reaction models, Mathematical modelling of gas-phase complex reaction systems: Pyrolysis and combustion, Computer aided chemical engineering, 1st. Ed., Elsevier, 2019, 45, 169-202, https://www.sciencedirect.com/bookseries/computer-aided-chemical-engineering/vol/45/suppl/C.

66. Evgeniy Redekop, Lecture handouts, KJM5810 Heterogenous catalysis, University of Oslo, Spring 2020.

67. Vunain E.; Mishra A. K.; Mamba B. B. 1 - Fundamentals of chitosan for biomedical applications, Chitosan based biomaterials, Woodhead publishing, 2017, 1, 3-30, DOI: https://doi.org/10.1016/C2014-0-03147-4.

68. Krasnikova, I. V.; Mishakov, I. V.; Vedyagin, A. A. Carbon-based nanofillers and their rubber nanocomposites, Fundamentals and applications, 2019, 75-137, DOI: https://doi.org/10.1016/B978-0-12-817342-8.00005-6.

69. Hiden analytical, Temperature programmed oxidation - a guide, Azo materials, 2018, https://www.azom.com/article.aspx?ArticleID=15899, (accessed 2021-09-10).

70. Auroux, A. Calorimetry and thermal methods in catalysis, Materials science, Springer, 1st. Ed., 2013, 154, 175-195.

71. Besselmann, S.; Freitag, C.; Hinrichsen, O.; Muhler, M. Temperature-programmed reduction and oxidation experiments with V_2O_5/TiO_2 catalysts, Physical chemistry chemical physics, 2001, 3 (21), 4633-4638, DOI: https://doi.org/10.1039/b105466j.

72. Fadoni, M.; Lucarelli, L. Temperature programmed desorption, reduction, oxidation and flow chemisorption for the characterisation of heterogeneous catalysts, Theoretical aspects, instrumentation and applications, Studies in surface science and catalysis, 1999, 120, 177-225, DOI: https://doi.org/10.1016/S0167-2991(99)80553-9.

73. Diffrac.EVA user manual, https://web.ua.es/es/arqueometria/documentos/documentos/difrac-eva.pdf, (accessed 2022-01-10).

74. Department of Chemistry, University of Oslo home page, Co-feed test rig, https://www-int.mn.uio.no/kjemi/english/research/groups/catalysis/internal/sop-sja/multiple-feed-test-rig(marius).html, (accessed 2020-09-15).

75. Zeolyst, Zeolite BETA, https://www.zeolyst.com/our-products/standard-zeolite-powders/zsm-5.html, (accessed 2020-03-14).

76. Rojo-Gama D.; Etemadi S.; Kirby E.; Lillerud K. P.; Beato P.; Svelle S.; Olsbye U. Time- and space-resolved study of the methanol to hydrocarbons (MTH) reaction – influence of zeolite topology on axial deactivation patterns, Faraday discussions, 2017, 197, 421-446, DOI: https://doi.org/10.1039/C6FD00187D.

77. Pawley, G. S. Unit-cell refinement from powder diffraction scans, Jornal of applied crystallography, 1981, 14, 357-361, DOI: https://doi.org/10.1107/S0021889881009618, (accessed 2021-08-15).

78. Wragg D. S.; Kalantzopoulos G. N.; Pappas D. K.; Pinilla-Herrero I.; Rojo-Gama D.; Redekop E.; Michiel M. D.; Beato P.; Lundegaard L. F.; Svelle S. Mapping the coke formation within a zeolite catalyst extrudate in space and time by operando computed x-ray diffraction tomography, Journal of catalysis, 2021, 401, 1-6, DOI: https://doi.org/10.1016/j.jcat.2021.07.001.

79. International zeolite association, Database of zeolites, BEA, zeolite Beta, http://www.iza-online.org/synthesis/Recipes/Zeolite%20Beta.html.

80. Beheshti, M. S.; Ahmadpour, J.; Behzad, M.; Arabi, H. Hydrothermal synthesis of H-ZSM-5 catalysts employing the mixed template method and their application in the conversion of methanol to light olefins, Reaction kinetics, mechanisms and catalysis, 2020, 130, 493–518, DOI: https://doi.org/10.1007/s11144-020-01771-2.

81. Sharman G. H.; Duncan S. The hygroscopic nature of H-ZSM—5, Zeolites, 1985, 5 (3), 173-178, DOI: https://doi.org/10.1016/0144-2449(85)90026-0.

82. Koegler J.H.; van Bekkum H.; Jansen J.C. Growth model of oriented crystals of zeolite Si-ZSM-5, Zeolites, 1997, 19 (4), 262-269, DOI: https://doi.org/10.1016/S0144-2449(97)00088-2.

83. Maarten, B. J.; Ameloot R.; Baruah M.; Uji-i H.; Bulut M.; Cremer G. D.; Müller, U.; Jacobs, A. P.; Hofkens, J.; Sels, B. F.; Vos, D. E. D. Morphology of large ZSM-5 crystals unraveled by fluorescence microscopy, Journal of the American chemical society, 2008, 130 (17), 5763-5772, DOI: https://doi.org/10.1021/ja7113147.

84. Sotomayor, F.; Cychosz, K.; Thommes, M. Characterization of micro/mesoporous materials by physisorption: accounts of materials surface research, 2018, 3, 34-50, DOI: https://www.hyomen.org/en/.

85. Singh, B.K.; Kim, Y.; Kwon, S.; Na, K. Synthesis of mesoporous zeolites and their opportunities in heterogeneous catalysis. Catalysts 2021, 11, 1541, 1-30, https://doi.org/10.3390/catal11121541.

86. Pinilla-Herrero I.; Borfecchia E.; Holzinger J.; Mentzel U. V.; Joensen F.; Lomachenko K. A.; Bordiga S.; Lamberti C.; Berlier G.; Olsbye U.; Svelle S.; Skibsted J.; Beato P. High Zn/Al ratios enhance dehydrogenation vs hydrogen transfer reactions of Zn-ZSM-5 catalytic systems in methanol conversion to aromatics, Journal of catalysis, 2018, 362, 146-163, DOI: https://doi.org/10.1016/j.jcat.2018.03.032.

87. Pinilla-Herrero I.; Borfecchia E.; Cordero-Lanzac T.; Mentzel U. V.; Joensen F.; Lomachenko K.; Bordiga S.; Olsbye U.; Beato P.; Svelle S. Finding the active species: The conversion of methanol to aromatics over Zn-ZSM-5/alumina shaped catalysts, Journal of Catalysis, 2021, 394, 416–428, DOI: https://doi.org/10.1016/j.jcat.2020.10.024.

88. Mikkelsen, Ø.; Kolboe, S. The conversion of methanol to hydrocarbons over zeolite H-beta, Microporous and mesoporous materials, 1999, 29 (1-2), 173-184, DOI: https://doi.org/10.1016/S1387-1811(98)00329-1.

89. Erichsen, M. The methanol-to-hydrocarbons reaction: Influence of acid strength on the mechanism of olefin formation, MSc. thesis, Department of chemistry, University of Oslo, Oslo, Norway, 2010, https://www.duo.uio.no/bitstream/handle/10852/12689/Erichsen_Master.pdf?sequence=1, (accessed 2021-19-10).

90. Bjørgen, M.; Akyalcin, S.; Olsbye, U.; Benard, S.; Kolboe, S.; Svelle, S: Methanol to hydrocarbons over large cavity zeolites: Toward a unified description of catalyst deactivation and the reaction mechanism, Journal of catalysis 2010, 275, 170–180, DOI: https://doi.org/10.1016/j.jcat.2010.08.001.

91. Zeolyst, Zeolite ZSM – 5, https://www.zeolyst.com/our-products/standard-zeolite-powders/zsm-5.html, (accessed 2020-03-14).